# Long-term stability of solid oxide fuel cell cathodes with different microstructures under critical operating conditions

PhD Thesis

Dipl.-Ing. Martin Perz

Chair of Physical Chemistry, Montanuniversitaet Leoben

Supervisor: Assoc.Prof. Dipl.-Ing. Dr. Edith Bucher

June 2018

# Eidesstattliche Erklärung

Ich erkläre an Eides statt, dass ich diese Arbeit selbstständig verfasst, andere als die angegebenen Quellen und Hilfsmittel nicht benutzt und mich auch sonst keiner unerlaubten Hilfsmittel bedient habe.

Seiersberg-Pirka, 09.06.2018

Dipl.-Ing. Martin Perz

# Danksagungen (Acknowledgements)

Zunächst danke ich ganz besonders Assoz.Prof. Dr. Edith Bucher für die exzellente Betreuung meiner Arbeit, die interessante Aufgabenstellung und die unzähligen Hilfestellungen und Anregungen. Mein Dank gilt auch Univ.-Prof. Dr. Werner Sitte für das Ermöglichen der Stelle als Projektmitarbeiter am Lehrstuhl für Physikalische Chemie der Montanuniversität Leoben und die Möglichkeit, meine Arbeit auf mehreren internationalen Kongressen zu präsentieren.

Ich danke allen Kolleginnen und Kollegen des Lehrstuhls für Physikalische Chemie für die freundliche Aufnahme, die konstruktive Zusammenarbeit und das angenehme Arbeitsklima. Insbesondere danke ich DI Nina Schrödl, Dr. Andreas Egger, Dr. Johannes Hofer und DI Christian Berger für die anregenden und oftmals hilfreichen Diskussionen und die Hilfsbereitschaft bei verschiedenen Problemstellungen. Ich danke Karin Stanglauer für die großartige Hilfe bei verschiedenen Tätigkeiten im Labor und die Durchführung von EDX-Analysen. Weiters danke ich Lukas Wiszniewski für die Präparation von Proben und die Durchführung von Impedanzmessungen im Rahmen seiner Bachelorarbeit.

Ich danke Dr. Christian Gspan und Dr. Stefan Mitsche vom FELMI-ZFE Graz sowie Gerhard Hawranek vom Department Metallkunde und Werkstoffprüfung der Montanuniversität Leoben für die Durchführung von (S)TEM und SEM-Analysen und insbesondere die Möglichkeit, bei diesen Analysen selbst dabei sein zu dürfen. Weiters danke ich Martina Dienstleder vom FELMI-ZFE für die gelungenen TEM-Präparationen meiner oftmals komplexen Proben.

Mein Dank gilt natürlich auch der Österreichischen Forschungsförderungsgesellschaft (FFG) und AVL List GmbH, welche diese Arbeit im Rahmen der Forschungsprojekte ELTSECCS, ASYSII und SOFC-SALT finanziell ermöglicht haben.

Schließlich möchte ich von ganzen Herzen meiner Familie danken. Ich danke meinen Eltern und meiner Schwester, dass sie mich auf meinem Weg immer begleitet und unterstützt haben. Ich danke meiner Tochter Luisa und meinem Sohn Emil, dass sie mich auf Trab halten und mir neue Sichtweisen auf das Leben eröffnet haben. Zu guter Letzt danke ich dir, Kristina, von ganzem Herzen für die Liebe, die du mit mir teilst und die Geduld, die du mir entgegenbringst.

# Abstract

Solid oxide fuel cells (SOFCs) are promising electrochemical power sources with potentially high efficiency. However, long-term performance degradation of SOFC stacks in operation is a critical issue for the commercial application of this technology. Especially the cathode is a sensitive component of the fuel cell, which can be affected by several stability issues.

The goal of this work was to investigate the impact of potentially critical operating conditions on the long-term performance of SOFC cathodes, and the influence of the cathode architecture and morphology on the degradation. Long-term degradation experiments were carried out in timeframes between 1500 and 4000 h at temperatures between 700°C and 850°C. The investigated degradation mechanisms were silicon-poisoning and chromium-poisoning in humid atmospheres, as well as the formation of secondary phases at the cathode-electrolyte interface.

The potential cathode materials $La_{0.9}Ca_{0.1}FeO_{3-\delta}$ (LCF91) and $LaNi_{0.6}Fe_{0.4}O_{3-\delta}$ (LNF64) were characterized by conductivity relaxation (CR) in van der Pauw geometry. Electrochemical impedance spectroscopy (EIS) measurements were performed on symmetrical cells with model cathodes of the state-of-the-art materials $La_{0.6}Sr_{0.4}CoO_{3-\delta}$ (LSC64) and $La_{0.6}Sr_{0.4}Co_{0.2}Fe_{0.8}O_{3-\delta}$ (LSCF) in three different architectures: Conventionally screen-printed cathodes, thin-film cathodes with thicknesses around 0.2 μm and infiltrated nanoscaled LSC64 inside a porous backbone of gadolinia-doped ceria (GDC). In order to identify the causes of degradation, post-test analyses with SEM, STEM and XPS were performed on fresh and degraded samples.

For Si-poisoning experiments, quartz glass parts were used as Si source and test gas mixtures of $O_2$ and Ar were humidified to enable formation and transport of volatile Si-species. In all of these experiments humidity affected the cathode performance negatively, but the observed degradation rates were strongly dependent on the cathode morphology. While the dense bulk samples of the CR experiments and the well-defined thin-film model cathodes with relatively low surface/bulk ratio showed a relatively strong performance decrease, the degradation of porous screen-printed and infiltrated cathodes with high surface/bulk ratio was quite low to almost negligible.

For Cr-poisoning experiments, wires of an Fe-Cr-Ni alloy were used as Cr-source and ambient air as testing atmosphere. Due to humidity, volatile Cr-species were formed and transported in the reactor. In these experiments, fast degradation was observed for all characterized cathode morphologies, but thin-film cathodes degraded at a higher rate than conventional screen-printed cathodes.

Degradation of the cathode-electrolyte-interface was investigated on samples with yttria stabilized zirconia (YSZ) electrolytes and LSC64 cathodes. As expected from similar findings in literature, this material combination caused a strong degradation due to formation of secondary phases at the interface. The cathode architecture had a significant influence as well, since thin-film cathodes degraded much faster than conventional screen-printed cathodes.

# Table of Contents

# 1 Introduction

We live in a time, where mankind has reached a state of wealth and development as never before in history. This is a gratifying process, which continues rapidly and is bringing more and more people out of poverty, but brings also challenges. One of the key issues today, which is inseparably linked to technical progress, is the world-wide growing demand for energy in the context of the existing problem of global warming, which is especially triggered by $CO_2$ emissions. In this situation, measures to reduce $CO_2$ emissions in power generation are necessary, especially in the countries of the so-called western world, which are still the largest energy consumers on the global scale. In this context fuel cell technologies could play an important role in the future energy systems.

Amongst other fuel cell concepts, solid oxide fuel cells (SOFC) are a promising technology. SOFCs are made of solid oxide ceramics, which are operated at temperatures between 600°C and 1000°C and can be powered by a variety of possible fuels. They provide an efficient way to convert chemical energy of fuels into electrical power, with potential electrical efficiencies of 50-60% and total net efficiencies up to 80%, when the excess heat is used [1]. SOFC technology is already used or at least tested in stationary applications for power plants in different dimensions [2, 3], but also in mobile and automotive applications [4, 5]. Nevertheless, SOFC development is still an active field of research where many discoveries are made. Concepts for new materials and synthesis routes are actively studied to further improve efficiency of the technology.

An issue, which is also of high relevance for the commercial utilization, is the long-term stability of SOFCs. Due to critical operating conditions, the power output of SOFCs can decrease. This behavior is practically impossible to suppress completely but can be slowed down to a reasonable level. To achieve this, it is necessary to understand the actual mechanisms which are causing the degradation. However, studying these effects is often challenging since it requires long experimental times, especially when the degradation is slow and becomes critical after a few thousand hours. Therefore, there are still many open questions on the topic of long-term stability.

The goal of the present thesis was to study the long-term stability of selected SOFC cathodes under critical conditions, which are close to real operating scenarios in SOFCs. New cathode materials, which according to literature show promising attributes in the short-term range, were characterized with respect to the time-dependent development of their kinetic parameters over time under degradation conditions. For electrochemical measurements, model cells were fabricated, which contained cathodes with different designs and either a porous microstructured, or a dense nanostructured morphology. Long-term experiments with different degradation modes were performed to investigate the development of the cathode polarization resistance over time and compare the influence of different cathode architectures and morphologies on the degradation. Pre- and post-test analyses by various complementary methods allowed for deeper insights into the mechanisms of degradation on the micro- to nano-scale.

# 2 Theoretical aspects

## 2.1 Solid oxide fuel cell (SOFC)

### 2.1.1 Basic principles

Solid oxide fuel cells are electrochemical cells which are made of oxide ceramics and operated at elevated temperatures up to 1000°C [6, 7]. As for every fuel cell, the working principle of an SOFC is the transformation of chemical energy of a fuel into electrical energy by electrochemical reactions. In case of the SOFC, the electrochemical reactions are happening as follows [6, 8, 9]: At the cathode, oxygen from the air is reduced to oxide ions, which are incorporated into the solid oxide structure:

$$O_2(g) + 4e^- \leftrightarrow 2O^{2-} \tag{1}$$

At the anode, a fuel, for example hydrogen, is oxidized:

$$2H_2(g) + 2O^{2-} \leftrightarrow 2H_2O(g) + 4e^- \tag{2}$$

Equations (1) and (2) form a redox pair, which can be combined to the well-known hydrogen combustion reaction:

$$2H_2(g) + O_2(g) \rightarrow 2H_2O(g) \tag{3}$$

By the separation of the oxidation and the reduction process, the free enthalpy of the reaction is transformed into electrical energy, which can be used in a controlled way, instead of releasing it uncontrollably in form of heat. The electrical output of a fuel cell is determined by the principles of electrochemistry. A basic parameter is the electromotoric force (EMF) or open circuit voltage (OCV), which can be calculated by the Nernst equation. In case of an SOFC, the Nernst equation is defined as follows:

$$OCV = E^0 - \frac{RT}{4F} ln\left(\frac{p(H_2O)^2}{p(H_2)^2\, p(O_2)}\right) \tag{4}$$

Here the OCV is dependent on the $p(O_2)$ gradient between the cathode side, which is usually exposed to ambient air, and the anode, where the fuel is supplied. The OCV of an SOFC is in the range of 1 V under usual operating conditions (800°C, hydrogen as fuel). As the name indicates, the OCV is the voltage of the cell when no current is flowing. When an electric current is drawn from the cell under real operating conditions, the SOFC shows a characteristic I-U curve, which indicates significant power losses. A typical trend of the cell voltage as function of the current is sketched in Figure 1 b).

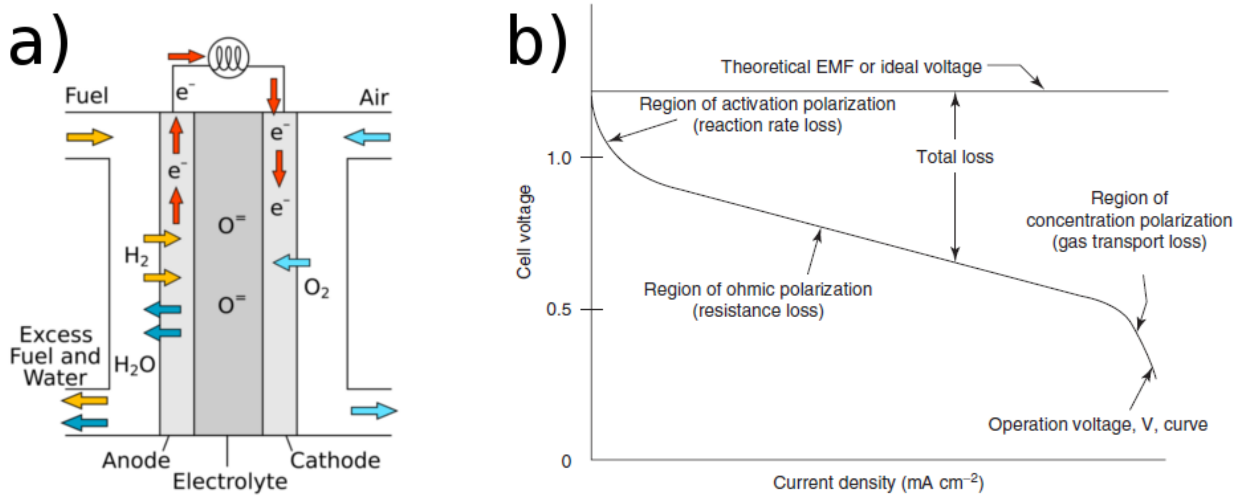

*Figure 1 a) Working principle of an SOFC, b) typical trend of voltage vs. current density of an SOFC, from [10]*

Equation (5) summarizes the losses which decrease the cell voltage U when an electrical current of current density i is flowing:

$$U = \mathrm{OCV} - iR - \eta_{\mathrm{Cathode}} - \eta_{\mathrm{Anode}} \qquad (5)$$

R describes the ohmic losses, which are proportional to i and are mainly caused by the ohmic resistance of the electrolyte of the fuel cell. The polarization losses of the electrodes are denoted as $\eta_{\mathrm{Cathode}}$ and $\eta_{\mathrm{Anode}}$ and are generally not linearly proportional to i. They are linked to specific physical and chemical processes occurring at the cathode and the anode [6, 10]. In principle, all efforts for optimization of SOFCs have the goal to keep these losses as small as possible. This requires the selection of suitable functional materials for the different components of an SOFC as well as a detailed knowledge of the physical and chemical processes.

From equation (1) and (2) it can be seen, that the essential tasks of an SOFC are the exchange of oxygen and the transport of $O^{2-}$-ions inside and between the electrodes. Transport of oxygen ions in solid oxides is a diffusion-based process, which requires point-defects in the oxygen sublattice, so called oxygen vacancies. Due to the outstanding importance of these defects in the electrochemical processes of SOFCs, a brief introduction to the concepts of defect chemistry will be given here.

Point defects in solids are frequently described by using the so-called Kröger-Vink notation, which takes not only the corresponding elements into account, but also lattice sites in solids and partial charges of point defects. This nomenclature is defined in detail by the IUPAC in [11], a short overview of the basics of this nomenclature can be found in [12]. At this point, some examples relevant for the description of processes and components in SOFCs are given to describe the basic concepts. In Kröger-Vink notation equation (1) is expressed as follows:

$$O_2(g) + 4e' + 2V_O^{\cdot\cdot} \leftrightarrow 2O_O^x \qquad (6)$$

$V_o^{\cdot\cdot}$ represents an oxygen vacancy in a solid oxide. The "V" denotes the vacancy, the "O" in the index describes the oxide site in the lattice and the two dots represent the partial charge of the point defect, which is double positive here due to the absence of an $O^{2-}$ ion at the lattice site. Partially negative charges are denoted by an apostrophe. On the right side of the equation $O_O^x$ represents an oxygen ion, which has been incorporated into the former vacant oxygen site, the "x" emphasizes the charge neutrality of the defect. Compared to equation (1), equation (6) delivers additional information, since it describes not only the reduction of $O_2$ but also the incorporation of $O^{2-}$ into the lattice by annihilation of oxygen vacancies.

In a similar way, the anode reaction (equation (2)) can be expressed in defect chemical notation as follows:

$$2H_2(g) + 2O_O^x \leftrightarrow 2H_2O(g) + 2V_O^{\cdot\cdot} + 4e' \qquad (7)$$

From the equations (6) and (7) the necessary properties for SOFC cathodes and anodes with respect to electrochemistry can be read out: SOFC electrodes must be ionically as well as electronically conductive to provide oxygen vacancies and electrons for the corresponding oxidation or reduction process. To enable supply of gaseous species (oxygen from air at the cathode, fuel at the anode) the microstructure has to be porous. Since oxygen vacancies are produced at the anode and annihilated at the cathode, a permanent transport of oxygen vacancies has to be sustained between the electrodes, while the electrical current is flowing over an external consumer. Therefore, the solid electrolyte must have a significant ionic conductivity but no electronical conductivity. Additionally, the electrolyte separates the gas spaces of the cathode and the anode, so it must have a high density (negligible porosity) and should be free of macroscopic defects like cracks.

Besides the porous cathode, the dense electrolyte and the porous anode, additional components are necessary for a functioning SOFC system. Since the voltage output is usually in the range of 1V, it is necessary to interconnect many single cells in series to get a usable power output. Usually, many planar SOFC single cells are stacked together, forming an SOFC stack. Interconnector plates with gas channels are placed in between the cells for electrical contact and for the supply of anode and cathode gases. For separation of the two gas volumes, sealants are applied.

This variety of components makes an SOFC stack a rather complex system. Besides the functional properties of the individual materials, the following requirements have to be met for all components used in the stack: Materials have to be thermodynamically stable under the operating conditions (temperatures between 600°C and 1000°C, oxidizing or reducing atmosphere or large $p(O_2)$ gradients). For mechanical stability, the thermal mismatch between the components, caused by different thermal expansion coefficients (TEC) should be as low as possible, so all materials should have a similar TEC. Thermal mismatches introduce mechanical stresses at heating and cooling, which are unfavorable for the lifetime of the fuel cell.

A critical and rather complex topic is the chemical compatibility between the different components and materials. There are many possible side reactions leading to undesirable secondary phases, which might reduce the performance of single components, and therefore increase the power losses of the whole stack. These could be solid-state reactions at interfaces, but also contaminations from outside, brought into the stack by the fuel or the cathode gas, as well as gas transport phenomena leading to cross-contaminations. The present thesis focuses on several of these degradation mechanisms, which are affecting SOFC cathodes. A more detailed overview over such degradation mechanisms, which are affecting the cathode performance, will be given in section 2.2.4.

### 2.1.2 Materials for SOFCs: Electrolytes, anodes and interconnectors

As described in section 2.1.1, an SOFC is a rather complex system of multiple compounds. Therefore, a basic understanding of all the components and possible compatibility issues between them is necessary for understanding and improving SOFC systems. The following section gives a short introduction of the basic components and materials used in SOFC today. The SOFC cathode, which is the main topic of interest in the present thesis, will be described in more detail in section 2.2.

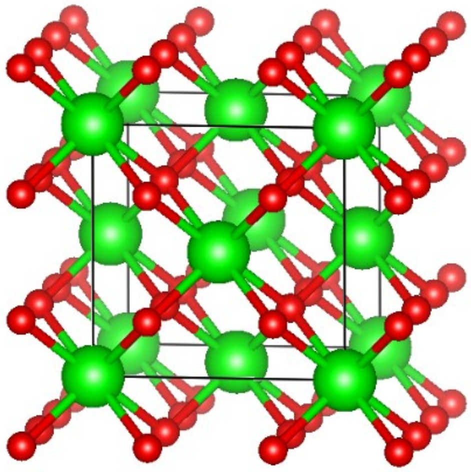

*Figure 2: Cubic fluorite structure, the typical crystal structure of most solid oxide electrolyte materials (Image generated with VESTA 3 [13])*

State-of-the-art solid electrolytes for SOFCs are based on doped zirconia. The most commonly used electrolyte material is yttria-stabilized zirconia (YSZ), $ZrO_2$ doped with $Y_2O_3$. This is a material, which is widely used as oxygen conductor for sensors, but also as structural ceramic material for various other applications. Doping zirconia with yttria has two purposes: On the one hand, the cubic fluorite phase (Figure 2), which is the high-temperature phase of pure zirconia, is stabilized at lower temperatures, which is a feature of interest for structural ceramic applications. On the other hand, the doping causes the formation of oxygen vacancies in the lattice, which is of high interest for SOFC electrolytes and various other electrochemical applications. The oxygen vacancy generation is a defect chemical phenomenon caused by partially negative lattice charges introduced by yttria doping due to the lower valence of the $Y^{3+}$-Ion compared to $Zr^{4+}$. These charges are compensated by oxygen vacancies, which have a positive charge. In Kröger-Vink notation, the defect chemical reaction is described as follows:

$$Y_2O_3 \overset{ZrO_2}{\longleftrightarrow} 2Y'_{Zr} + 3O_O^x + V_O^{\cdot\cdot} \tag{8}$$

[6]. Usually, a composition with 8 at-% yttria in zirconia (8YSZ) is used as electrolyte material due to its good mechanical stability and its reasonably high ionic conductivity [1, 14]. The TEC of YSZ is about $10\times10^{-6}$ $K^{-1}$ [15, 16].

Besides YSZ, there are several approaches for alternative electrolyte materials. The most common alternative electrolytes are based on doped ceria, for example $Ce_{1-x}Gd_xO_{2-\delta}$ (gadolinia-doped ceria, GDC) [17] or $Ce_{1-x}Sc_xO_{2-\delta}$ (scandia-doped ceria, SDC) [18]. The defect chemical mechanisms of doping ceria are in principle equivalent to the doping of zirconia, as described in equation (7). While zirconia- and ceria-based materials are crystallizing in the fluorite structure, there are also electrolyte materials with perovskite structure. The most common to name here is lanthanum gallate doped with strontium and magnesium ($(La,Sr)(Ga,Mg)O_{3-\delta}$, LSGM) [19]. These materials show a higher ionic conductivity than YSZ. However, there are several issues preventing a full replacement of YSZ electrolytes. Doped ceria shows an increasing (and undesirable) electronical conductivity at low $p(O_2)$, which is the case under the reducing conditions of an SOFC anode [18]. With LSGM there are several chemical stability issues under typical SOFC operating conditions. A more common use for these materials, which has been widely adopted in commercial SOFCs, is the application of double-layer structured electrolytes, where a conventional YSZ electrolyte is covered by a layer of GDC or LSGM on the cathode side, which acts as diffusion barrier to prevent unfavorable solid-state reactions between the cathode material and YSZ [20]. However, in basic research for SOFC cathodes, doped cerias are frequently used as electrolytes of model cells which are operated only under cathodic conditions. Model cells with GDC as electrolyte and substrate have also been used for the major part of the experimental investigations of the present thesis, as described in section 3.2.1.

State-of-the-art SOFC anodes are made of a porous composite structure, which is a mixture of YSZ and metallic Ni [21]. While this cermet composite approach has been widely used in commercial SOFC systems, other materials and concepts for SOFC anodes are actively explored. The investigated approaches range from simple modifications of the Ni-YSZ cermet to completely new material concepts, for example composites of nickel and doped ceria or single phase mixed-conducting perovskite anodes [16, 22].

The first SOFCs were built as electrolyte-supported cells (ESC): The electrolyte was the mechanically supporting structure, onto which anode and cathode were put as functional films. This design has the disadvantage that a high electrolyte thickness results in a high ohmic resistance. Today, the state-of-the-art cell design is the anode-supported cell (ASC). In this design, the anode is the mechanically supporting structure and the electrolyte is reduced to thicknesses of a few µm to keep its ohmic resistance as small as possible [21]. The cathode is a functional layer on top of this structure. Another cell design which has gained increasing interest in SOFC development is the metal-supported cell (MSC): Here the metallic interconnector becomes the mechanically supporting substrate, onto which the electrochemical components are put as thin functional layers [23-25].

## 2.2 SOFC cathodes

The cathode is one of the most critical components of the SOFC system. It has the highest contribution to the polarization losses of a cell, as described in equation (5). Most of the known long-term stability issues of SOFCs are related to the cathode. Therefore, the SOFC cathode is a topic of active research.

The following sections give an overview over state-of-the-art cathode materials and new material concepts. Different approaches for cathodes in micro- and nanostructured morphologies and the corresponding methods for synthesis will be described. Finally, a comprehensive overview over the most critical degradation mechanisms, which have been investigated in the scope of the present thesis, will be given.

### 2.2.1 State-of-the-art cathode materials

#### *2.2.1.1 General properties*

Most state-of-the-art cathode materials are oxides crystallizing in the perovskite structure. Generally, perovskites have the chemical formula $ABO_3$. Figure 3 shows an elementary cell of the cubic perovskite structure. In this representation, the oxide ions are positioned on the faces of the cube. It is a convention that the atom positions on the corners, which have a 12-fold coordination, are denoted as A-site and those in the center with 6-fold coordination are the B-site. While the A-site cations are typically rare earth or alkaline earth elements, the B-site elements are d-block elements (transition metals). It has to be noted that the cubic perovskite structure is an idealization for illustration here, since most of the cathode materials are crystallizing in rhombohedrically, tetragonally or orthorhombically distorted perovskite structures.

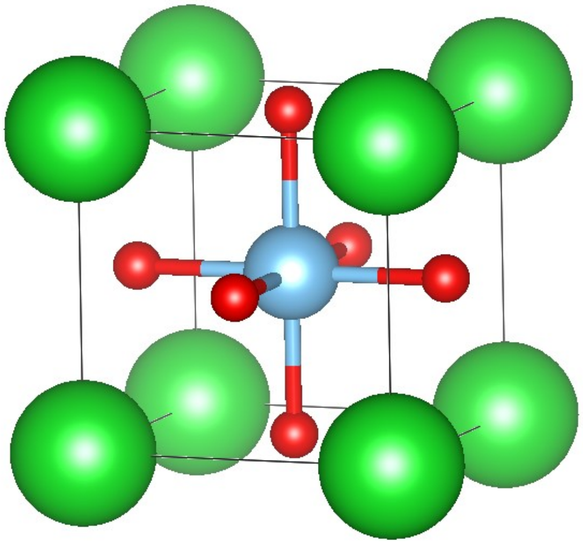

*Figure 3: Elementary cell of the cubic perovskite structure (Image generated with VESTA 3 [13])*

In general, cathode materials are solid solutions, where the A-sites and/or B-sites are occupied by two or more elements. The aim of these substitutions is usually the generation of electrically charged point defects, which are improving the electronic and ionic conductivity of the material. A desired property for cathode materials is the oxygen nonstoichiometry, which is caused by high concentrations of oxygen vacancies. The nonstoichiometry is denoted by the index “3-δ” for O in the chemical formula [26].

#### 2.2.1.2 $La_{1-x}Sr_xMnO_{3\pm\delta}$ (LSM)

In earlier SOFC developments, cathodes were made of porous layers of Sr-doped lanthanum manganate ($La_{1-x}Sr_xMnO_{3\pm\delta}$, LSM) on the YSZ electrolyte. LSM is an oxide with perovskite structure, where La on the A-sites is partially substituted by Sr. It is widely used due to several beneficial properties: It has a good thermal and chemical stability at operating conditions, high electronic conductivity, and a high catalytic activity for oxygen reduction at high temperatures. The TEC of LSM-based cathodes is about $11\times10^{-6}$ $K^{-1}$, which is close to that of YSZ [15]. The material is also chemically inert to YSZ electrolytes when the Sr doping level is below 30% [27]. However, the ionic conductivity of this material is rather low, so the oxygen reduction reaction is locally limited to the triple-phase boundaries (TPB), where a pore, the LSM and the YSZ electrolyte are in contact [1, 27]. Additionally, surface diffusion of adsorbed oxygen species on LSM grains to the TPB might be a rate-limiting step of the cathode reaction [28]. An improvement of cathodes using LSM are composite-cathodes, where an ionically and an electronically conducting material are mixed in a fine-grained and porous structure. With this approach, the total length of TPB is increased, which improves the cathode performance [29-32]. Thus, LSM-based state-of-the-art cathodes for high-temperature SOFCs are fabricated as LSM-YSZ composites. Anyway, the operating temperatures have to be above 800°C to get a reasonably small polarization resistance below 0.5 Ωcm² [32].

### 2.2.1.3 $La_{1-x}Sr_xCoO_{3-\delta}$ (LSC) and $La_{1-x}Sr_xCo_{1-y}Fe_yO_{3-\delta}$ (LSCF)

A main goal of SOFC development in the last two decades has been the reduction of the operating temperature to a range between 500°C and 800°C to reduce costs and complexity and improve the long-term stability of the SOFC system [33]. SOFCs working in this temperature range are often denoted as “intermediate temperature SOFCs” or IT-SOFCs [1, 34, 35]. For a sufficiently good cell performance at reduced temperatures, lowering the polarization resistance of the cathode is necessary. This is achieved by using mixed ionic-electronic conductors (MIECs) as cathode materials, instead of the purely electronically conducting LSM or LSM-YSZ composites.

The most common materials of this class, which have been studied intensively, are perovskites based on Sr-doped lanthanum cobaltite ($La_{1-x}Sr_xCoO_{3-\delta}$, LSC) [36-38]. The mixed-conducting behavior of these materials can be explained by defect chemistry: By substitution of $La^{3+}$-ions with $Sr^{2+}$, a partially negative charge is induced on the A-site positions (denoted as $Sr_{La}'$ in Kröger-Vink notation), which is compensated either by oxidation of cobalt ions in the lattice ($Co_{Co}^{\cdot}$), or by the introduction of oxygen vacancies ($V_O^{\cdot\cdot}$). While the former delivers p-type charge carriers for electronic conductivity, the latter causes ionic conductivity. Both compensation mechanisms occur simultaneously, but the individual concentrations of these defects are strongly dependent on temperature and $p(O_2)$ [38]. In the LSC series , $La_{0.6}Sr_{0.4}CoO_{3-\delta}$ (LSC64) shows the highest electronic conductivity [37] and fast oxygen reduction kinetics [38, 39].

However, a critical disadvantage of LSC is the high TEC, which is $20\times10^{-6}$ $K^{-1}$ [1, 15]. This TEC is significantly higher than those of common solid electrolyte materials. Materials based on Sr-doped lanthanum ferrite ($La_{1-x}Sr_xFeO_{3-\delta}$, LSF) show a slightly smaller TEC than the equivalent cobaltites [40], however their oxygen reduction kinetics are significantly slower [41]. A compromise between these two requirements are solid solutions of La-Sr-cobaltites and -ferrites ($La_{1-x}Sr_xCo_{1-y}Fe_yO_{3-\delta}$, LSCF) [40, 42, 43], which are the most widely used MIEC materials for IT-SOFC cathodes. However, there are alternative approaches to overcome the thermal mismatch issue by different cathode morphologies, which are presented in section 2.2.3.

There are some issues with LSC and LSCF, which have a negative influence on the long-term stability of these materials under operating conditions of IT-SOFCs. A general drawback of LSC and LSCF compared to LSM is the high reactivity with YSZ electrolytes, which is causing the formation of secondary phases (zirconates) during heat treatment in fabrication, but also during cell operation, which are blocking oxygen transport at the cathode-electrolyte interface [44, 45]. Another issue with LSC and LSCF is the tendency of Sr to segregate to the surface [46], which could lead to performance losses. These and other effects, which are lowering the performance of cathodes, will be explained in more detail in section 2.2.4.

### 2.2.2 New cathode materials

Despite the fact that LSM and LSC/LSCF are well-known and widely used materials for SOFC cathodes, there are ongoing research efforts in finding alternative cathode materials with improved properties, especially with regard to long-term stability. Since Sr has the tendency of surface segregation, and Co is causing high thermal expansion coefficients, alternative cathode materials without these two elements are considered to be more stable against the commonly known degradation mechanisms (surface poisoning, cathode delamination). In the scope of the present thesis, two alternative materials with perovskite structure are investigated: $La(Ni,Fe)O_{3-\delta}$ (LNF) and $(La,Ca)FeO_{3-\delta}$ (LCF). Basic properties of these two materials are described in the following paragraphs.

#### 2.2.2.1 $(La,Ca)FeO_{3-\delta}$ (LCF)

Many efforts to replace LSCF with alternative materials for SOFC cathodes are based on replacing the A-site dopant Sr with other elements from the group of alkaline earths. This is an obvious approach due to the similarities in chemical properties of elements of the same group. In the last few years, perovskites with Ca instead of Sr on the A-site have gained interest in research. Substitution of $La^{3+}$ with $Ca^{2+}$ on the A-site is considered advantageous to $Sr^{2+}$ in terms of chemical stability, since the mismatch of ionic radii between $Ca^{2+}$ and $La^{3+}$ is lower than between $Sr^{2+}$ and $La^{3+}$, which lowers the driving force for dopant surface segregation [47].

A few studies have been published on $La_{0.9}Ca_{0.1}FeO_{3-\delta}$ (LCF91). Fundamental properties of this material, like oxygen nonstoichiometry and electrical conductivity have been investigated by Geary et al. [48]. They found a rather low, but significant oxygen nonstoichiometry at the $p(O_2)$ level of ambient air.

Possible technical applications were investigated first in the context of oxygen permeation membranes [49-52]. First short-term characterizations under operating conditions relevant for IT-SOFCs revealed promising oxygen exchange parameters [47].

#### *2.2.2.2 La(Ni,Fe)$O_{3-\delta}$ (LNF)*

LNF is a material with perovskite structure, where only the B-sites of the structure are substituted, but no A-site doping is applied. LNF was investigated first by Chiba et al. and has been considered as potential cathode material due to its relatively high electrical conductivity (about 580 S/cm at 800°C) and simultaneously low thermal expansion coefficient, which is in the same order of magnitude as typical electrolyte materials [53]. They found that the composition $LaNi_{0.6}Fe_{0.4}O_{3-\delta}$ (LNF64) has the highest electrical conductivity. Therefore this composition has been investigated further in many studies [54-57].

Despite the large number of publications on LNF64, many properties of this material are still uncertain due to discrepancies of parameters obtained by different authors. For example, experimental values found for the electrical conductivity at IT-SOFC operating temperatures vary in the range between 100 and 600 S/cm in different studies [58]. While Niwa et al. found a relatively high oxygen nonstoichiometry for LNF64 of about 2.90 for the $3-\delta$ index [59], Chen et al. [57] and Sereda et al. [58] found values above 2.99. However, there is general agreement, that the electrochemical performance of LNF64 is significantly lower than that of LSC or LSCF. Therefore, many studies focused on additional optimization strategies, e.g. by infiltration techniques.

LNF64 has been considered as a potential cathode material with high stability against Cr-poisoning [60, 61]. However, there is also contradicting evidence, showing severe degradation of LNF-based cathodes due to Cr-contamination [62, 63].

In the present thesis, the oxygen exchange parameters of LNF64 were investigated by the dc-conductivity relaxation method at temperatures between 500°C and 800°C. In a long-term experiment, the degradation of oxygen exchange kinetics in dry and humid atmospheres was investigated.

### 2.2.3 Alternative cathode architectures with nanostructured morphology

Despite improvements in cathode materials, also the architecture and morphology of SOFC cathodes has a significant influence on the short-term and long-term performance. State-of-the-art SOFC cathodes are designed in layers with a thickness of 10-50 µm with high porosity (typically 30%) and grains of a few microns in diameter. These structures are usually made by screen-printing of inks (fabricated from oxide powders and a liquid organic binder) on an electrolyte or half-cell substrate, and subsequent burn-out of the binder at high temperatures.

In recent years, many investigations have been made on cathodes with layer thicknesses in the sub-µm range and nanostructured morphology. Minimizing grain sizes and dimensions of the cathode to the sub-µm range has two effects, which potentially increase the cathode performance:

By reducing the dimensions, the length of diffusion paths is minimized, so performance losses caused by bulk diffusion are reduced. By minimizing grain sizes down to a few nanometers, the surface area is increased. Since the oxygen reduction reaction is a surface-related effect at MIECs, this means an increase in the kinetics of the reaction.

### *2.2.3.1 Thin-film cathodes*

There are several methods of thin-film deposition, which have been investigated and discussed in literature [64]. A common method for the deposition of thin oxide films is pulsed laser deposition (PLD). By PLD, a target is ablated using a pulsed high-energy laser beam. The evaporated material from the target is deposited on a substrate to form a thin film. A major advantage of this method is the fact that the stoichiometry of the target is well reproduced in the deposited film [64-66]. This makes the method useful for the preparation of thin-film electrolytes and electrodes for SOFCs, which usually have a rather complex chemical composition with well-adjusted dopant concentrations. Disadvantages of PLD are high costs and complexity of the technology. Upscaling the process for mass-production is a difficult task, but there have been efforts to achieve this goal [67]. Due to their well-defined structure and morphology, PLD-derived thin-film cathodes have been a common object for fundamental investigations of the cathode reaction mechanisms [68-72], but have also been suggested as alternative concept for cathodes with lower polarization resistance [73, 74].

Alternative thin-film deposition techniques, which might be more feasible for the mass-production of fuel cells, are based on liquid precursors. This is a common approach in the synthesis of oxide ceramics, where the salts of cations of the desired oxide (e.g. metal nitrates, carbonates or acetates) are dissolved in a liquid solution, as well as additives for homogenization and gelation. The liquid is dried to a polymeric gel film, which is transformed into an oxide layer by annealing. The annealing step is frequently supported by self-combustion of the gel, for example in the glycine-nitrate synthesis. There are various ways to adapt these sol-gel methods to the synthesis of oxide thin-films.

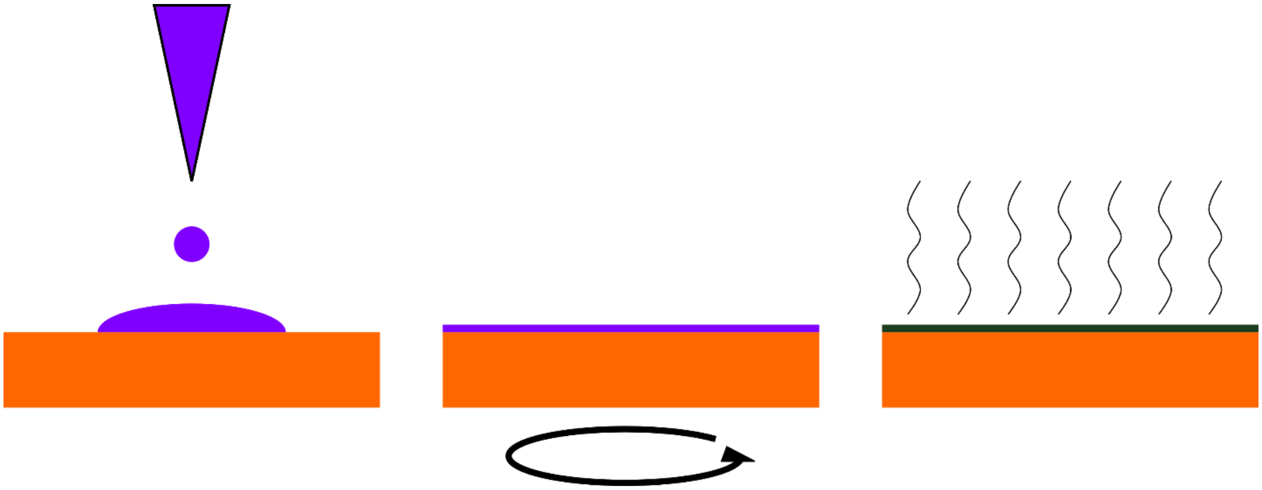

*Figure 4: Schematic representation of the spin-coating process: A liquid precursor solution is dropped on the substrate (left). A thin layer of the liquid solution is formed by rotation (center), which is transformed into an oxide film by thermal annealing (right).*

Amongst others, dip-coating and spin-coating have been investigated as promising methods for the synthesis of very thin oxide films with thicknesses in the sub-µm range. Both methods result in a thin layer of the liquid precursor on the substrate surface. By dip-coating, a substrate is immersed into a precursor solution. At withdrawal from the solution, a thin film of the liquid is adhered on the substrate surface. With spin-coating, the liquid solution is dropped on the surface of the substrate and a homogeneous thin liquid layer is formed by fast rotation of the substrate (Figure 4). The thickness of the layer depends on various parameters of the precursor solution, like viscosity and wetting properties, and parameters of the spin-coater (rotation velocity and time). After deposition, the liquid films are transformed into thin solid oxide layers by drying and annealing. The annealing steps are usually performed at temperatures between 600°C and 800°C within relatively short timeframes [64].

Detailed studies on electrochemical properties of spin-coated or dip-coated thin-film cathodes of LSC have been performed by Peters et al. [75], Januschewsky et al. [76, 77] Hayd et al. [78, 79] and Klotz et al. [80]. In [78] and [79], the morphology (grain size and porosity) of the thin-films was optimized by adjusting temperature and duration of the annealing steps and a polarization resistance of 0.023 $\Omega cm^2$ was found. In a follow-up study, the long-term stability of these cathodes under the influence of humidity and $CO_2$ was investigated [81].

### 2.2.3.2 Infiltrated cathodes

An interesting variant, which combines the classical screen-printing of porous layers with liquid precursor synthesis, are wet infiltration methods. By infiltration, a liquid precursor solution is brought into a porous backbone structure and annealed to form fine particles with diameters of a few nanometers (Figure 5). These methods are widely used in the synthesis of catalysts, but have also been investigated for the development of SOFC cathodes in the last 20 years [82-84]. The infiltration approach has a high flexibility regarding to material combinations and reveals promising properties for SOFC cathodes. It has been demonstrated to improve the performance of LSM cathodes by infiltration with MIECs [85]. Also, MIECs like LSC and LSCF have been used as backbones, where the performance and stability could be enhanced by infiltration with other materials [86, 87].

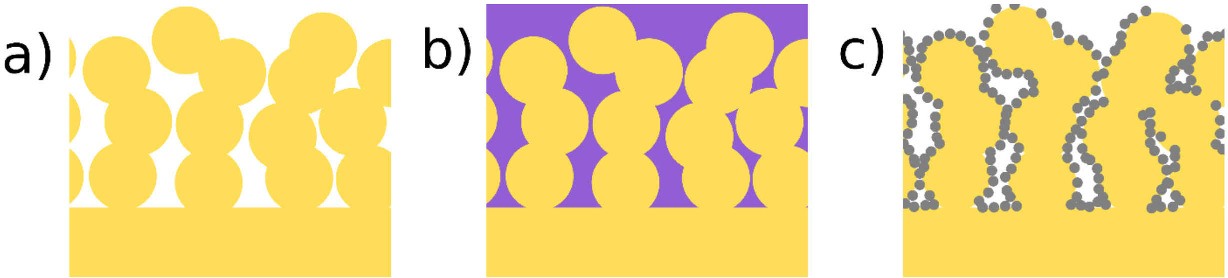

*Figure 5: Schematic illustration of wet infiltration: a) A porous backbone structure is prepared; b) the liquid precursor solution is soaked in the backbone; c) by thermal annealing nanoscaled grains are formed on the surface of the backbone.*

Most of the experiments with infiltrated cathodes found in literature have been performed with an electrolyte backbone infiltrated with an electronically or mixed-conducting cathode material [83]. Cathodes built in this structure show promising properties. Zhao et al. showed that infiltration might be a solution for the issue of thermal mismatch between cathode and electrolyte materials by demonstrating a high durability of cathodes of LSC64 infiltrated into SDC under several heating-cooling cycles [88]. Shah et al. demonstrated a high performance of cathodes with LSCF infiltrated into GDC at 600°C and investigated optimization strategies [89]. In a follow-up work, the long-term performance of these cathodes at different ageing temperatures in ambient air was investigated [90]. In this work, grain coarsening of the nanoparticles was identified as the main source of degradation, but a reasonable long-term performance at the desired temperature for a timeframe of 40.000 hours was predicted. Similar results on the long-term degradation at 620°C of cathodes of LSCF and LSC infiltrated in scandia-stabilized zirconia were found by Zhan et al. [91]. Samson et al. performed tests on anode-supported cells with infiltrated cathodes of LSC in GDC at 700°C and didn’t find any performance degradation at all [92].

### 2.2.4 Cathode degradation mechanisms

A critical issue for the commercialization of SOFC technology is the reliability and long-term stability of the components in an SOFC stack. Several mechanisms are known, which can lead to an increase of performance losses at the cathode [93]. Some of the degradation mechanisms are inherent properties of the cathode materials, but most can be attributed to external contamination effects. The sources of contamination are coming from the cathode atmosphere (e.g. $CO_2$, $H_2O$ and $SO_2$) or from other components of an SOFC stack. The present thesis focuses on degradation mechanisms, which are triggered by humidity in the cathode atmosphere, and degradation effects at the cathode-electrolyte-interface. The most important ones will be described in detail in the following section.

### *2.2.4.1 Strontium-segregation and -transport*

A drawback of state-of-the-art cathode materials doped with Sr, is the tendency of the dopant to segregate towards grain boundaries and the surface [46]. This segregation influences the chemical composition of the MIEC near the surface and therefore the electrochemical properties. Driving forces for this segregation are chemical properties like the mismatch of cation radii as well as electrostatic forces [94]. It could be demonstrated that the segregation could be influenced and partly suppressed by applying a dc bias voltage [95], or by applying mechanical stresses [96].

Another effect, which is related to surface segregation, is transport of Sr through the gas phase. When humidity is present in the cathode atmosphere (which is usually the case for ambient air), volatile strontium hydroxide is formed according to the following equation:

$$\mathrm{SrO\ (s) + H_2O\ (g) \rightarrow Sr(OH)_2\ (g)} \qquad (9)$$

This species is transported via the gas phase, which possibly leads to morphological changes of the cathode affecting the electrochemical performance. This effect has been documented for LSC64 by Hjalmarsson et al. [97] and for LSCF by Tietz et al. [98] in humidified atmospheres. Liu et al. found relatively large amounts of SrO on top of LSCF cathodes which were exposed to highly humidified atmospheres with up to 10 vol-% $H_2O$ [99]. As already mentioned in section 2.2.3, Hayd et al. investigated performance degradation of thin-film cathodes of LSC64 in humid atmospheres [81]. In this study, a significant irreversible degradation of the cathode was demonstrated in presence of $H_2O$ in the atmosphere. No indications for chemical or morphological changes of the surface were found, but it is very likely that Sr gas phase transport played a role in this experiment.

### *2.2.4.2 Chromium-poisoning*

Chromium poisoning is a critical degradation mechanism due to the wide use of metallic interconnectors based on Cr-based or Fe-Cr-based alloys in SOFC stacks [100-102]. These materials have a good thermal stability at typical operating temperatures of IT-SOFCs, due to the formation of passivating $Cr_2O_3$ scales. However, various volatile species, Cr-oxides, -hydroxides and -oxyhydroxides, can be formed out of $Cr_2O_3$ [103]. These species have a negative effect on the cell performance, because they are transported to the cathode and deposited on the surface. This leads to the formation of secondary phases on the cathode surface, which are hindering the oxygen reduction reaction and therefore increase the polarization resistance ("Cr-poisoning").

The most important volatile Cr-species are $CrO_2(OH)_2$ (g) and $CrO_3$ (g) [104]. $CrO_2(OH)_2$ is formed from $Cr_2O_3$ according to the following equation:

$$\mathrm{Cr_2O_3(s) + 1.5\ O_2(g) + 2\ H_2O(g) \rightarrow 2\ CrO_2(OH)_2(g)} \qquad (10)$$

Since $H_2O$ is necessary for the formation of the oxyhydroxide, this reaction predominates in humid atmospheres. In dry atmospheres, the formation of $CrO_3$ (g) is predominant:

$$\mathrm{Cr_2O_3(s) + 1.5\ O_2(g) \rightarrow 2\ CrO_3(g)} \qquad (11)$$

The concentration of $CrO_3$ (g) is much lower than that of $CrO_2(OH)_2$ (g) at typical operating temperatures for IT-SOFCs. For example, at 700°C, the partial pressure of $CrO_2(OH)_2$ is about 0.05 Pa, while the one of $CrO_3$ is only $10^{-5}$ Pa [105]. Therefore, Cr-poisoning is a critical mechanism in humid atmospheres but might also be a long-term issue in dry atmospheres.

The reaction between cathode materials and volatile Cr species has several possible outcomes, like the incorporation of Cr into the perovskite structure, deposition of $Cr_2O_3$ on the surface, or the formation of secondary phases (chromates). All these surface modifications have potentially negative consequences for oxygen reduction kinetics. On perovskite materials containing Sr, like LSM, LSC and LSCF, the preferentially formed product at operating conditions of an IT-SOFC is strontium chromate, $SrCrO_4$. This has been demonstrated in thermodynamic calculations by Yokokawa et al. [106] and experimentally found in various long-term studies [107-110]. This phase is electrically insulating and therefore reduces the oxygen reduction kinetics of the cathode.

The main strategy against Cr-poisoning is the prevention of chromium evaporation from interconnector materials. The formation of the volatile Cr compounds can be minimized to some extent by optimized alloying of interconnector materials. Alloys with a sufficient amount of Mn tend to form a spinel layer of $(Cr,Mn)_3O_4$ on top of the $Cr_2O_3$ scale, which significantly reduces the Cr evaporation [102]. A further reduction can be achieved by actively depositing barrier layers on the surface of the interconnector [111, 112].

Another approach is the development and investigation of alternative cathode materials with higher stability against Cr-poisoning. This is a quite complex task, which is still an active subject of research. The formation of $SrCrO_4$ is promoted by the segregation of Sr to the surface, which is explained in the subsection above [95]. Therefore, a possible strategy against Cr-poisoning could be the selection of cathode materials without Sr. Amongst others, LNF64 has been considered as a potential cathode material with high stability against Cr-poisoning [60, 61].

In the present thesis, the influence of the cathode morphology on the degradation due to Cr contamination was investigated. For these studies Cr-poisoning experiments were performed on model cathodes with different nanostructured and microstructured morphologies.

### 2.2.4.3 Silicon-poisoning

Another possible degradation mechanism for SOFC cathodes is silicon-poisoning. It is a contamination effect similar to Cr-poisoning, which takes place when sources of Si are present in the volume of the cathode atmosphere, which has a significant level of humidity. In this case, the volatile species is silicon hydroxide $Si(OH)_4$, which is formed from $SiO_2$ at elevated temperatures under oxidizing conditions in presence of water according to the following reaction:

$$\mathrm{SiO_2(s) + 2\ H_2O\ (g) \rightarrow Si(OH)_4\ (g)} \qquad (12)$$

[113]. Other species, like SiO(OH), are present in significant amounts only at temperatures far above 1000°C [114] and are therefore not relevant for IT-SOFC operating conditions. Possible Si-sources in SOFC stacks are glasses or glass-ceramics, which are widely used as sealants [115]. When volatile Si species are present in the cathode gas, Si can be transported to the cathode, where it is deposited on the surface. Si is mainly deposited in the form of thin silicate layers, which are electronically and ionically isolating and therefore block oxygen exchange.

Si-poisoning of LSCF has been reported first on oxygen permeation membranes, which were operated for a few thousand hours at 800°C [116, 117]. In these studies it was found that the deposited Si formed a mixed silicate phase with Sr in a thin layer on the surface. This phase formation is eventually triggered by segregation of Sr.

Several studies by Bucher et al. revealed that Si-poisoning is an issue as well at operating conditions for IT-SOFCs. During long-term experiments with conductivity relaxation measurements (as described in 2.3.1) with LSC and LSCF, a strong degradation of the oxygen reduction kinetics was demonstrated at temperatures between 600°C and 700°C in humid atmospheres, which could be attributed to the transport and deposition of Si [118-120]. Post-test analyses of samples from these experiments showed that thicknesses of only a few nm for the silicate layer have a significant influence on the cathode degradation [121].

Despite this evidence for the significant influence of Si on the oxygen exchange activity of MIECs, Si-poisoning has drawn less attention in research on SOFC cathodes than Cr-poisoning. One reason for this might be that traces of Si are hard to detect in presence of large amounts of Sr, since both elements have a similar X-ray energy in EDX spectra [121]. Another reason might be that the morphological and geometrical properties of the tested samples in conductivity relaxation (CR) experiments are different from those of impedance analyses or cell tests. While with CR, dense bulk samples of MIECs of about 0.5 cm in diameter are characterized, typical cathodes have a porous morphology with high specific surface areas and might have cross-sectional areas of ~100 $cm^2$, depending on the format of the cell. These parameters might have a significant influence on the degradation rates under Si-poisoning conditions.

To investigate the influence of the cathode morphology on the degradation due to Si-poisoning, long-term impedance spectroscopy measurements were performed on model cathodes of LSC64 under conditions similar to those of CR experiments described in [119] and [120]. Additionally, long-term CR experiments similar to [119] and [120] were applied on samples of new potential cathode materials to investigate their sensitivity to Si-poisoning.

#### 2.2.4.4 Degradation at the cathode-electrolyte interface

As already mentioned in section 2.2.1, a fundamental issue with LSC and LSCF is the instability of these materials in direct contact with Zr-based solid electrolytes. When the cathode material and the zirconia are in direct contact at typical SOFC operating temperatures, secondary phases like $La_2Zr_2O_7$ or $SrZrO_3$ can be formed at the interfaces [44, 45, 122]. These phases are blocking the transport of oxygen ions and therefore reducing the electrochemical performance of the cell. As already explained in section 2.1.2, the usual way to avoid these reactions is the application of a bilayer structure for the electrolyte, where a diffusion barrier layer separates the YSZ electrolyte and the cathode. This diffusion barrier is usually made of doped ceria like $Ce_{0.9}Gd_{0.1}O_{2-\delta}$ (GDC) [42, 123], but other ionically conducting materials have been investigated for this task as well [20]. However, such a barrier might not suppress the zirconate formation completely. Several studies documented the formation of $SrZrO_3$ at these interfaces due to Sr diffusion, even through the GDC barrier layer, during sintering [45, 124, 125].

A question of interest in this context is, whether these interfacial reactions takes place only during sintering of the cathode, which is typically performed at temperatures above 1000°C, or also during cell operation, at temperatures of 800°C or below. If these reactions were limited to high temperatures, alternative synthesis routes without the need of high temperature sintering steps, as described in section 2.2.3, could be an interesting and cost-effective alternative to the barrier-layer approach. However, there are partly contradictory interpretations on the question. Tu et al. investigated the reactivity of LSCF (and similar perovskites) and YSZ at temperatures between 800°C and 1000°C for 96 hours in air. They found that $SrZrO_3$ was formed at 900°C and 1000°C, but no interface reaction took place at 800°C [126]. On the other hand, Mai et al. found the formation of $SrZrO_3$ after 360 hours in air at 800°C [45]. Dieterle et al. investigated spin-coated thin-films of LSC on YSZ, which were prepared with rapid thermal annealing at max. 900°C and long-term annealed at temperatures between 700°C and 1000°C. They found $SrZrO_3$ on all characterized samples [122]. To further investigate the impact of operating conditions on the interface degradation, long-term degradation experiments with model cathodes of LSC on YSZ substrates were performed in the scope of the present thesis.

# 2.3 Electrical and electrochemical characterization

## 2.3.1 DC-conductivity and conductivity relaxation measurements

From the electrochemical point of view the most important material parameters for development and selection of promising materials for SOFC cathodes are the electrical conductivity and oxygen ion transport properties. Since ionic transport in solids is a diffusion-related process, the transport properties can be determined by diffusion experiments. An in-situ method, which is widely used for the characterization of MIECs is electrical dc-conductivity relaxation (CR). In the CR experiment chemical diffusion, i.e. diffusion triggered by gradients of the chemical potential, is induced in a sample and time-dependent changes of the electrical conductivity due to diffusion are observed. It makes use of the effect that the dc-conductivity of a MIEC is usually dependent on the oxygen (vacancy) concentration.

In this experiment, a dense bulk sample of a MIEC is electrically contacted in and exposed to an atmosphere with a defined $p(O_2)$. While an electrical dc-current is applied, and the voltage is measured continuously, the $p(O_2)$ is increased or decreased instantaneously. This leads to a reversible change in the oxygen vacancy concentration, which causes the specific electronic conductivity $\sigma$ of the sample to increase or decrease correspondingly. A sketch of the CR experiment is represented in Figure 6.

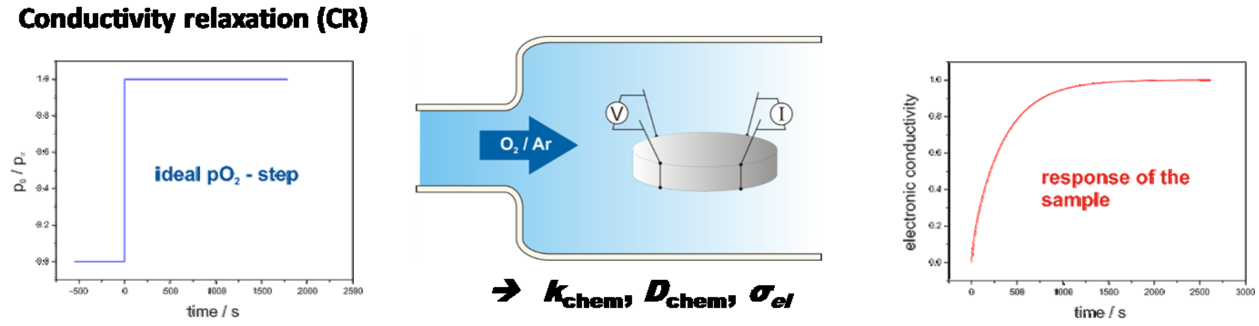

*Figure 6: Measurement principle of the conductivity relaxation experiment (from [127])*

In order to obtain meaningful diffusion parameters from the experiment, the bulk sample must have a well-defined geometry. In the present thesis, CR experiments were performed on samples in van der Pauw geometry, which is also shown graphically in Figure 6. Hereby the samples have the shape of thin plates and are contacted on four points, usually on the corners. This geometry has the advantage, that the relaxation process can be assumed as a one-dimensional diffusion problem. This facilitates the diffusion modelling and also improves the precision, since the only relevant geometric parameter to measure is the sample thickness [128].

In response to the stepwise change in the $p(O_2)$, the conductivity $\sigma$ undergoes a time-dependent relaxation towards a new equilibrium value. The conductivity function is normalized by the following formula:

$$\bar{\sigma}(t) = \frac{\sigma(t) - \sigma_0}{\sigma_\infty - \sigma_0} \tag{13}$$

In this relation $\sigma_0$ is the equilibrium value of the dc-conductivity at the beginning of the $p(O_2)$ step and $\sigma_\infty$ is the conductivity at infinite time. For the latter an average value of σ(t) is chosen from a timeframe, where the relaxation is practically completed. In principle, $\bar{\sigma}(t)$ is directly proportional to the time-dependent profile of oxygen vacancy concentration in the sample during relaxation, c(x,t), which follows Fick's laws of diffusion. Fick's first law describes the flux density of a diffusing species (here $O^{2-}$ ions) in a bulk as function of concentration gradients. In the one-dimensional case it is defined as follows:

$$J = -D_{chem} \frac{\delta c}{\delta x} \tag{14}$$

Here J is the flux density and c is the concentration. $D_{chem}$ is the chemical bulk diffusion coefficient, which describes the kinetics of oxygen diffusion in the bulk. Fick's second law describes the time-dependence of a concentration profile:

$$\frac{\delta c}{\delta t} = D_{chem} \frac{\delta^2 c}{\delta x^2} \tag{15}$$

An assumption for equation (15) is that $D_{chem}$ is constant against concentration. This assumption is valid if the concentration gradients are small. Therefore, the $p(O_2)$ should be increased or decreased only by a small factor in the same order of magnitude. Typical $p(O_2)$-steps are for example between 0.10 and 0.15 bar or between 0.010 and 0.015 bar.

Additionally, a starting condition and a boundary condition are necessary to solve the diffusion problem for a sample with defined geometry. The starting condition is that the vacancy concentration at the beginning of the relaxation process is the equilibrium concentration at the respective $p(O_2)$:

$$c(x, t = 0) = c_0 \tag{16}$$

In case of a thin plate sample with thickness 2a the following boundary conditions for the flux density at the sample boundaries (x=-a and x=+a) apply:

$$J(-a) = -k_{chem}[c(-a) - c_\infty] \tag{17}$$

$$J(a) = k_{chem}[c(a) - c_\infty]$$

Here c(-a) and c(a) are the concentrations at the surfaces and $c_\infty$ is the equilibrium concentration reached after the relaxation. The parameter $k_{chem}$ is the chemical surface exchange coefficient, which describes the kinetics of oxidation or reduction of oxygen on the surface of the sample. For SOFC cathodes, the surface exchange coefficient is one of the most relevant parameters to achieve good performance. The overall oxygen surface exchange process involves several steps like $O_2$-adsorption, dissociation, surface diffusion, reduction and incorporation of oxygen into the crystal lattice, which are not yet fully elucidated. As already explained, the solution for the diffusion problem defined by equations (14)-(17) is the concentration profile $c(x,t)$. The normalized concentration profile is defined analogous to equation (13):

$$\bar{c}(x,t) = \frac{c(x,t) - c_0}{c_\infty - c_0} \tag{18}$$

By integration of $\bar{c}(x,t)$ over the sample volume (or, in the one-dimensional case, the sample thickness) the normalized conductivity $\bar{\sigma}(t)$ is obtained under the assumption, that both parameters are directly proportional. From the solution of the diffusion problem and integration, the following infinite series is found for $\bar{\sigma}(t)$ [129-131]:

$$\bar{\sigma}(t) = 1 - \sum_{n=1}^{\infty} \frac{2L_\alpha^{\ 2}}{\alpha_n^{\ 2}(\alpha_n^{\ 2} + L_\alpha^{\ 2} + L_\alpha)} \exp(\frac{t}{\tau_n}) \tag{19}$$

In this equation, $L_\alpha$ is a dimensionless parameter taking into account the sample geometry (sample thickness 2a) and the kinetic parameters $k_{chem}$ and $D_{chem}$:

$$L_\alpha = \frac{a \cdot k_{chem}}{D_{chem}} \tag{20}$$

The relaxation time $\tau_n$ of the n-th term of the series is defined as follows:

$$\tau_n = \frac{a^2}{D_{chem} \cdot \alpha_n^2} \tag{21}$$

In order to define the individual terms of the series, the eigenvalues $\alpha_n$ have to be calculated. These are defined as the n-th root of the following equation:

$$\alpha_n \cdot \tan(\alpha_n) = L_\alpha \tag{22}$$

An algorithm for an efficient estimation of $\alpha_n$ is explained by den Otter et al. in [132].

The parameters $k_{chem}$ and $D_{chem}$ are the fitting parameters of equation (19). By fitting this function numerically to a measured conductivity relaxation curve, the kinetic parameters of a relaxation experiment are obtained. However, care has to be taken with the rate-limiting mechanism. An accurate simultaneous determination of both parameters $k_{chem}$ and $D_{chem}$ in one experiment is only possible if the relaxation process is mixed-controlled by both bulk diffusion and surface exchange. If one of the two mechanisms is significantly faster, the relaxation is limited either by diffusion or by surface exchange. In this case only one rate-limiting parameter can be calculated accurately.

An indication whether bulk diffusion, surface exchange or both are the rate-limiting mechanism is the parameter $L_\alpha$. If $L_\alpha$ is around 1, the relaxation is mixed-controlled. A large value for $L_\alpha$ relates to a diffusion-controlled process, where the relaxation curve becomes independent from $k_{chem}$. A small value for $L_\alpha$ indicates a surface exchange-limited behavior. As the definition of $L_\alpha$

(equation(20)) indicates, the rate-limiting mechanism can be influenced by the sample dimension a.

As pointed out by den Otter et al, the general solution of equation (19) can be simplified if only one mechanism is rate-limiting [129]. For example, in case of a relaxation limited only to $k_{chem}$ the relaxation curve function simplifies to

$$\bar{\sigma}(t) = 1 - exp(-\frac{k_{chem}}{a}t) \tag{23}$$

## 2.3.2 Electrochemical impedance spectroscopy

Electrochemical impedance spectroscopy (EIS) is a common method to characterize processes in electrochemical systems. In EIS, a defined harmonic ac-signal (current or voltage) is applied to an electrochemical sample, which itself responds with an ac-signal (voltage or current). Since the input and output signals are harmonic sine functions, they can be expressed as complex numbers with magnitude and phase angle. If the voltage U and the current I are expressed by Ohm's law as complex numbers

$$\mathrm{Z} = \frac{\mathrm{U}}{\mathrm{I}} \tag{24}$$

the result is a complex-valued resistor Z which is called the impedance. Since the impedance is usually dependent on the excitation frequency the impedance spectrum can be defined as a complex-valued function of the angular frequency:

$$\mathrm{Z} = \mathrm{Z}(\omega) \tag{25}$$

The impedance spectrum is acquired by measuring the impedance at different excitation frequencies, for example in the range between $10^{-2}$ Hz and $10^{6}$ Hz. For a complete visualization of impedance spectra, a three-dimensional plot is would be principally needed, as shown in Figure 7. Since this kind of plot is not practicable, projections of the three-dimensional data in two dimensions are usually used for data visualization. The most common kind of impedance data visualization is a Cole-Cole plot or Nyquist plot, where the data points are plotted on the complex plane (Im(Z) over Re(Z)). In this kind of plot the impedance spectra often appear as single or multiple semicircles. If this is the case, Cole-Cole plots can be very instructive since ohmic resistances can be estimated quite easily from the diameter of the respective semicircle in the graph. However, the information of the frequency dependence is lost in complex plane plots. To get this information, a frequency dependent projection of the data, a so-called Bode plot is needed. There are four possible variables to plot against the frequency f: The real part and the imaginary part of the impedance, or alternatively the absolute value of the impedance and the phase angle. In the upcoming chapters of the present thesis, most of the impedance spectra will be visualized by Cole-Cole plots and by Bode plots showing Im(Z) over f, since these deliver most of the information needed. Example plots of this kind are shown in Figure 8.

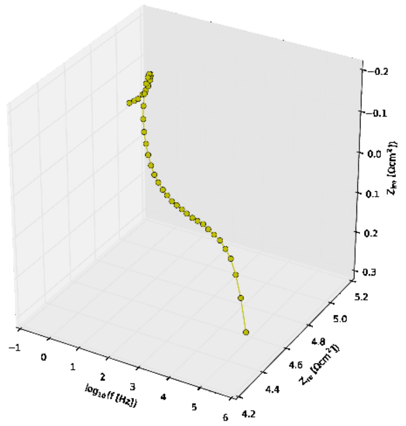

*Figure 7: Three-dimensional example plot of an impedance spectrum*

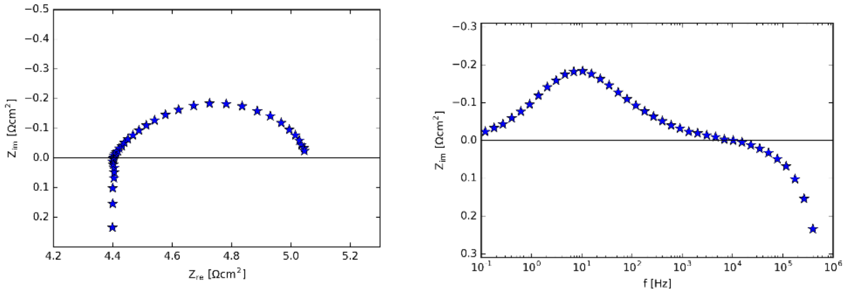

*Figure 8: Examples for a complex plane- or Cole-Cole plot (left) and a frequency-dependent Bode plot (right), showing the imaginary part of the impedance on the ordinate.*

The correct interpretation of an impedance spectrum in terms of physical phenomena may be quite challenging. Generally spoken, the impedance of a sample can depend on multiple processes of mass or charge transport with different relaxation times, which result in a typical impedance spectrum with characteristic peak frequencies. The first step to deal with real impedance data is to find a model function for the impedance spectrum which represents the data best. The usual way of impedance modelling is the definition of an equivalent circuit. The most basic elements known from electrical engineering are ohmic resistors, capacitors and inductors. The impedance of a capacitor $Z_C$ and an inductor $Z_L$ are

$$Z_C(\omega) = \frac{1}{j\omega C} \tag{26}$$

and

$$Z_L = j\omega L \tag{27}$$

with C as the capacitance and L as the inductance. Usually in electrochemical systems only capacitive impedances occur. However, the wiring in experimental setups often results in inductive effects measured at higher frequencies. Therefore, an inductive element is usually necessary in an equivalent circuit.

The easiest way to model an impedance spectrum resulting in a semicircle is an equivalent circuit with an ohmic resistor and a capacitor in parallel, which leads to the following impedance function $Z_{RC}$:

$$Z_{RC} = \frac{1}{\frac{1}{R} + j\omega C} \tag{28}$$

This RC-circuit creates an impedance spectrum, which appears in the form of an undistorted semicircle in the Cole-Cole plot. However, in real impedance data very often suppressed semicircles occur. In this case the data can be modeled by a resistor in parallel with a so-called constant-phase element (CPE). The most common definitions of the impedance function of an RCPE-circuit are

$$Z_{RCPE} = \frac{1}{\frac{1}{R} + (j\omega)^n T} = \frac{1}{\frac{1}{R} + (j\omega Q)^n} \tag{29}$$

Both formulations are equivalent. In the present work the second definition with Q under the exponent is used, wherever an RCPE-element is used in an equivalent circuit. The RCPE-element is a generalized form of the RC-element with the exponent n as additional parameter. The value of n can be between 0 and 1 but should usually be higher than 0.5. When n equals to 1, the RCPE circuit becomes a perfect RC-circuit and T or Q equals to the capacitance. Therefore, these parameters are sometimes called "pseudo-capacitance".

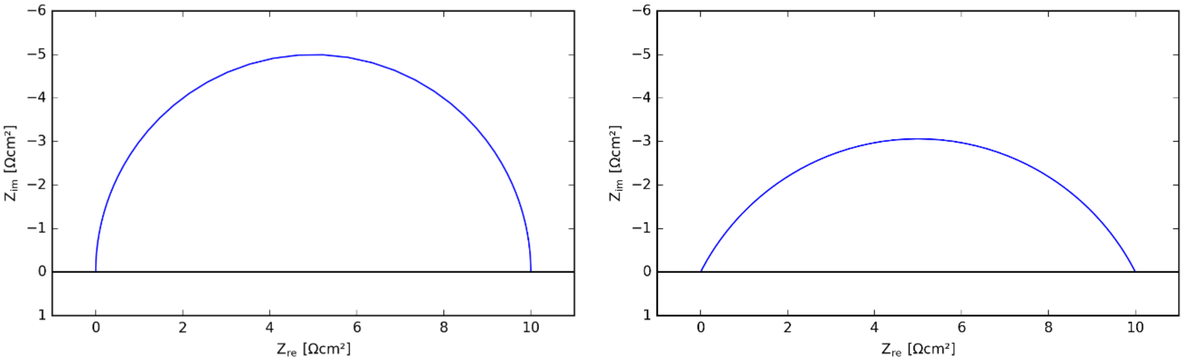

*Figure 9: Impedance spectra visualized in the form of Cole-Cole (complex plane) plots of an R||C circuit (left) and an R||CPE circuit (right)*

RCPEs are used quite often in equivalent circuit modelling. However, the physical interpretation of the RCPE element is not trivial. One of the interpretations is that a suppressed semicircle occurs when the impedance is dependent on processes with a distribution of relaxation times [133].

A special circuit element which has been used in the present work is the Gerischer element. There are two equivalent definitions found in literature. Boukamp et al. use the following definition:

$$\mathrm{Z}_{\mathrm{Gerischer}} = \frac{\mathrm{Z}_0}{\sqrt{\mathrm{k} + \mathrm{j}\omega}} \tag{30}$$

[134]. Adler et al. define the Gerischer-type impedance by

$$\mathrm{Z}_{\mathrm{Gerischer}} = \frac{\mathrm{R}_{\mathrm{chem}}}{\sqrt{1 + \mathrm{j}\omega \mathrm{t}_{\mathrm{chem}}}} \tag{31}$$

[135]. The Gerischer model fits well to porous SOFC electrodes made of mixed conducting perovskites, where the kinetics are controlled simultaneously by the rates of the oxygen exchange process at the surface and by bulk diffusion of oxygen [136]. The two parameters of the Gerischer model, $\mathrm{R}_{\mathrm{chem}}$ and $\mathrm{t}_{\mathrm{chem}}$, are dependent on the kinetic parameters $\mathrm{k}_{\mathrm{chem}}$ and $\mathrm{D}_{\mathrm{chem}}$ as well as on the morphology of the porous cathode.

If the Gerischer impedance is a suitable model element for the experimental data, the Cole-Cole representation of the impedance spectrum appears in the shape of a half-drop with the curve showing a slope of 45° at high frequencies. This is a typical feature in impedance spectra which is a characteristic indication for a diffusion process in a semi-infinite space, also known from the Warburg impedance. At low frequencies it has the shape of an RC element.

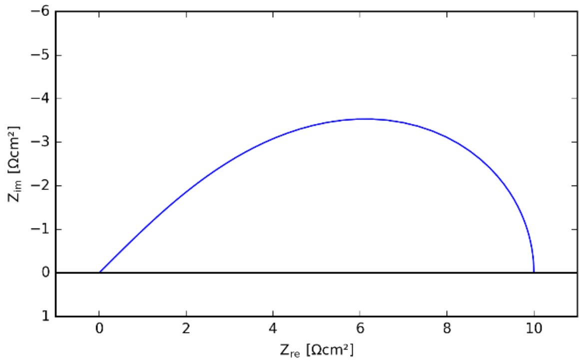

*Figure 10: Impedance spectrum of a Gerischer element*

Similar to the RC circuit, the Gerischer model often doesn't fit perfectly to real impedance data. Therefore, Boukamp et al. proposed a "Fractal Gerischer" model [134]

$$Z = \frac{Z_0}{(k + j\omega)^n} \tag{32}$$

where n ≤ 0.5.

When the data can be described by an equivalent circuit, the next step is the interpretation of the obtained parameters. The goal is to link these parameters to the physical processes which are causing the measured impedance behavior. In this context it is quite helpful to look not only on the resistivities, which are usually the parameters of interest, but also on the capacitances. From the parameters R, Q and n of the R-CPE (see equation(29)), a mean capacitance can be calculated by

$$C = QR^{\frac{1-n}{n}} \tag{33}$$

[137]. In the case of a Gerischer impedance, the chemical capacitance can be obtained from $t_{chem}$ and $R_{chem}$ (see equation (31)) by

$$C_{chem} = \frac{t_{chem}}{R_{chem}} \tag{34}$$

[135]. The order of magnitude of the calculated capacitance gives a hint on the underlying physical mechanism of the respective circuit. An overview of typical capacitive values are given in the following table, which is based on references [137] and [69].

*Table 1: Capacitance fingerprints for processes occurring in fuel cells*

| Order of magnitude of capacitance | Assumed mechanism |
|---|---|
| $10^{-6}$-$10^{-3}$ F/cm² | Charge transfer on the cathode-electrolyte-interface |
| $10^{-3}$-$10^{-1}$ F/cm² | Cathode polarization (oxygen adsorption, surface diffusion, reduction) |
| 1-10 F/cm² | Gas diffusion/transport of oxygen to the cathode and inside pores |

However, these classifications have to be seen as rough estimations, not as general rule. The correct interpretation of impedance spectra requires detailed knowledge of the sample and the measurement conditions.

## 2.4 Analytical methods

### 2.4.1 X-ray diffraction

X-ray diffraction (XRD) is a widely used standard method for the analysis of crystal structures in solids. Diffraction causes a specific pattern of the intensity at characteristic angles. Since X-ray radiation has a wavelength of a few Å, which is in the same order of magnitude as typical interatomic distances, it is diffracted at atomic structures. For crystalline solids the angle of diffraction θ caused by a set of atomic planes with distance d is calculated according to Bragg's law:

$$2\,d\sin(\theta) = n\,\lambda \tag{35}$$

where λ is the wavelength and n is the order of diffraction (usually the first order is used).

By XRD analysis a monochromatic X-ray beam originating from characteristic radiation of elements (usually Cu Kα-radiation) is directed to the sample, which is usually a powder. The intensity of the diffracted radiation is measured as function of the diffraction angle by a detector. In order to extract information about the crystal structure from the diffraction pattern, databases of crystal structures and their corresponding patterns are used. More detailed information about structures can be gained by mathematical modelling approaches like Rietveld refinement [138].

### 2.4.2 X-ray photoelectron spectroscopy

X-ray photoelectron spectroscopy (XPS) is an analytical method which makes use of the photoelectric effect. When a solid sample is irradiated by monochromatic X-ray radiation, electrons are elastically scattered and might escape the solid. By detecting these electrons and measuring their kinetic energy, conclusions on the electronic structure of the sample can be drawn. The information gained from the kinetic energy is the bonding state of the electron in the solid. Therefore, elemental concentrations as well as bondings of chemical compounds can be characterized.

Since photoelectrons are emitted only from a few nanometers below the surface, XPS is an analytical method with high surface sensitivity. This makes the technique suitable for the analysis of thin-film systems. By additional application of sputtering techniques, depth-profiling analyses of solids can be performed [139-141].

### 2.4.3 Scanning electron microscopy and scanning transmission electron microscopy

Electron microscopy techniques are frequently used in structural investigations, imaging, and chemical analyses of solids in orders of magnitude from a few µm down to atomic resolution. Due to its high resolution and the possibility to apply corresponding methods for chemical analyses, it has become a basic analytical tool in solid state chemistry. With scanning electron microscopy (SEM) an electron beam of a few keV is scanned over a solid surface. Interaction of the electron beam with matter leads to the emission of electrons of various kinetic energies, which are detected and analyzed. From the electron signals, information about the sample is delivered and images are generated.

By interaction with the primary electron beam, electrons inside the solid are elastically scattered. Due to a cascade of elastic scattering events inside the interaction volume, a few electrons are emitted and can be detected. These are the so-called backscattered electrons (BSE), which have a kinetic energy of about 0.8 to 0.9 times the energy of the primary electron beam. Since the kinetic energy of BSE is influenced by interaction with atoms in the solid, BSE generated images have a so-called Z-contrast, where regions containing atoms with higher order number appear brighter than those with lighter atoms. Therefore, BSE images deliver qualitative information about the chemical composition to some extent.

The most important sources of topological information are the so-called secondary electrons (SE). These are electrons which are mobilized by inelastic scattering events inside the solid. Due to their low energy of about 0.5 eV, only secondary electrons from a region of 5-10 nm beneath the surface can escape the solid and reach the detector. Therefore, the SE-mode delivers information about the surface topology of the sample.

Besides electrons, characteristic X-ray radiation is generated by excitation of bonded electrons and refilling empty bonding states with electrons from higher orbitals. The spectra of these X-ray signals deliver information on the chemical composition of the sample and can be detected by an energy-dispersive detector (EDX) or a wavelength-dispersive detector (WDX). However, the local resolution of these analyses is limited by the size of the interaction volume of the electron beam with the sample [142].

Scanning transmission electron microscopy (STEM) is a similar technique, which delivers images in higher lateral resolution, but the setup is technically more sophisticated. With STEM, a thin sample with a thickness of a few nm, which is prepared by etching or by a focused ion beam, is scanned by an electron beam. The transmitted electrons are detected and the information is used for imaging.

In principle there are two imaging modes for STEM: In bright field mode, the electrons which are not scattered, or scattered only by small angles, are detected. In dark field mode, electrons which are scattered in a larger angle from the incident beam are detected. These electrons provide additional information on the chemical composition due to Z-contrast. In the scope of the present thesis, most images from STEM are dark field images acquired with a high angle annular dark field detector (HAADF).

Besides imaging, also chemical analysis is possible with STEM. The analysis of characteristic X-ray spectra is performed by EDX and WDX analogous to SEM. Additionally, the energy loss of directly transmitted electrons delivers information about the chemistry of the sample (EELS) [143].

# 3 Experimental

## 3.1 Conductivity relaxation experiments

### 3.1.1 Sample preparation

Powders of $LaNi_{0.6}Fe_{0.4}O_{3-\delta}$ (LNF64) and $La_{0.9}Ca_{0.1}FeO_{3-\delta}$ (LCF91) were synthesized by a glycine-nitrate combustion route, which is described in detail in [47]. The powders were analyzed by XRD in order to ensure phase purity. XRD patterns are shown in Figure 11.

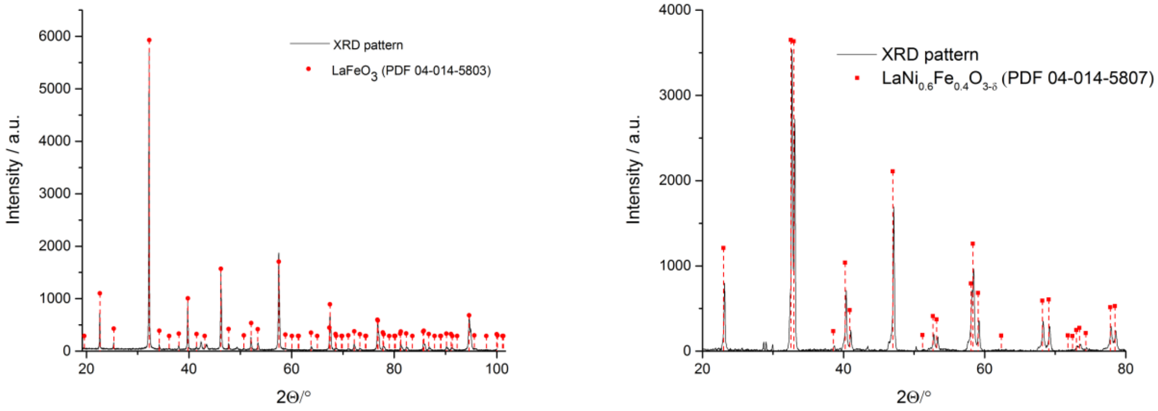

*Figure 11: XRD patterns of LCF91 (left) and LNF64 (right), the peaks were evaluated using the denoted patterns from the PDF4+ database*

The powders were isostatically pressed into cylindrical shapes with a diameter of about 8 mm at a pressure of 2.5 kbar. The pressed pellets were sintered with the following parameters: LCF91 was heated up to 1350°C with a heating rate of 5 K/min, held at this temperature for 2 hours and cooled to room temperature with 5 K/min. LNF64 was sintered at 1250°C for 2 hours with heating and cooling rates of 5 K/min. After sintering the LCF91 sample had a relative density of about 95% of the theoretical density. The relative density of the LNF64 sample was even higher with about 97%.

Thin quadratic plates with an edge length of 5-6 mm and thicknesses below 1 mm were cut out of the sintered pellets by a diamond wire saw. The plates were grinded and polished with diamond lapping sheets to a thickness, where based on previous measurements mixed-controlled kinetics was expected to prevail at a $p(O_2)$ of 0.1 bar (see section 2.3.1 on page 19 about the theory of conductivity relaxation). The thickness of the LNF64 sample was 471 μm, that of LCF91 was 221 μm.

Besides the plate samples for CR measurements, secondary samples of the same material were prepared with the goal to use those for post-test analyses. These samples were small pieces from the sintered pellet with an edge length of 1-2 mm and arbitrary thickness. These samples were polished the same way as the CR samples on one side, so that the surfaces of CR samples and secondary samples was comparable.

The plate samples were electrically contacted in 4-wire mode for van der Pauw conductivity measurements. This was achieved by contacting the corners of the plates with gold wires of 0.1 mm diameter, fixed with a gold ink. The ink was hardened by sintering the samples at 850°C for 10 minutes with heating and cooling rates of 10 K/min. The secondary samples were annealed the same way to keep them in a state comparable to the CR samples.

### 3.1.2 Setup and measurements

The reactor was made of a quartz glass tube with an inner diameter of 12 mm, which was placed in an oven regulated by a Eurotherm temperature controller. The CR samples were attached horizontally in a sample holder (small piece of quartz glass tube) by the Au wires and placed in the reactor. Together with the CR samples also three secondary samples were put into the reactor. These samples, which were used for post-test analyses, were placed nearby the CR sample to ensure that all the samples were exposed to the same conditions during the experiment.

Electrical and electrochemical characterizations were performed in atmospheres with Ar-$O_2$ test gases of different composition, which were brought into the test tubes at flow rates of about 2 liters per hour. For all samples, the electrical conductivity $\sigma$ was measured in test gases with oxygen partial pressures of 0.10 and 0.15 bar and the kinetic parameters $k_{chem}$ and $D_{chem}$ were determined by conductivity relaxation measurements at $p(O_2)$-steps between these two gases. These gas concentrations were chosen with the goal to get meaningful values for $\sigma$, $k_{chem}$ and $D_{chem}$ at atmospheres similar to ambient air, the usual cathode gas. However, in case of the LCF91 sample it was difficult to get trustworthy values for $k_{chem}$ at temperatures above 650°C in this $p(O_2)$ range. To overcome this problem, gas supply was changed to test gases with p(O2) of 0.010 bar and 0.015 bar, and the measurements of the long-term experiment were performed at lower oxygen concentration.

Relaxation curves were evaluated with the mathematical methods explained in Section 2.3.1. These methods were implemented in the *Python* programming language, using various tools for scientific computing, especially *NumPy* [144] and *pandas* for data exchange, *SciPy* and *LmFit* [145] for the data optimization algorithms and the *Jupyter Notebook* as workspace and user interface. Results were visualized with the plotting package *Matplotlib* [146]. By default, all the CR curves were fitted with three different diffusion models, the diffusion-controlled model, the surface-exchange controlled model and the mixed-controlled model. In most cases the data optimization worked with all the three models, but it was possible to identify the most meaningful one by comparison of the residuals and chi² (the sum of the squared residuals). Generally, the relaxation curves were mixed-controlled in the fresh state and surface-controlled when degradation (which specifically affects the surface oxygen exchange activity) had occurred.

# 3.2 Electrochemical impedance spectroscopy experiments

## 3.2.1 Sample preparation

Symmetric cells are a variant of electrochemical half-cells. These are frequently used for electrochemical impedance spectroscopy in order to characterize particular components of an SOFC, for instance the cathode. These half-cells consist of a solid electrolyte substrate (oxygen ion conductor), which is covered on both sides with layers of the electrode to characterize. This is a common approach for the characterization of potential SOFC cathodes since it has a few advantages over full-cell tests: The symmetric cell can be stored in a single gas chamber, so no efforts for gas separation have to be made (in contrast to the a full-cell measurement setup with separated cathode and anode gas compartments). The interpretation of the obtained impedance spectra is also facilitated, since there is no need to separate signals of the cathode and the anode. This is a helpful approach in particular for prototyping and testing new materials or electrode concepts, but of course it doesn't replace necessary tests on full-cells in later, technically oriented stages of the SOFC development.

In the present thesis, SOFC cathodes of LSC64 with different morphologies in the µm- or nm-scale were characterized on symmetrical button-sized cells with diameters between 1.5 and 2 cm. These cells were made of electrolyte substrates of $Ce_{0.9}Gd_{0.1}O_{2-\delta}$ (GDC) or $Zr_{0.92}Y_{0.08}O_{2-\delta}$ (YSZ), coated with different types of cathode layers of LSC64 or LSCF, which were fabricated by three different techniques. Together with the symmetric cells also secondary samples were prepared, which had the same cathode layers as the symmetric cells but were only coated on one side. These specimens were accompanying samples, which were partly exposed to the same conditions as the cells itself and were used for post-test analyses afterwards. In the following sections the preparative steps are described in detail:

### *3.2.1.1 Fabrication of electrolyte substrates*

Substrates of $Ce_{0.9}Gd_{0.1}O_{2-\delta}$ (GDC) and $Zr_{0.92}Y_{0.08}O_{2-\delta}$ (YSZ) were prepared from commercially available powders (GDC: Treibacher Industrie AG, Austria; YSZ: Tosoh Corporation, Japan). The powders were uniaxially pressed: For the GDC disks 3 g of GDC powder was pressed in a form with a diameter of 2 cm at a force of around 1 kN, while for the YSZ disks 2 g of YSZ powder was pressed in a form of 2.5 cm in diameter at 1 kN. The respective uniaxially pressed green body was pressed isostatically in a second step, by putting it in plastic bags into a pressing chamber of 3 cm diameter and applying a force of 241 kN. The disks were sintered at 1450°C for 10 h with a heating rate of 2 K/min and a cooling rate of 1 K/min.

After sintering, the surfaces of the disks were grinded and optionally polished, depending on the desired surface roughness. The surfaces were grinded with SiC paper disks with a roughness up to 600 Grit. The substrates for sol-gel spin-coating were additionally polished with diamond suspensions with grain sizes of 9 µm, 3 µm, and 1 µm to obtain a mirror-smooth surface.

The resulting substrate disks of GDC and YSZ had diameters of 1.6 cm and 1.8 cm respectively and thicknesses between 1 and 2 mm. The relative densities of the samples were higher than 96% for both materials.

#### *3.2.1.2 Screen-printing of micro-scale porous cathode layers*

In state-of-the-art solid oxide fuel cells, the cathode layers are usually fabricated by screen-printing of ceramic inks onto half cells at industrial scale. The inks for this procedure are a mixture of the ceramic powder and a viscous vehicle, for example a terpineol-based organic liquid. By screen-printing and subsequent sintering (pore formation due to burn-out of organic binder), layers with a thickness of 30-50 µm and a porous microstructure are fabricated.

In the scope of this thesis microstructured cathodes were prepared from inks of LSCF and LSC64. The screen-printing ink of LSCF was provided by Fraunhofer IKTS (Dresden, Germany). The ink for LSC64 was prepared in-house by mixing the respective powder, which was synthesized by the spray pyrolysis method at EMPA (Dübendorf, Switzerland) and a terpineol-based ink vehicle (fuelcellmaterials, USA). Prior to the ink fabrication, the particle size distribution of the powder was measured by a particle size analyzer (CILAS 1064 L). The average particle diameter $d_{50}$ was 0.9 µm and the size distribution was monomodal. The powder was mixed with the ink vehicle so that the mass amount of LSC64 in the resulting ink was 70%. After mixing, the ink was homogenized by a three-roll-mill (EXAKT 50 I).

Films were screen-printed onto GDC and YSZ substrates through a screen-printing frame with an 80T-mesh. Afterwards the printed layers were dried at 100°C for half an hour, until the terpineol-based vehicle was dried out. For symmetrical cells, the printing procedure was repeated afterwards on the opposite side of the substrate. The LSCF layers were sintered at 1250°C, the LSC64 layers at 1050°C. The optimized sintering temperatures were chosen according to the results of preliminary tests on samples sintered at different temperatures and subsequent microstructure analysis with SEM.

#### *3.2.1.3 Thin film cathode synthesis by sol-gel spin-coating*

The properties of thin-film cathodes and common synthesis methods were introduced in section 2.2.3.1 on page 12. In the present work, a spin-coating synthesis route originally published by Januschewski et al. [77] was used and adapted to fabricate samples and symmetrical cells with nanoscaled thin-film electrodes with thicknesses of about 100-200 nm.

A precursor solution containing the acetates of lanthanum ($La(CH_3COO)_3.1.5H_2O$, Aldrich, >99.9%), strontium ($Sr(CH_3COO)_2$, Aldrich, puriss. p.a.) and cobalt ($Co(CH_3COO)_2.4H_2O$, Sigma-Aldrich, >98%) in the appropriate ratios to synthesize LSC64 was prepared as follows: 411.7 mg of La-acetate, 164.6 mg of Sr-Acetate and 498.2 mg of Co-acetate were dissolved in 7 ml glacial acetic acid (Fluka, puriss. p.a.) and stirred at around 80°C. During stirring, 76 mg of polyvinyl alcohol (Fluka) and 400 µl of formamide were added to the solution. The precursor was stirred until all components were dissolved and cooled to room temperature afterwards.

Spin-coating was performed on a Schaefer SCV-10 spin-coater, using a water jet pump to attach the samples on the rotary plate. The substrate disks were prepared for every single coating procedure as follows: An organic glue was prepared by dissolving a few mg of polystyrol into methyl-isobutyl-ketone (MIBK). The substrate was pasted on a piece of plastic foil and the edge surface was sealed with this glue. These preparative steps were necessary to make sure that the substrates were sucked to the rotary table adequately by the water jet pump during coating and the precursor didn't cover the edge surface or the opposite side of the disk.

For the coating procedure, a few drops of the precursor solution were dropped on the substrate and distributed over the whole surface. The rotation was performed for 30 seconds at a speed of 30 rounds per second. After stopping, the samples were immediately dried at a temperature around 150°C on a heating plate. When the gel film was completely dry, the sample was put into a furnace at 500°C for about half an hour to anneal the layer and transform it to an oxide film. The spin-coating procedure was repeated once on every surface. Symmetric cells were prepared with two layers of thin films on both sides, while the secondary samples for post-test analyses were prepared with two layers on one side only. After the coating steps were finished, the samples were annealed at 700°C for additional 2 hours.

Some symmetrical cells were fabricated with an additional current collector layer on top of the thin-films to improve the electrical contact for the electrochemical measurements. The current collector was prepared by screen-printing a layer of LSCF on both sides of the cell (for details on the screen-printing procedure see above.).

### *3.2.1.4 Sol-gel wet infiltration*

An introduction and overview on infiltrated SOFC cathodes was given in section 2.2.3.2 on page 13. In the present work, cathodes consisting of backbone layers of $Ce_{0.9}Gd_{0.1}O_{2-\delta}$ (GDC) and nanocrystalline $La_{0.6}Sr_{0.4}CoO_{3-\delta}$ (LSC64) were prepared by infiltration, following a synthesis route described by Nicholas et al. [147]. Two GDC disks with a diameter of 16 mm and a thickness of 1.6 mm were prepared as described above and grinded with SiC paper of 600 Grit. The dimensions of the disks were measured and the mass was weighed in a high precision scale (Mettler Toledo MT5).

For fabrication of the backbone layer, a screen printing ink was prepared by mixing the same GDC powder (Treibacher AG, Austria) with a viscous ink vehicle (fuelcellmaterials, USA), so that the particle load was 60 wt-%. The ink was screen-printed on the GDC-disks using a printing mask, so that the backbone layers on the disks had the shape of a circle with 1 cm in diameter. The disk which ought to become the symmetrical cell, was coated with backbone layers on both sides, while the other one, which was used for post-test analyses with SEM and STEM, was coated on one side only. After a layer was screen-printed, it was dried at 100°C and weighed again to determine the mass of the backbone layer. The samples were sintered at 1350°C for 3 h.

For the infiltration, aqueous stock solutions of nitrate salts of La, Sr and Co with molarity 1 M were prepared by dissolving $La(NO_3)_3.6H_2O$, $Sr(NO_3)_2$ and $Co(NO_3)_2.6H_2O$ in deionized water. The actual concentrations of the stock solutions were determined by complexometric titration with EDTA. The solutions were mixed together in the appropriate stoichiometric amounts. Afterwards citric acid (Fluka) was added to the solution so that the molar ratio between metal nitrates and acetic acid was 0.75:1. Ammonium hydroxide was added to the solution until it had a pH of 5 (controlled via pH test strips). Finally, the wetting behavior of the precursor solution was improved by adding a few drops of Erkantol NR, a commercial wetting agent.

For infiltration a few drops of the precursor solution were placed on the backbone and soaked in for a minute. Afterwards the surplus precursor liquid was swiped away by tissue paper, so that only small amounts of the solution remained in the pores of the backbone layer. Afterwards the samples were dried at 100°C for a few minutes and annealed at 500°C for half an hour to one hour. After annealing, the samples were weighed again on the high-precision scale to measure the weight gain of every infiltration step. This procedure was repeated 8-10 times, until the mass percentage of infiltrated material in the backbone structure was between 8 and 10%.

After finishing the infiltration procedure, current collector layers of LSCF were screen-printed on top of the infiltrated layers of the symmetrical cell. This was mandatory to achieve a good electrical contact for impedance spectroscopy measurements, since the lateral electrical conductivity of the infiltrated cathode without current collector was too low. The samples with the current collector were annealed at 700°C.

### 3.2.2 Setup and measurements

Two different reactors were used for electrochemical impedance spectroscopy: A quartz glass tube reactor and a NORECS *ProboStat* reactor. In both setups the cathodes on symmetrical cells were contacted with noble metal meshes of either Au or Pt and the cells were fixed by spring forces. In close vicinity to the cells, also secondary samples were placed to achieve comparable environmental conditions between the cells and the secondary samples. The testing atmospheres used for the experiments were either ambient air or test gases with 20% $O_2$ in Ar, which were brought into the reactors with flow rates around 2 liters per hour.

Electrochemical impedance measurements were performed in pseudo-4-wire mode, meaning that both contact meshes for the cell were connected with two wires respectively. The measurements were performed by a Novocontrol *Alpha-A* impedance analyzer connected with either a Novocontrol *ZG4* testing interface or with a *PotGal 15V10A* testing interface. All the analyzers were calibrated prior to each experiment. The measurements were controlled by the *WinDeta* software from Novocontrol.

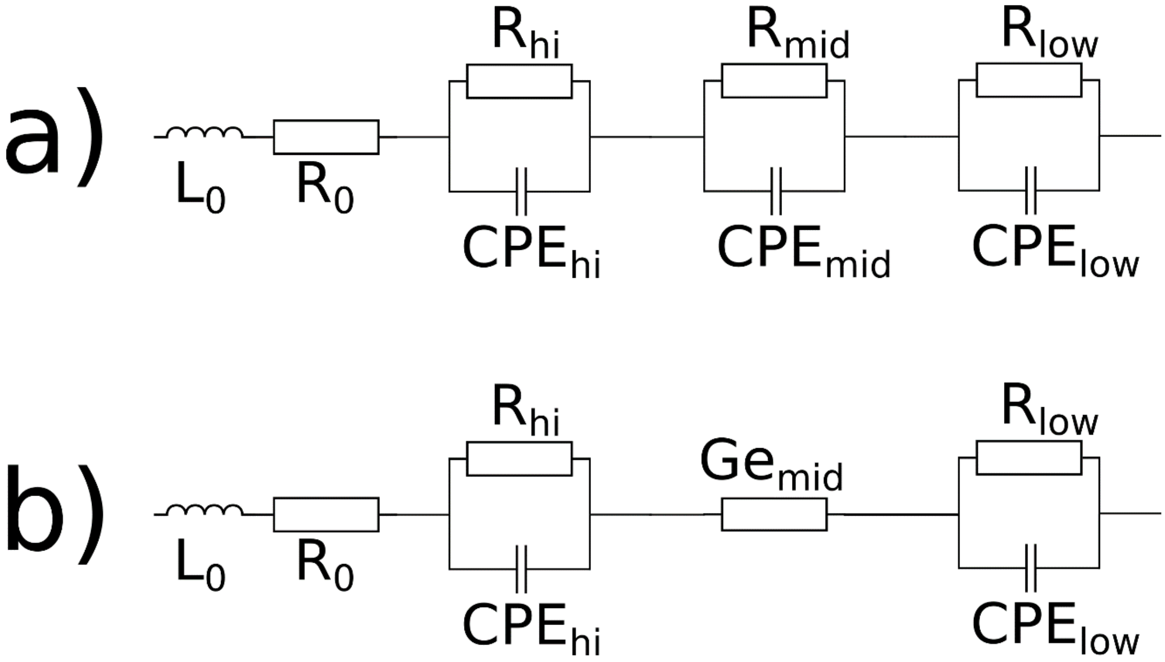

*Figure 12: The two equivalent circuits used for modelling and evaluation of the measured impedance spectra; a) Circuit with three R-CPE elements, b) Circuit with a Gerischer Impedance covering the intermediate frequency range*

The measurement results were evaluated by complex nonlinear least-squares fitting of the measured impedance spectra, using the equivalent circuit models sketched in Figure 12. All the circuit models contained the following base elements:

- $L_0$: Inductor, which is covering the stray inductance of the testing equipment; This is usually affecting impedance spectra at high frequencies
- $R_0$: Ohmic resistance in series, which represents the pure ohmic component of the impedance spectra (the real axis intercept in complex-plane plot); caused by the electrolyte resistance and the total ohmic resistance of the setup

The characteristic shape of impedance spectra was fitted by additional elements. In most cases it was possible to model the measured impedance data by two or three R-CPE elements. The number of elements was depending on the actual data, especially the number of recognizable arcs in the spectra. It has to be noted that this is an empirical approach. However, by calculation of the apparent capacitance from the CPE parameters and comparing it with known data from literature (see Table 1 on page 26) it was possible to identify physical causes for the individual impedance parameters in most cases. In some cases, it was meaningful to fit data with a model, where one of the three R-CPE elements was replaced by a Gerischer impedance (either ideal or generalized).

To distinguish the many parameters gained by these quite extensive fitting models, the following naming convention will be used in the present thesis: In the respective context of the measurement, the parameters are denoted by the indices “hi”, “mid” or “low”, depending on the frequency range, where the individual parameters have the main influence on the impedance spectrum.

CNLS-fits were performed either by Zview software from Scribner or by self-developed algorithms written in the *Python* programming language (Version 3), using the corresponding tools for scientific computing as described in section 3.1.2.

## 3.3 Temperature- and time-dependent characterization of SOFC cathode materials and -cathodes

With both characterization techniques, conductivity relaxation and impedance spectroscopy, short-term investigations followed by long-term experiments were performed. In the short term, the temperature dependencies of the measured parameters were investigated at temperatures above 500°C. The maximum temperatures were 700°C for impedance measurements and 850°C for conductivity relaxation measurements. These temperatures are in the range of typical operating temperatures for SOFCs. The long-term investigations took between 500 and 4000 hours. Almost all long-term experiments were carried out at 700°C, except two, which were performed at 800-850°C due to practical reasons.

The executed long-term experiments can be classified in the following three categories:

### 3.3.1 Humidity-controlled long-term experiments under silicon-poisoning conditions

As explained in section 2.2.4, there are several mechanisms of cathode performance degradation, which are triggered by humidity of the cathode gas. To examine the influence of humidity on different cathode materials and model cathodes with different morphologies in detail, the two CR-experiments as well as most of the EIS studies were long-term experiments, where the humidity of the testing atmospheres surrounding the samples was varied. Since the reactors were made of quartz glass they acted as possible sources of Si, so Si-poisoning of the cathode, as introduced in section 2.2.4.3, was the expected degradation mechanism for this kind of experiments. But also gas-phase transport of Sr, as described in section 2.2.4.1, had to be considered as possible mechanism occurring during the experiments.

Mixtures of $O_2$ and Ar in various concentrations were used as testing atmospheres. The test gases were humidified by using bubblers in a thermostat, where deionized $H_2O$ was held at a constant temperature to achieve a defined $p(H_2O)$ in the testing gas. For a systematical characterization, the time runs were split into three periods, in which the testing atmosphere was humidified at a defined level. Table 2 shows the parameters of the used testing program. The relative humidities were defined in relation to the equilibrium partial pressure of $H_2O$ at 25°C, which is 3.169 kPa. Thermodynamic data for $H_2O$ partial pressures as function of temperature was taken from the CRC Handbook of Physics and Chemistry, Table 6-15 [148].

*Table 2: Overview of the testing periods of humidity-controlled long-term experiments*

| | Relative humidity in test gas | $p(H_2O)$ / kPa | Thermostat temperature |
|---|---|---|---|
| 1st period | Dry atmosphere | 0 | - |
| 2nd period | 30% | 0.935 | 6°C |
| 3rd period | 60% | 1.938 | 17°C |

The duration for every period was between 500 and 1500 hours, depending on the degradation rate of the actual samples. At the end of each period the reactors were cooled to room temperature and one of the secondary samples was removed. Afterwards the experiment continued with the next period. By this procedure it was possible to analyze samples from different stages of the long-term experiments.

### 3.3.2 Long-term experiments under chromium- and silicon-poisoning conditions

As explained in section 2.2.4.2 on page 15, Cr-poisoning is one of the most critical degradation mechanisms for SOFC cathodes. In the present thesis, the influence of the morphology and architecture of LSC and LSCF cathodes on the impact of Cr-contamination at typical SOFC operating conditions was investigated by long-term impedance measurements.

The experiments were performed at 700°C in static ambient air, which was expected to provide a sufficient level of humidity for the known transport mechanisms of volatile contaminants, as described in section 2.2.4.2 and 2.2.4.3. Wires of an Fe-Cr-Ni alloy were present in the testing chamber which acted as a source of Cr. Additionally, the quartz tube of the reactor, as well as the quartz glass sample holder, were considered as sources of Si.

### 3.3.3 Interface-degradation experiments on YSZ electrolytes

As explained in section 2.2.4.4, there is still contradicting evidence, whether the formation of $SrZrO_3$ or $La_2Zr_2O_7$ in reactions between La and Sr species from cathode materials and YSZ electrolytes are only occurring during high-temperature sintering or also at operating temperatures of IT-SOFCs. To investigate this possible degradation mechanism EIS long-term measurements were performed on symmetric cells, where LSC64 cathodes of different morphologies were in direct contact with the YSZ electrolyte (accelerated ageing).

Nanostructured thin films were prepared by Sol-Gel spin-coating as described in section 3.2.1.3. Screen-printed layers were prepared according to section 3.2.1.2, but they weren't sintered at high temperatures to avoid pyrochlore formation. Instead the cathode layers were in-situ sintered during EIS characterization at max. 700°C. According to Nielsen et al LSC64 shows good sintering capabilities even at temperatures between 650°C and 950°C [149].

These experiments were performed in a Norecs *ProboStat* reactor. The samples were contacted with Pt-meshes by spring-force. Both electrodes were held in a dry test gas atmosphere containing of 20% $O_2$ in Ar.

## 3.4 Post-test analyses

After the long-term experiments the characterized samples (CR sample or symmetric cell) as well as secondary samples were analyzed by various techniques, in order to gain information on chemical and morphological changes. The analyzing techniques are described in the following section. Details on the performed analyses will be described in the results chapter.

After all experiments, fresh and degraded samples were analyzed by scanning electron microscopy (SEM). These analyses gave information about structure and morphology of the samples at length scales from a few µm down to the sub-µm-range. Local analyses of the chemical composition were obtained by energy-dispersive X-ray spectroscopy (EDX). In the most cases these analyses were performed on sample surfaces. Additionally, some samples were analyzed at the cross-section. Cross-sectional cuts were prepared by two different methods: Some samples were embedded in epoxide resin, cut and polished at the cut. Alternatively, some samples were prepared by an ion cutting technique using a Gatan Ilion II system.

Selected samples from the experiments were analyzed by transmission electron microscopy in scanning mode (STEM) to obtain structural and chemical information on the sub-µm scale. For STEM analyses a thin lamella of the sample's cross-sections was prepared by focused ion beam

(FIB) using a FEI Nova200 FIB/SEM dual beam microscope. STEM analyses were performed on a FEI Tecnai F20 microscope. Images were obtained in STEM-HAADF mode. Additional localized chemical analyses were obtained by EDX and electron energy loss spectroscopy (EELS).

In two cases, additional information on the chemistry of the samples was obtained by analyses with X-ray photoelectron spectroscopy (XPS). This is an analyzing technique with a high surface-sensitivity. By alternating XPS analysis and surface sputtering it was possible to obtain elemental depth-profiles of the sample beneath the surface.

## 3.5 Overview of experiments

The following table lists all the long-term experiments, which have been performed in the scope of the present thesis.

*Table 3: Overview of the long-term experiments*

| Category | Sample | Temperature and atmosphere | Duration | Results in section |
|---|---|---|---|---|
| Humidity-controlled CR experiments under Si-poisoning conditions | LCF91 dense sample | 700°C,<br>1% $O_2$ in Ar (dry and humidified) | Dry,<br>30% rel. hum.,<br>60% rel. hum. | 4.1.1,<br>page 40 |
| | LNF64 dense sample | 850°C,<br>10% $O_2$ in Ar (dry and humidified) | Dry,<br>30% rel. hum.,<br>60% rel. hum. | 4.1.2,<br>page 60 |
| Humidity-controlled EIS experiments under Si-poisoning conditions | LSC64 thin-film | 700°C,<br>20% $O_2$ in Ar (dry and humidified) | 600h dry,<br>600h 30% rel. hum.<br>600h 60% rel. hum. | 4.2.1,<br>page 68 |
| | LSC64 infiltrated | 700°C,<br>20% $O_2$ in Ar (dry and humidified) | 1000h dry<br>1000h 30% rel. hum.<br>1000h 60% rel. hum. | 4.2.2,<br>page 86 |
| | LSC64 screen-printed | 700°C,<br>20% $O_2$ in Ar (dry and humidified) | 500h dry,<br>1500h 30% rel. hum.<br>1500h 60% rel. hum. | 4.2.3,<br>page 101 |
| EIS experiments under Cr-poisoning conditions | LSC64 thin-film | 700°C, ambient air | 500h | 4.3.1,<br>page 122 |
| | LSC64 thin-film with current collector | 700°C, ambient air | 1200h | 4.3.2,<br>page 137 |
| | LSCF screen-printed | 700°C, ambient air | 2000h | 4.3.3,<br>page 144 |
| Interface degradation EIS experiments | LSC64 thin-film | 800°C,<br>20% $O_2$ in Ar (dry) | 1000h | 4.4.1,<br>page 152 |
| | LSC64 screen-printed | 700°C,<br>20% $O_2$ in Ar (dry) | 666h | 4.4.2,<br>page 173 |

# 4 Results and Discussion

## 4.1 Oxygen exchange kinetics and long-term stability in dry and humid atmospheres

### 4.1.1 Oxygen exchange kinetics and long-term stability of LCF91

A plate-shaped sample of LCF91 was characterized by conductivity relaxation. The sample had a thickness of 221 µm and an edge length of about 5 mm. Measurements of the electrical conductivity and of the conductivity relaxation were performed in van der Pauw geometry. For the measurements a dc current of 40 mA was applied.

For short-term characterization the conductivity relaxation was measured by $p(O_2)$-steps between 0.10 bar and 0.15 bar in a temperature range between 500°C and 850°C. Since the values for $k_{chem}$ had a relatively high uncertainty, the atmosphere was changed to lower $p(O_2)$ with $p(O_2)$-steps between 0.01 bar and 0.015 bar. A second temperature run and the long-term study were carried out at these lower oxygen partial pressures.

The long-term experiment was carried out for 2092 hours at 700°C with a variation of the humidity of the testing atmospheres, as described in section 3.3.1. The experiment was divided into the following three testing periods:

- Period 1; dry atmosphere; 0 h - 669 h
- Period 2; humidified atmosphere with 30% relative humidity; 669 h – 1272 h
- Period 3; humidified atmosphere with 60% relative humidity; 1272 h – 2092 h

#### *4.1.1.1 Short-term characterization*

Electrical conductivity and conductivity relaxation were measured between 500°C to 850°C. The following figure shows selected relaxation curves (normalized conductivity over time) measured in this temperature range.

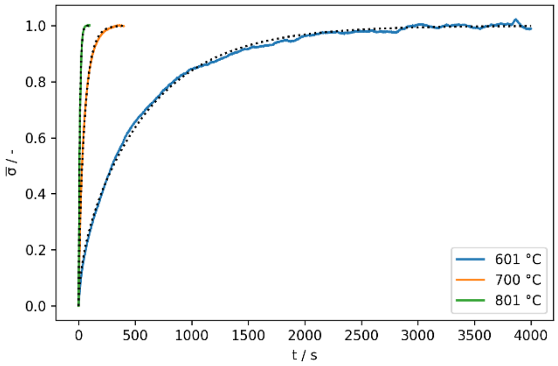

*Figure 13: Selected conductivity relaxation curves of LCF91 at p(O₂) of 0.10 bar (solid lines) and fits to the diffusion model (dotted lines)*

Most of the measured relaxation curves could be fitted well with the mixed-controlled model, from which the relevant parameters, $k_{chem}$ and $D_{chem}$, could be derived. The results are presented in Figure 14.

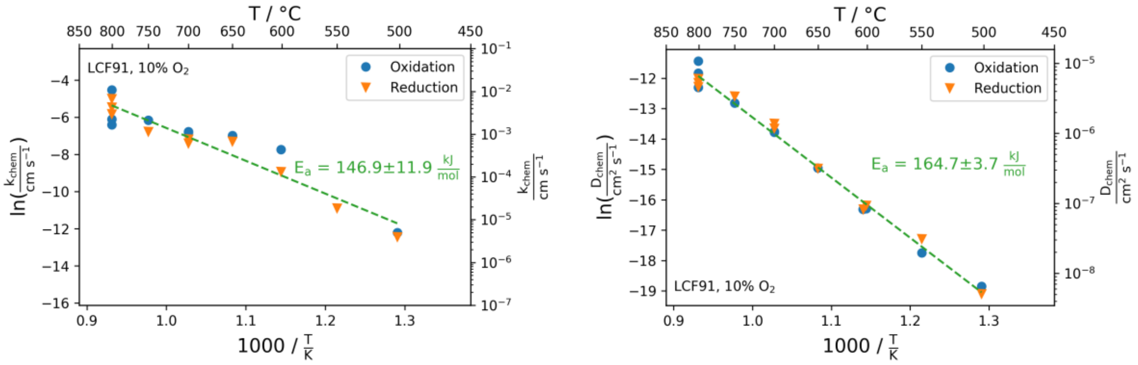

*Figure 14: Arrhenius-plots of chemical oxygen surface exchange coefficient $k_{chem}$ and chemical diffusion coefficient of oxygen $D_{chem}$ of LCF91, measured by conductivity relaxation at p(O₂) of 0.10 bar*

While $D_{chem}$ followed a perfectly linear trend in the Arrhenius-plot, $k_{chem}$ seemed to have a deviation from ideal behavior between 600 and 650°C. One reason for this deviation could be, that $k_{chem}$ is relatively high so that the relaxation behavior is on the border to diffusion-controlled behavior. This usually means that the determination of parameter $k_{chem}$ from the nonlinear fit of the diffusion model to the experimental data is affected by higher uncertainties.

In order to ensure mixed-controlled behavior for the long-term experiment, the testing atmospheres were changed from 10% and 15% $O_2$ in Ar to 1% and 1.5% $O_2$ in Ar respectively. Figure 15 shows selected relaxation curves and Figure 16 the evaluated parameters $k_{chem}$ and $D_{chem}$ acquired in these atmospheres at temperatures between 600 and 800°C.

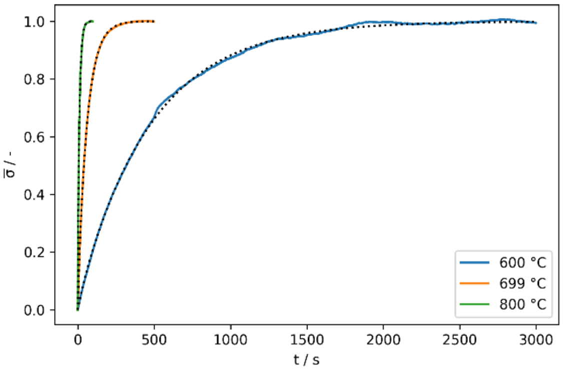

*Figure 15: Selected conductivity relaxation curves of LCF91 at a p(O₂) of 0.010 bar (solid lines) and fits to the diffusion model (dotted lines)*

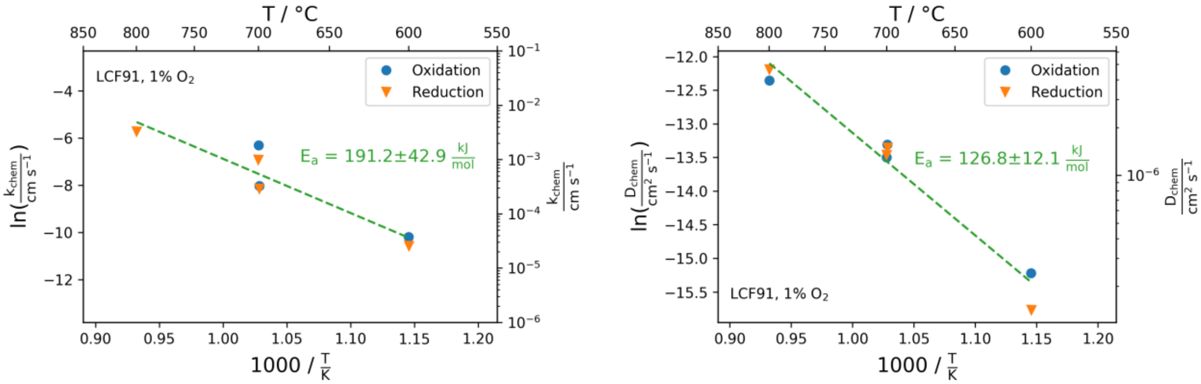

*Figure 16: Arrhenius-plots of chemical oxygen surface exchange coefficient $k_{chem}$ and chemical diffusion coefficient $D_{chem}$ of LCF91, measured by conductivity relaxation at p(O₂) of 0.010 bar*

These data points were measured in a temperature run, starting at 600°C, going up to 700°C and 800°C and returning to 700°C. The sample was kept at the respective temperature for about one day. The measured values for $k_{chem}$ at 700°C were higher after the 800°C-step. This might be due to an activation of the surface at 800°C.

Figure 17 shows the electrical conductivity σ as function of temperature for the different atmospheres, in linear scale and as Arrhenius plot. The conductivity of LCF91 is relatively low compared to state-of-the-art materials like LSC (>1000 S/cm). There is a clear p($O_2$)-dependence of σ and the differences of σ for the p($O_2$)-steps are sufficiently high for conductivity relaxation experiments.

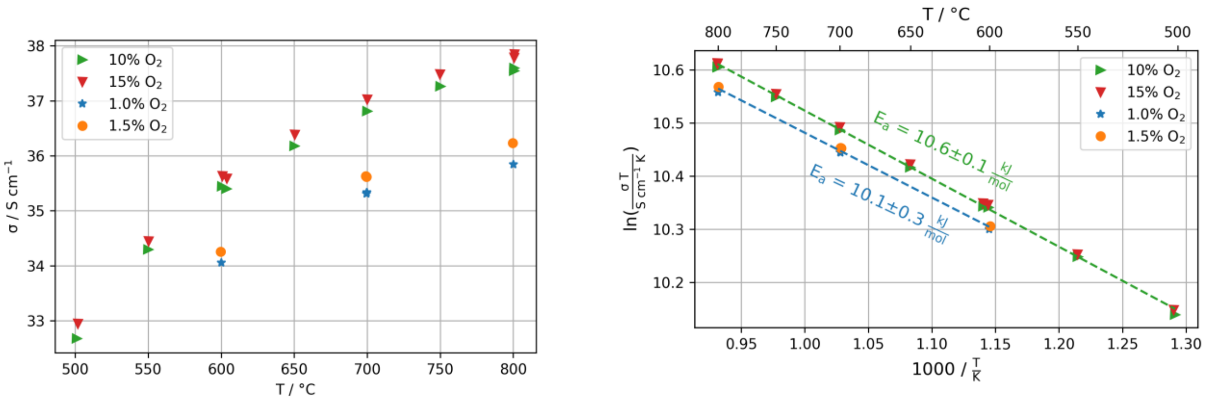

*Figure 17: Electrical conductivity of LCF91 at different p(O₂) as function of temperature; left: linear plot; right: Arrhenius plot and activation energies*

### 4.1.1.2 Long-term characterization

Figure 18 shows selected conductivity relaxation curves measured during the long-term experiment. The relaxation was quite fast and smooth at the beginning of the experiment, which is an indication of fast oxygen exchange kinetics. With increasing degradation, the relaxation times increased significantly and the data became noisier.

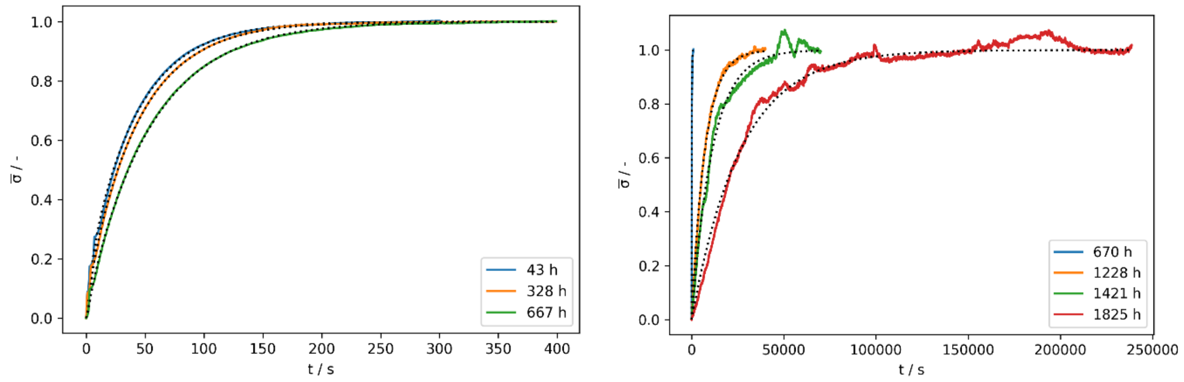

*Figure 18: Selected conductivity relaxation curves measured during the long-term experiment at 700°C, p(O₂)=0.010 bar (solid lines) and fits to the diffusion model (dotted lines)*

During the first period of the experiment $D_{chem}$ remained constant while $k_{chem}$ decreased slightly from $1 \times 10^{-3}$ cm/s to $6 \times 10^{-4}$ cm/s (Figure 19).

Humidification of the testing atmospheres caused a strong and immediate degradation of the measured $k_{chem}$. It decreased from $6 \times 10^{-4}$ cm/s to $2 \times 10^{-6}$ cm/s during the second period with 30% relative humidity. After additional 500 h with 60% humidity the final value was $3 \times 10^{-7}$ cm/s. This is a well-known behavior which has been observed in several long-term experiments with cathode materials like LSC64 [120] and LSCF [119] and is usually caused by chemical and morphological changes on the surface, caused by contaminants from outside and/or segregated ions/elements from inside the sample. The cause of degradation in the present study has been analyzed in post-test analyses, which are presented in the next subsection.

Also, $D_{chem}$ decreased by more than one order of magnitude from $1\times10^{-6}$ cm²/s to $3\times10^{-8}$ cm²/s. However, after approximately 1000 h the oxygen exchange kinetics became limited by the rate of the strongly decreased surface exchange process and the determination of $D_{chem}$ was not possible during the rest of the experiment. Since post-test analyses show that the degradation affects mainly the surface region rather than the bulk, it is possible that slow diffusion in the surface region leads to an apparent limitation of the kinetics. In the degraded state the measured $D_{chem}$ values should therefore be understood as effective parameters which may include contributions from the degraded near-surface region in addition to the bulk diffusion of oxygen.

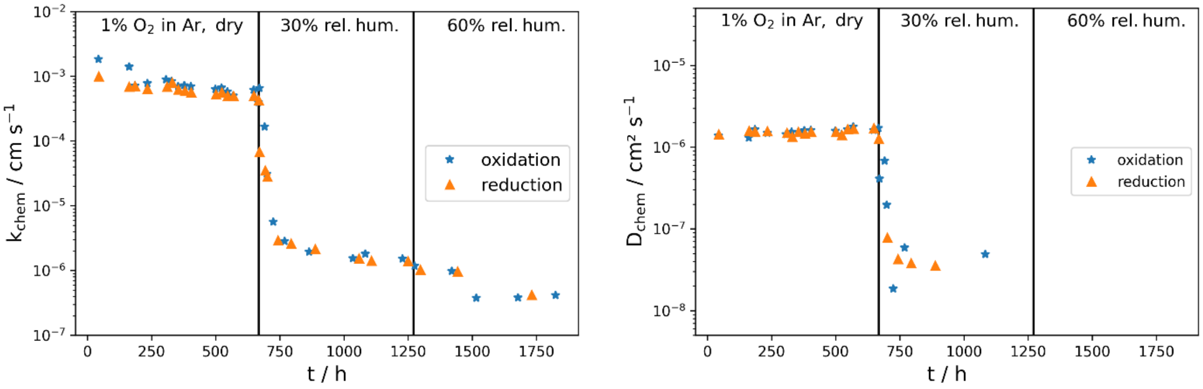

*Figure 19: Time-dependent degradation of $k_{chem}$ and $D_{chem}$ during the long-term experiment at 700°C in atmospheres with increasing humidity*

The electrical conductivity remains almost constant over time. As Figure 20 shows, there are slight variations in the conductivity values of about 0.3 S/cm. However, this is less than 1% of the measured values and thus in the range of the measurement uncertainty. The constant conductivity (i.e. a bulk property) is an indication that the bulk of the sample is indeed not affected by the degradation at the surface. This is also confirmed by post-test analyses (see below).

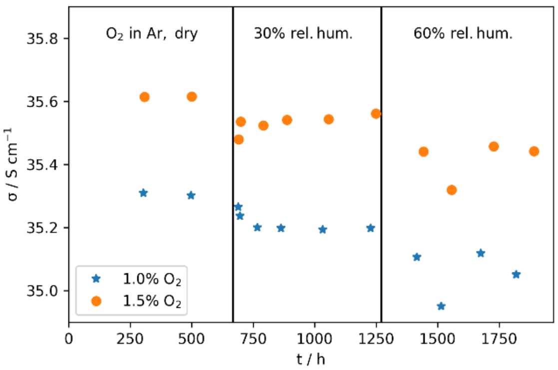

*Figure 20: Electrical conductivity of LCF91 as function of time at 700°C*

### 4.1.1.3 Post-test analyses

In order to gain deeper insights into the degradation mechanisms, post-test analyses by complementary methods were performed on selected samples. A fresh specimen representing the as-prepared state and samples which were removed from the reactor at the end of each testing period and the CR plate sample itself, which has undergone the whole long-term experiment have were by SEM on the surface and XPS elemental depth-profiling. From the surface-near region of the degraded CR-sample a TEM-lamella of the cross-section was prepared by focused ion beam (FIB) technique and analyzed by STEM.

*Table 4: Overview of the analyzed samples and carried out analyses*

| | SEM | STEM | XPS |
|---|---|---|---|
| LCF91 0 h, as prepared | ✓ | | ✓ |
| LCF91 669 h, dry | ✓ | | ✓ |
| LCF91 1271 h, max. 30% rel. hum. | ✓ | | ✓ |
| LCF91 2092 h, max. 60% rel. hum. (CR sample) | ✓ | ✓ | ✓ |

#### SEM analyses of the surface

Figure 21 shows the SEM images of a fresh LCF91 bulk sample in the state after preparation. The surface was quite rough and contained several pores. Smaller pores or pits on the surface are filled by material, probably debris from polishing. A few huge pores were found, in which the grain structure was visible well. These pores are probably a result of sintering due to densification of the green body. The fact, that the grain structure is visible inside the pores but not at the surface is an indication that the surface structure was damaged due to mechanical forces of polishing and recrystallized during annealing at 850°C.

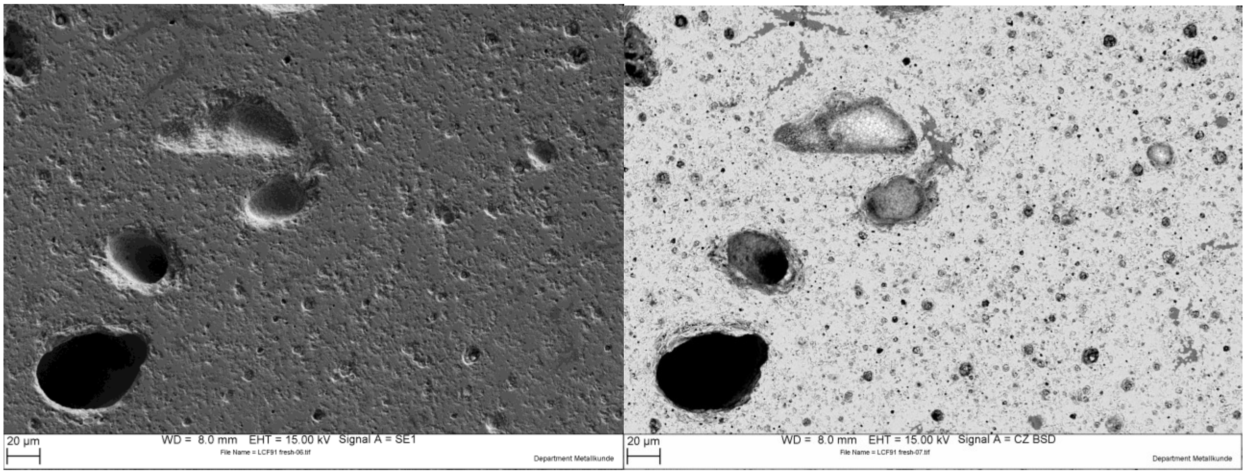

*Figure 21: SEM images of the surface of a fresh LCF91 sample; left: secondary electron image; right: backscattered electron image*

The backscattered electron images with Z-contrast indicate that also the chemical composition was not homogenous over the whole sample. EDX analyses (Figure 22) showed that the darker spots found in the sample had a higher amount of Fe than the surrounding matrix. Therefore these zones are probably secondary phases of $FeO_x$, which were formed during powder preparation, at sintering of the sample or at the final annealing step.

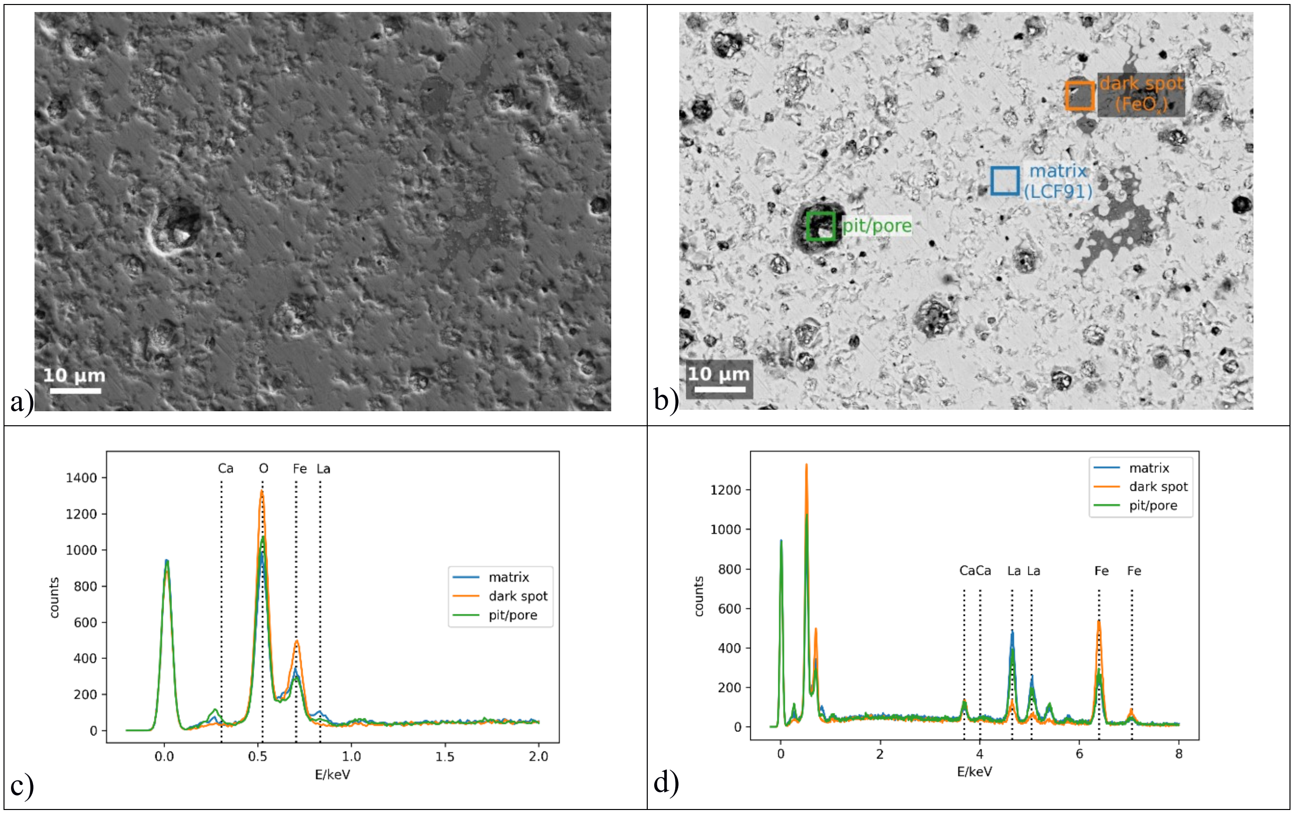

*Figure 22: a) SEM-SE- and b) SEM-BSE image of the fresh LCF91 surface in high magnification; c) and d) EDX spectra acquired at positions marked in b)*

The sample removed after 600 hours, at the end of the first period of the long-term experiment in dry atmosphere, was similar to the fresh sample. The surface images (acquired in SE and BSE mode) showed the same features as in the fresh sample: Large empty pores with grain structures, small pits filled with debris and the secondary phase $FeO_x$, visible in the form of dark spots in the backscattered electron images.

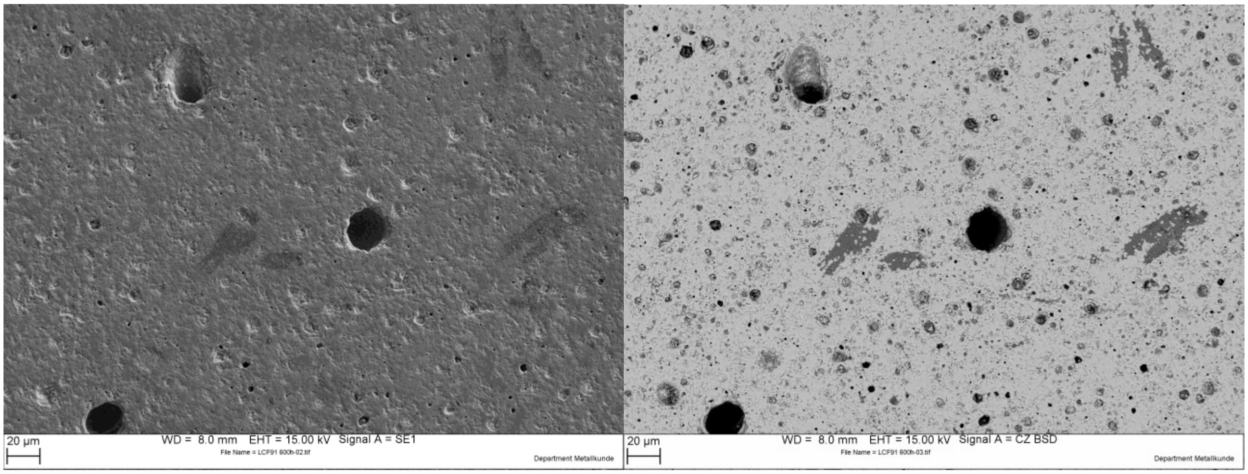

*Figure 23: SEM images of the surface of an LCF91 sample after 669h in dry atmosphere; left: Secondary electron image; right: backscattered electron image*

Also, EDX analyses (Figure 24) didn’t reveal any significant chemical changes compared to the freshly prepared sample. These findings are in good agreement with the data of the oxygen exchange kinetics since only a moderate degradation of $k_{chem}$ occurred in the first period of the long-term experiment.

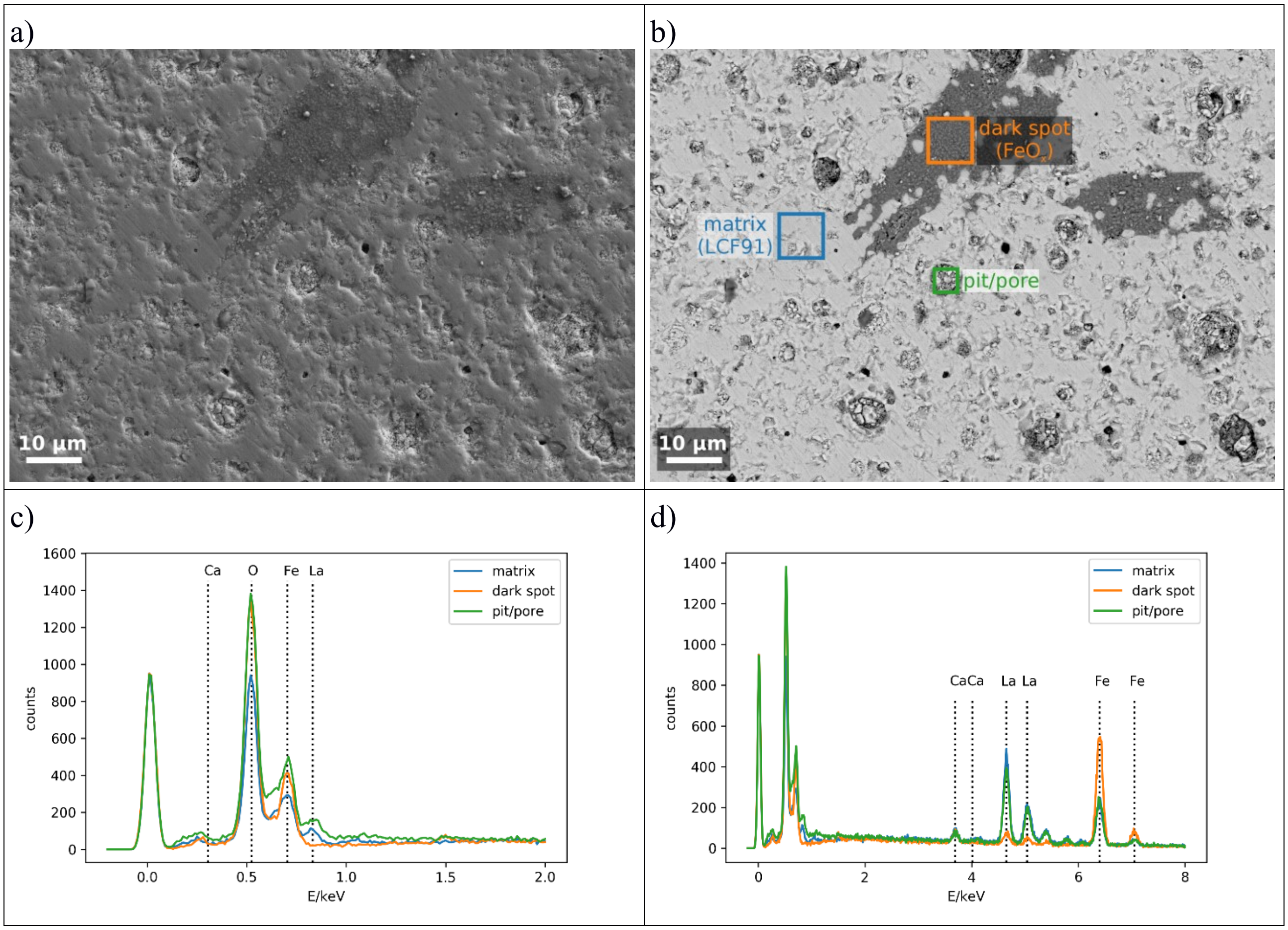

*Figure 24: a) SEM-SE- and b) SEM-BSE image of the surface of LCF91 after 600h in dry atmosphere in high magnification; c) and d) EDX spectra acquired at positions marked in b)*

In contrast to the first two samples from the long term experiment, significant changes occurred in the third sample, which was removed after the second period of the long-term experiment, where it was exposed to 30% relative humidity for about 600 hours. These changes were not detectable by SEM imaging of the surface. The images in Figure 25 didn't show significant differences to the previously shown surfaces of non-degraded samples. However, EDX analyses, which are presented in Figure 26, gave evidence of small but significant amounts of Si on the surface. It could be found at all analyzed positions, but the highest concentration was detected at the position of a small pore. This is an indication that Si was deposited on the surface due to the well-known gas transport mechanism in humid atmospheres (see section 2.2.4.3, page 17).

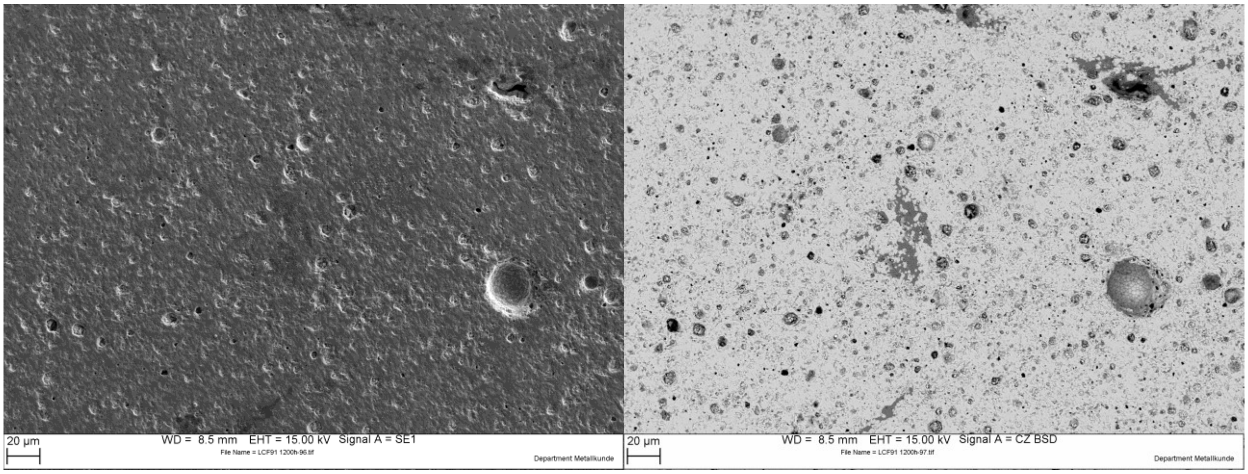

*Figure 25: SEM-SE- (left) and SEM-BSE-images of the surface of LCF91 after 1272 h in max. 30% relative humidity*

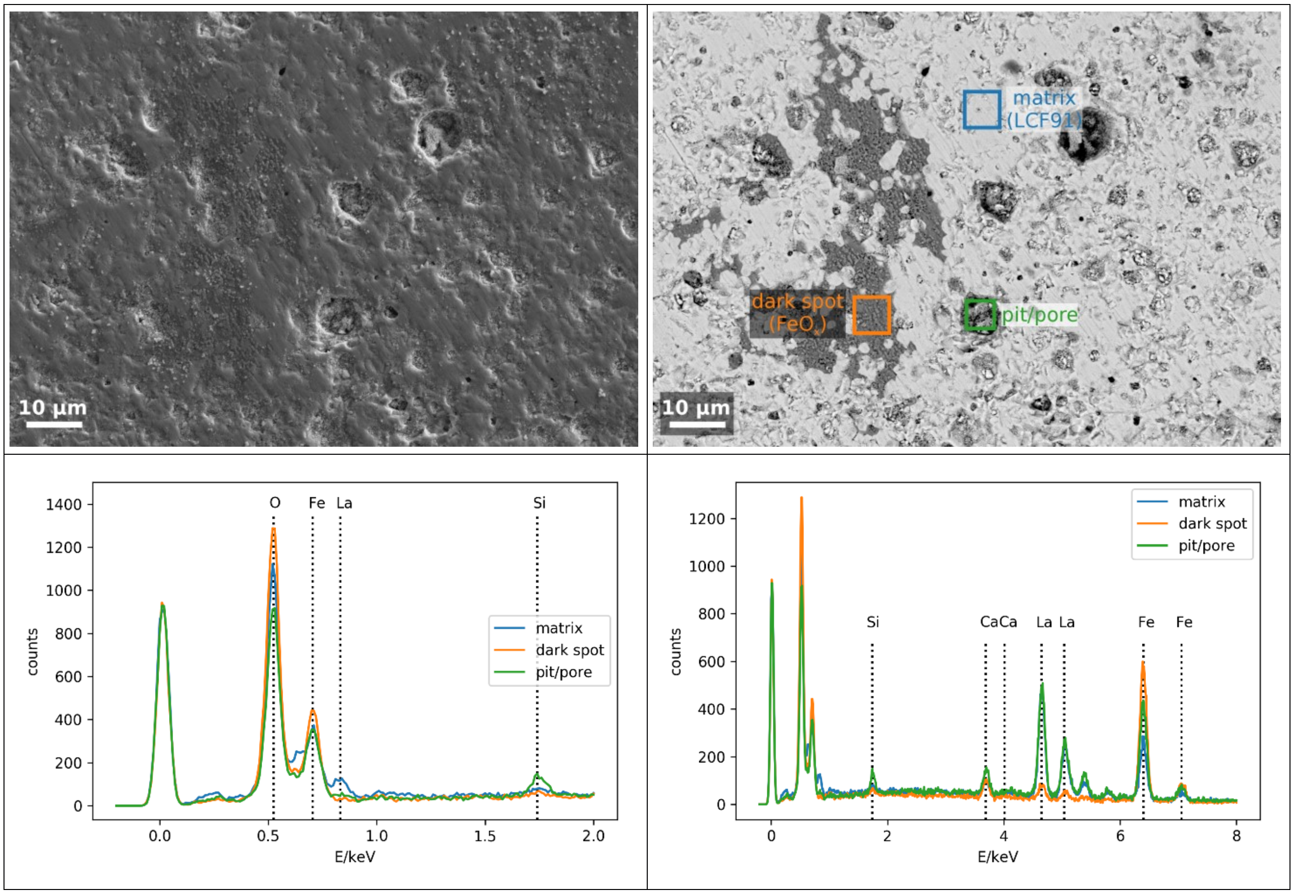

*Figure 26: a) SEM-SE- and b) SEM-BSE images of the surface of LCF91 after 1272 h in max. 30% relative humidity in high magnification; c) and d) EDX spectra acquired at positions marked in b)*

Finally, the CR sample itself, which had undergone the whole experimental program and was exposed to humid atmospheres up to 60% relative humidity, was analyzed by SEM and EDX. On this sample some bright spots were visible. These spots are metallic Au, which originates from the Au paste which was used for electrical contacting of the CR sample. During contacting small drops of the Au ink were spread over the surface.

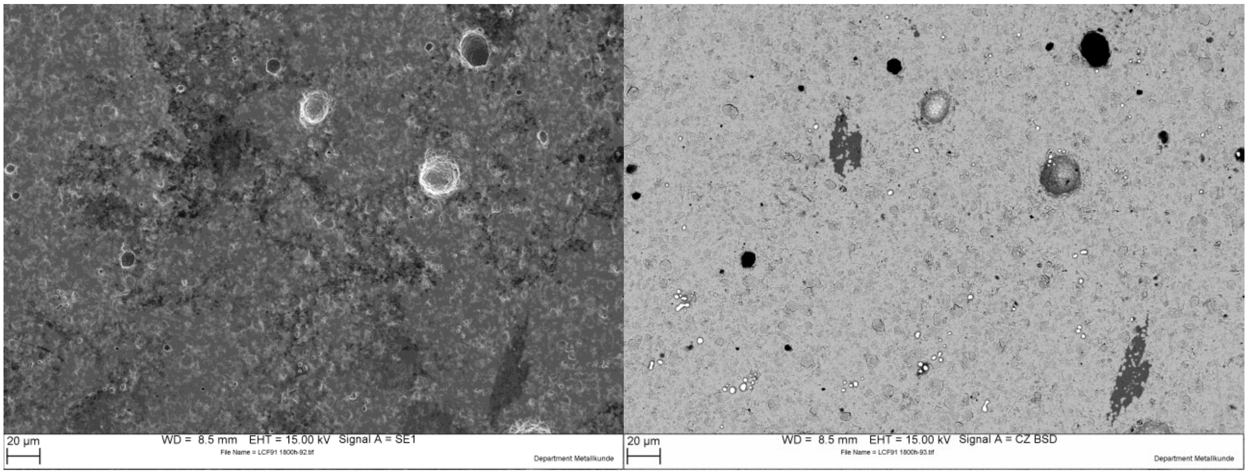

*Figure 27: SEM-SE- (left) and SEM-BSE-images of the surface of LCF91 after 2092 h in max. 60% relative humidity*

By EDX analyses Si was found also on this sample. It was distributed over the whole surface and was found in slightly larger amounts at positions with higher roughness and pores. Also, $FeO_x$ spots were found again at selected positions of the sample.

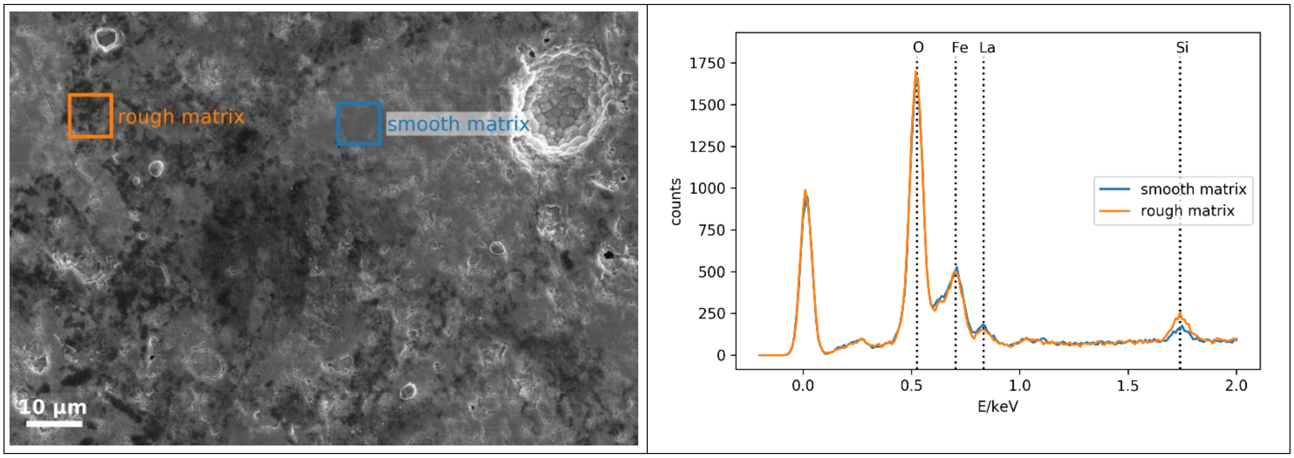

*Figure 28: a) SEM-SE-image of the surface of LCF91 after 2092 h in max. 60% relative humidity in high magnification; b) EDX spectra acquired at a rough and a smooth region*

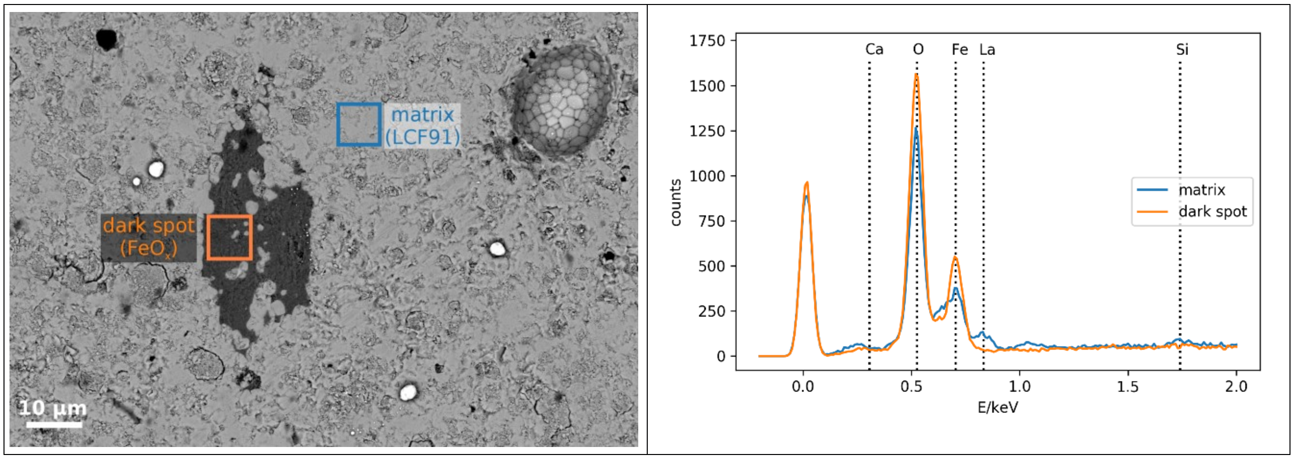

*Figure 29: a) SEM-BSE-image of the surface of LCF91 after 2092 h in max. 60% relative humidity in high magnification; b) EDX spectra of the matrix and an* $FeO_x$ *spot*

### *STEM of the cross-section*

Figure 30 shows an overview image of the sample acquired by STEM-HAADF. The STEM images reveal a homogeneous bulk structure with grains of 2 µm in diameter, which is covered by a fine-grained heterogeneous layer on the surface. It has to be noted that this surface is not a product of the long-term degradation, but has been present on the sample already after preparation and prior to the long-term experiment. The morphological differences between the surface and the bulk have already been found on SEM images with visible large pores (e.g. Figure 21,Figure 25Figure 29). As already pointed out, an explanation for these morphological characteristics is, that damages and defects were brought into the material during the sample preparation by grinding and polishing. Annealing at 850°C for hardening the Au contacts caused a recrystallization of the mechanically deformed surface.

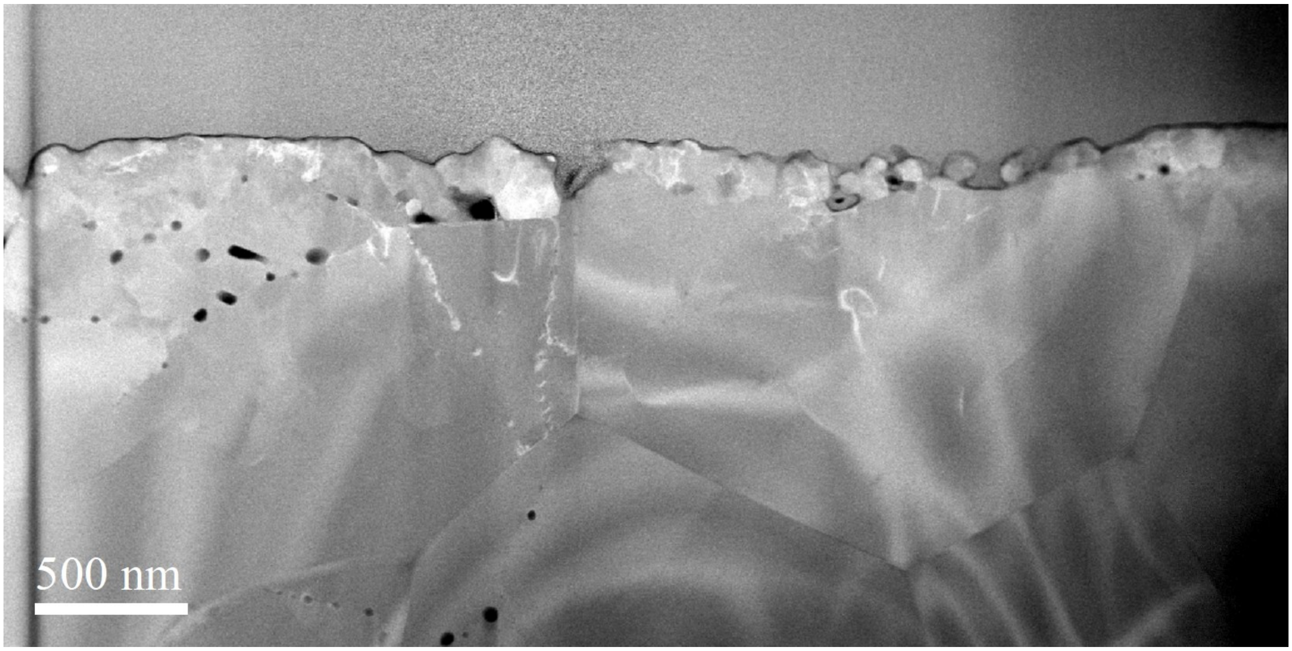

*Figure 30: STEM-HAADF image of the cross-section of the degraded LCF91 CR sample*

The chemical compositions of the bulk and the surface layer were analyzed in detail by EDX and EELS. Figure 31 shows an EDX analysis at a position inside a bulk grain. According to the Z-contrast the chemical composition of the bulk grains was quite homogeneous. A detailed line scan analysis of a grain boundary in the bulk (Figure 32) revealed that the Fe concentration is slightly higher at the grain boundary. This is an indication that Fe in LCF91 has a tendency to segregate.

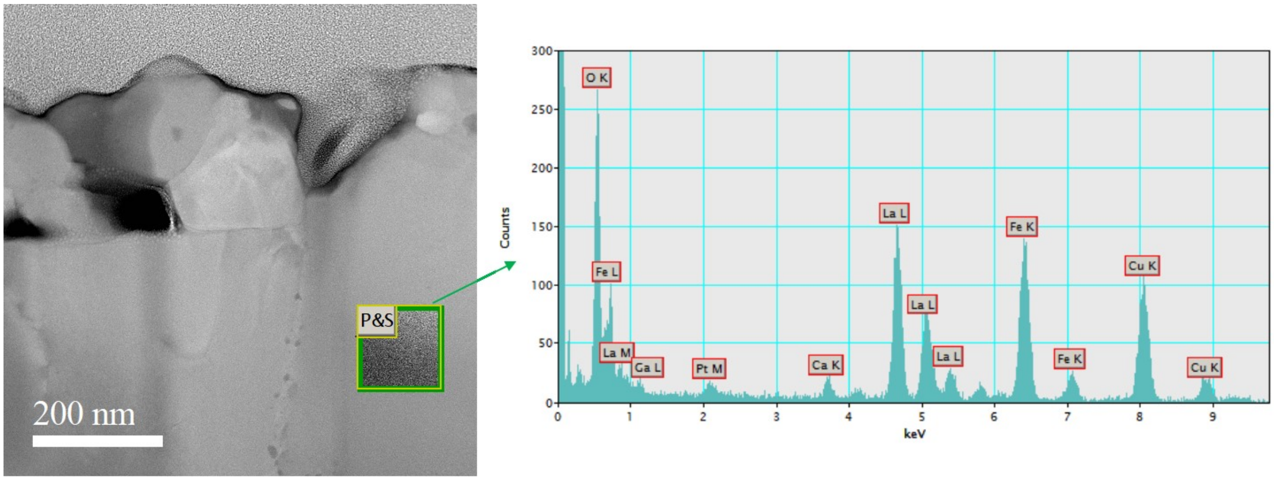

*Figure 31: STEM-HAADF cross-sectional image of the near-surface region and EDX spectrum of a bulk grain of the LCF91 sample*

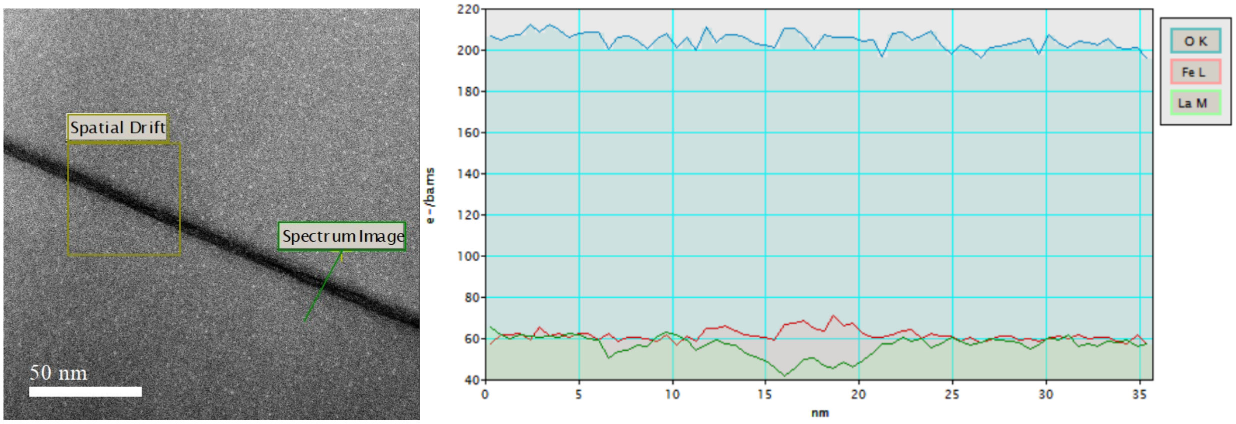

*Figure 32: STEM-HAADF image and EDX line scan analysis of a grain boundary in the LCF91 bulk*

In contrast to the bulk, the surface structures are relatively heterogeneous. Figure 33 shows the results of EDX- and EELS analyses at three different positions. The surface layer consists of grains with higher amounts of Fe between other particles consisting of La, Fe and Ca with similar composition as the bulk. According to the chemical composition in the surface layer it can be assumed, that surface wearing and recrystallization might have been an accelerating factor for Fe segregation. This could also be the reason for the large $FeO_x$ islands which were found at the sample surfaces by SEM.

The occurrence of Si could be confirmed as well on the STEM sample. As Figure 34 shows, Si was found by EDX in a thin film on the surface.

Additional information on the composition of the surface layer was gained by EDX mapping analysis. Figure 35 shows elemental maps of a part on the surface of the sample. The elements La, Fe and Ca could be analyzed well, while the mapping of Si was not possible due to methodical reasons. According to the elemental maps, segregation of Fe and Ca occurred on the surface. While Fe formed individual grains, Ca was found in significantly higher concentrations in a thin layer on the surface.

These observations suggest that the surface of the degraded LCF91 sample was covered by a double layer consisting of a Si- and O-rich impurity layer on top and an underlying Ca- and O-rich region, with a total thickness of 10 to 20 nm. These films may consist of silica ($SiO_2$) and calcium oxide (CaO) or of calcium-silicate (compound $CaSiO_3$ or solid solution $Ca_xSi_yO_z$ with variable stoichiometry as a function of depth). However, it was not possible to determine the exact chemical composition or crystal structure due to the small thickness of the impurity region.

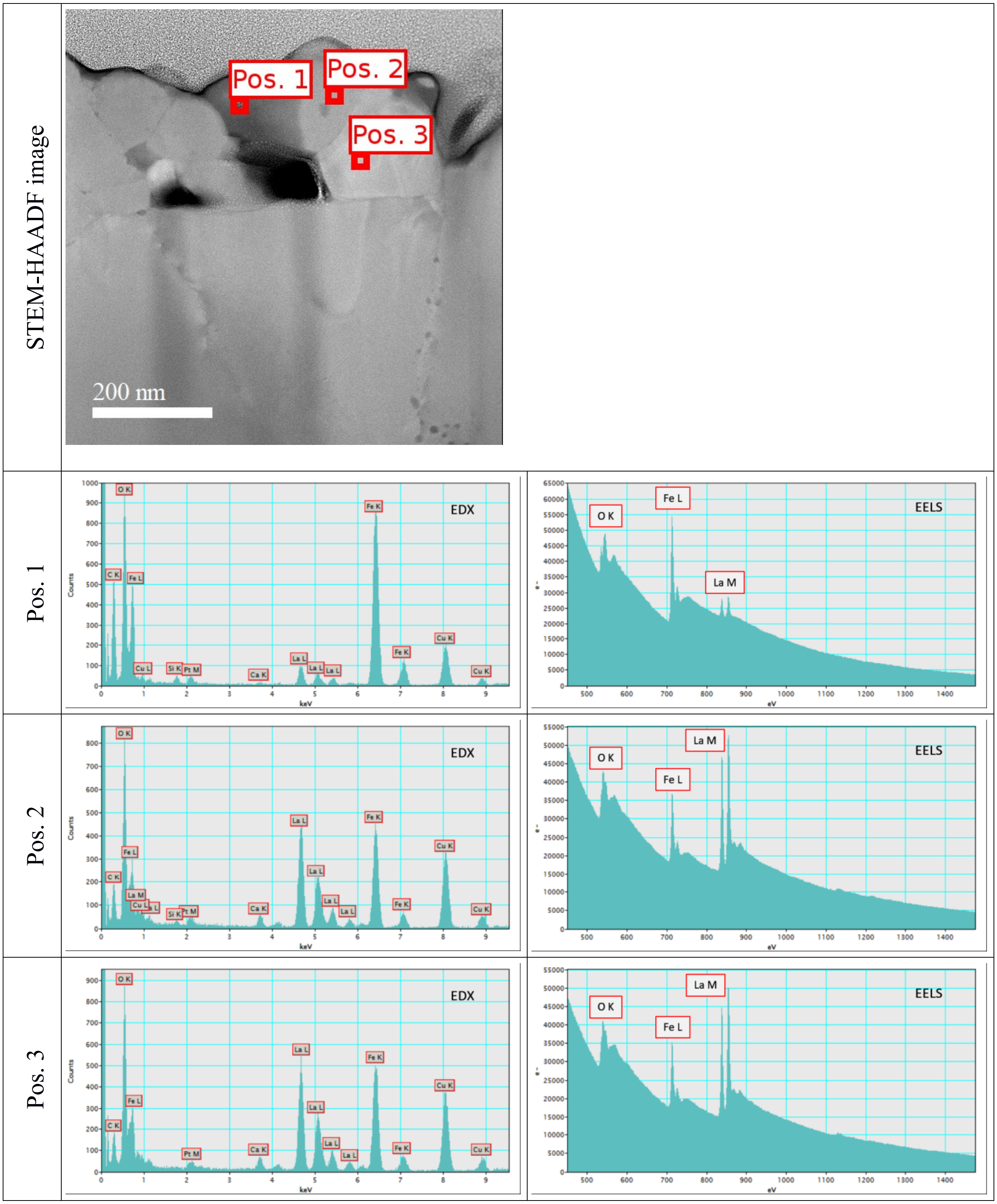

*Figure 33: STEM-HAADF image and EDX/ EELS analyses at surface grains of the degraded LCF91 sample*

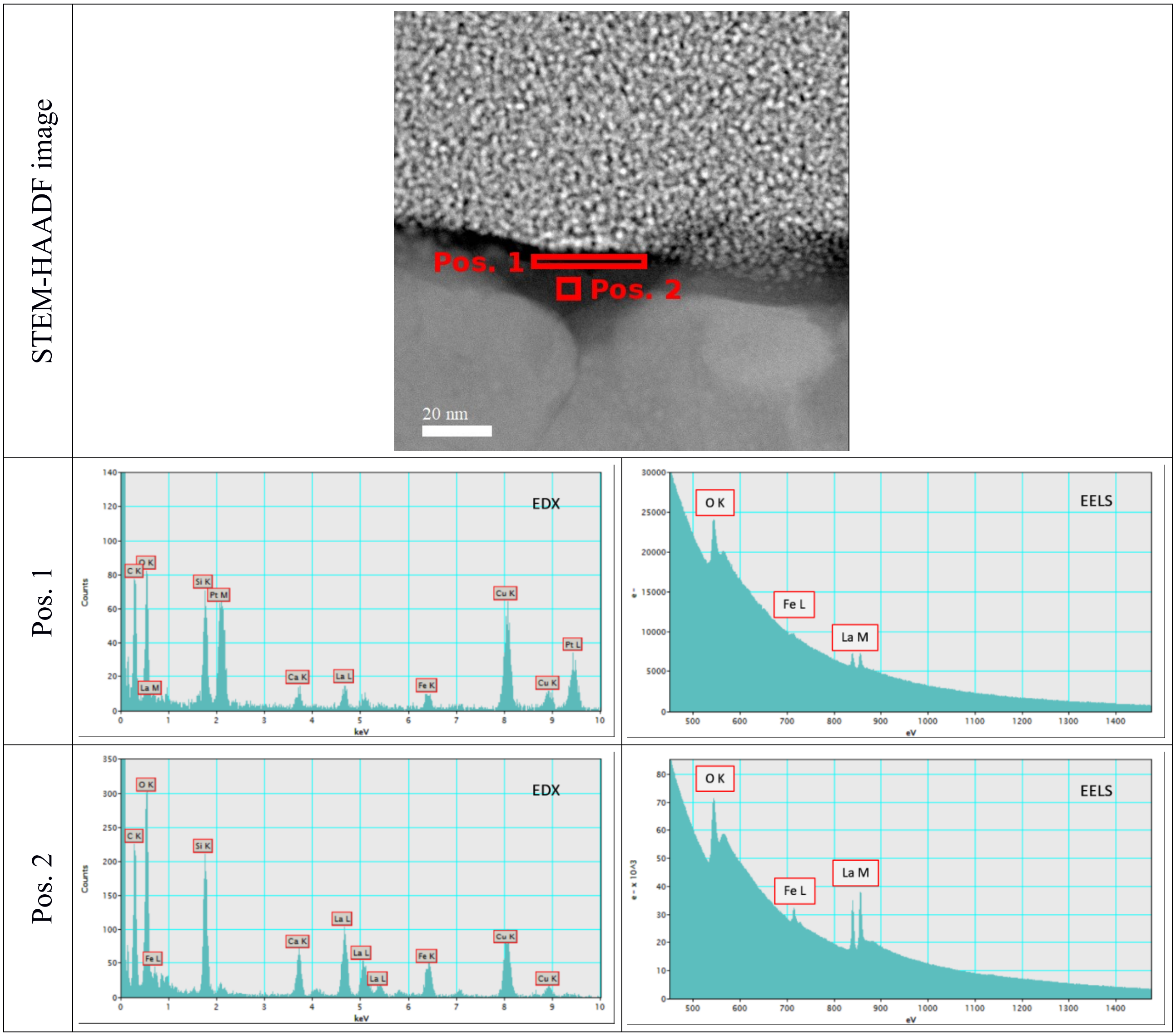

*Figure 34: STEM-HAADF image and EDX/ EELS analyses of the Si-rich impurity region at the immediate surface of the LCF91 sample*

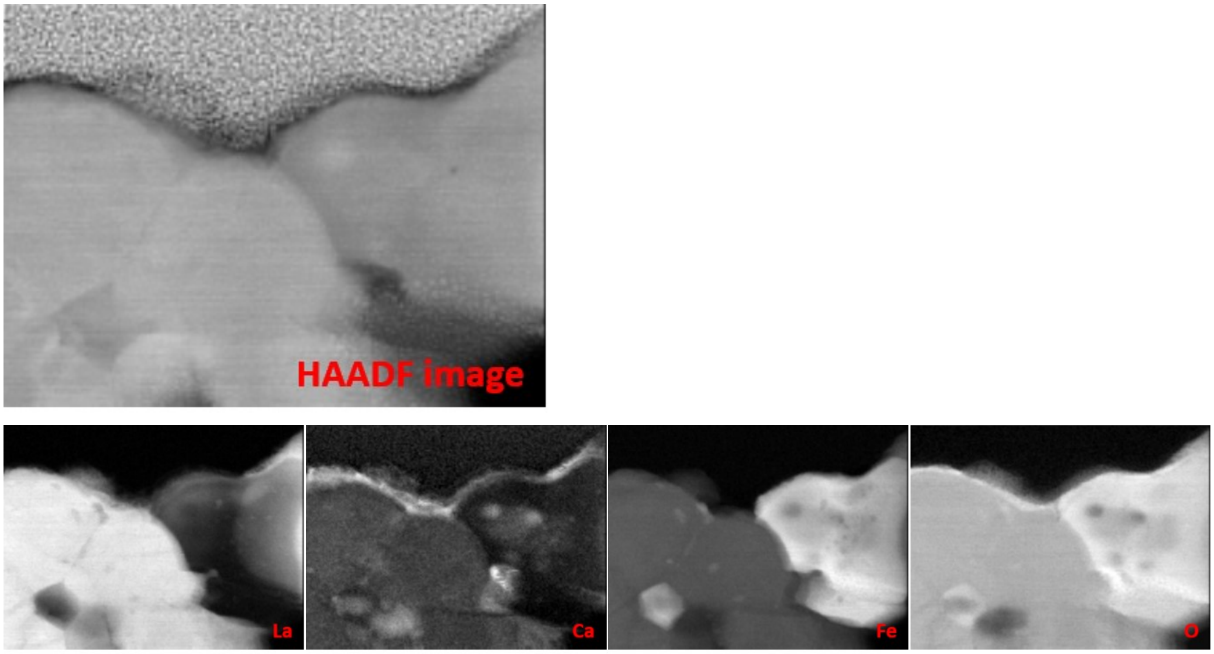

*Figure 35: STEM-HAADF image of the near-surface region and EELS elemental mapping analyses of the degraded LCF91 sample*

### *XPS depth profiling analyses*

XPS elemental depth-profiling analyses were performed on four samples from the long-term experiment. The depth-profiles were acquired in consecutive steps of surface-sensitive XPS-analyses, followed by sputtering a few nm from the surface, respectively.

Figure 36 shows the elemental depth-profiles of the analyzed samples. Due to experimental reasons, carbon is found at the surfaces of the samples. However, this is an artifact caused by C-deposition in the high-vacuum chamber during the XPS-analyses. In order to obtain the concentration profiles of the relevant elements, the profiles were recalculated using only the concentrations of the cations, here La, Ca, Fe, Cr and Si. The recalculated concentration profiles are shown in the right column. According to the profiles, Ca is accumulated on the surface of all samples, while the amounts of La and Fe are smaller. The thickness of the Ca-rich zones is between 20 and 50 nm. This result corresponds well to the STEM-EDX mapping analyses shown in Figure 35.

According to the depth-profiles, Si and Cr impurities were found on all four samples. However, it has to be noted, that on the two samples which were not exposed to humid atmospheres, these elements were found only directly on the surface, and even there only in concentrations below 3 at-% (see the full profiles of Figure 36). On those samples which were exposed to humidity the amounts of Cr were negligible, but Si was found in high concentration within the first 50 nm. This is a clear indication for the deposition of Si on the surface, which happened by transport of volatile Si species in the presence of humidity in the testing atmospheres.

| Full profiles | Recalculated profiles |
|---|---|
| 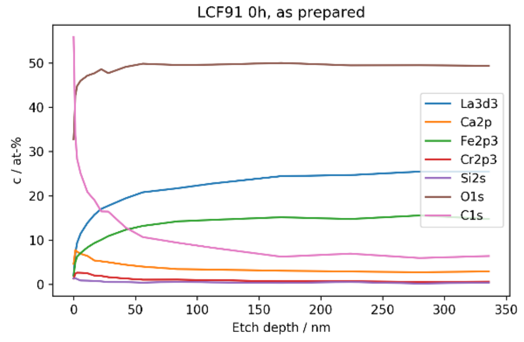 | 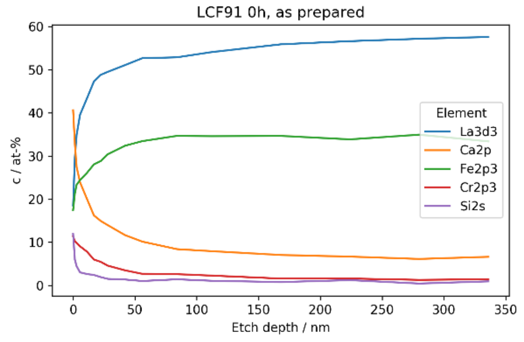 |
| 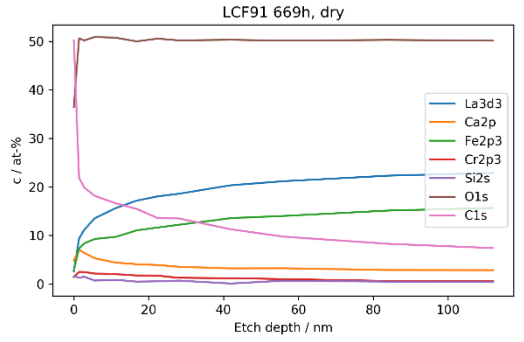 | 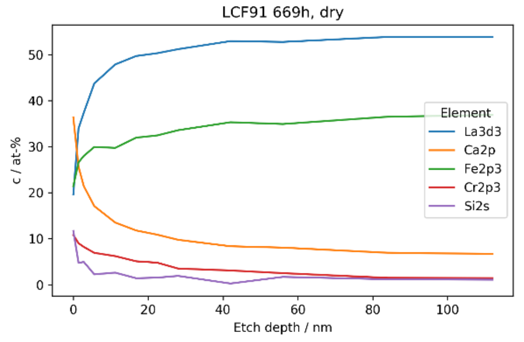 |
| 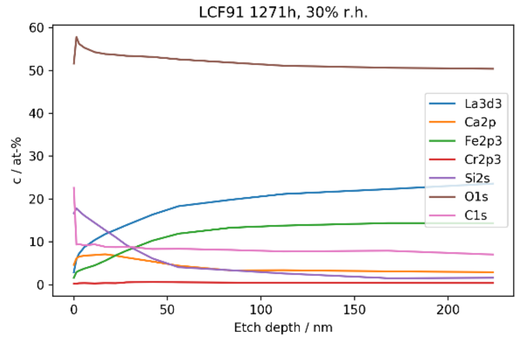 | 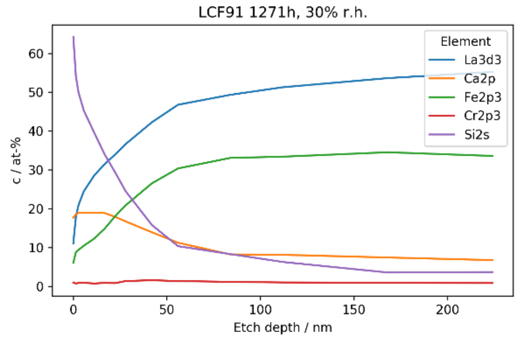 |
| 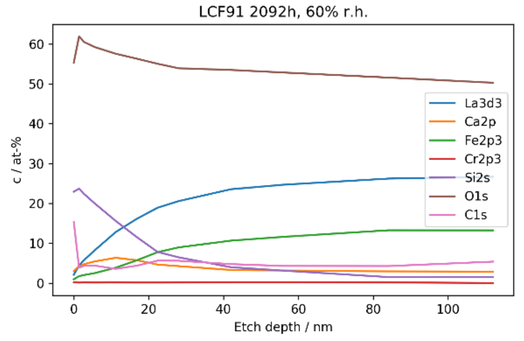 | 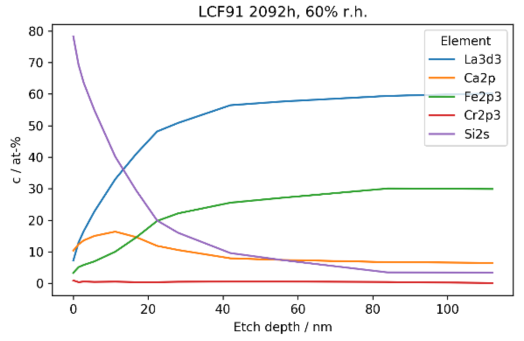 |

*Figure 36: XPS elemental depth profile analyses on LCF91 samples from different stages of the long-term experiment; in the left column all analyzed elements are shown; the right column shows the depth profiles with the carbon signal subtracted*

Figure 37 shows the concentration depth profiles of Si and Ca from the four samples respectively. While an enrichment of Ca can be found on all samples, also in the state after preparation, the deposition of Si on the surface could be clearly related to humidity of the testing atmospheres. The comparison of the four samples shows the high influence of humidity in the test gas on the surface chemistry of the samples.

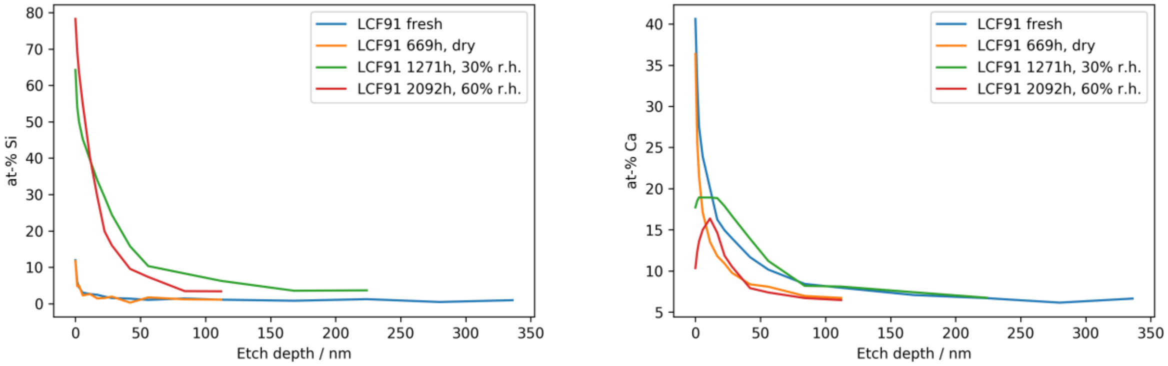

*Figure 37: Comparison of XPS elemental depth profiles of Si (left) and Ca (right) on the four analyzed samples*

The Si layer on the sample removed after 2092 hours seems to have a smaller thickness than on the sample removed after 1271 hours. However these differences might be caused by different roughnesses of the two samples.

From the findings of the post-test analyses it can be concluded that the severe degradation of $k_{chem}$ in humidified atmospheres during the long-term experiment was primarily caused by the deposition of Si on Ca-enriched surface, leading to the formation of a thin surface layer of silica and eventually calcium silicate, which blocked the oxygen exchange at the surface. This explanation fits well with similar findings on other cathode materials [118-120].

## 4.1.2 Oxygen exchange kinetics and long-term stability of LNF64

Another long-term study with conductivity relaxation was performed on the alkaline earth-free perovskite material LNF64. The sample was a thin plate with a thickness of 471 µm and an edge length of 8 mm.

Short-term characterization was performed in the temperature range between 600°C and 850°C. The long-term experiment was carried out for 2092 hours at 700°C with a variation of the humidity of the testing atmospheres, as described in section 3.3.1. The experiment was divided into the following three testing periods:

- Period 1; dry atmosphere; 0 h - 1090 h
- Period 2; humidified atmosphere with 30% relative humidity; 1090 h – 2131 h
- Period 3; humidified atmosphere with 60% relative humidity; 2131 h – 3166 h

All CR measurements were performed with p($O_2$)-steps between 0.10 bar and 0.15 bar.

### *4.1.2.1 Short-term characterization*

The oxygen exchange kinetics of LNF64 were characterized at temperatures between 600°C and 850°C and with p($O_2$)-steps between 10% $O_2$ in Ar and 15% $O_2$ in Ar in oxidizing and reducing direction. Below 600°C no relaxation signal could be detected. However also at 600°C and above the evaluation of the data was difficult. The changes in conductivity in response to the p($O_2$)-step were very small, which lead to a small signal to noise ratio. Therefore, the determination of the kinetic parameters from the fits of the diffusion model to the CR curves was affected by increased uncertainties. Figure 38 shows selected relaxation curves measured at different temperatures.

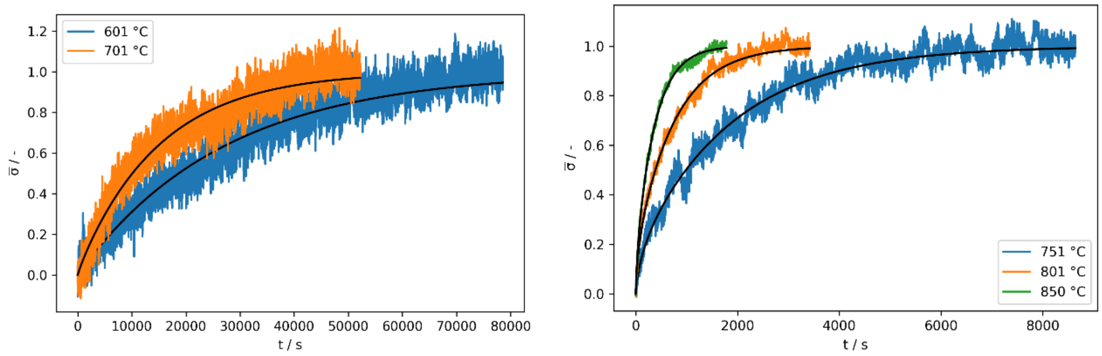

*Figure 38: Relaxation curves of CR measurements on the LNF64 plate sample at different temperatures; the black lines show the corresponding fitted functions*

As Figure 39 shows, the determined values for $k_{chem}$ and $D_{chem}$ exhibit some amount of scattering. At temperatures of 700°C and below, most of the relaxation steps, especially the reduction reactions, were diffusion controlled, meaning that the determination of $k_{chem}$ was not possible.

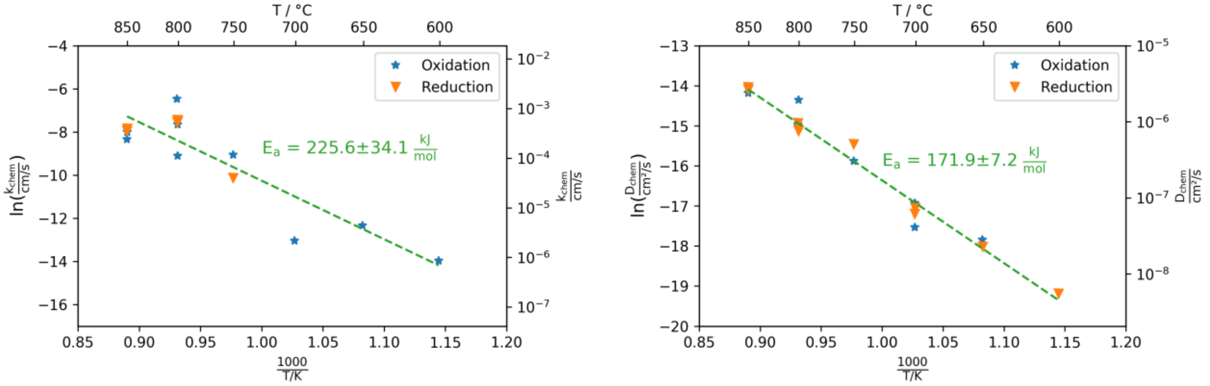

*Figure 39: Temperature dependence of $k_{chem}$ and $D_{chem}$ and corresponding activation energies of LNF64 measured by conductivity relaxation*

The temperature- and $p(O_2)$-dependence of the electronic conductivity, compare Figure 40, shows that the changes in conductivity at the established $p(O_2)$-step between 10% and 15% $O_2$ were indeed very small at temperatures below 800°C. The small variation of σ over the $p(O_2)$ is a consequence of the defect chemistry of LNF and has been reported by Niwa et al. [59] and Budiman et al. [150]. At 850°C, the difference of σ in 10% $O_2$ and 15% $O_2$ is 2.5 S/cm. With the absolute conductivity being in the range of 520 S/cm that is a relative difference of 0.5%. This is relatively low, but measurable with the given experimental setup. Therefore, the long-term experiment was performed at 850°C.

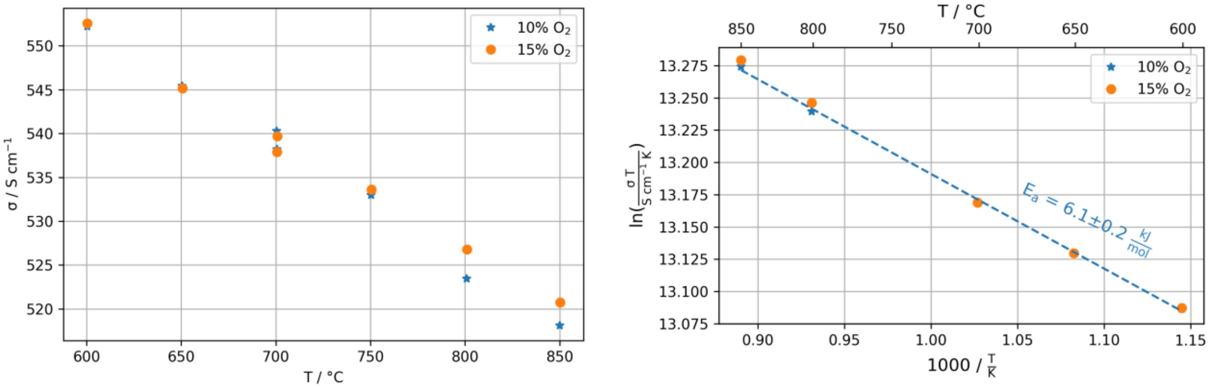

*Figure 40: Temperature dependence and activation energy of the electrical conductivity of LNF64*

### 4.1.2.2 Long-term characterization

Examples of the relaxation curves, which were measured during the long-term experiment, are shown in Figure 41.

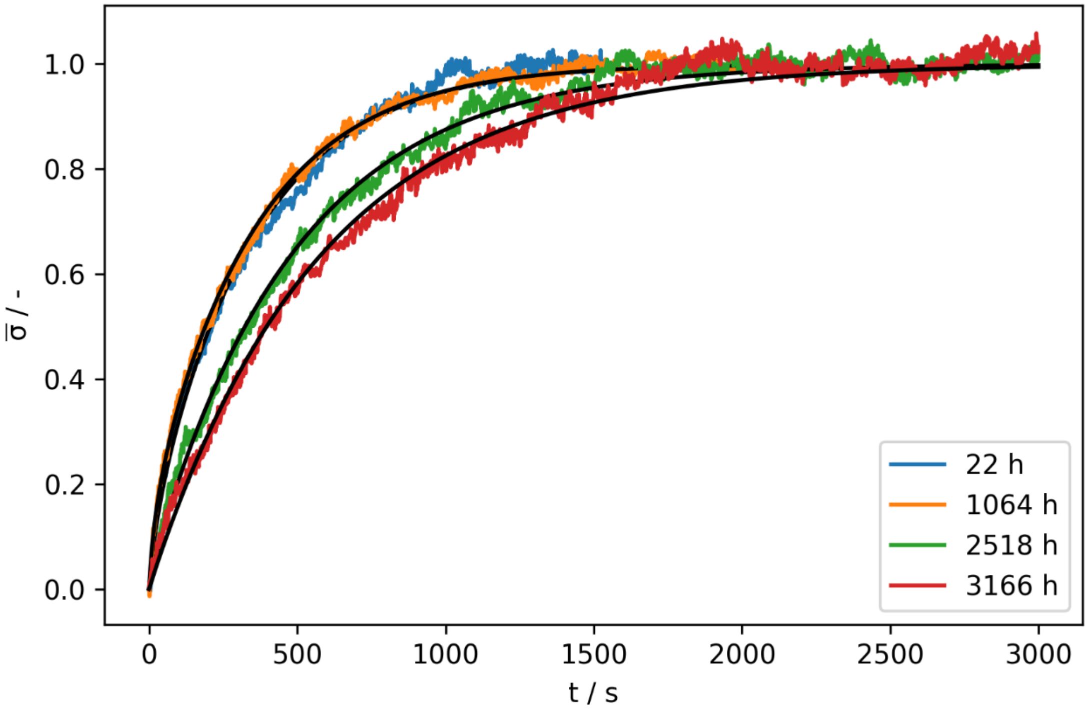

*Figure 41: Selected relaxation curves of LNF64 from the long-term experiment*

Figure 42 shows $k_{chem}$ and $D_{chem}$ as a function of time at 850°C. During the first period in dry atmosphere the values of $k_{chem}$ were scattering between $10^{-4}$ and $10^{-3}$ cm/s. In the presence of humidity there seemed to be a small activation of $k_{chem}$ (up to ~$5\times10^{-3}$ cm/s), followed by a moderate degradation. However, the scattering of the data is quite high.

$D_{chem}$ could be determined with higher accuracy and varied between $7\times10^{-7}$ and $1\times10^{-6}$ cm²/s in dry atmospheres. It remained constant when humidity was added to the testing atmospheres. However, the scattering in the data increased during the second and third period.

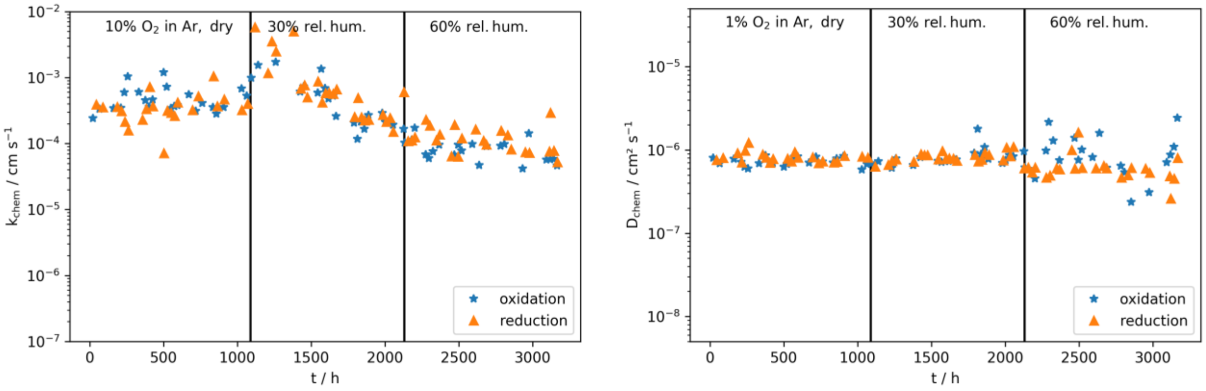

*Figure 42: Time dependences of $k_{chem}$ and $D_{chem}$ at 850°C in dry and humidified atmospheres*

The electrical conductivity of the sample was increasing during the long-term experiment from 520 to 550 S/cm (Figure 43). This is a relatively strong increase, but the trend seems to be only time-dependent and not influenced by the humidity content of the atmosphere, since no transient behavior was observed when switching from dry to humidified conditions.

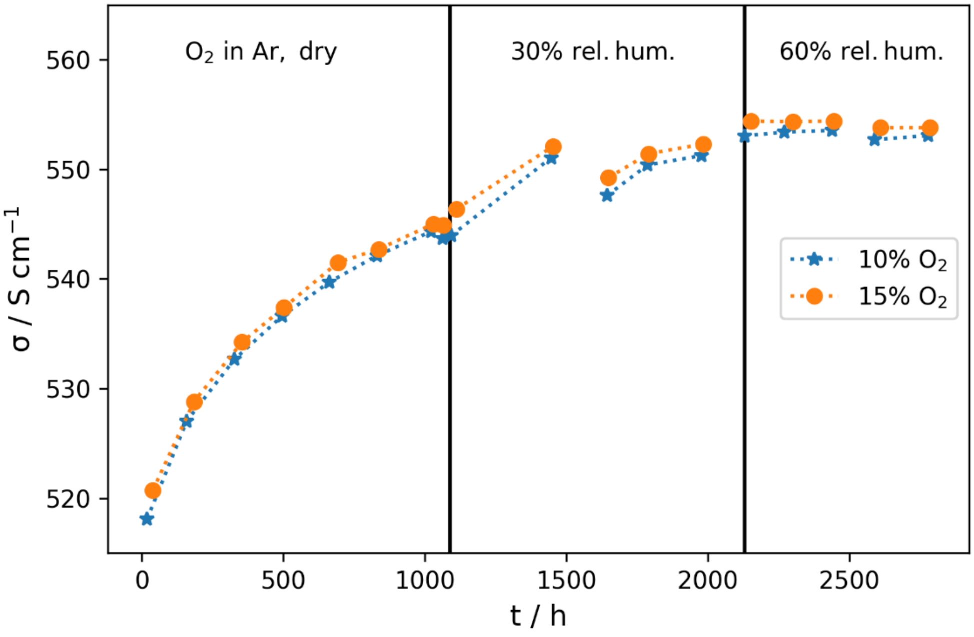

*Figure 43: Time dependence of the electrical conductivity of LNF64 at 850°C*

### 4.1.2.3 Post-test analyses

In order to further investigate the degradation mechanisms, selected samples were analyzed by SEM on the surface. Analyses were performed on the fresh specimen representing the as-prepared state, samples which were removed from the reactor at the end of each testing period, and the CR plate itself, which had undergone the whole long-term experiment.

### *SEM+EDX of the surface*

Figure 44 shows an overview of the surface images of the samples from different periods of the experiment.

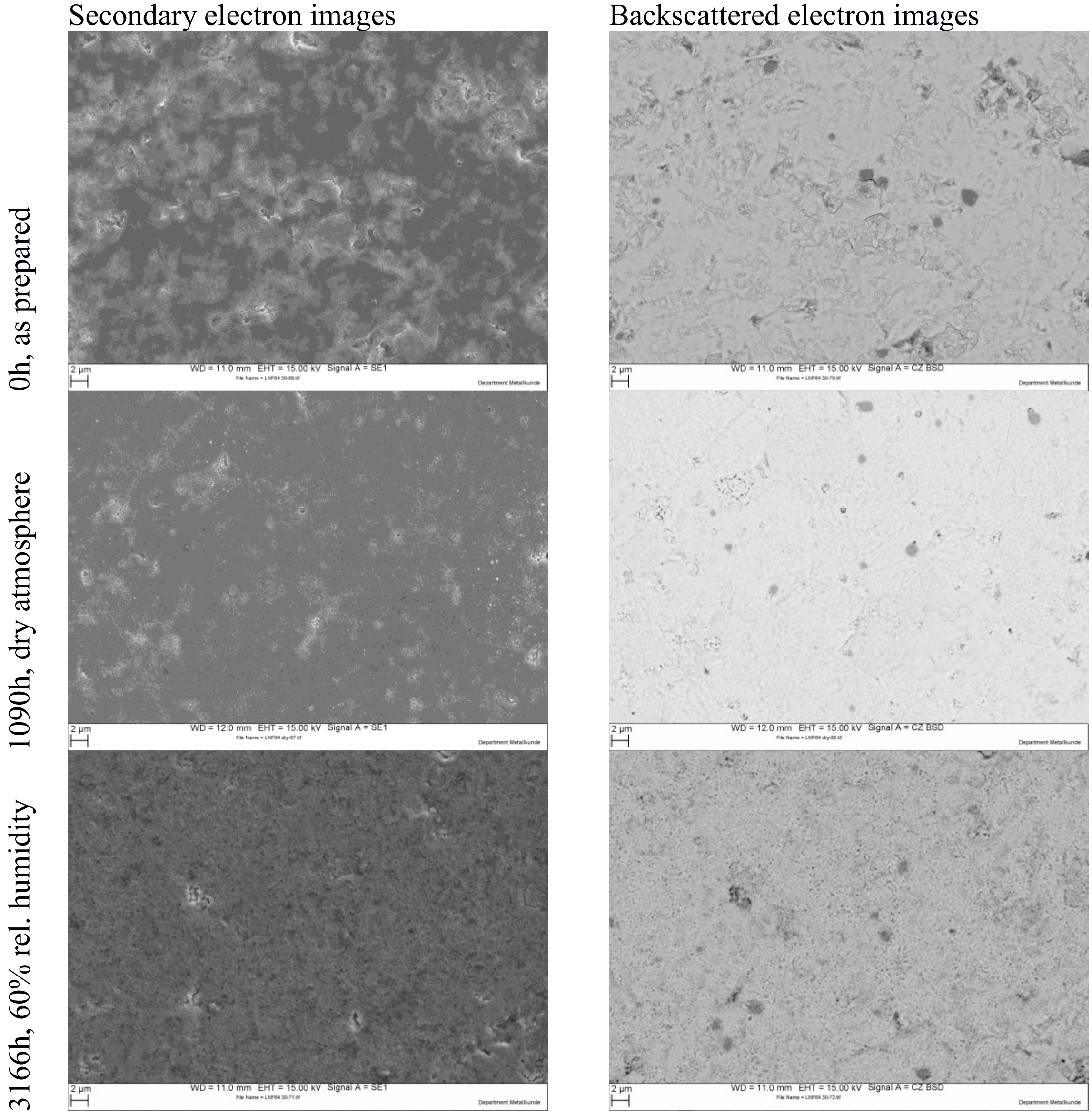

*Figure 44: Post-test analyses of LNF64 samples from different periods of the long-term experiment*

The fresh sample shows a relatively smooth surface with a few pits and cracks. The BSE image shows a few darker grains, which exhibit a higher amount of Ni in the EDX, and are most likely precipitates of NiO. The sample removed from the reactor after 1000 hours seemed to be a bit smoother on the surface. The grain structure is more visible on this sample which indicates that the sample might have been thermally etched during the experiment.

The samples which were exposed to 30% and 60% relative humidity showed a different morphology. A fine-grained structure seems to be growing on the surface due to the presence of $H_2O(g)$ in the atmosphere. The presence of Si could be detected on these samples by EDX. Figure 45 shows the surface of this sample at higher magnification.

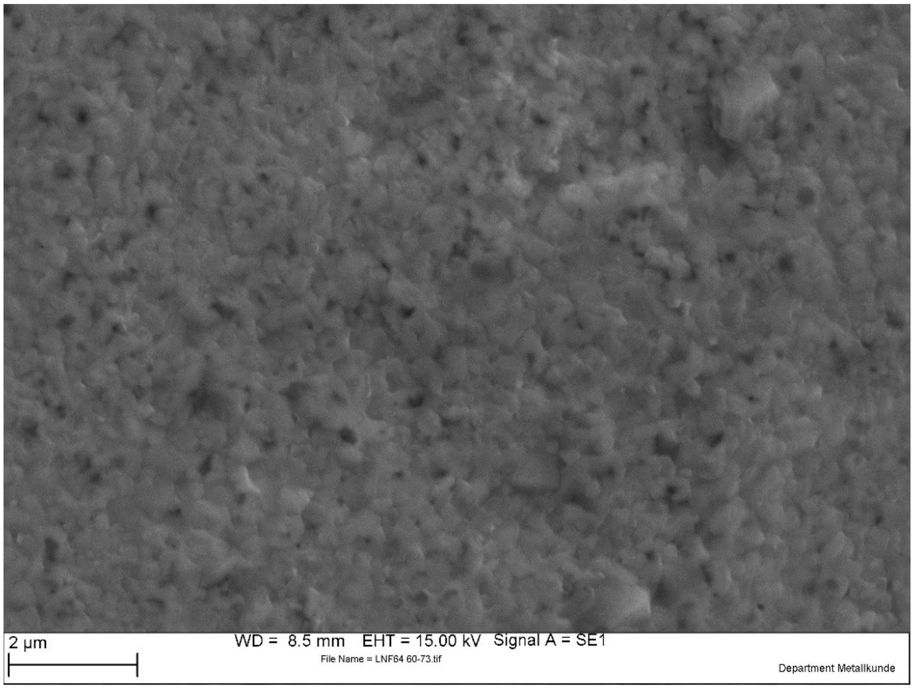

*Figure 45: High-magnification SEM-SE image of the surface of the degraded LNF64 sample*

Chemical analyses were performed by EDX surface scans. Figure 46 shows selected EDX spectra of the fresh and the degraded samples. From these spectra quantitative analyses were performed by the INCA software.

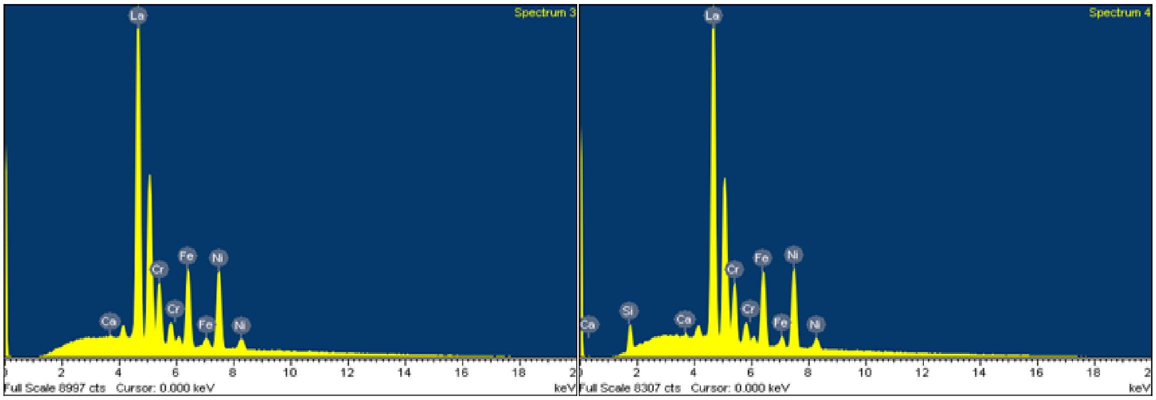

*Figure 46: EDX spectra of the fresh LNF64 sample (left) and the sample which was degraded in the long-term experiment (right)*

The analyses were calculated two times for all four samples, using calibrations with an Fe and Ni standard, respectively. Both methods gave similar results without significant differences. The results of these analyses are listed in Tables Table 5-Table 8. The concentrations of La, Ni and Fe correspond well to the nominal composition of LNF64. Si was found only on the samples which were exposed to humid atmospheres during the experiment. The Si content increased with exposure time. Besides La, Ni, Fe and Si, also Cr was found on all samples and Ca and Br were found in some cases. However, the estimated concentrations are quite small und have a high uncertainty. While Cr and Ca might have been present in traces on the sample surfaces, the findings of other elements were probably mathematical artifacts from the fitting algorithm for the quantitative analysis. According to the results of the post-test analyses it can be concluded, that Si-poisoning in humid atmospheres (see section 2.2.4.3, page 17) was the dominant degradation mechanism. However, the influence of Si-deposition on $k_{chem}$ seems to be rather small, compared to the results of the long-term experiment with LCF91 (section 4.1.1.2, page 43) and previous experiments with LSC64 [118].

*Table 5: Results of quantitative EDX analyses of the LNF64 sample in the state after preparation (elements below the detection limit are written in cursive letters)*

| | Calibrated with Fe at-% | Calibrated with Ni at-% |
|---|---|---|
| La | 48.8 | 48.3 |
| Ni | 28.6 | 29.3 |
| Fe | 21.3 | 20.7 |
| *Cr* | *1.0* | *1.1* |
| *Ca* | *< 0.5* | *< 0.5* |

*Table 6: Results of quantitative EDX analyses on the LNF64 sample from the long-term experiment in dry atmosphere (elements below the detection limit are written in cursive letters)*

| | Calibrated with Fe at-% | Calibrated with Ni at-% |
|---|---|---|
| La | 49.3 | 49.4 |
| Ni | 29.6 | 29.5 |
| Fe | 20.2 | 20.2 |
| *Cr* | *< 1* | *< 1* |
| *Br* | *< 1* | |

*Table 7: Results of quantitative EDX analyses on the LNF64 sample from the long-term experiment, which was exposed to max. 30% relative humidity (elements below the detection limit are written in cursive letters)*

| | Calibrated with Fe at-% | Calibrated with Ni at-% |
|---|---|---|
| La | 46.7 | 46.7 |
| Ni | 27.9 | 27.7 |
| Fe | 20.4 | 20.5 |
| Si | 3.7 | 4.0 |
| *Cr* | *< 1* | *< 1* |
| *Ca* | *< 1* | *< 1* |
| *Al* | | *< 1* |
| *Br* | *< 1* | |

*Table 8: Results of quantitative EDX analyses on the LNF64 sample from the long-term experiment, which was exposed to max. 60% relative humidity (elements below the detection limit are written in cursive letters)*

| | Calibrated with Fe at-% | Calibrated with Ni at-% |
|---|---|---|
| La | 46.61 | 46.82 |
| Ni | 27.74 | 27.95 |
| Fe | 19.57 | 19.98 |
| Si | 5.09 | 4.33 |
| *Cr* | *< 1* | *< 1* |
| *Ca* | *< 1* | *< 1* |

## 4.2 Electrochemical properties and long-term stability of cathodes with different microstructures under Si-poisoning conditions

The electrochemical properties and long-term stability of model cathodes with complementary microstructures were investigated with electrochemical impedance spectroscopy in dry and humid atmospheres under Si-poisoning conditions. Tests were executed on symmetrical cells with cathodes of the same material (LSC64) but different microstructures (thin-film architecture, in infiltrated architecture and conventionally screen-printed cathode, see Figure 47). The experiments were carried out at 700°C according to the parameters described in section 3.3.1. Each experiment had a different duration, depending on the degradation rate. Details are given in the following sections.

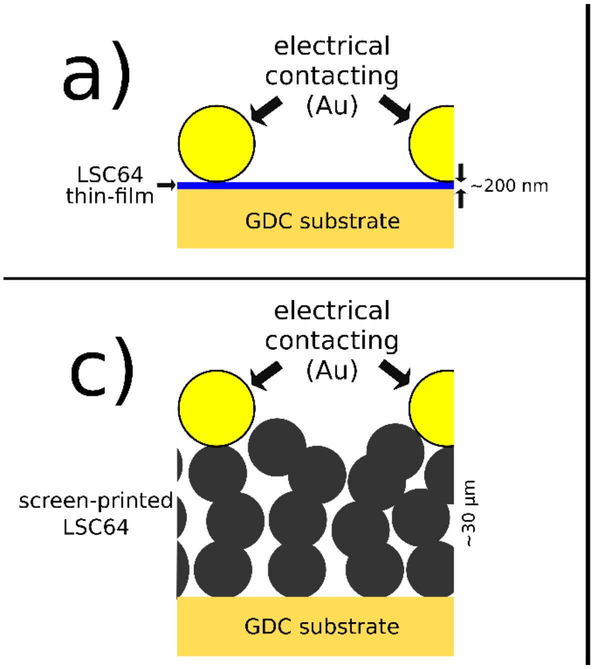

*Figure 47: Architectures of the LSC64 cathodes on which the long-term experiments were performed: a) Thin-film cathode, b) infiltrated LSC64 in GDC backbone with current collector and c) screen-printed cathode*

### 4.2.1 Thin-film cathodes of LSC64

A symmetric electrochemical cell with thin-films of LSC64 on GDC substrates, which were prepared by sol-gel spin-coating, was characterized in dry and humid atmospheres by electrochemical impedance spectroscopy. The thin-films were contacted directly with an Au mesh; no screen-printed current collector was applied on the cell. Short-term characterization was performed in a temperature range between 500°C and 700°C. Afterwards the long-term experiment was performed at 700°C. The durations of the three testing periods were as follows:

- Period 1, dry atmosphere: 0-516 h
- Period 2, 30% relative humidity: 516-1080 h
- Period 3, 60% relative humidity: 1080-1612 h

Additional samples with an LSC64 thin-film on one side were placed in the reactor. These samples were exposed to the same conditions as the cathodes of the cell. At the end of every period one sample was removed from the reactor. Therefore, these samples represent the conditions of the cathode at different states of the experiment. The cell and the additional samples were analyzed in post-test analyses by SEM, STEM, EDX and EELS.

#### *4.2.1.1 Short term characterization and temperature dependence*

Figure 48 shows selected impedance spectra measured on the fresh cell at temperatures between 500 and 700°C. At 500°C the impedance spectrum showed a shape similar to a Gerischer impedance. However, it was not possible to fit the data well with a Gerischer impedance since the curve on the low-frequency side was slightly depressed. With increasing temperature, the impedance spectrum of the sample overlapped with the inductivity of the reactor. At temperatures above 550°C a low-frequency arc appeared.

In some impedance spectra, data points with a decreasing ohmic resistance are found at the low-frequency side. This is probably an artefact caused by temperature fluctuations or by self-heating of the sample due to the applied electrical power. These points were not considered for the CNLS-fits. To prevent self-heating, the ac-voltage of the signal was reduced from 0.5 V to 0.25 V in the subsequent measurements.

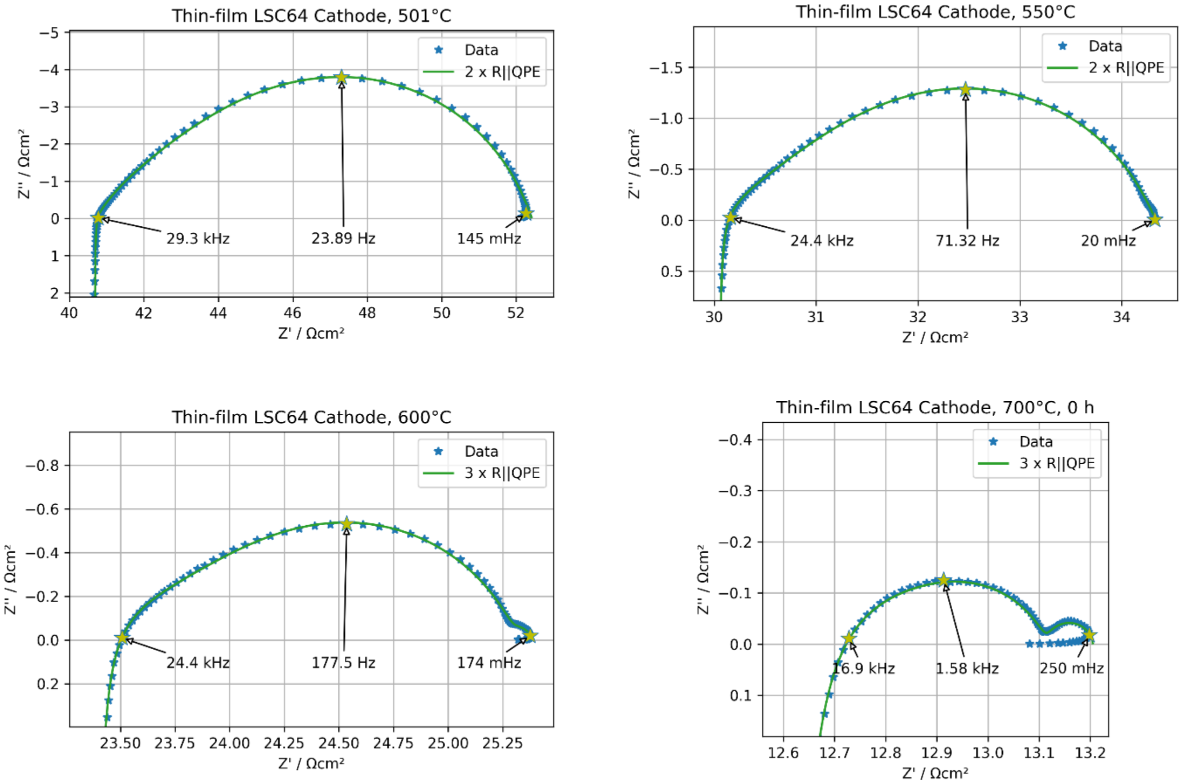

*Figure 48: Impedance spectra of the LSC64 thin-film cathode measured at different temperatures*

For fitting the data, the equivalent circuit model with three R-CPE elements, as described in Figure 12 a) on page 35, was applied. In the following text, the parameters of the R-CPE circuits are denoted by the indices "hi", "mid" and "low" for the high frequency, intermediate frequency and low frequency R-CPE element respectively. In the current case, the two R-CPE elements indexed with "hi" and "mid" covered the asymmetrical semicircle at higher frequencies and the third one fitted the low-frequency arc, which was a nearly perfect RC-semicircle. In Figure 49 the results of the fits, the ohmic resistance and apparent capacitance of the R-CPE-elements, are presented as a function of temperature in an Arrhenius plot. The data show a significant temperature dependence of $R_{hi}$ and $R_{mid}$, and a temperature-independent low-frequency resistance $R_{low}$.

The capacitances are almost independent of temperature. $C_{low}$ has a high value above 1 $F/cm^2$. A comparison of this parameter with literature data summarized in Table 1 on page 26 leads to the conclusion that the low frequency arc is caused by gas diffusion limitation to the cathode. Another indication supporting this assumption is the fact, that the corresponding resistivity $R_{low}$ is practically temperature invariant.

Some care has to be taken with the interpretation of $C_{hi}$ and $C_{mid}$. The high-frequency capacitance varies from $2\times10^4$ at 500°C to $5\times10^5$ at 700°C. This strong variation might be caused by uncertainties of the data fitting due to the influence of the inductivity at high frequencies. Both capacitances differ by only one order of magnitude. Since both capacitances are calculated from the overlapping R-QPE-elements fitting a single arc, both should be seen as part of the same rate-limiting mechanism.

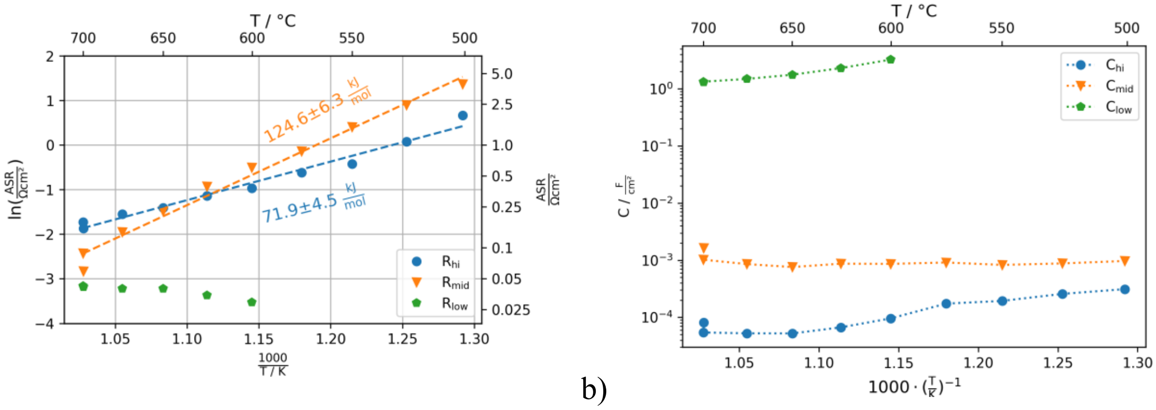

a)

b)

*Figure 49: a) Resistances and b) capacitances acquired from impedance spectroscopy as functions of temperature*

It turned out to be useful to combine the ohmic parameters $R_{hi}$ and $R_{mid}$ and consider the sum of both resistances. In the following section this summarized resistance will be called $ASR_{pol}$. As Figure 50 shows, the summarized resistance follows a perfect linear trend in the Arrhenius plot. The low-frequency resistance can be ascribed to gas diffusion and will be denoted by $ASR_{gas\text{-}diff}$.

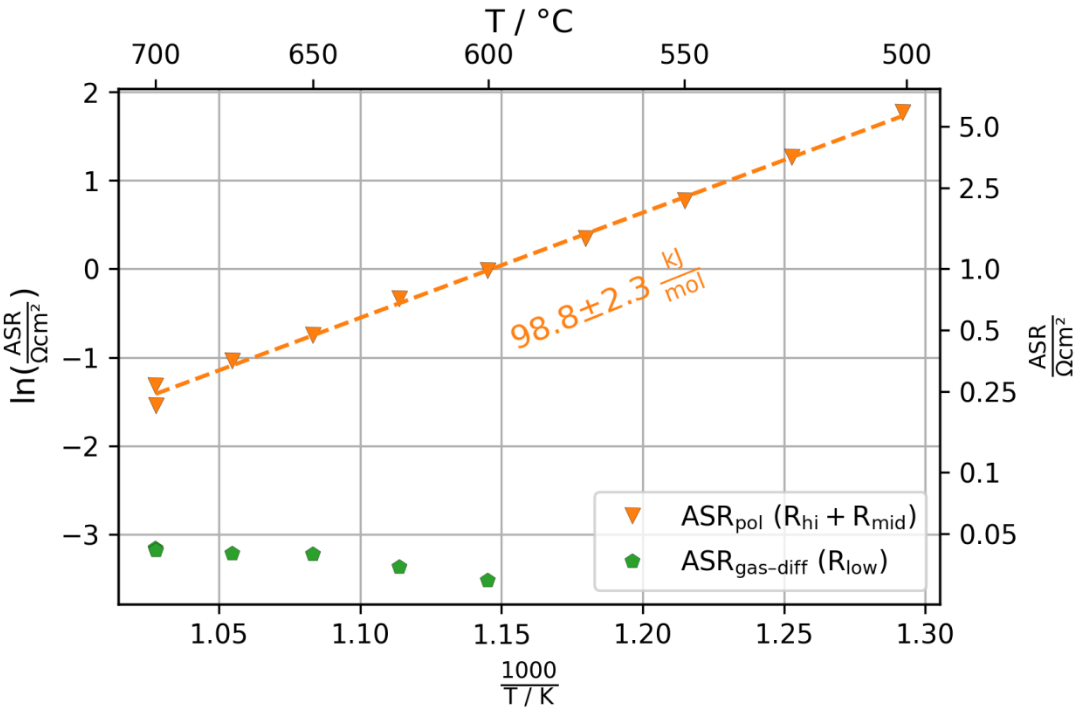

*Figure 50: Polarization resistance, activation energy, and low-frequency resistance as functions of temperature*

### 4.2.1.2 Long-term characterization

During the long-term experiment at 700°C, the measured impedance spectra of the sample showed significant changes. In the first period, the high-frequency arc showed a significant decrease, while the low-frequency arc remained constant. For an accurate fit an equivalent circuit with only two R-QPE-Elements was sufficient. Introducing humidity into the testing atmosphere however caused a significant degradation. Due to changes in the shape of the impedance spectra, which are shown for selected measurements in Figure 51, using the three R-CPE-model became necessary again.

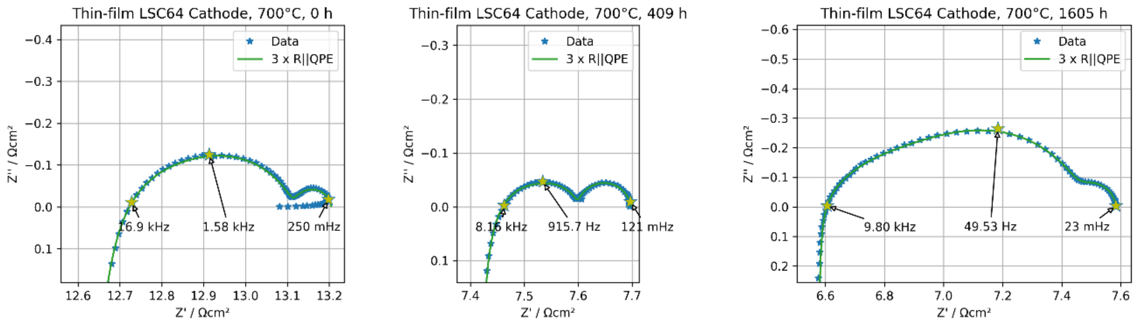

*Figure 51: Selected impedance spectra measured at different periods of the long-term experiment*

Figure 52 gives an alternative view on the cathode degradation, in the form of Bode plots of the imaginary part of Z for selected impedance spectra. Figure 52 a) shows the decrease of the high-frequency arc during the first period of the experiment, b) and c) the degradation during the experimental periods in humid atmospheres. The degradation is causing a shift of the peak frequency from about 2 kHz to 80 Hz.

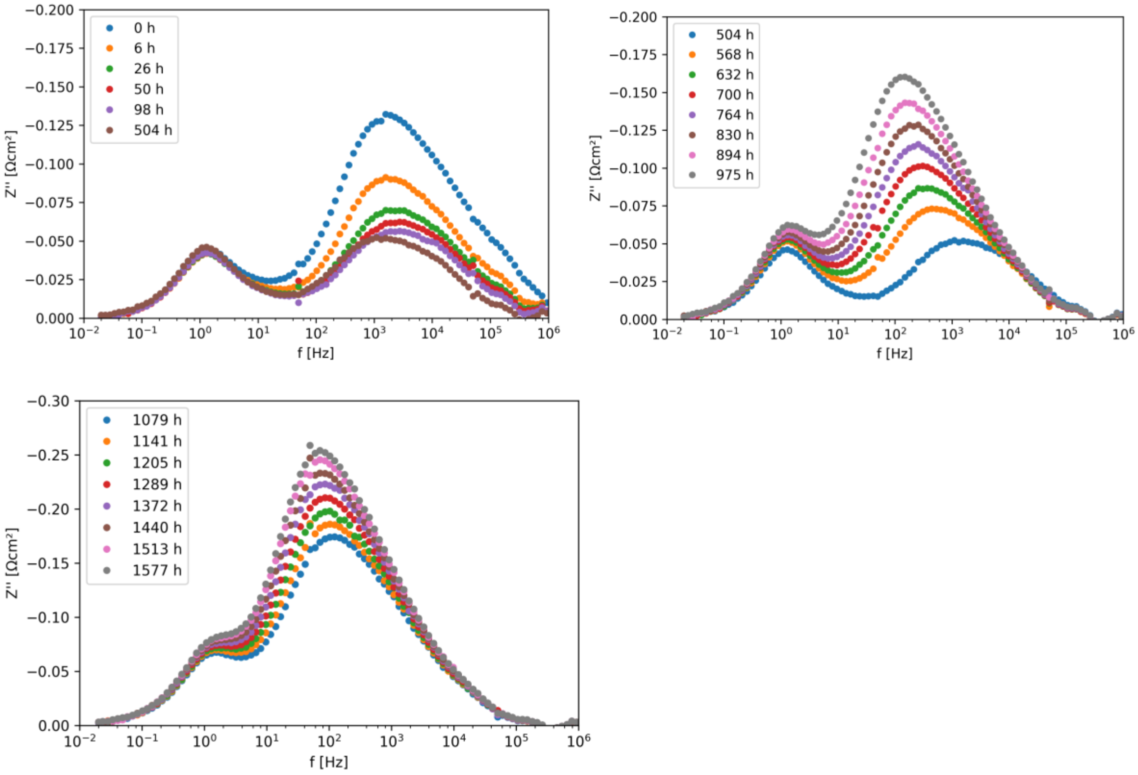

*Figure 52: Bode-plots (Z'' vs. frequency) of selected impedance spectra measured during the long-term experiment; inductivity was subtracted from the plotted data*

Figure 53 shows the plots of the fitted resistive parameters and the calculated apparent capacitances. The values of $R_{hi}$ and $R_{mid}$ show a relative high uncertainty when plotted separately, but the sum of the two parameters, which is defined as polarization resistance $ASR_{pol}$ leads to stable values with a continuous evolution over time (Figure 54).

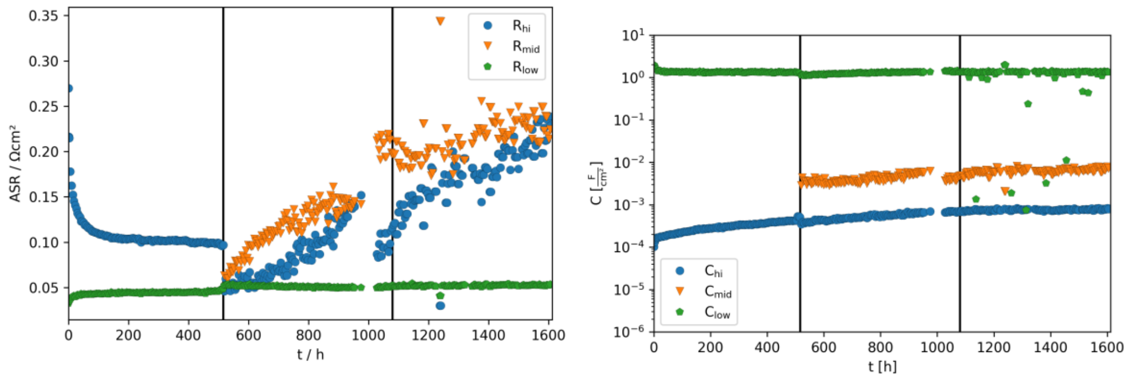

*Figure 53: Time-dependent evolution of resistances (left) and capacitances (right) acquired from impedance spectroscopy measurements of the long-term experiment*

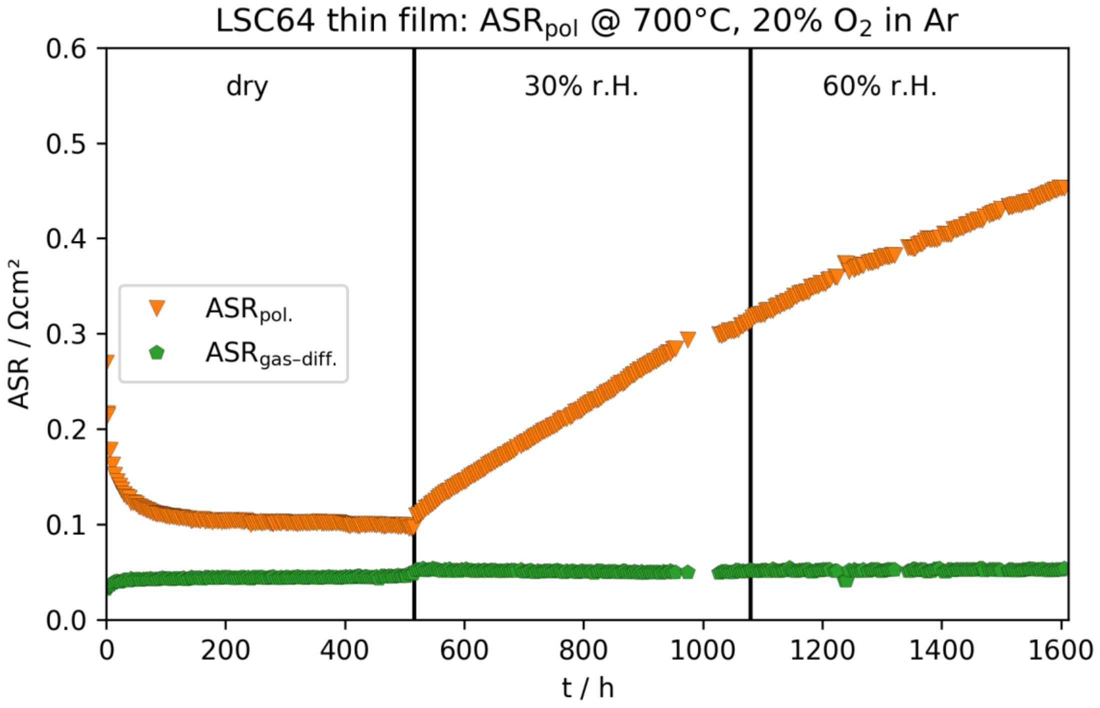

*Figure 54: Area-specific polarization resistance and gas-diffusion resistance as function of time*

The polarization resistance $ASR_{pol}$ showed a relatively strong increase in humidified atmospheres, with a degradation rate between 0.2 and 0.4 Ωcm² per 1000 hours. The gas diffusion resistance remained constant over the whole experiment.

At the end of the first and of the third period of the experiment additional temperature-dependent EIS measurements between 500°C and 700°C were carried out during cooling the reactor. The results of these temperature runs are shown in Figure 55. The decrease of the polarization resistance $ASR_{pol}$ during the first period in dry atmosphere was also measured at lower temperatures, while the activation energy increased slightly from around 100 kJ/mol to 120 kJ/mol.

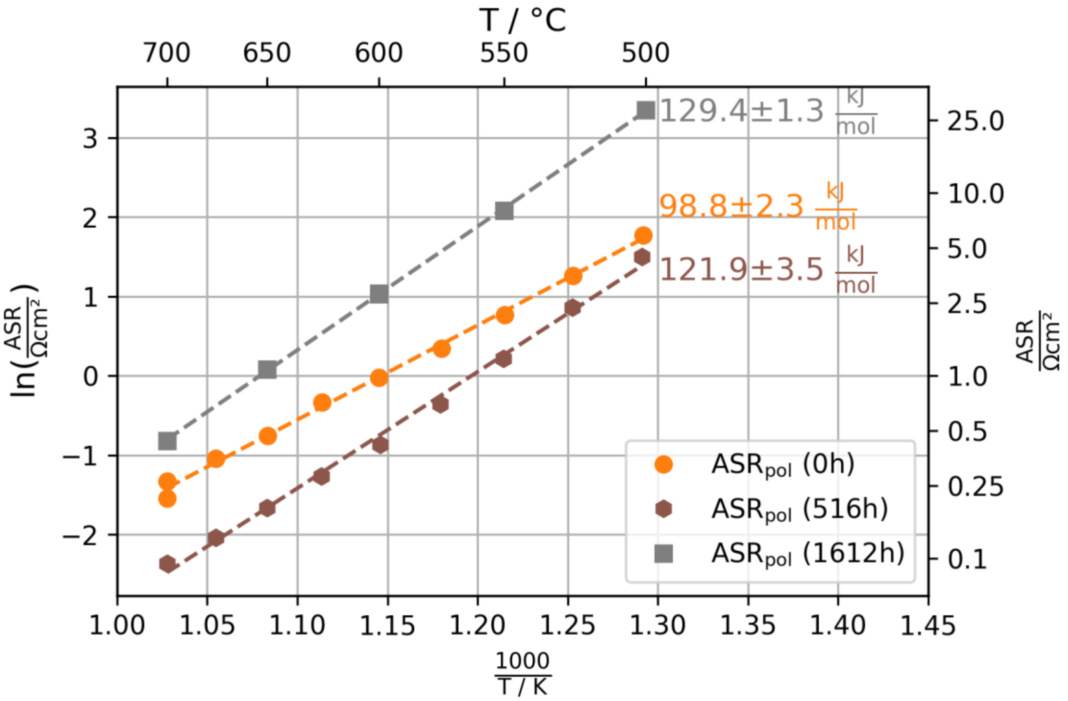

*Figure 55: Area-specific polarization resistance as function of temperature, measured at different periods of the long-term experiment*

Finally, it should be noted that the ohmic resistance $R_0$, which is obtained from the high-frequency intercept of the impedance spectra in the fitting model, also showed a time-dependent behavior: It decreased from 12.5 Ωcm² to 6.6 Ωcm² (Figure 56). Taking into account literature data for the ionic conductivity of GDC (0.0544 S/cm for GDC at 700°C, according to [17]) and the thickness of the electrolyte substrate (1.720 mm), the area-specific electrolyte resistance should be significantly lower, about 3.16 Ωcm². These are indications that besides the electrolyte resistance additional parameters contributed to $R_0$. It is very likely that due to its low thickness the in-plane electrical resistance of the thin-film cathodes contributed significantly to $R_0$. The continuous decrease of $R_0$, which didn't show any influence of the atmospheric humidity could be explained by an increasing electrical conductivity of the thin-films due to annealing during the long-term experiment.

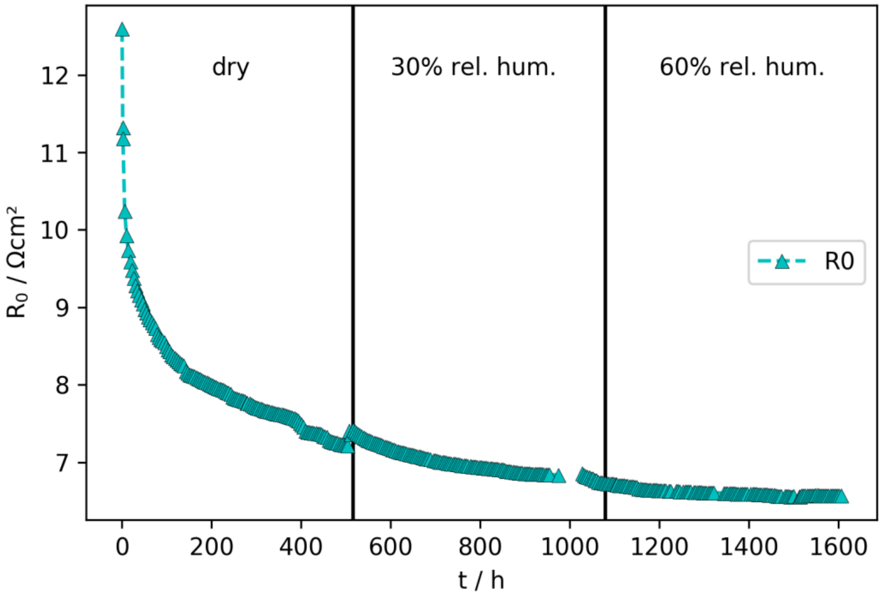

*Figure 56: Time dependence of the ohmic resistance $R_0$ during the long-term experiment*

### 4.2.1.3 Post-test analyses

For post-test analyses, selected samples of the long-term experiment were analyzed by SEM and STEM and corresponding analytical techniques (EDX and EELS) to gain information about the degradation mechanisms. A sample with a freshly prepared LSC64 thin-film, the degraded cell and samples which were removed from the experimental setup at the end of each testing period were analyzed to investigate the degradation and its time-dependent evolution. Table 9 gives an overview on the samples and the performed analyses:

*Table 9: List of analyzed samples and performed analyses*

| **Sample** | **SEM-EDX surfaces** | **SEM-EDX cross-sections** | **STEM-EDX/EELS** |
|---|---|---|---|
| SC-LSC64 as prepared | ✓ | ✓ | |
| SC-LSC64 after 516 h (dry) | ✓ | | |
| SC-LSC64 after 1080 h (max. 30% rel. hum.) | ✓ | | |
| SC-LSC64 cell after 1610 h (max. 60% rel. hum.) | ✓ | ✓ | ✓ |

### *SEM of the surfaces*

Figure 57 shows a surface survey image of the freshly prepared LSC64 film and the surface of the degraded cathode. The images were acquired in the secondary electron imaging mode, so the different greyscales are indicators for surface roughness. The left picture shows a characteristic morphology with wave-like patterns on the surface, which originate from the coating process due to fast annealing directly after spin-coating. In comparison, the surface of the degraded film is much smoother. This change in the surface roughness obviously happened during the experiment, so significant mass transport must have taken place.

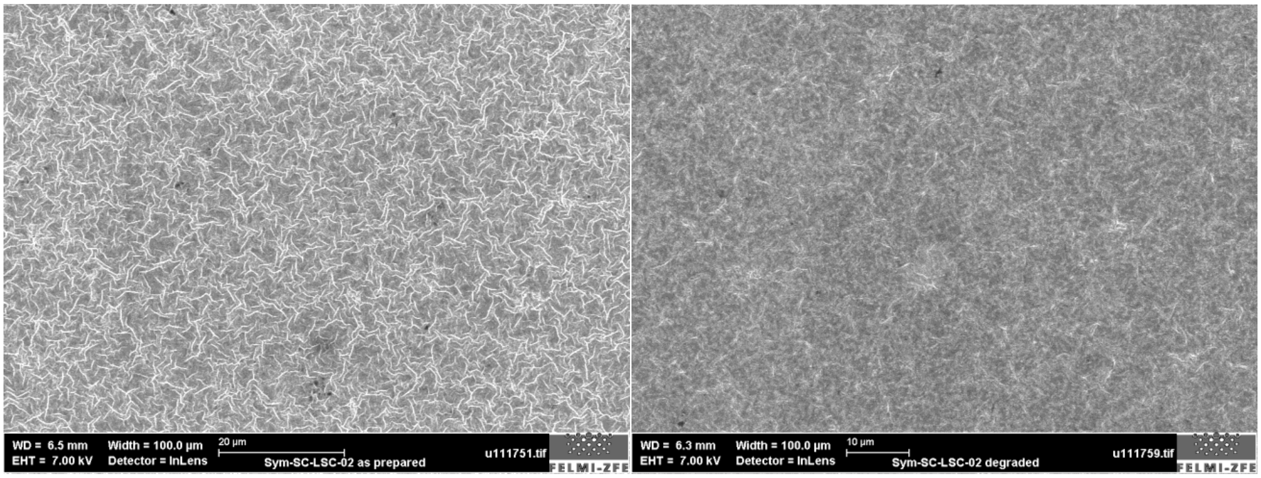

*Figure 57: SEM surface survey images of a fresh LSC64 thin-film (left) and the degraded thin-film cathode from the long-term experiment (right)*

Figure 58 shows images of the fresh and the degraded samples in higher magnification. The images in the left column were acquired by a secondary electron detector, those in the right column by a backscattered electron detector.

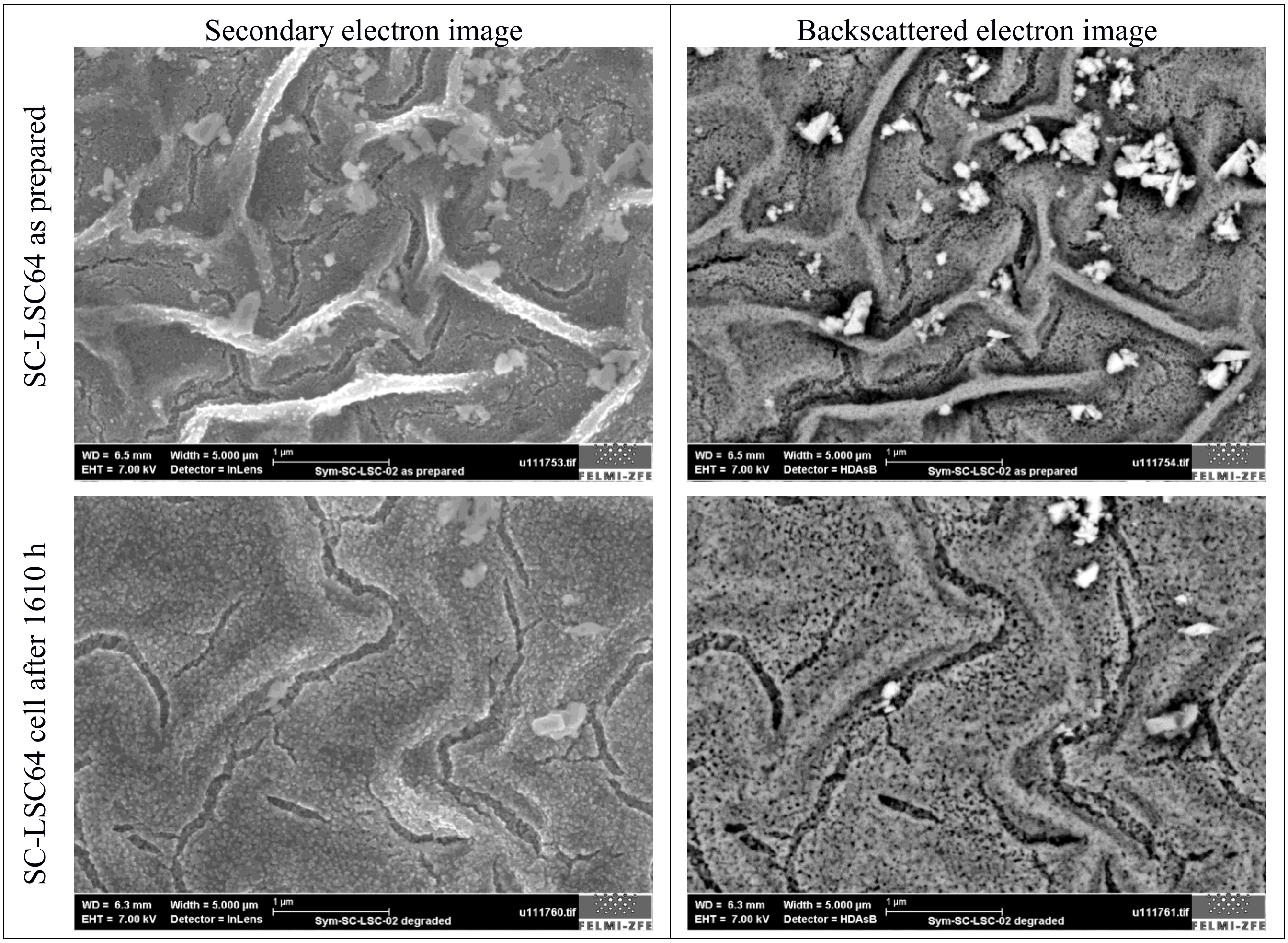

*Figure 58: SEM images of the fresh and the degraded LSC64 thin-film sample*

The images of the fresh sample show a fine-grained structure with grain sizes below 100 nm. In comparison, the degraded films had a significantly larger grain size. The coarse grains which appear brighter in the backscattered electron images were identified as GDC particles by EDX. These grains are residues from sample preparation: The originally disk-shaped spin-coated samples were cut into pieces for several analyses. Cutting was performed with a diamond wire saw, but no cutting liquid was used to prevent contamination. However, a certain amount of dust from the GDC electrolyte was deposited on the samples. Since more intensive cleaning steps were omitted to prevent possible damages of the surfaces it was not possible to remove the GDC particles completely. However, since the particles were introduced after the electrochemical experiment they can be excluded as a cause of degradation.

Images observed in the highest zoom levels are shown in Figure 59. As far as it can be estimated, the grains might have doubled in size during the long-term experiment, but the grain size was still below 100 nm at the end.

Besides the morphological changes in surface structure, no evidence for chemical degradation effects (e.g. secondary elements) could be found in corresponding EDX analyses.

|  | Secondary electron images | Backscattered electron images |
|---|---|---|
| SC-LSC64 as prepared | 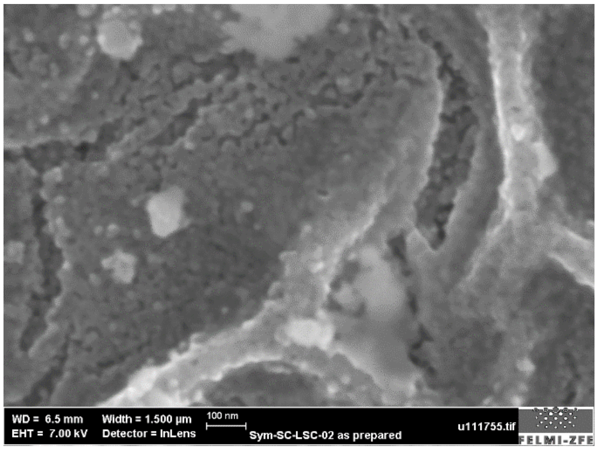 | 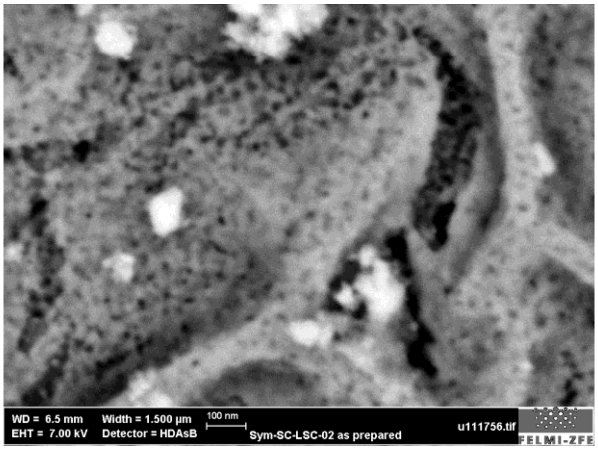 |
| SC-LSC64 cell after 1610 h | 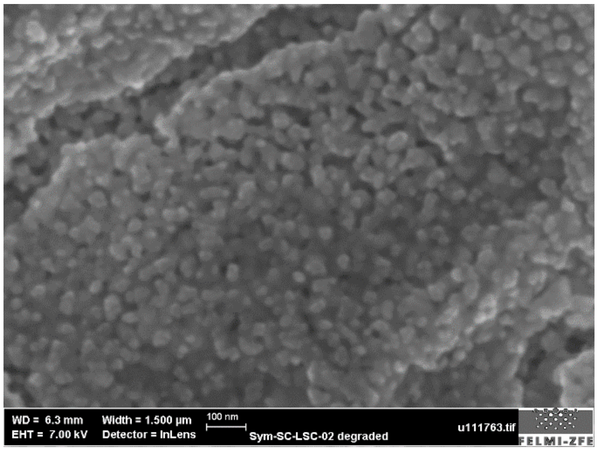 |  |

*Figure 59: SEM images of the fresh and the degraded LSC64 thin-film sample at the highest possible zoom levels*

By analyses of samples, which were removed during intermediate steps of the long-term experiment, the evolution of the morphology could be illustrated. Figure 60 shows the state of a thin-film after preparation, after about 500 hours at 700°C in dry atmosphere, after additional 500 hours at 30% relative humidity and at the end of the experiment with a maximum relative humidity of 60%. These images indicate that the morphological changes in the thin-films happened in presence of humidity in the testing atmosphere, while in dry atmosphere no significant grain growth could be found.

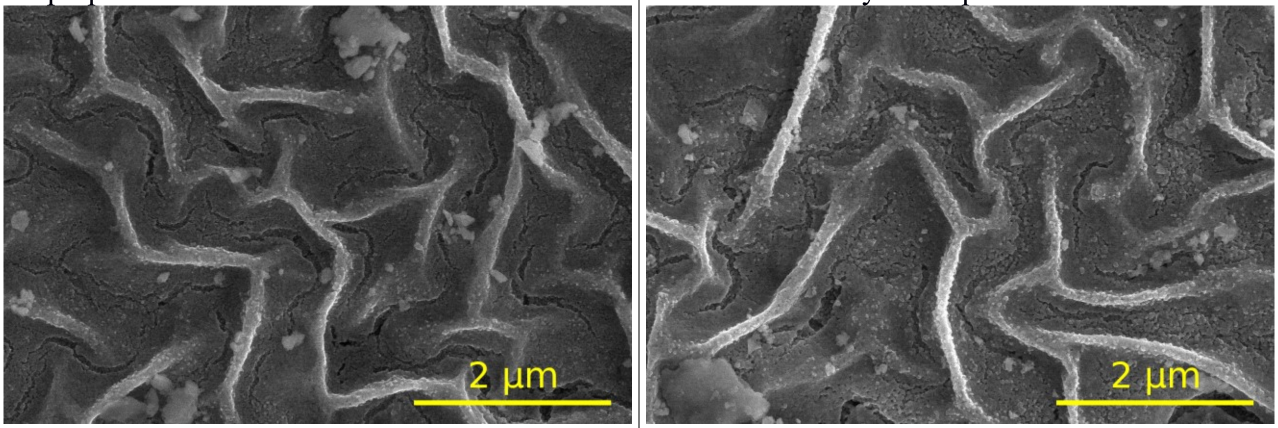

As prepared:

After 516 h in dry atmosphere:

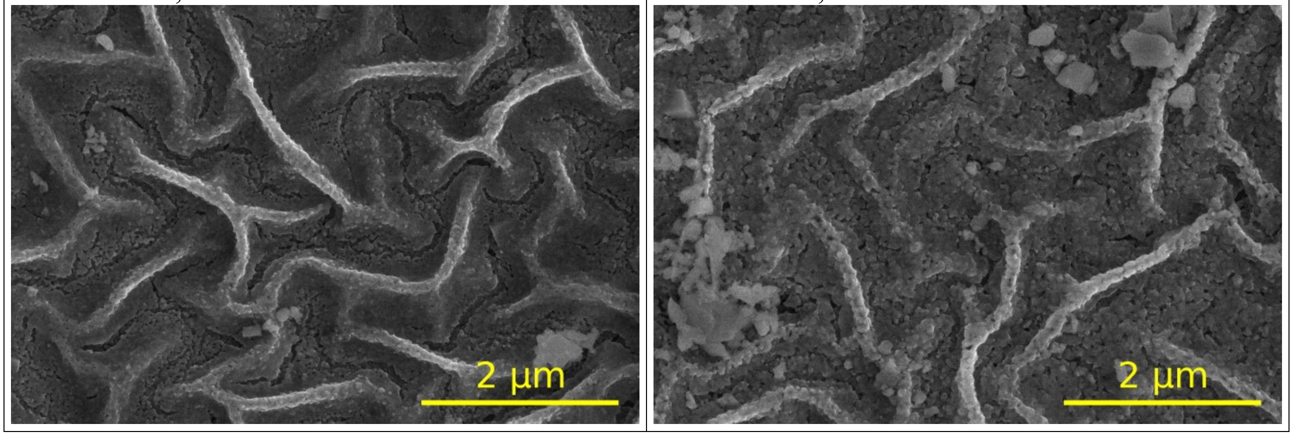

After 1080 h, max. 30% rel. hum.:

After 1610 h, max. 60% rel. hum.:

*Figure 60: SEM-SE surface images of LSC64 thin-film samples from different periods of the long-term experiment*

### *SEM of the cross-sections*

Further SEM analyses were performed on cross-sections of the samples which were prepared by an ion sputtering technique. Figure 61 shows images of the fresh and the degraded sample.

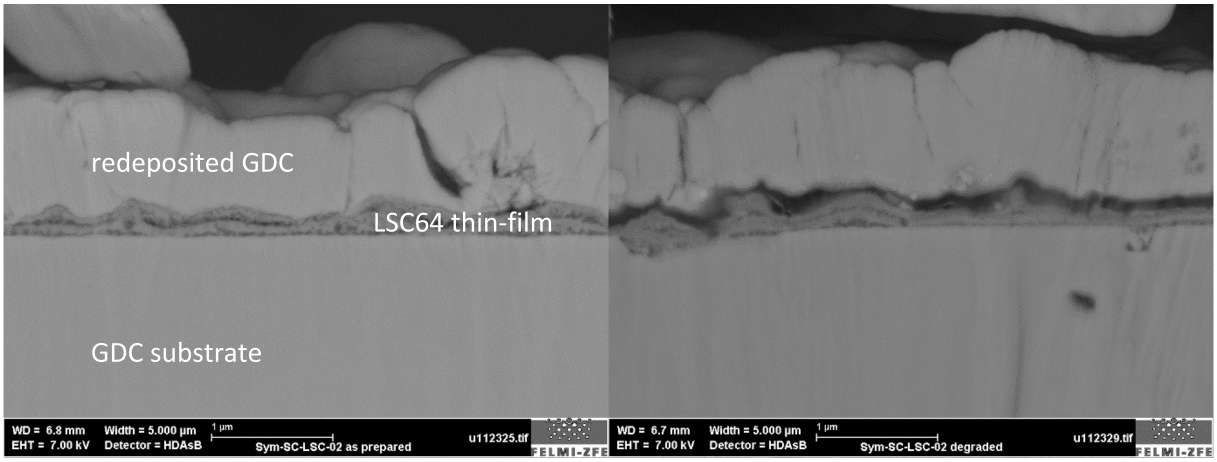

*Figure 61: SEM cross-sectional images of the fresh (left) and the degraded (right) sample*

The preparation of the cross-sections was quite problematic. As Figure 61 shows, huge amounts of GDC from the electrolyte were redeposited on top of the cathode layers. From these images no conclusive differences between the fresh and the degraded sample could be discerned.

### *STEM of the cross-sections*

An overview image of the cross-section of the degraded thin-film cathode obtained by STEM-HAADF is given in Figure 62. It shows the GDC substrate with grains of about 2 µm, with the spin-coated LSC64 cathode layer on top. For preparation of the TEM lamella the cathode layer was covered with Pt, which forms a 1 µm thick film on top of the LSC64 thin-film.

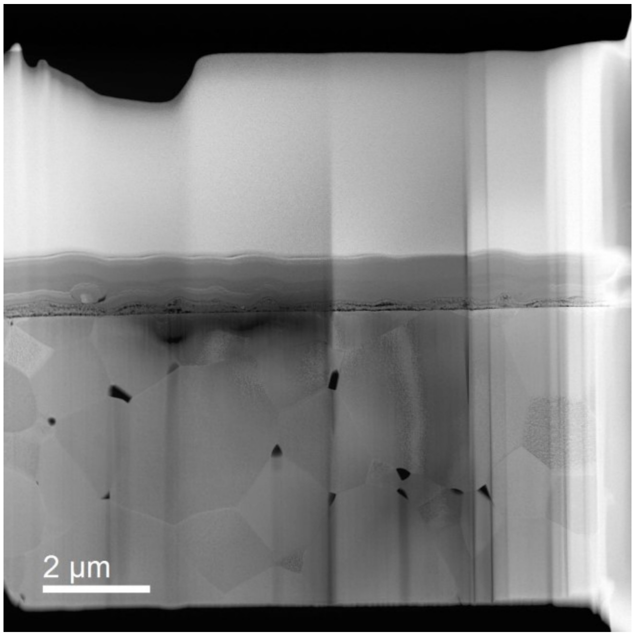

*Figure 62: STEM-HAADF survey image of the degraded LSC64 thin-film on GDC substrate*

The left image in Figure 63 shows the spin-coated LSC64 layer in higher magnification. For comparison, an image of a fresh sample is given in the right image in Figure 63. This image was taken from the analyses which are presented in detail in section 4.3.1.3 (see Figure 116 on page 130). Both samples were prepared using the same parameters and are therefore comparable, although variations in thickness occurred due to experimental reasons.

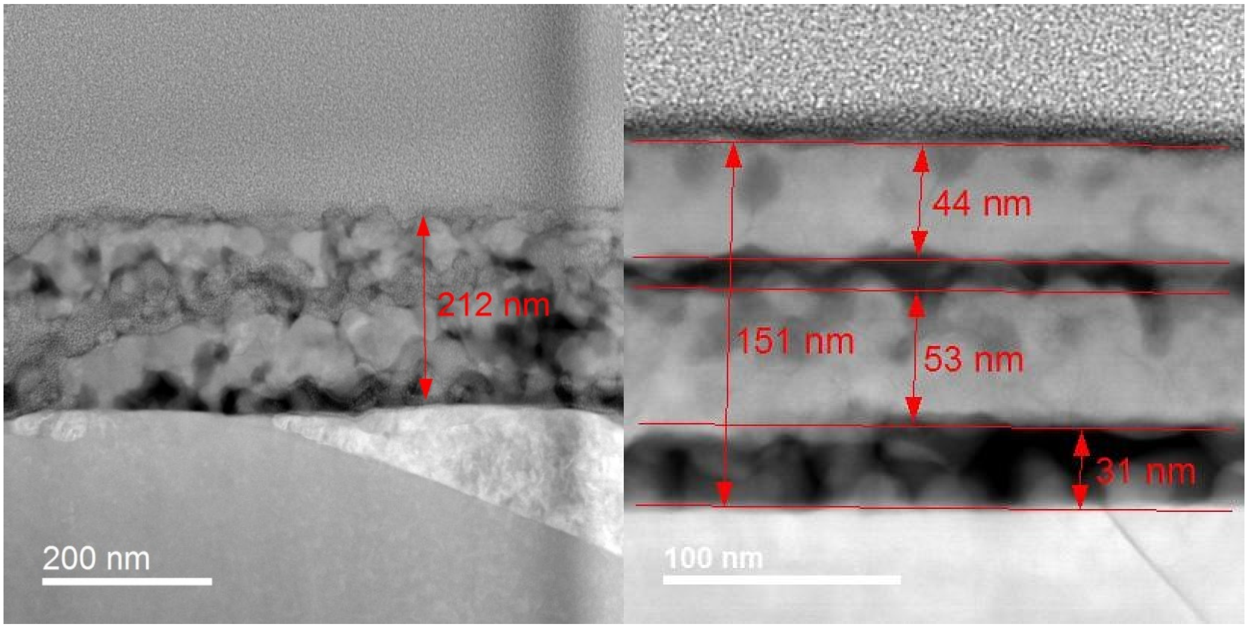

*Figure 63: STEM-HAADF image of the degraded LSC64 thin-film cathode (left) and a fresh LSC64 thin-film after preparation (right, from section 4.3.1.3, see Figure 116 on page 130).*

Both samples show a characteristic double-layered morphology. This layered structure is a result of the thin-film synthesis process, which was carried out in two cycles of spin-coating, drying and annealing, as explained in section 3.2.1.3 on page 32. The total film thickness of the current sample is between 180 and 210 nm, which is significantly higher than the sample from section 4.3.1, which was about 150 nm. In the current sample the porous zones between the GDC substrate and the bottom layer and between the bottom and top layer seem to be larger. The sample from the current experiment also seems to be more rough and uneven. These morphological differences might be caused by deviations in the viscosity of the precursor solutions.

Chemical analyses were performed by STEM-EDX measurements on selected positions of the sample. These analyses gave crucial information about the mechanisms causing the electrochemical degradation. As Figure 64 shows, the porous layers of the thin-film structure contain significant amounts of Si and Pt, while the dense layers contain the expected elements La, Sr and Co. While Pt was introduced during the TEM sample preparation (Pt was sputtered on top of the sample prior to the FIB preparation of the lamella) Si is a critical contaminant which was brought into the cathode during the long-term experiment.

The same observation could be verified at another position of the TEM sample, where the analyses shown in Figure 65 were performed. These analyses also show the influence of Pt: While the upper porous layer (Position 10D in Figure 65) had been filled by Pt during TEM sample preparation, the bottom layer (Position 10C) was Pt-free, but Si was still observable at both positions.

Si was not only found in the cathode, but also inside the bulk of the GDC electrolyte, see Figure 66. Si was observed in quite high concentration near the cathode-electrolyte interface. With increasing depth, the Si concentration was decreasing. From the EDX analyses it can be assumed that the Si concentration follows a typical diffusion profile with a penetration depth of about 200 nm. These characteristics indicate that Si was deposited in the cathode and at the cathode-electrolyte interface and subsequently diffused into the dense GDC bulk.

These findings are a strong indication that the well-known Si gas-phase transport mechanism in humid atmospheres, as described in section 2.2.4.3 on page 17, occurred in the long-term experiment. The fact that Si is found preferably in the porous layers of the thin-film cathode can be explained by the gas-phase transport and by the fact, that Si forms silicate layers on the surface, but doesn't diffuse to significant extent into the bulk of the perovskite [116, 121]. Since these silicate layers are reducing the oxygen surface exchange activity of the cathode, it is assumed that it is the main cause of the observed electrochemical degradation in the present long-term experiment.

Since Si was also found inside the GDC electrolyte, the influence of Si on the electrochemical properties of solid electrolytes should be mentioned here. Due to the fact that Si is a ubiquitous impurity in most ceramic materials, its negative impact on the conductivity is a well-known issue. Si tends to segregate to the grain boundaries, which causes a high grain boundary resistance. This effect is known for zirconia as well as for ceria electrolytes [17, 151, 152]. Today most relevant manufacturers of ceramic materials are able to deliver ultrapure ceramic powders with a Si content less than 50 ppm to omit this undesirable effect [17]. Due to these low levels of Si inside the material, Si-contamination of the electrolyte from outside via the gas phase, as observed here, could theoretically have a negative influence on the electrolyte conductivity. In the present experiment, Si obviously didn't have any measurable influence on the electrolyte performance, since the ohmic resistance didn't increase during the long-term experiment (see Figure 56 on page 76). This is probably because the permeation depth of Si found in STEM was with only 200 nm negligible compared to the total thickness of the electrolyte substrate, which was about 1.6 mm. It could however have a measurable effect on thin-film electrolytes and barrier layers with thicknesses of a few µm, which are state-of-the-art in SOFC cell development (see section 2.1.2 on page 5). To the knowledge of the author, such a degradation mechanism has not been acknowledged yet in literature, probably because other phenomena are dominating cell degradation.

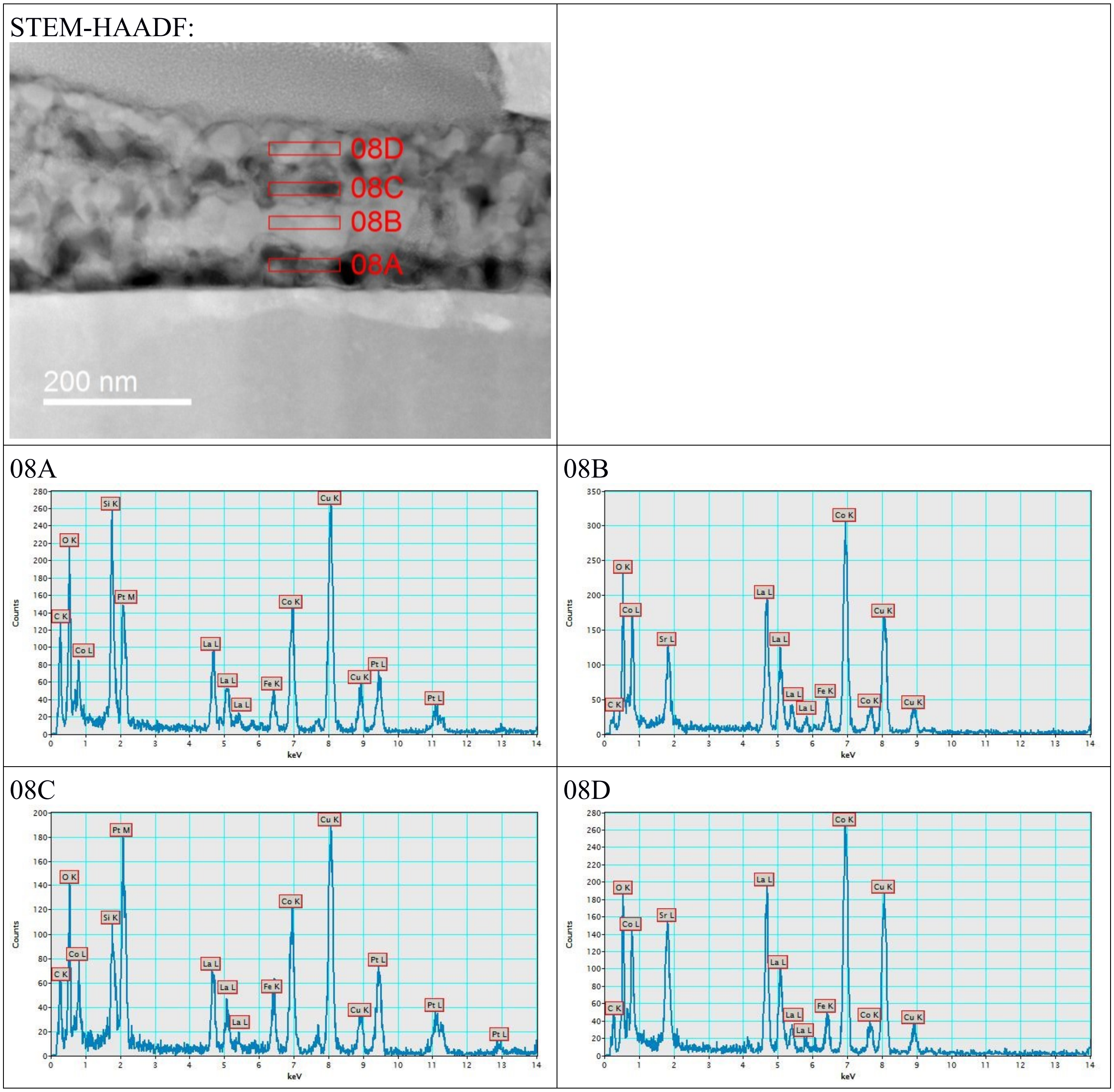

*Figure 64: STEM-HAADF cross-sectional image and STEM-EDX analyses of the degraded thin-film cathode at marked positions; Si was detected in the porous intermediate layers (08A and 08C)*

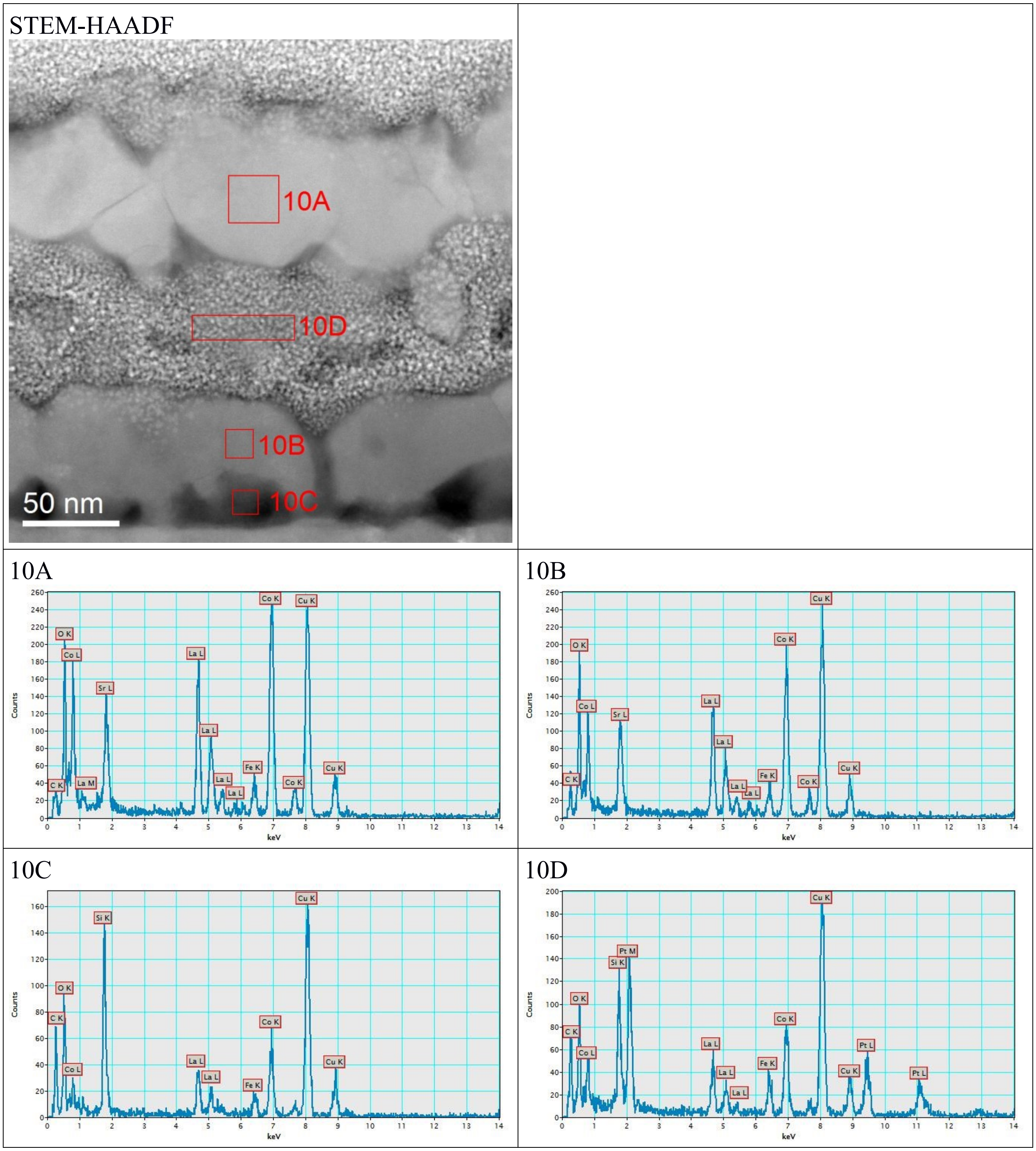

*Figure 65: STEM-HAADF cross-sectional image and STEM-EDX analyses of the degraded thin-film cathode at marked positions; Si was detected in the porous intermediate layers (10C and 10D)*

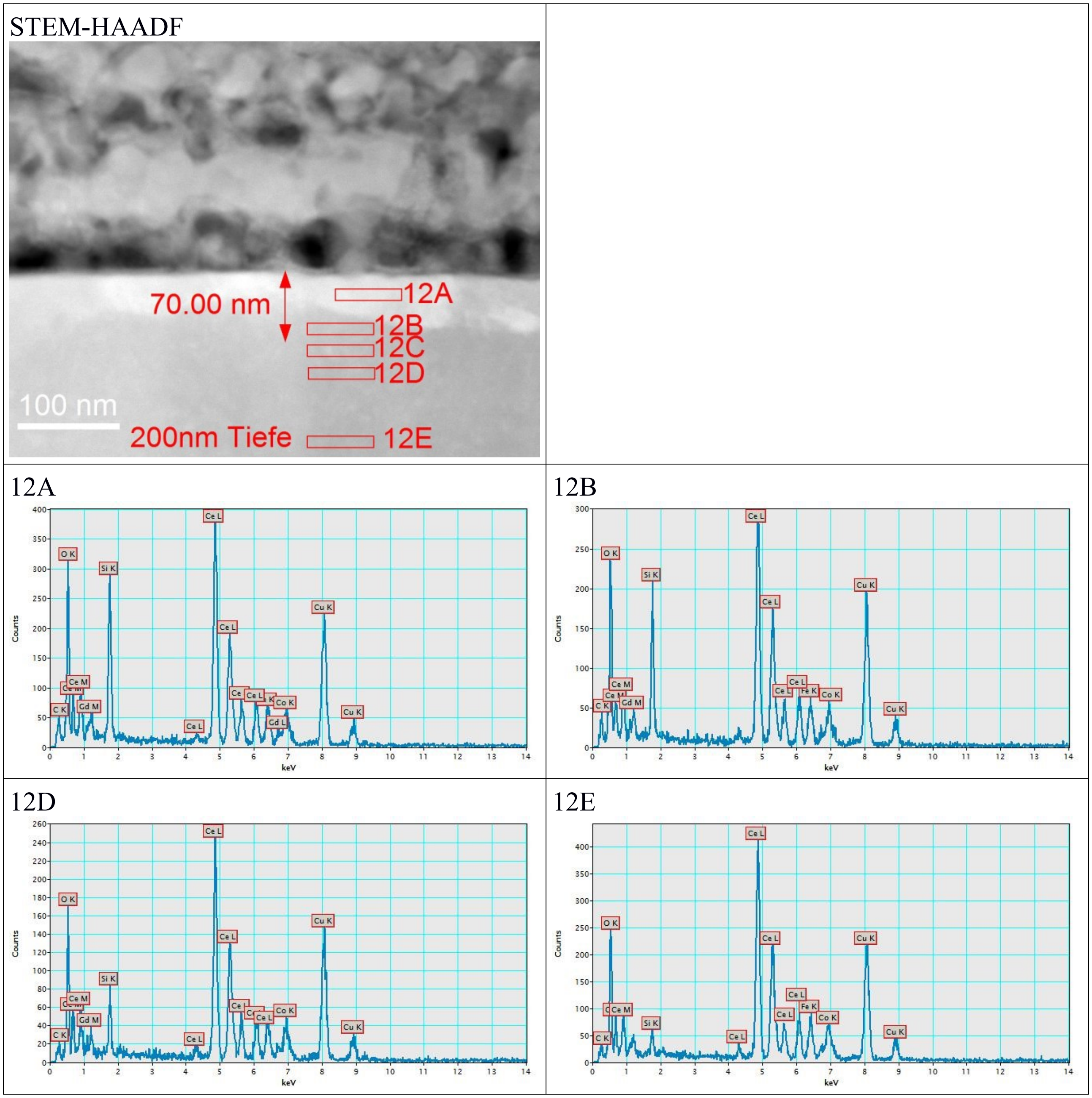

*Figure 66: STEM-HAADF cross-sectional image and STEM-EDX analyses of the GDC electrolyte at marked positions near the cathode-electrolyte interface of the degraded cell; Si-content decreases with depth*

### 4.2.2 Infiltrated nanoscale LSC64 cathodes in GDC-backbones

The symmetric cell with cathodes of GDC-backbones infiltrated with LSC64 was characterized by electrochemical impedance spectroscopy. Short-term characterization was performed in a temperature range between 500°C and 700°C. At 700°C a long-term experiment with increasing humidity was performed as described in section 3.3.1. The durations of the testing periods were as follows:

- Period 1 (dry atmosphere): 0-1098 h
- Period 2 (30% relative humidity): 1110-2170 h
- Period 3 (60% relative humidity): 2170-3210 h

Together with the symmetric cell secondary samples were added to the reactor with the purpose to cover the conditions of the actual cathode and investigate different degradation states in post-test analyses. These samples had the same infiltrated layer as the cell, but only on one side and without a current collector. Between two testing periods the reactor was cooled to room temperature and one of the secondary samples was removed. During cooling at the end of the Periods 1 and 3, additional temperature-dependent EIS measurements between 700°C and 500°C were performed to gain information on the electrochemical behavior of the sample.

#### 4.2.2.1 Short-term characterization and temperature dependence

The area-specific polarization resistance (ASR) of the symmetric cell with infiltrated cathodes was characterized by EIS in a temperature range between 500°C and 700°C in steps of 25°C. The sample was surrounded by a test gas atmosphere of 20% $O_2$ in Ar. The frequency range was between 1 MHz and 20 mHz. The applied ac RMS voltage was 0.5 V. The infiltrated cathode was high-performant and showed very low polarization resistances, even at 500°C. This has also been reported for similar infiltrated cathodes in the literature [88, 92, 153]. Thus, another temperature run was performed, where additional impedance spectra were measured at temperatures between 230°C and 500°C.

Figure 67 shows examples of impedance spectra of the fresh cell at temperatures between 237°C and 700°C. The spectra measured below 500°C showed a characteristic drop-shaped arc, as well as depressed semicircles at higher frequencies. In principle, these spectra could be modeled well by the equivalent circuits described in Figure 12 on page 35. However, the equivalent circuits had to be adapted to fit the data properly, since the impedance spectra showed different characteristics at different temperatures. For example, the spectra from the temperature range below 500°C showed two arcs, which were fitted by a high-frequency R-CPE element and a Gerischer impedance at intermediate frequencies. The spectrum measured at the lowest temperature (237°C) even showed three arcs. However, the big arc on the left, which was probably the contribution of the GDC bulk resistance, was neglected for fitting. With increasing temperature, the resistance of the Gerischer arc decreased. Due to an overlap with the high-frequency arc, the characteristic shape couldn't be identified any more at 500°C and above, so the Gerischer element was replaced by an additional R-CPE element in the fitting model. In the temperature range between 500°C and 700°C also an additional low-frequency arc occurred. At 600°C the intermediate-frequency arc had nearly disappeared, so it wasn't possible to fit it with sufficient accuracy.

Inductivity of the test setup had a significant contribution to the impedance at temperatures above 450°C and frequencies higher than 10 kHz. There was an overlap between the high frequency arc and the inductivity contribution, which had to be taken into account.

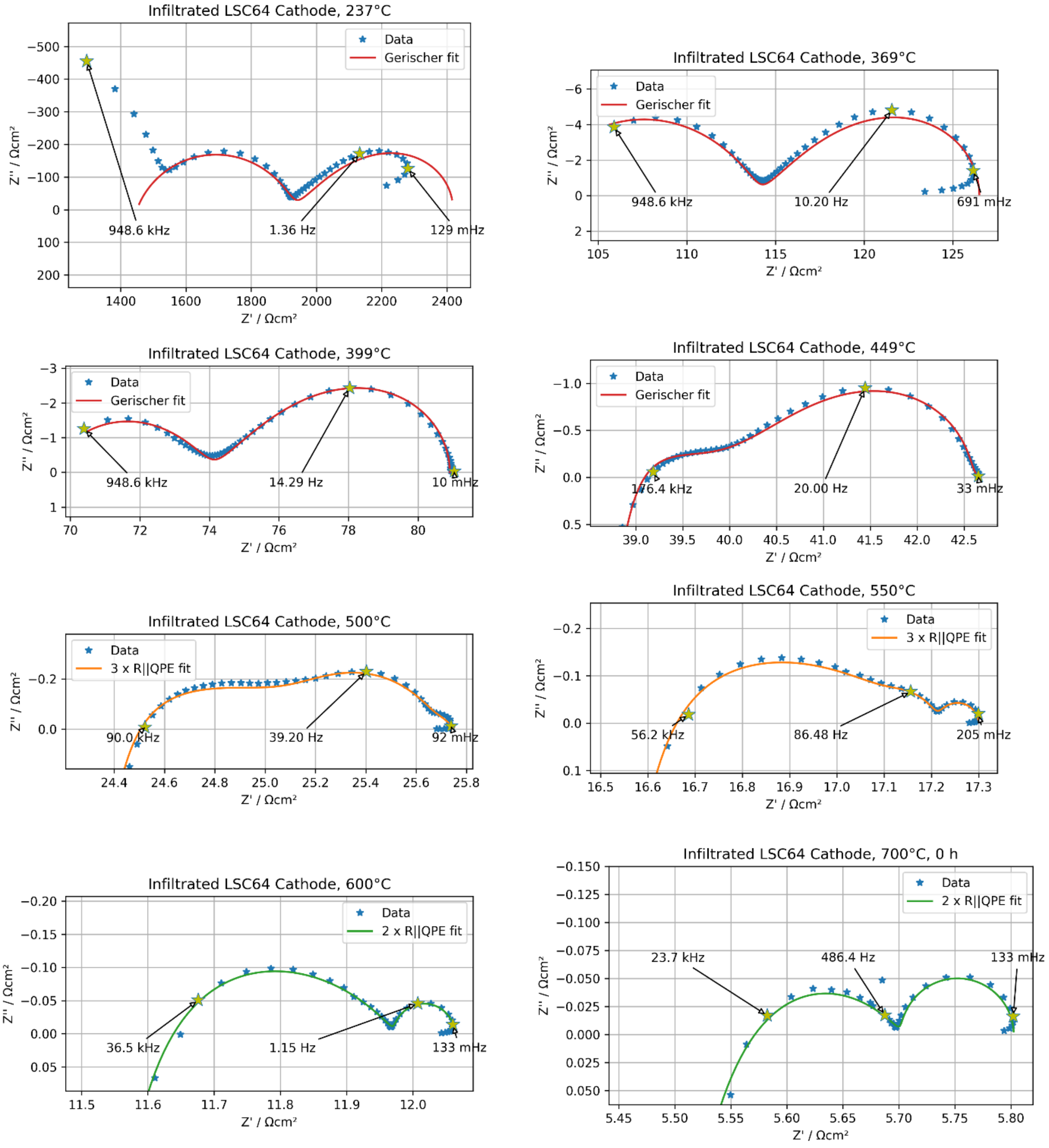

*Figure 67: Impedance spectra of the symmetric cell with infiltrated LSC64 cathodes, measured at different temperatures*

In the following text, the parameters of the R-CPE circuits are denoted by the indices “hi”, “mid” and “low” for the high frequency, intermediate frequency and low frequency R-CPE element respectively. As already mentioned above and denoted in Figure 67, the equivalent circuit models used for fitting the data had to be adapted to model all the spectra at different temperatures. For example, $R_{mid}$ was the resistance of the Gerischer impedance below 450°C, but of an R-CPE element at higher temperatures. At 600°C and above, the intermediate frequency arc vanished so $R_{mid}$ couldn’t be evaluated any more. A similar case was $R_{low}$, which was not observable below 500°C.

Figure 68 shows the temperature dependence of the three ohmic parameters of the infiltrated cathode in fresh state. While $R_{low}$ was nearly temperature independent, $R_{mid}$ and $R_{hi}$ had a significant temperature dependence. The activation energy of $R_{hi}$ was estimated to about 65.8 kJ/mol. The activation energy of $R_{mid}$ seemed to change at 500°C. Below this temperature it was about 84 kJ/mol, above 500°C 219.6 kJ/mol. This change can be explained partly by the fact that different fitting models were used at different temperature ranges. Anyway, the activation energy of $R_{mid}$ between 500°C and 575°C was notably high. However, it has to be noted that the values of $R_{mid}$ obtained in this temperature range were already difficult to evaluate and had a higher uncertainty. Following the trend of $R_{mid}$ in the Arrhenius plot, and assuming that it can be extrapolated to higher temperatures, the values of this parameter can be estimated to $2\times10^{-4}$ $\Omega cm^2$ at 700°C and $4\times10^{-3}$ $\Omega cm^2$ at 600°C. These values are one to two orders of magnitude smaller than those of $R_{hi}$ and $R_{low}$, which is the reason that they can’t be evaluated by impedance spectroscopy at these temperatures.

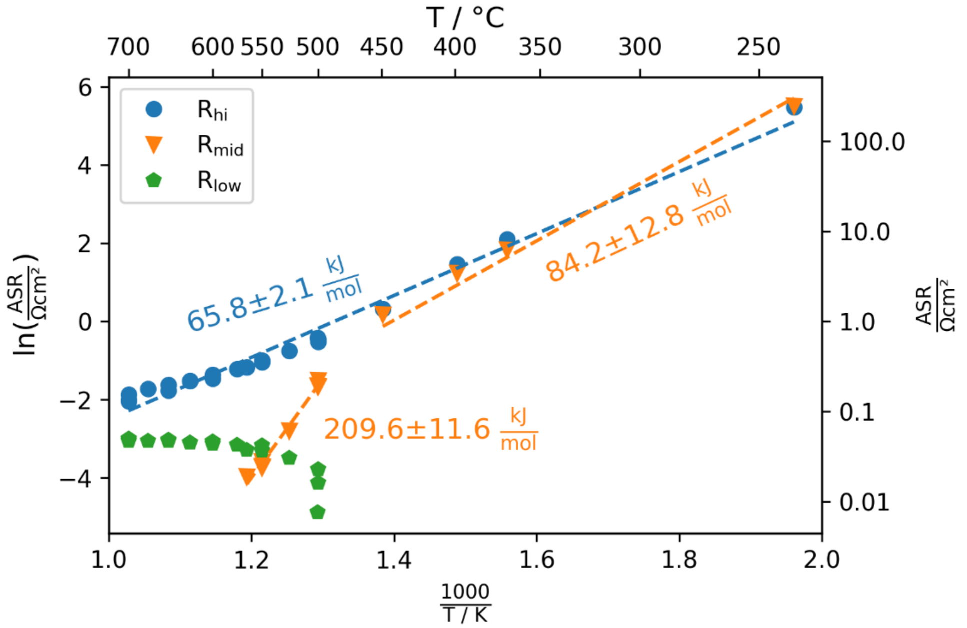

*Figure 68: Area specific resistances obtained from the CNLS-fits of the impedance spectra as functions of temperature*

The capacitances obtained from CNLS-fits of the respective equivalent circuit to the impedance spectra are plotted in Figure 69. The capacitances were almost temperature independent. From the orders of magnitude of the different capacitances some assumptions for the underlying physical and chemical mechanisms can be drawn, according to Table 1 on page 26. The values of the capacities are $10^{-5}$ F/cm² for $C_{hi}$, $10^{-2}$ F/cm² for $C_{mid}$ and 1-2 F/cm² for $C_{low}$. The high capacitance for the low-frequency arc and the fact, that the corresponding resistivity $R_{low}$ is practically temperature invariant leads to the conclusion, that the low frequency arc is caused by gas diffusion limitation to the cathode. The value for $C_{mid}$ is in the typical range for a chemical capacitance, so the intermediate frequency arc is probably linked to the oxygen surface exchange and bulk diffusion process. The fact that $R_{mid}$ was below the measurement uncertainty above 550°C is an indication for outstandingly fast oxygen reduction kinetics for this type of cathode.

The low capacitance of $C_{hi}$ indicates that $R_{hi}$ is probably linked to charge transfer at the interface between cathode and electrolyte. Because of the small or even negligible value of $R_{mid}$, the high-frequency arc is the main contribution to the total cathode polarization resistance.

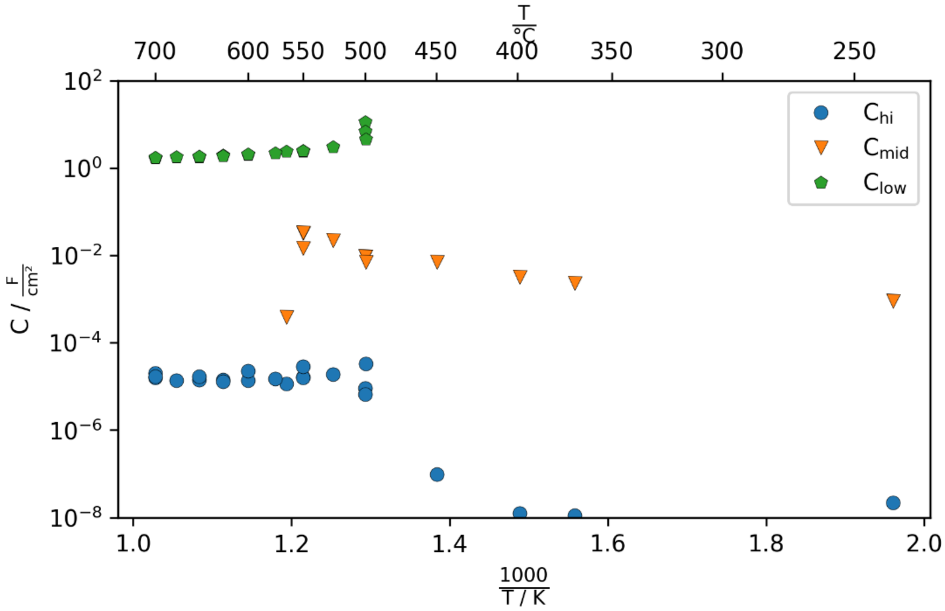

*Figure 69: Capacitances obtained from the CNLS-fits of the impedance spectra as function of temperature*

The following figure shows the polarization resistance $ASR_{pol}$, which is defined as the sum of $R_{mid}$ and $R_{hi}$, and the gas diffusion resistance $ASR_{gas\text{-}diff}$, which is equal to $R_{low}$, in an Arrhenius plot.

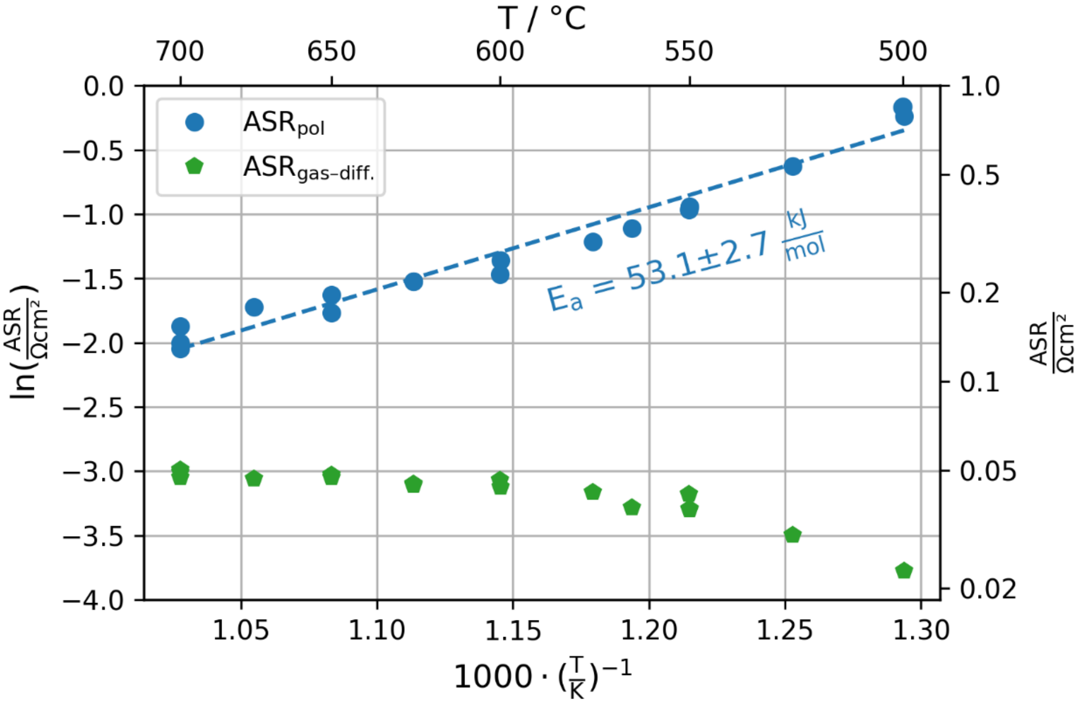

*Figure 70: Arrhenius plot of the polarization resistance and the resistance caused by gas diffusion limitation.*

#### 4.2.2.2 Long-term characterization

Figure 71 shows examples of impedance spectra measured at different stages of the long-term experiment. All of the impedance spectra showed similar characteristics as in the temperature dependent measurements. During the first period of the experiment, the middle-frequency arc was not detectable, so the fitting model with two R-CPE elements was used. While $R_{low}$ remained nearly constant $R_{hi}$ declined significantly from 0.14 Ωcm² to 0.06 Ωcm². Such an activation mechanism has been found in several similar studies [89, 90, 154]. Reasons for this increase of the cathode performance might be recrystallization of the material.

In humidified atmospheres a change in the impedance characteristics was found. The intermediate frequency arc appeared once again and its contribution increased during the time-run. As a plot of the imaginary part of the impedance Z'' against the frequency (Figure 72) shows, it had a peak frequency of around 200 Hz.

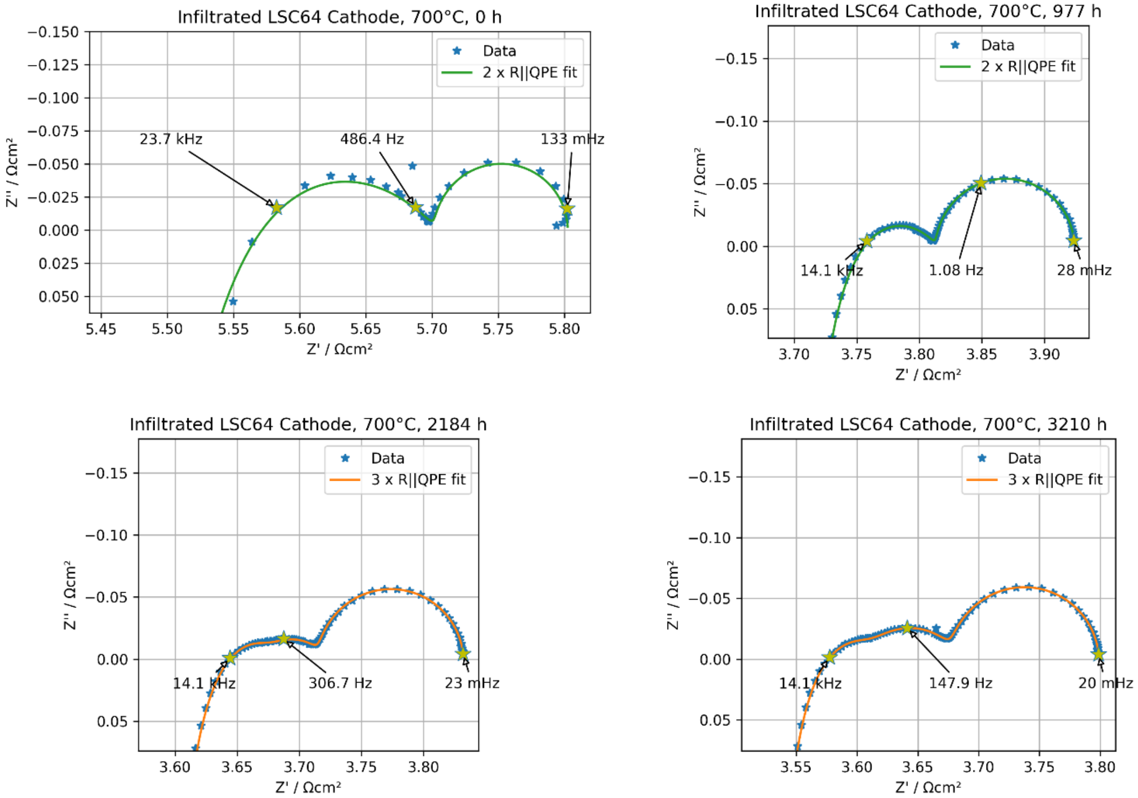

*Figure 71: Selected impedance spectra from the long-term experiment at 700°C*

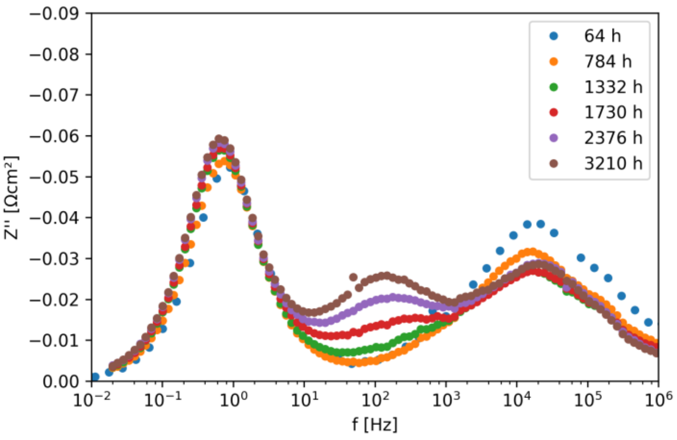

*Figure 72: Bode-plot of selected impedance spectra (imaginary part vs. frequency) from the long-term experiment; the influence of inductivity is subtracted from the data*

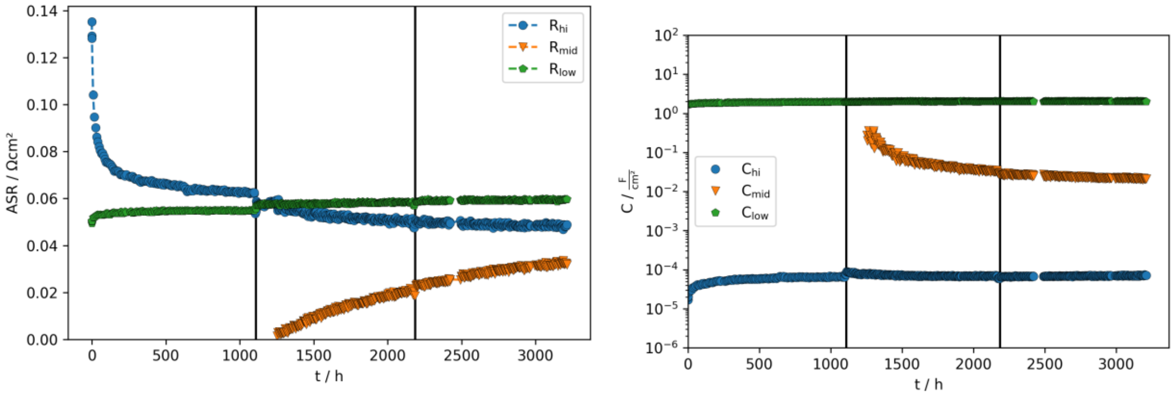

*Figure 73: Calculated resistances (left) and capacitances (right) from the long-term experiment as function of time*

Figure 73 shows the resistive and capacitive parameters obtained from the impedance spectra by CNLS-fits over the whole experiment. While $R_{hi}$ and $R_{low}$ remained constant or even declined over time, $R_{mid}$ was increasing continuously. Since the calculated capacitances from the time-run were in the same order of magnitude as in the temperature-run, it can be assumed that the corresponding mechanisms were the same. Therefore, the high-frequency arc was attributed to the transport at the cathode-electrolyte-interface, the intermediate frequency arc to the oxygen reduction reaction and the low-frequency arc to gas diffusion. The oxygen exchange kinetics seemed to be negatively affected by a degradation mechanism, which occurred in the presence of humidity.

Figure 74 shows the area-specific polarization resistance of the infiltrated cathode, which was defined as the sum of $R_{hi}$ and $R_{mid}$. Due to the low value of $R_{mid}$, the main contribution to the polarization resistance is the interfacial resistance, while oxygen reduction reaction had a gaining influence by time.

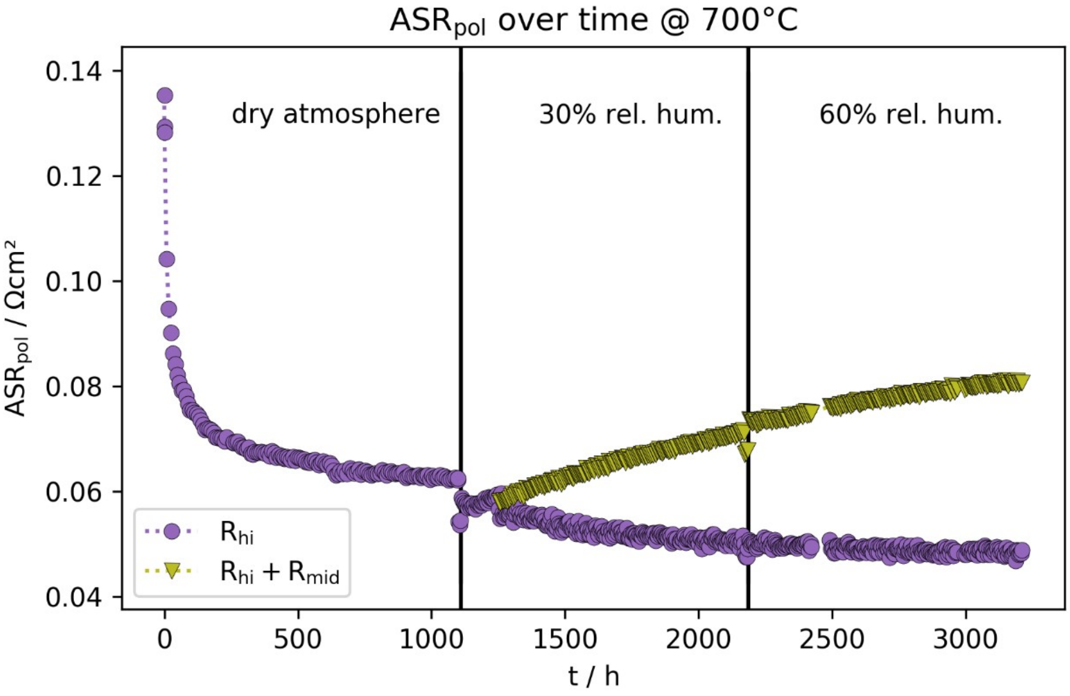

*Figure 74: Polarization resistance of the infiltrated cathode as a function of time*

It has to be noted that the cathode degraded only to a very small extent. During 2000 hours of operation in humid atmosphere, the area specific resistance increased by 25 mΩcm² only and was thus still below 1 Ωcm². This is a promising result with respect to long-term applications of infiltrated cathodes.

At the end of period 1 (1098 h in dry atmosphere) and period 3 (after 3210 h in humid atmospheres) of the long-term experiment, additional temperature-dependent impedance measurements were performed. The following Arrhenius plots show the evolution of the temperature-dependence of $R_{mid}$ and $R_{hi}$ at different stages of the experiment:

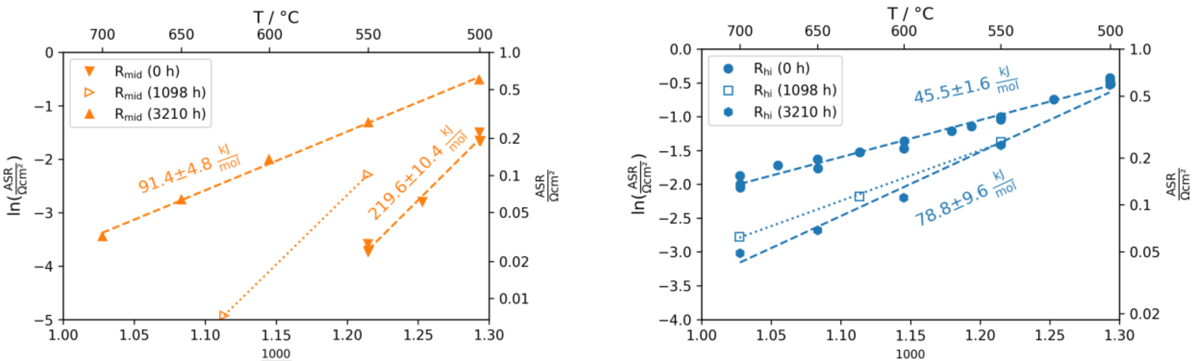

a) b)

*Figure 75: Ohmic resistances obtained from a) intermediate-frequency range and b) high-frequency range of the impedance spectra as function of temperature, measured at different stages of the long-term experiment*

According to the data shown in Figure 75 a), $R_{mid}$ already increased in the first period of the long-term experiment at 700°C in dry atmosphere. At 700°C, the resistivity was still below the detection limit, but at 550°C a higher value for $R_{mid}$ was found. Since $R_{mid}$ was only measured at two temperatures, only a rough estimation on the activation energy at this stage of the experiment can be given. At the end of the experiment, after 3210 h, $R_{mid}$ had increased and the activation energy was significantly smaller.

$R_{hi}$ seems to show an opposite trend: The resistance had decreased during the experiment while the activation energy was higher at the end.

### 4.2.2.3 Post-test analyses

#### SEM of the surfaces

A detailed view of the microstructure of fresh and degraded samples was obtained by SEM analyses of the surface (Figure 76). For the samples which were exposed only to dry atmospheres the secondary electron images show the microcrystalline GDC backbone structure with some smaller particles in between. There was no significant difference between the sample in the as-prepared state and the one after 1098 hours of the long-term experiment. For the samples which were removed from the test setup during the later periods of the long-term experiment, where humidity was present in the testing atmosphere, the surface structure looked different: Secondary phases seem to cover the surfaces.

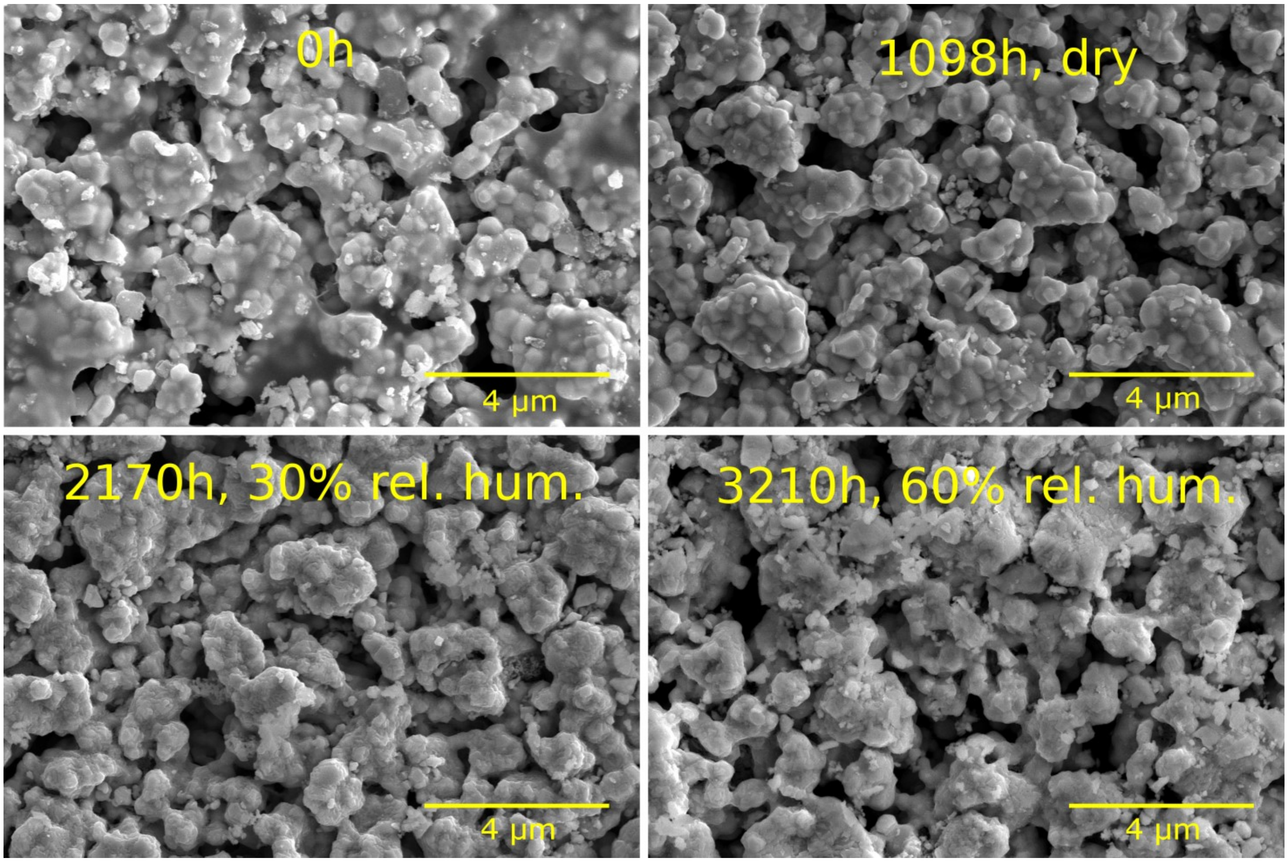

*Figure 76: SEM-SE surface images of the infiltrated cathodes at different periods of the long-term experiment*

The differences between the dry and humidified samples indicate a remarkable change in the surface chemistry due to the humidification, which could be determined by EDX, which is shown in Figure 77. On the sample which was exposed only to dry test gas atmosphere, only the elements Ce and Gd of the GDC backbone could be detected by EDX, while the amount of La, Sr and Co from the infiltrated LSC64 was below the detection limit. However, on the samples exposed to humid atmospheres a significant signal from Sr was detected. Since only Sr was found in significant amounts, while La and Co were still not detected, the origin of the Sr can't be the infiltrated material. The most plausible explanation for this Sr-enrichment is that the additional Sr originates from the LSCF current collector and was transported to the infiltrated layer through the gas phase.

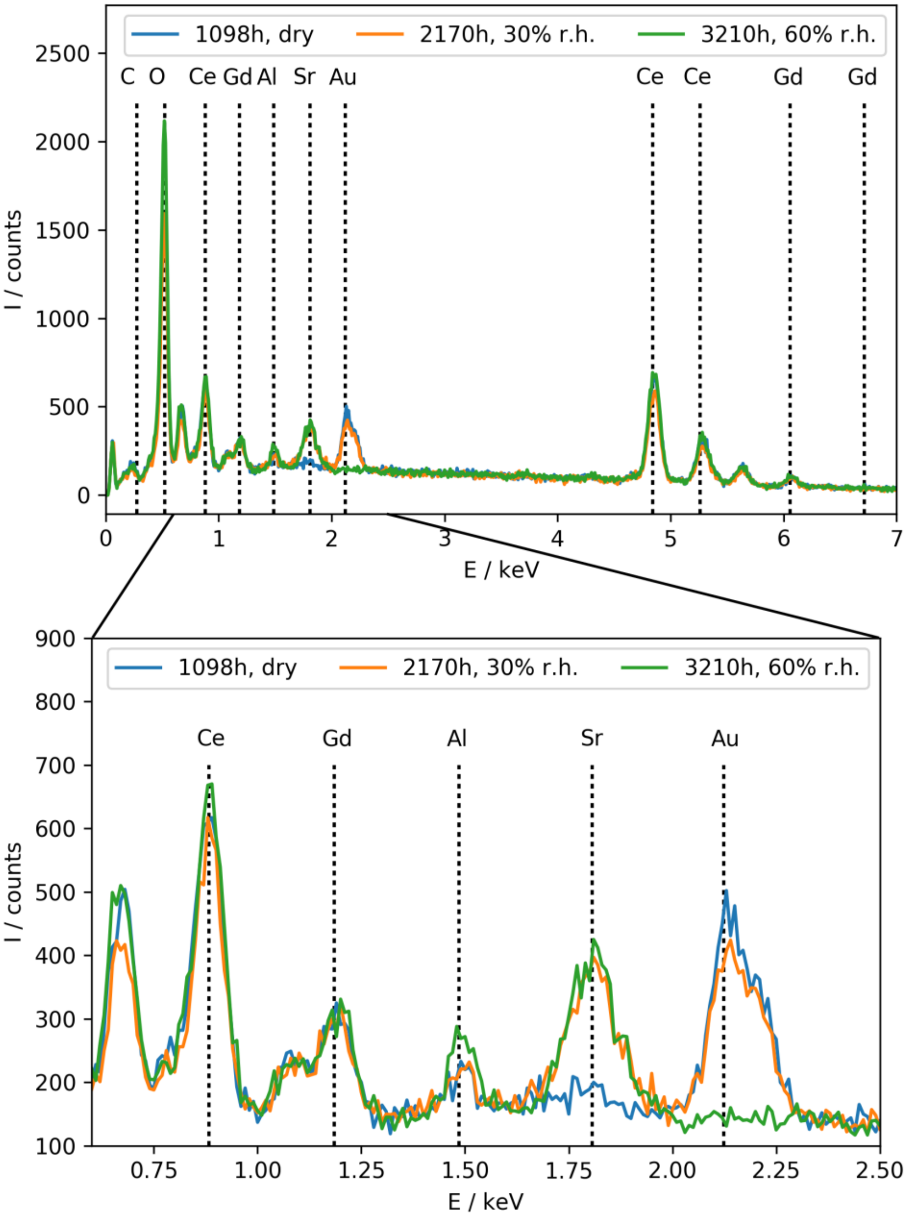

*Figure 77: EDX spectra of the LSC64-infiltrated cathodes at different periods of the long-term experiment.*

### *SEM of the cross-sections*

A part of the degraded cell was prepared for cross-sectional imaging by embedding the specimen in epoxide resin, cutting and polishing.

Figure 78 shows an overview image of the cross-section. It depicts the double-layer structure of the cell, composed of the LSCF current collector layer and the infiltrated GDC backbone on the dense GDC substrate. Both layers were quite homogeneous and had a thickness of about 30 µm.

Detailed images of the infiltrated backbone structure are shown in Figure 79. In these images there are regions where no infiltrated material is visible, especially in bigger pores. This is probably due to the embedding resin which is covering the fine grained infiltrated material.

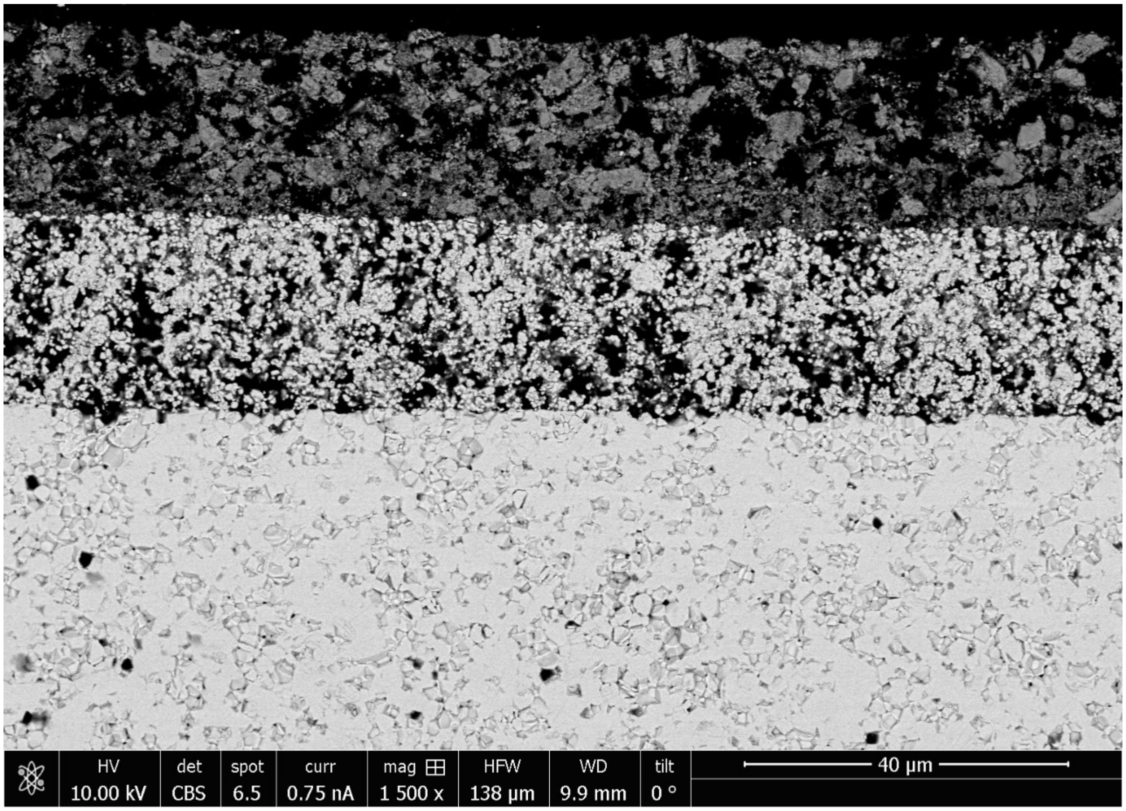

*Figure 78: Cross-section of the degraded cell; the SEM-BSE image shows the LSCF current collector layer on top of the infiltrated GDC backbone layer on the dense GDC substrate.*

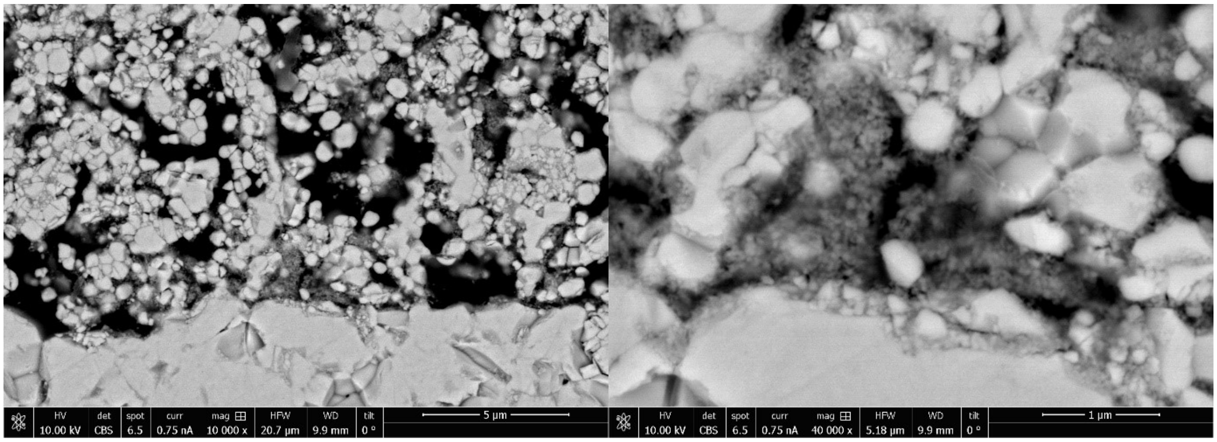

*Figure 79: SEM cross-sectional images with detailed views of the infiltrated GDC backbone.*

*STEM of the cross-sections*

A sample for scanning transmission electron microscopy was prepared from the secondary sample which was exposed to the whole long-term experiment together with the symmetric cell. Figure 80 shows a STEM-HAADF-image of the cross-section of the infiltrated layer. It shows the porous GDC backbone structure with nanoscale infiltrated LSC64-grains in between. The backbone structure was covered well by the infiltrated material. Smaller pores were partially filled up by nanograins. A few grains consisting of secondary phases were found as well. Figure 81 shows a detailed view of the sample on a position, where the backbone phase, the infiltrated material and the secondary phase are visible. EDX analyses were performed on all three phases.

The secondary phases, which were formed in a few pores across the backbone structure, consisted of Sr as well as Cr, S and O. A quantitative analysis showed that the Sr:S:Cr-ratio was about 50:40:10 at-%. Therefore, it is assumed, that this secondary phase is a solid solution of $SrSO_4$ and $SrCrO_4$. The formation of such phases has been found by Schuler et al. for LSM [108] and LSC64 cathodes which were exposed to Cr- and S-impurities [155].

The following assumptions are made to explain the formation of the secondary phases: As shown in Figure 77 on page 97, the samples exposed to humidity showed significantly higher amounts of Sr. The Sr probably originated from the LSCF current collector and was transported via the gas phase into the porous backbone structure, where it accumulated in the secondary phases. The contaminants Cr and S originated from outside. S is an impurity which is present in traces of a few ppb in testing gases in the form of $SO_2$. Due to the long duration of the experiment these small amounts were enough to accumulate on the found positions. Cr probably originated from the experimental setup. There was no Cr source present in the current experiment, but former Cr-poisoning experiments had been performed in the same setup, from which traces of Cr still were remaining in the equipment. Therefore, small amounts of the volatile compound $CrO_2(OH)_2$ were formed in humid atmospheres and transported to the cathode (see section 2.2.4.2 on page 15).

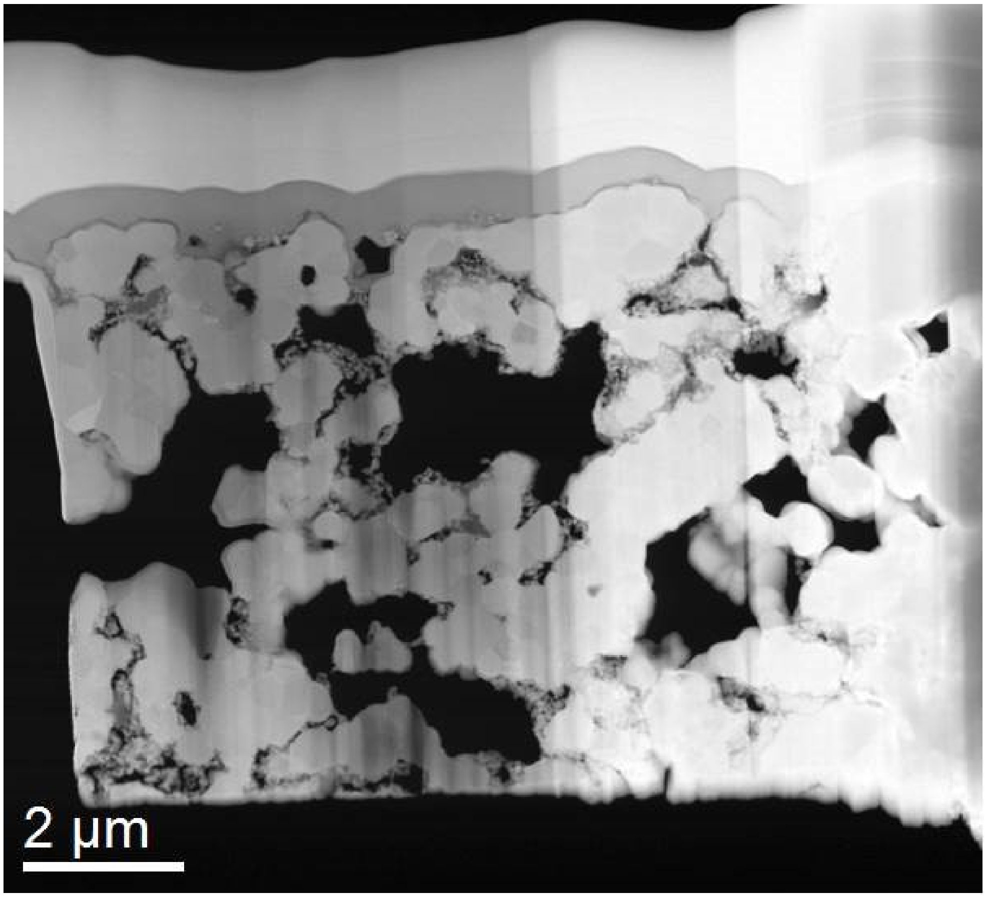

*Figure 80: STEM-HAADF image of the infiltrated cathode*

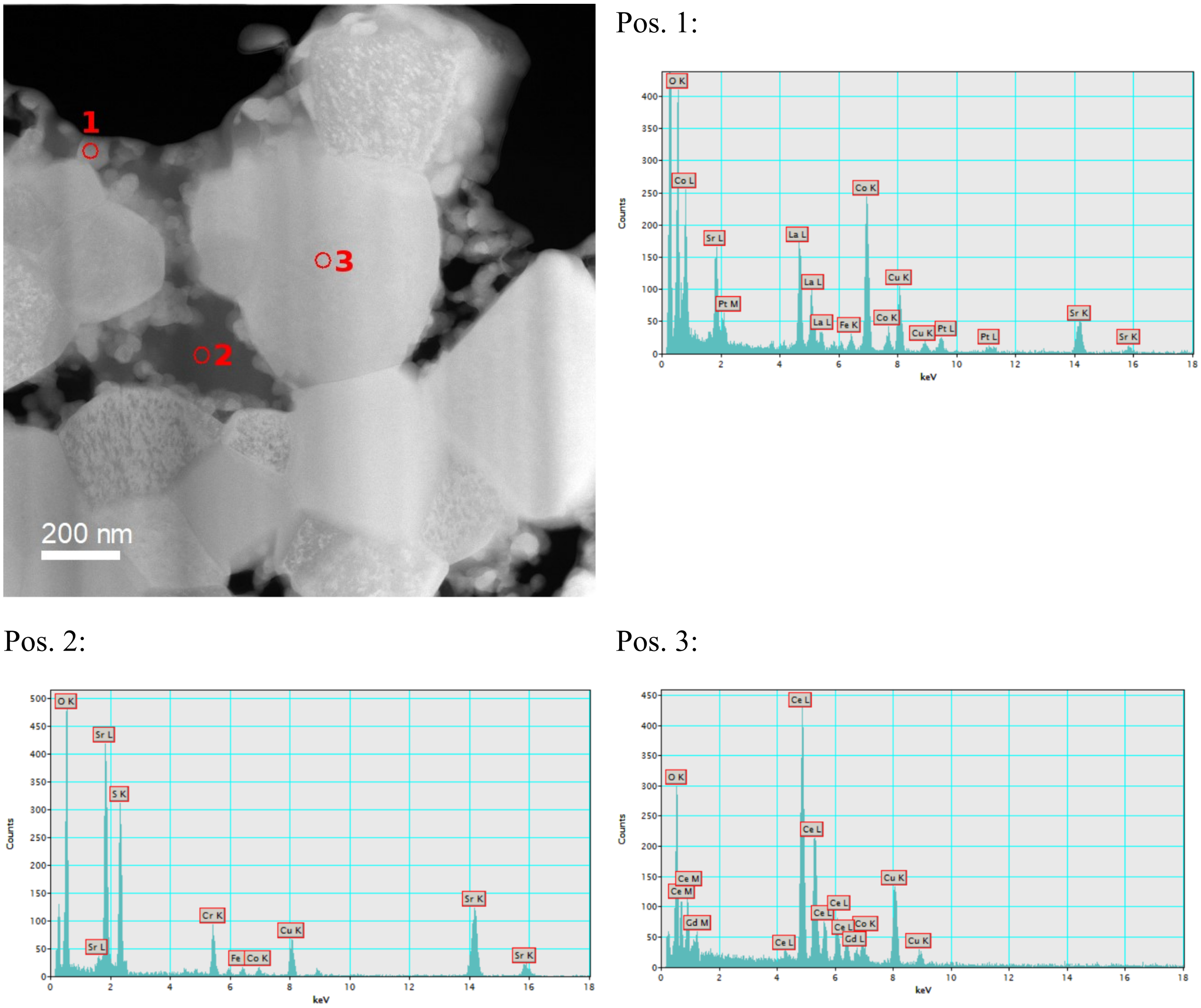

Pos. 1:

Pos. 2:

Pos. 3:

*Figure 81: STEM-HAADF detailed view of the infiltrated layer and EDX analyses performed on selected positions of the sample*

### 4.2.3 Screen-printed LSC64 cathodes

A symmetric electrochemical cell with screen-printed cathodes of LSC64 was characterized by EIS for over 3800 hours in dry and humid atmospheres. Short-term characterization was performed in a temperature range between 500°C and 700°C. At 700°C a long-term experiment with defined humidity was performed as described in section 3.3.1 on page 36. The durations of the testing periods were as follows:

- Period 1, dry atmosphere, no humidification: 0-508 h
- Period 2, 30% relative humidity: 508-1910 h
- Period 3, 60% relative humidity: 1910-3856 h

Additional samples with the same kind of cathode layer were placed in the reactor. The purpose of these samples was to expose them to the same conditions of the actual cathode and remove one of them after every period. Therefore, these samples represent the state of the actual cathode at different states of the experiment. The cell and the additional samples were investigated in post-test analyses by SEM, STEM, EDX and EELS.

During heating at the begin of the long-term experiment as well as during cooling at the end temperature-dependent EIS measurements between 700°C and 500°C were performed to gain additional information about the electrochemical behavior of the sample.

#### *4.2.3.1 Short-term characterization and temperature dependence*

In the first step impedance spectra were acquired between 500°C and 700°C. Figure 82 shows examples of impedance spectra of the fresh sample at 500°C, 600°C, 650°C and 700°C. Three different equivalent circuit models were chosen to fit the data: First the model with three R-CPE elements (Figure 12a on page 35) was applied in the CNLS-fit. However, since the impedance spectra from the first heating run showed a half-drop shaped arc at intermediate frequencies, which is a typical feature of the Gerischer impedance, the model was adapted by replacing the middle-frequency R-CPE with either a Gerischer impedance or a fractal Gerischer impedance (see Figure 12b on page 35). At least for the temperature-dependent measurements and the first period of the long-term experiment, the Gerischer fitting models were found to be more suitable to describe the data.

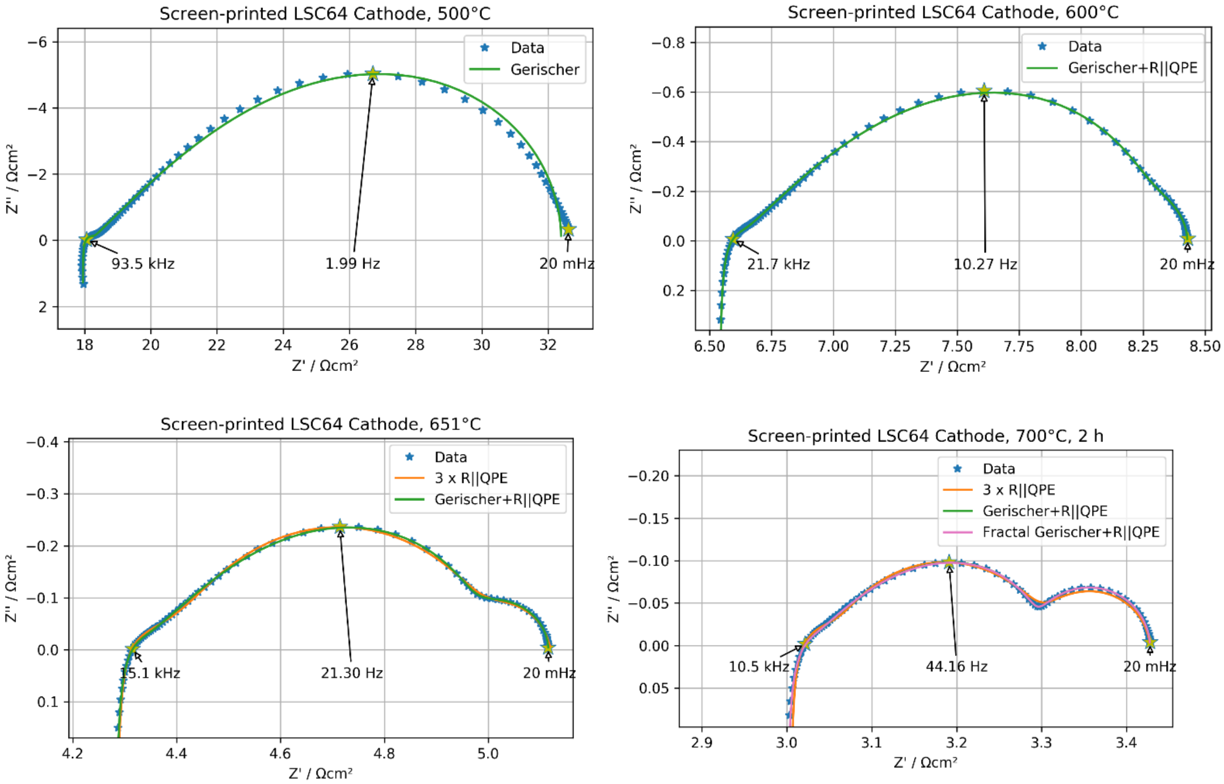

*Figure 82: Selected impedance spectra of the screen-printed cathode measured at different temperatures*

In the following plots, the temperature dependences of selected parameters from the CLNS fits are presented. The parameters are denoted by the indices "hi", "mid" and "low" according to the frequency range. For instance, the resistivity of the high-frequency arc is called $R_{hi}$, those of the Gerischer impedance $R_{mid}$ and the low-frequency arc $R_{low}$. The Arrhenius plot in Figure 83 shows the T-dependence of the resistances.

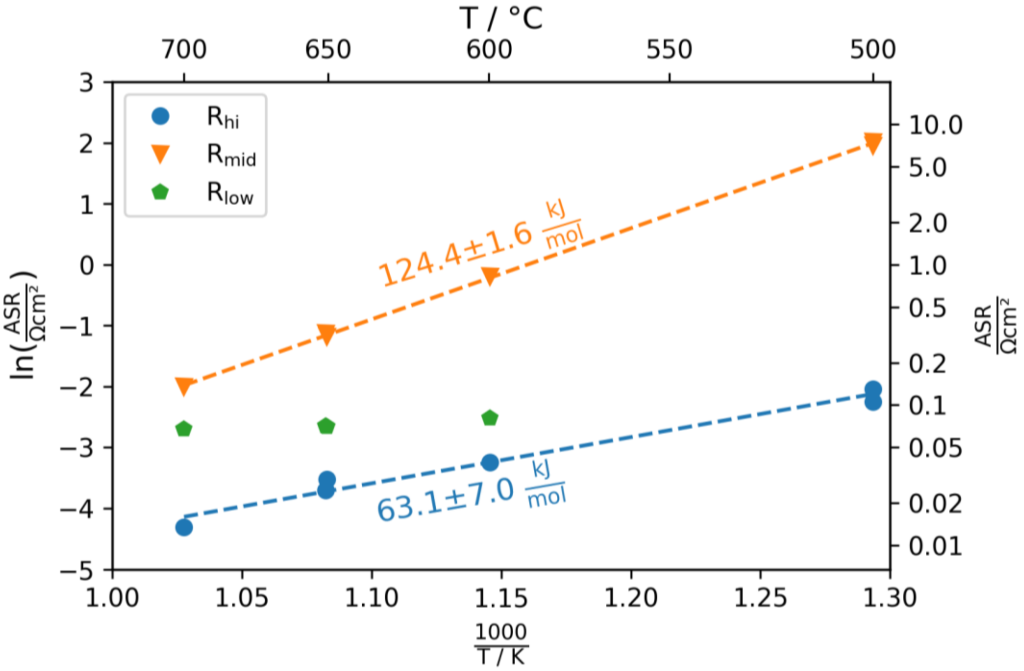

*Figure 83: Resistances acquired from the impedance spectra plotted against (inverse) temperature*

As expected, the ohmic resistances decrease with increasing temperature. One exception is the parameter $R_{low}$, which is temperature independent.

Figure 84 presents the apparent capacitances $C_{hi}$, $C_{mid}$ and $C_{low}$, which are corresponding to the resistances with the same indices, again as function of the temperature.

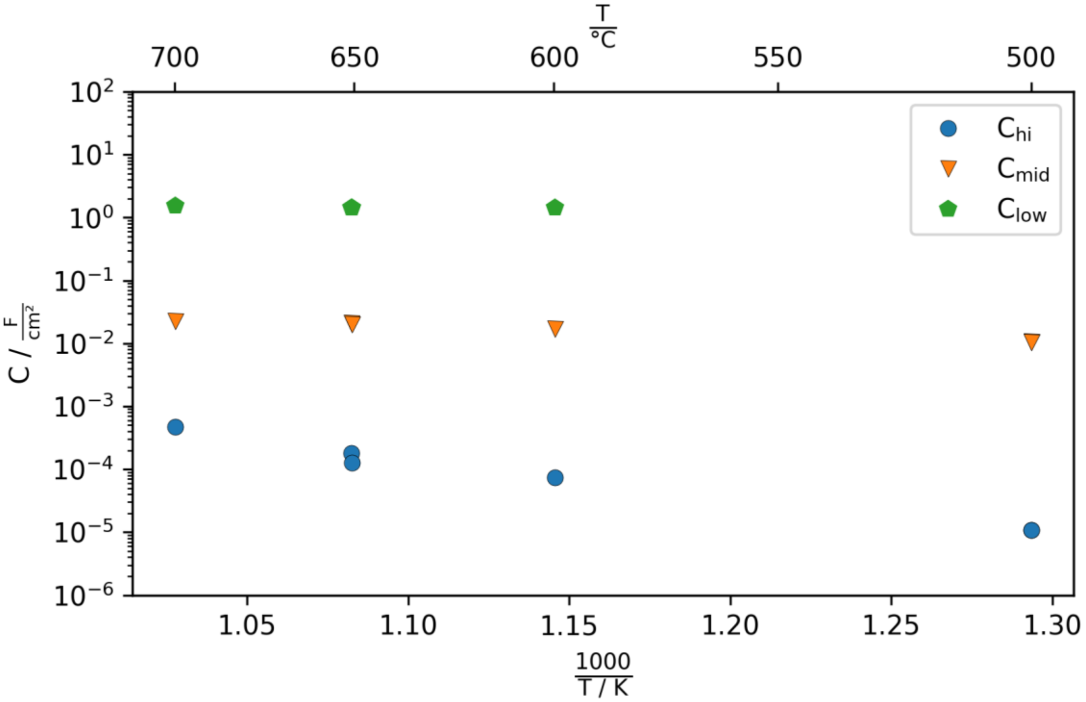

*Figure 84: Capacitances acquired from the impedance spectra plotted against (inverse) temperature*

$C_{mid}$ and $C_{low}$ are independent of temperature. $C_{low}$ has a high capacitance of 1 F/cm², which is, in addition to the temperature independence of $R_{low}$, an indication that the low-frequency arc can be attributed to the gas diffusion to the cathode.

$C_{mid}$ is the apparent capacitance of the Gerischer impedance, as defined by Adler et al. [135]. The values are between $10^{-2}$ and $10^{-1}$ F/cm², which are typical values for chemical capacities.

The values for R and C of the high-frequency arc have to be interpreted with caution. The high frequency arc is difficult to fit properly since it overlaps with the inductivity of the reactor and the resistance is low compared to $R_{mid}$.

### 4.2.3.2 Long-term characterization

The sample was characterized for at least 3850 hours at 700°C, exposing the sample to increasing amounts of humidity. In Figure 85 selected impedance spectra from different periods of the long-term experiment are shown.

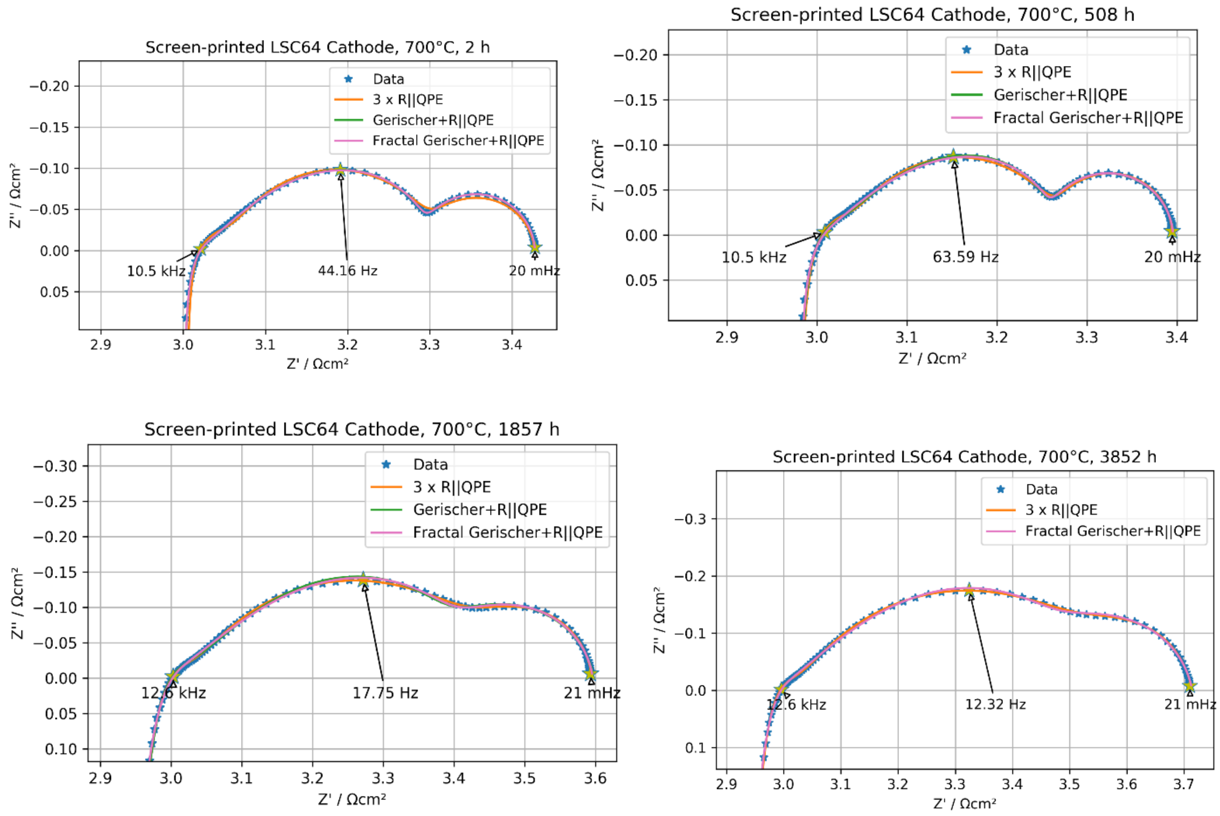
Screen-printed LSC64 Cathode, 700°C, 2 h

Screen-printed LSC64 Cathode, 700°C, 508 h

Screen-printed LSC64 Cathode, 700°C, 1857 h

Screen-printed LSC64 Cathode, 700°C, 3852 h

*Figure 85: Impedance spectra measured at different stages of the long-term experiment*

The impedance spectra were fitted with multiple equivalent circuit models: At the beginning, the impedance spectra were fitted best with the model including two R-CPE elements and a Gerischer (or Fractal Gerischer) element (see Figure 12b on page 35). When humid atmospheres were present, the impedance arc at intermediate frequencies changed its shape, so that the Gerischer model was not suitable any more. The data was fitted better by using the model with three R-CPE elements (see Figure 12a on page 35) for the intermediate frequency arc. This change of the best fitting model can be seen well in the plots of the residuals from selected measurements in Figure 86. Another indicator for the quality of the fits is evaluating chi², the sum of the squared errors of the fit, which is shown for all fits of the degradation experiment in Figure 87.

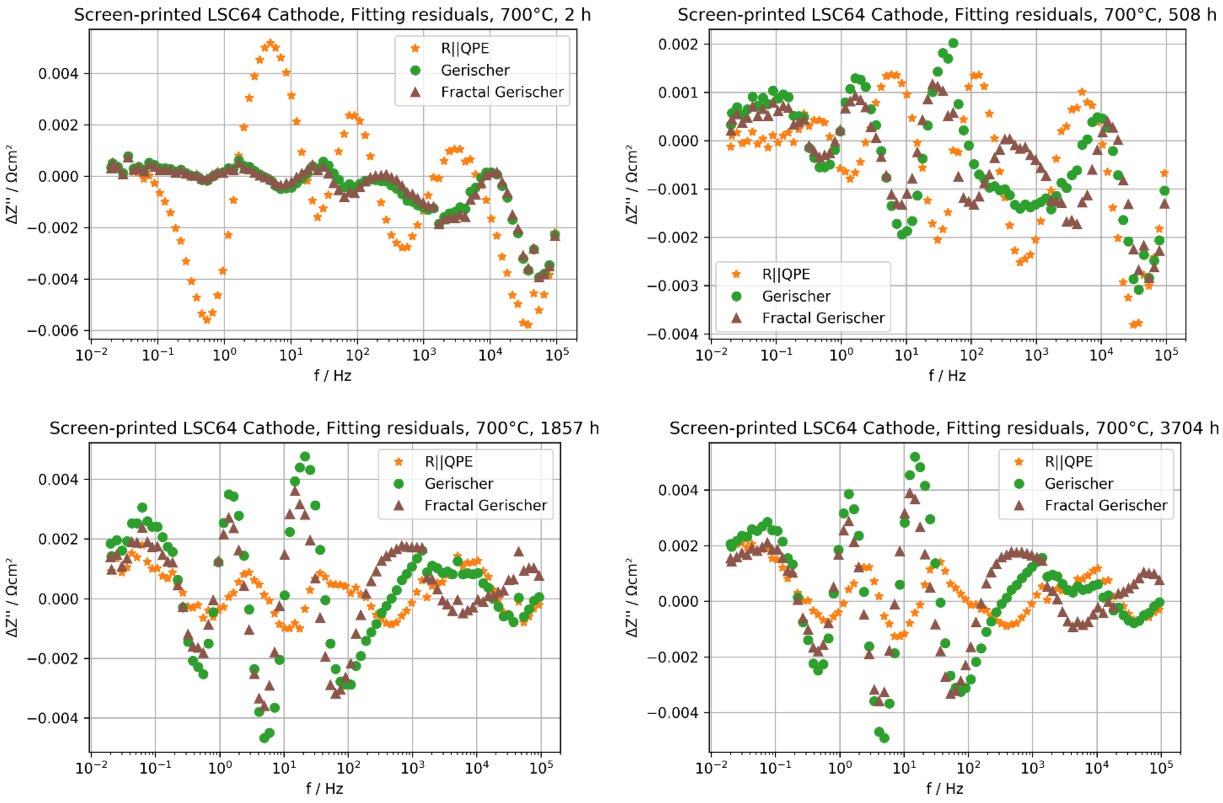

*Figure 86: Fitting residuals of selected impedance measurements, fitted with three different equivalent circuit models. At the beginning, the Gerischer models fit best, with increasing time the R-CPE model gave the best description of the data.*

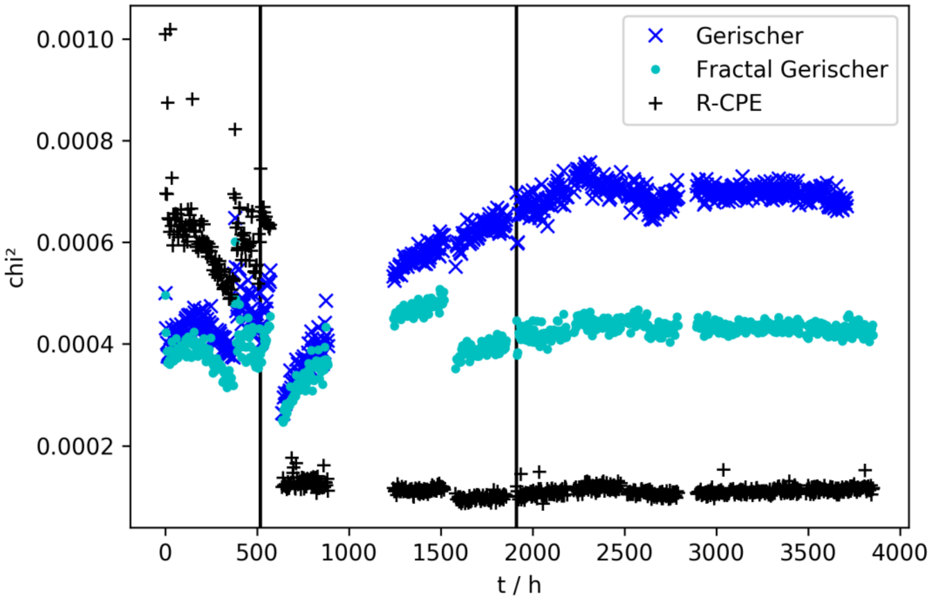

*Figure 87: Sum of squared errors of the CNLS-fits for every evaluated impedance measurement of the long-term experiment*

Figure 88 shows the time-dependent evolution of the resistances and the capacitances. As described above, the parameters were taken from the fits with the Gerischer impedance in the first period of the experiment (“dry”) and from the model with three R-CPE-elements in the second and third period (“30% rel. hum” and “60% rel. hum.”). In dry atmosphere, the cathode had a stable performance and $R_{mid}$ even showed a small decrease at the beginning. The presence of humidity led to an increase of $R_{mid}$, while $R_{low}$ remained constant.

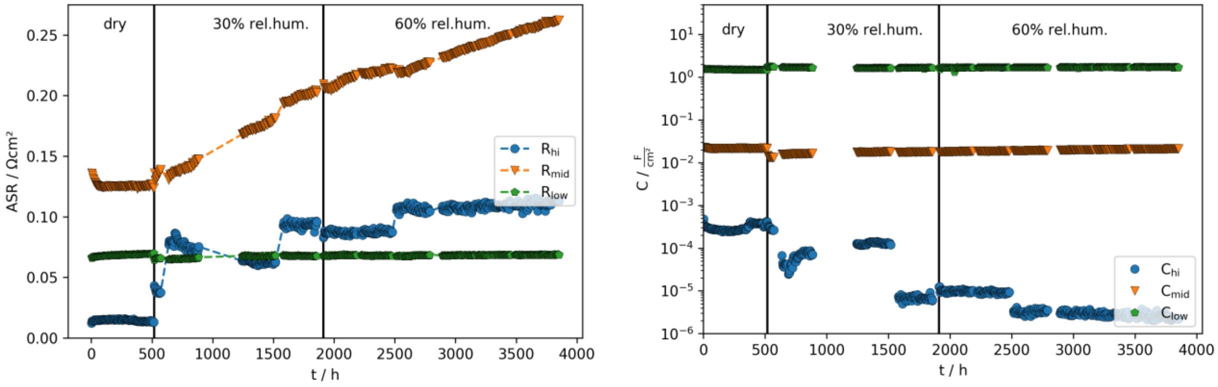

*Figure 88: Resistances (left) and capacitances (right) acquired from impedance spectroscopy as functions of the elapsed time of the long-term experiment*

For the interpretation of the data, it was assumed that $R_{low}$ is correlated to gas diffusion limitation and $R_{mid}$ is the actual polarization resistance of the cathode, which is linked to the oxygen exchange reaction at the cathode. Therefore, $R_{mid}$ was interpreted as polarization resistance $R_{pol}$, and $R_{low}$ as gas transport resistance $R_{gas\text{-}diff}$. Figure 89 shows the evolution of $R_{pol}$ and $R_{gas\text{-}diff}$ over time during the experiment. While $R_{pol}$ increased moderately over time, $R_{gas\text{-}diff}$ remained almost constant.

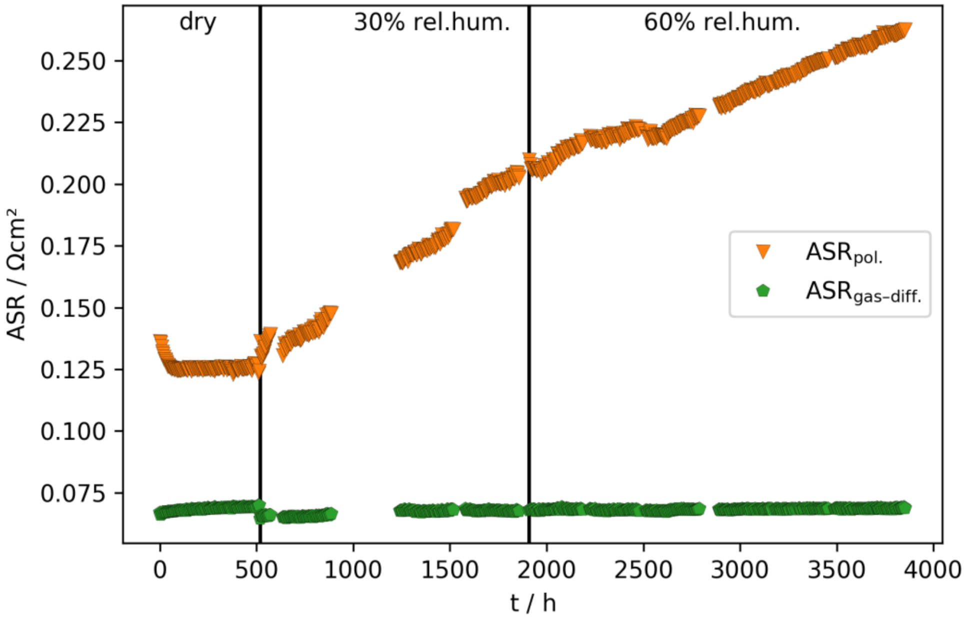

*Figure 89: Area-specific polarization resistance and gas-diffusion resistance as functions of time*

The parameters for the high-frequency arc, $R_{hi}$ and $C_{hi}$ have to be interpreted with caution. As shown in the impedance spectra in Figure 85 (page 106), the high-frequency arc overlaps with the inductivity of the equipment, making quantitative estimations rather difficult. The discontinuous changes in the values of $R_{hi}$ and $C_{hi}$ might be artifacts of the fitting routine or from changes of the impedance measurement equipment, rather than real physical effects.

As Figure 90 shows, the increase of $R_{hi}$ is partly related to a decrease in the ohmic resistance $R_0$. Due to this correlation it might be useful to sum up $R_0$ and $R_{hi}$. This is shown in Figure 91, where the sum of the two resistances is varying between 3.00 and 3.06 Ωcm². This is close to the estimated ASR of the GDC electrolyte, which was calculated to 3.14 Ωcm², taking into account the thickness of 1.803 mm of the electrolyte substrate an assumed ionic conductivity of 0.0544 S/cm for GDC at 700°C (according to [17]).

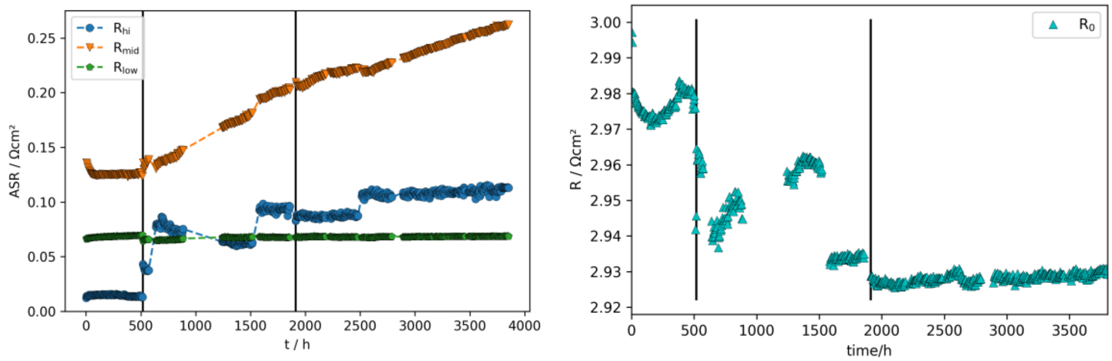

*Figure 90: Comparison of the polarization resistances and the ohmic resistance $R_0$*

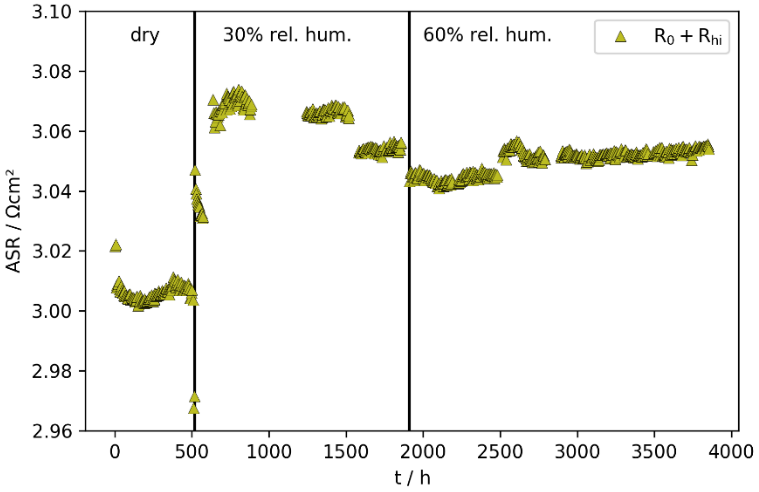

*Figure 91: Sum of $R_0$ and $R_{hi}$ as function of time*

During cooling of the reactor at the end of the experiment, additional temperature-dependent EIS measurements between 500°C and 700°C were performed. As shown in Figure 92, the slight increase of the polarization resistance during long-term testing could also be found at lower temperatures. The estimated activation energy showed a small decrease, which however might be inside the range of uncertainty.

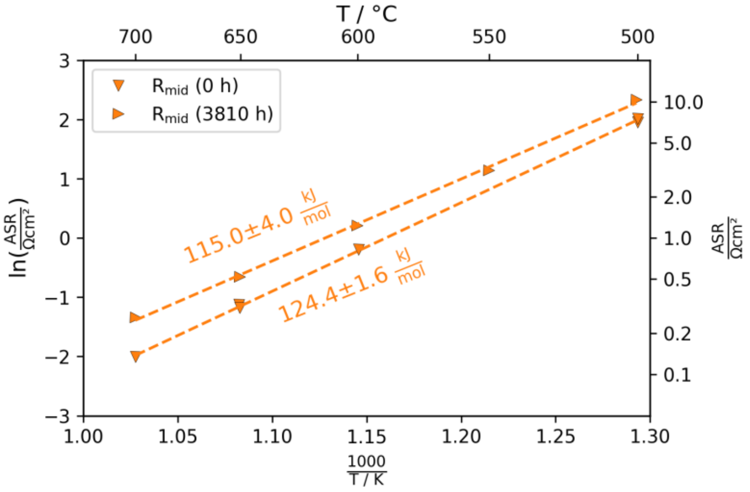

*Figure 92: Temperature dependence of the cathode polarization resistance at the beginning and at the end of the long-term experiment*

### 4.2.3.3 Post-test analyses

After finishing the long-term experiments, post-test analyses were performed on selected samples to gain information about the causes of the degradation. Analyses were performed by SEM and STEM on fresh samples, on the degraded cell and on samples which were removed from the experimental setup at the end of each testing period. Table 10 gives an overview on the samples and the performed analyses, which are presented in the following subsections.

*Table 10: Overview over the analyzed samples and performed analyses*

| **Sample** | **SEM-EDX surfaces** | **SEM-EDX cross-sections** | **STEM-EDX/EELS** |
|---|---|---|---|
| Screen-printed LSC64 as prepared | ✓ | ✓ | |
| Screen-printed LSC64 after 508 h (dry) | ✓ | | |
| Screen-printed LSC64 after 1910 h (max. 30% rel. hum.) | ✓ | | |
| Screen-printed LSC64 after 3856 h (max. 60% rel. hum.) | ✓ | | |
| Symmetric cell with screen-printed LSC64 cathodes after 3856 h (max. 60% rel. hum.) | ✓ | ✓ | ✓ |

### *SEM of the surfaces*

Figure 93 shows survey images of the surface of the fresh and the degraded screen-printed layer. There are a few larger gaps, which are caused by inhomogeneities in the screen-printing ink (this issue will be explained in detail in the following section about the cross-sectional SEM analyses).

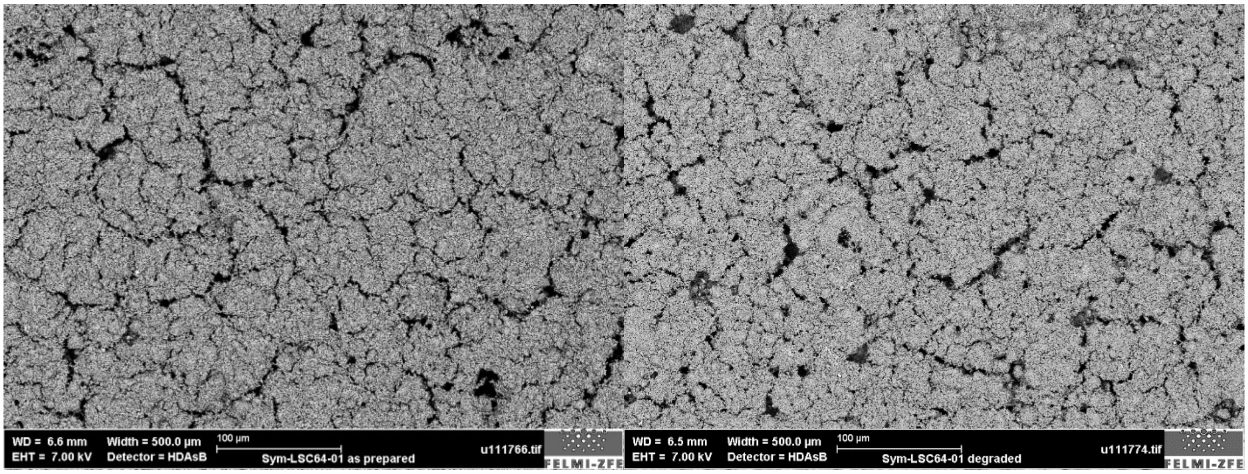

*Figure 93: SEM-BSE surface survey images of the freshly prepared LSC64 layer (left) and the degraded cathode (right) from the long-term experiment*

A closer zoom reveals the grain structure of the screen-printed layer. It consists of grains with an average size of about 1 µm, which are sintered together well. Despite the macroscopic inhomogeneities, the local morphology is quite homogenous. As expected for screen-printed films, the porosity is high due to burn-out of the organic binder during sintering.

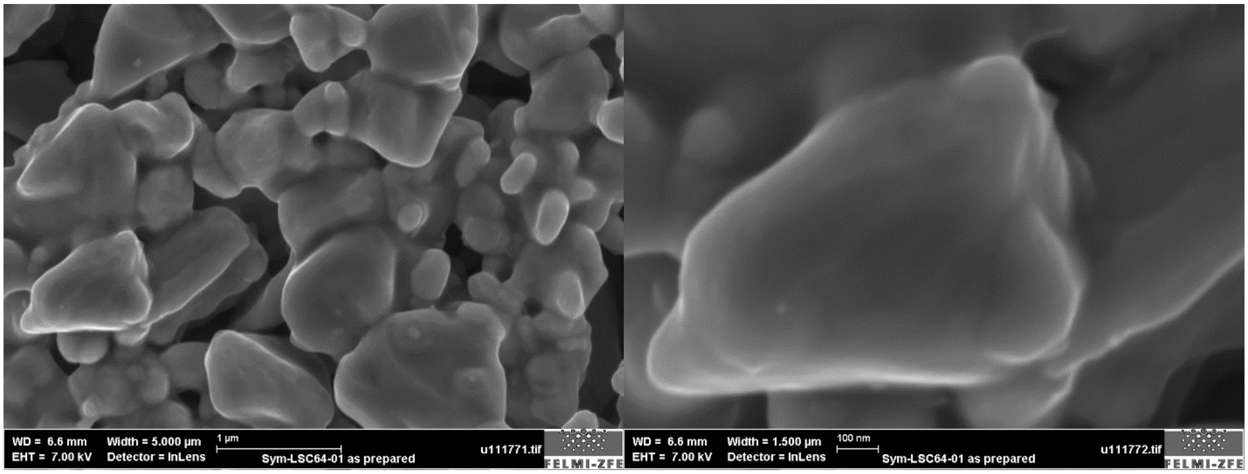

*Figure 94: SEM-SE surface images of the freshly prepared screen-printed LSC64 layer*

On the degraded cell, the grains show interesting morphological features. There are nanoscale secondary phases growing out of the grain surfaces. As Figure 95 shows that these fine-grained precipitates are spread homogeneously over the whole surface.

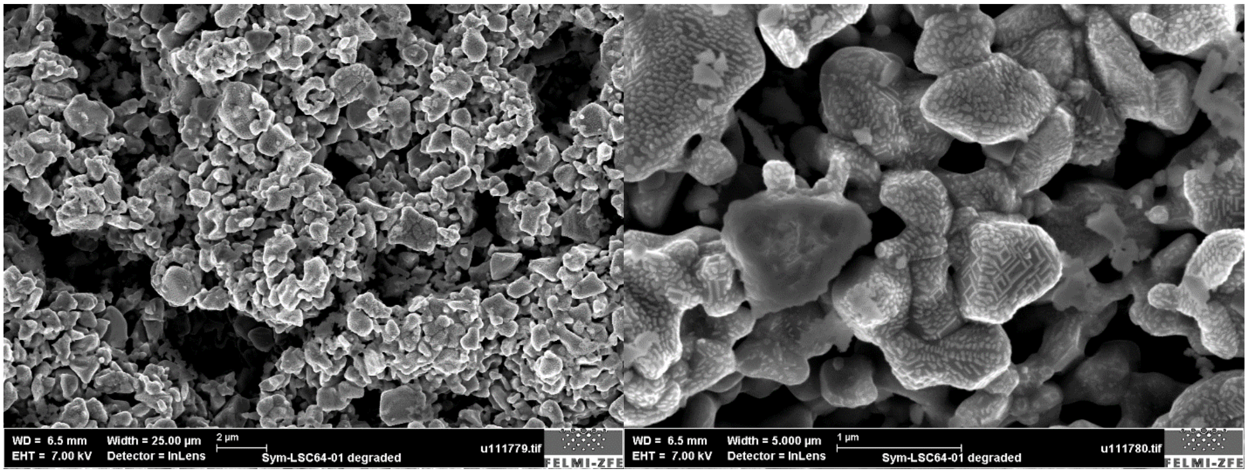

*Figure 95: SEM-SE surface images of the degraded cathode from the long-term experiment; grain surfaces are covered by surface precipitates*

The precipitates are present either in form of burls or in characteristic geometrical patterns. The latter seems to be the case on individual flat grain surfaces which might follow a dedicated crystallographic orientation. An example for such a structure is shown in Figure 96.

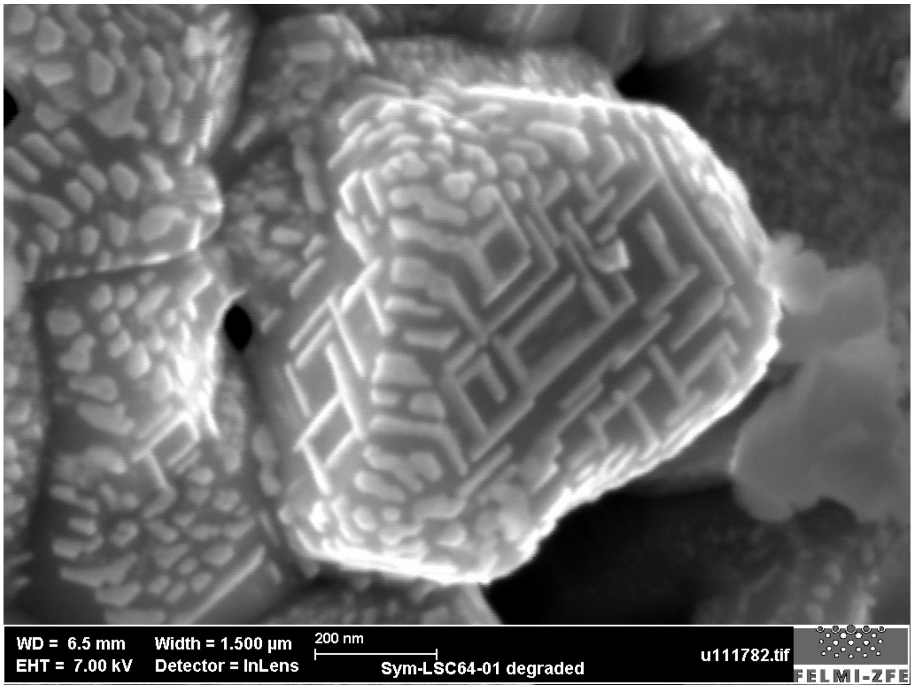

*Figure 96: High-magnification SEM-SE image of the degraded LSC64 cathode; surface precipitates form characteristic geometrical shapes*

EDX point analyses on the secondary phases show that they contain La, Sr, Co and O, the same elements as the underlying grains, but no impurities. Therefore, these structures are probably a decomposition product of LSC64. As Figure 97 shows, there is some hint that they might have a higher amount of Sr than the bulk, which would suggest that it is strontium oxide, SrO. However, the excitation volume of the EDX analyses (sphere with approx. 1 µm diameter) is far larger than the surface structures. Thus, the signal obtained on the small crystals is overlaid by the chemical composition of the underlying bulk phase.

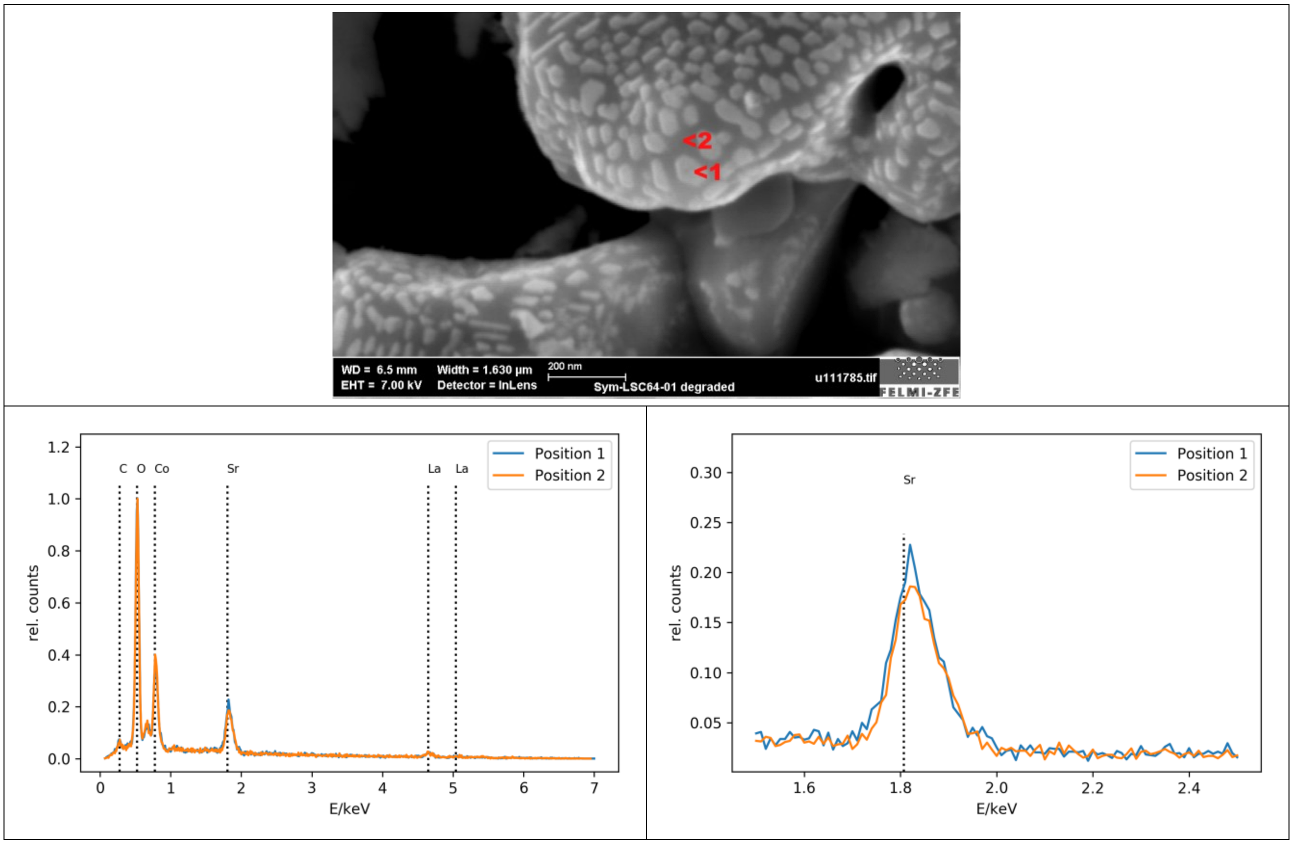

*Figure 97: SEM-SE surface image and EDX point-analyses on selected positions of the sample give a hint for higher Sr-concentration in surface precipitates*

Nevertheless, the assumption that the surface phase is SrO, is supported by a similar finding in literature. As described in detail in section 2.2.4.1 on page 15, it is well known that Sr in LSC64 tends to segregate to the surface. Yu et al. found surface precipitates in similar shapes on PLD-deposited LSCF thin-films, which were characterized as SrO by STEM-HAADF. In this work the formation of these phases was triggered by annealing the samples at 800°C in an atmosphere containing high amounts of $CO_2$ [156].

The finding of these secondary phases raises the question at which time of the long-term experiment these surface precipitates are formed. To answer this question the surfaces of the samples from different periods of the experiment were analyzed. The images in Figure 98 give an overview of the time-dependent evolution of these phases.

While the first sample, which was exposed only to dry testing atmosphere during the experiment, looks similar to the fresh sample and doesn't have precipitates on the grain surfaces, the samples degraded at humid atmospheres clearly show these structures. They seem to be growing with time. According to these results it is very likely that the formation of these surface structures is directly linked to humidity. A possible explanation for this effect is the Sr transport mechanism via the gas phase, as described in section in section 2.2.4.1 on page 15. Due to this effect it could be assumed that Sr from the surface was partly transported via the gas phase and recrystallized on the surface in the found structures.

Comparing the images in Figure 95 and Figure 98, it seems that the secondary samples were much more covered by surface precipitates than the cell itself. This can be explained by the fact that these samples were completely exposed to the testing atmospheres while the cell was covered by the electrical gold contacts and alumina plates and therefore a bit more isolated from the testing environment.

| | |
|---|---|
| After 508 h in dry atmosphere | 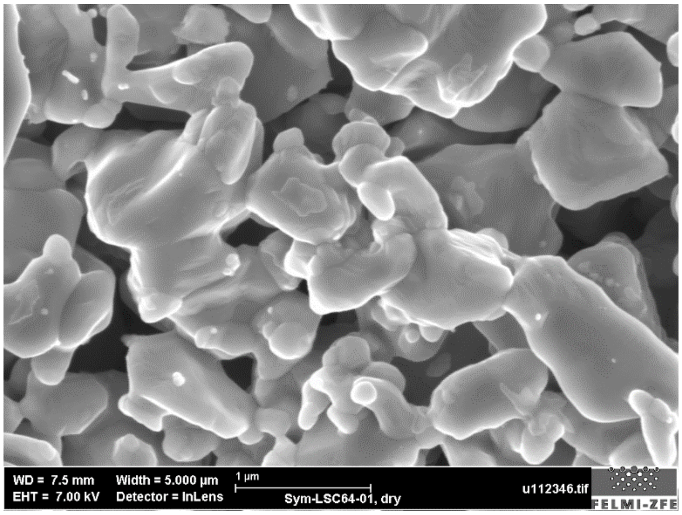 |
| After 1910 h at max. 30% rel. humidity | 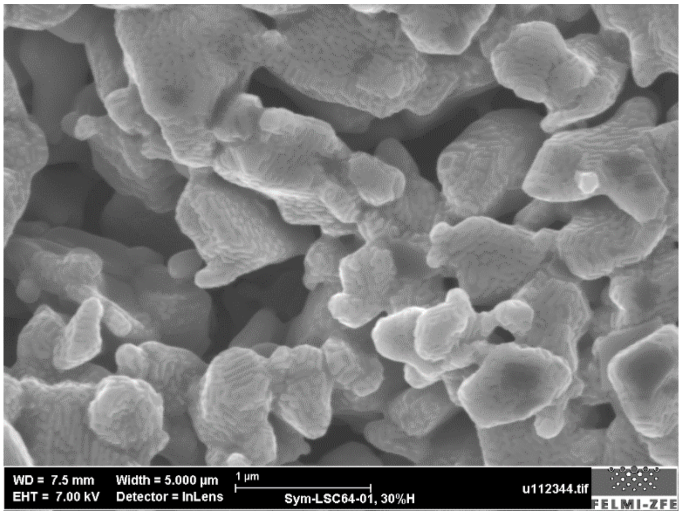 |
| After 3856 h at max. 60% relative humidity | 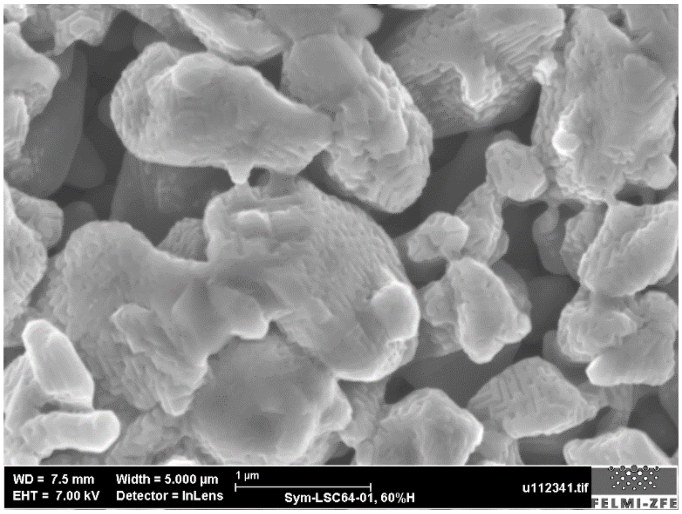 |

*Figure 98: SEM-SE surface images of samples taken from different stages of the long-term experiment reveal information about the time-dependent evolution of the surface structures*

### *SEM of the cross-sections*

Additional analyses were performed on the cross-section of the cathode layer, which was prepared by an ion sputtering technique. These analyses gave additional insights into the morphology of the screen-printed cathodes. However, it turned out that this kind of preparation was problematic for these samples: During preparation, material was evaporated from the dense GDC electrolyte and redeposited into the porous structure of the screen-printed LSC64 layer.

Figure 99 shows an overview of cross-sectional images of the fresh and the degraded sample. The figures indicate that the morphology of the screen-printed layers is quite inhomogeneous. There are globular clusters with higher density and more porous zones in between. These globular structures are agglomerates of the LSC64 powder which was used for fabrication of the screen-printing ink and originated from the spray-pyrolysis synthesis. For further experiments, the microstructure can be improved by additional roll-milling of the powder before paste preparation.

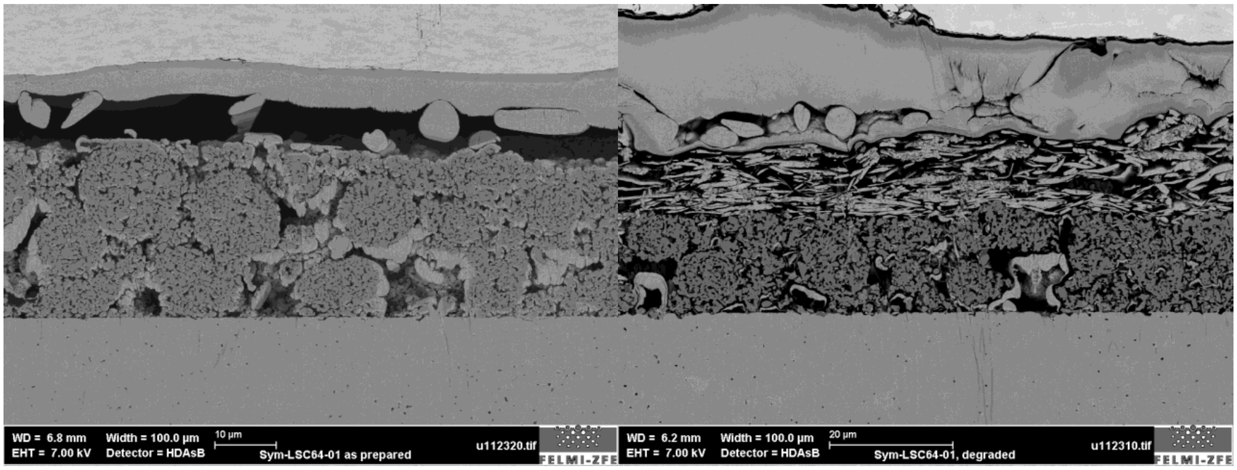

*Figure 99: SEM-BSE cross-sectional images of the freshly prepared LSC64 layer and the degraded cathode from the long-term experiment*

From the cross-sectional images, no indication for the surface precipitates could be found. Some features which are marked in Figure 100 might be indications for these structures, but due to the suboptimal preparation of the cross-section for SEM, the interpretation is difficult. Therefore, from the SEM cross-sectional analyses no clear conclusion can be drawn, whether these structures occurred only on the surface of the cathode or also inside the pores.

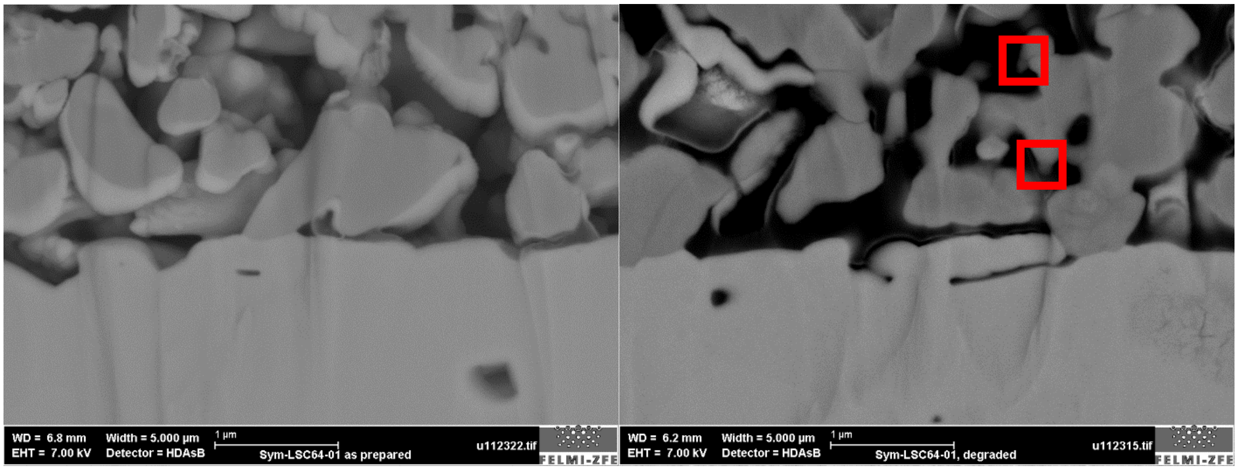

*Figure 100: SEM cross-sectional images of the freshly prepared LSC64 layer and the degraded cathode from the long-term experiment; features marked by red boxes might be indications for the surface precipitates found in Figure 95*

### *STEM of the cross-sections*

For analyses in the STEM, thin samples were prepared from the degraded cell by FIB.

Figure 101 gives an overview image of the TEM lamella, which was prepared from the degraded cathode in a region near the surface. It shows a porous, but in this relatively narrow region of the cathode homogeneous, grain structure.

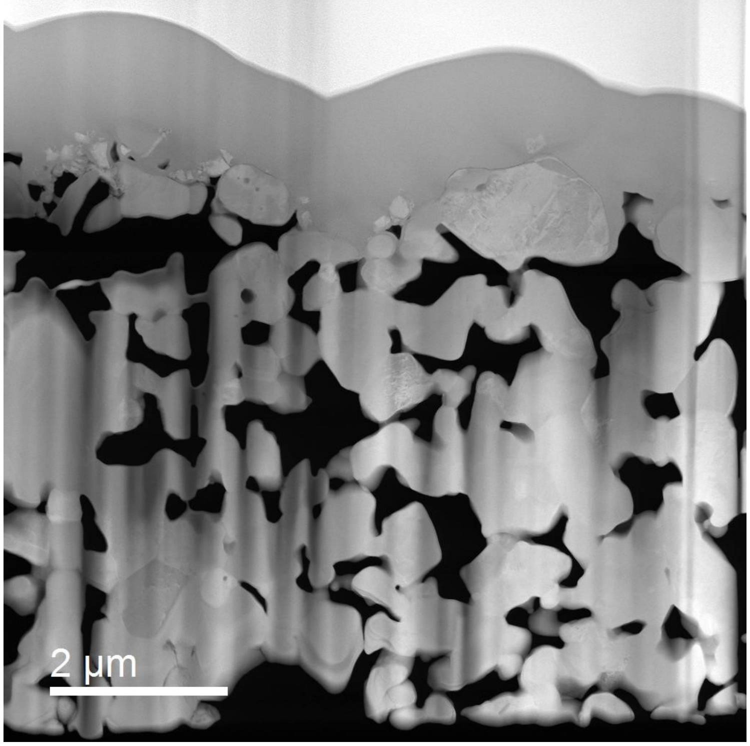

*Figure 101: STEM-HAADF cross-sectional image of the degraded LSC64 cathode*

Figure 102 shows a grain from the surface of the cathode layer. The HAADF contrast reveals inhomogeneities in the chemical composition. As an EDX analysis shows, there are regions inside the grain, which contain a high amount of C. These regions are probably a carbide phase inside the grain, which is a leftover from the powder synthesis. The secondary phase is surrounded by zones with a lower amount of Sr. It is very likely that this Sr-deficiency is caused by the carbide phase. However, a correlation between this finding and the observed degradation of the electrochemical cell in the long-term experiment is very unlikely since these carbide phases seem to be localized in only a few grains and should neither influence the electrical conductivity of the bulk nor the oxygen exchange and oxygen diffusion kinetics of the cathode.

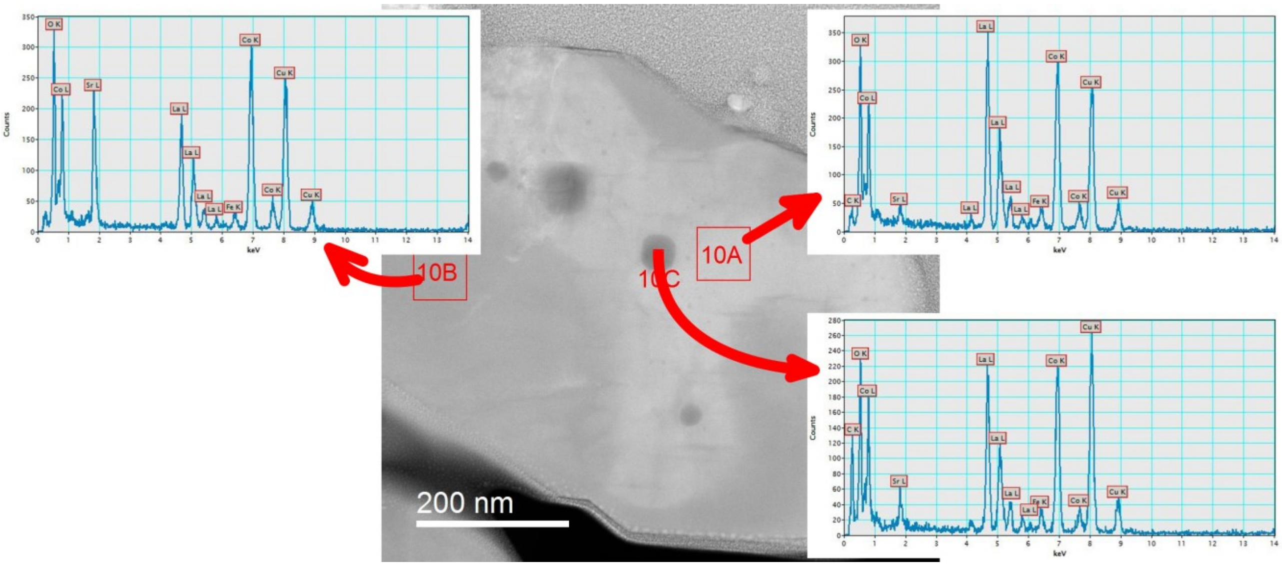

*Figure 102: STEM- HAADF image and EDX analyses of the LSC64 cathode at selected positions; small regions containing carbon are found inside the grain*

A goal of the current STEM analyses was to analyze the surface precipitates, which were observed in the SEM surface analyses, chemically by EDX and/or EELS. However, it was almost impossible to actually find any precipitates on the TEM sample. Figure 103 shows an image, where positions 14A and 14C might be such precipitates. However, there are no clear indications for secondary phases. According to EDX, the chemical composition is similar at all four analyzed positions. Only at 14A there is a hint for a slightly higher Sr content.

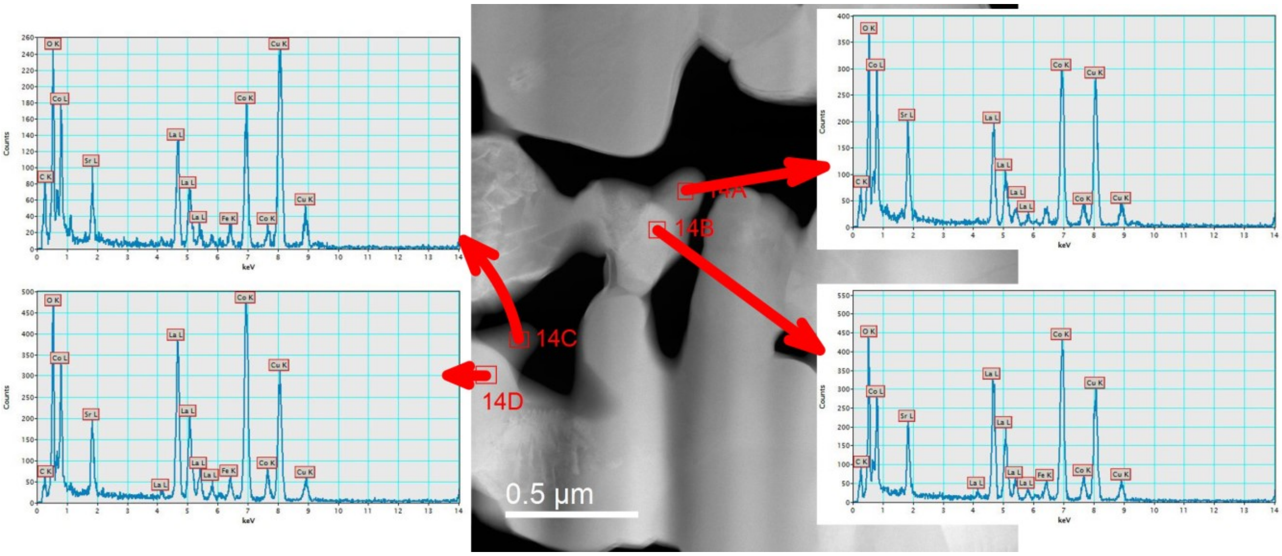

*Figure 103: STEM-HAADF image and EDX analyses of the LSC64 cathode at selected positions; no clear indications for Sr-enrichment in the small surface particles are found*

## 4.3 Electrochemical properties and long-term stability of cathodes with different microstructures under Cr- and Si-poisoning conditions

Long-term investigations with electrochemical impedance spectroscopy were performed on symmetrical cells with cathodes of LSC64 or LSCF on GDC electrolytes with different cathode architectures. The goal of these experiments was to characterize changes in the cathode performance when the cathode was exposed to volatile Cr-species.

The cathode architectures investigated in this experimental series were a thin-film cathode of LSC64, prepared by sol-gel spin-coating, an identically fabricated thin-film cathode but with additional current collector layer on top, and a conventional screen-printed cathode of LSCF (see Figure 104).

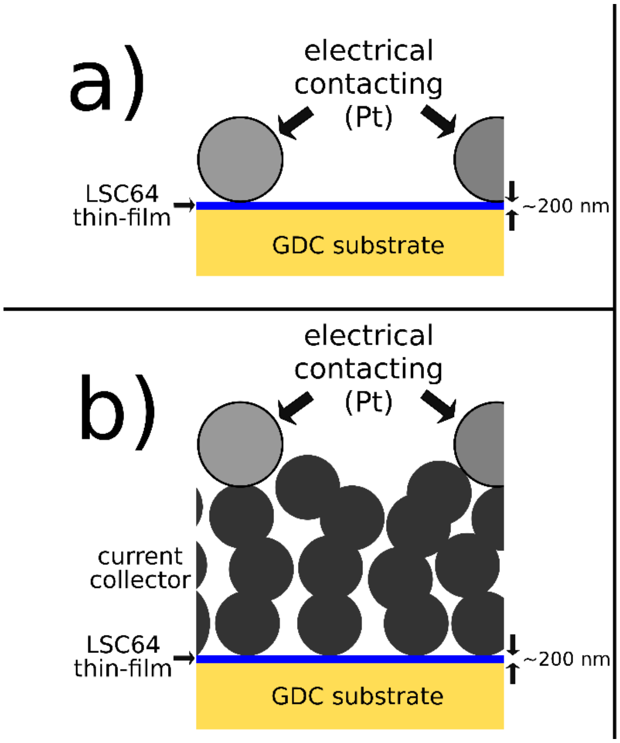

*Figure 104: Sketches of the cathode architectures characterized in the Cr-poisoning experiments: a) LSC64 thin-film, b) LSC64 thin-film with current collector, c) screen-printed LSCF*

All the experiments included temperature-dependent characterizations of the impedance spectra in the range between 500 and 700°C, followed by a long-term study at 700°C under combined Cr- and Si-poisoning conditions, as described in section 3.3.2 on page 37.

Since it turned out that the quartz glass parts of the reactor might not provide significant amounts of gaseous Si-species, the long-term experiment with the screen-printed LSCF cathode was separated into two periods. At the first testing period the sample was kept at 700°C in ambient air in the testing chamber with the Cr-sources. After about 1000 hours the sample was cooled down to room temperature and removed from the experimental setup. Si was artificially brought onto both cathode layers of the sample by sputtering a 5 nm thick layer on top of it. The sample prepared with Si was put back into the setup and the long-term experiment was continued at 700°C for another 1000 hours. The goal of this modification was to investigate the influence of a Si layer similar to those found on degraded CR samples (see section 4.1) on the cathode performance. The results of the long-term experiment with the screen-printed LSCF cathode have been also reported in [157].

### 4.3.1 Thin-film cathodes of LSC64 without current collector

The symmetric cell with thin-film LSC64 cathodes without current collector was characterized by EIS between 500 and 700°C. Afterwards, a long-term experiment was performed at 700°C, which was stopped after 570 hours.

#### *4.3.1.1 Short-term characterization*

In the temperature runs, the thin-film cathodes showed impedance spectra with two characteristic semicircles: At high frequencies a relatively large resistance was measured, while the low-frequency resistance was significantly smaller. The spectra were fitted using an equivalent circuit model with two R-CPE elements in series with an ohmic resistance and an inductivity. Figure 105 shows selected impedance spectra between 500°C and 650°C with the fitted impedance functions.

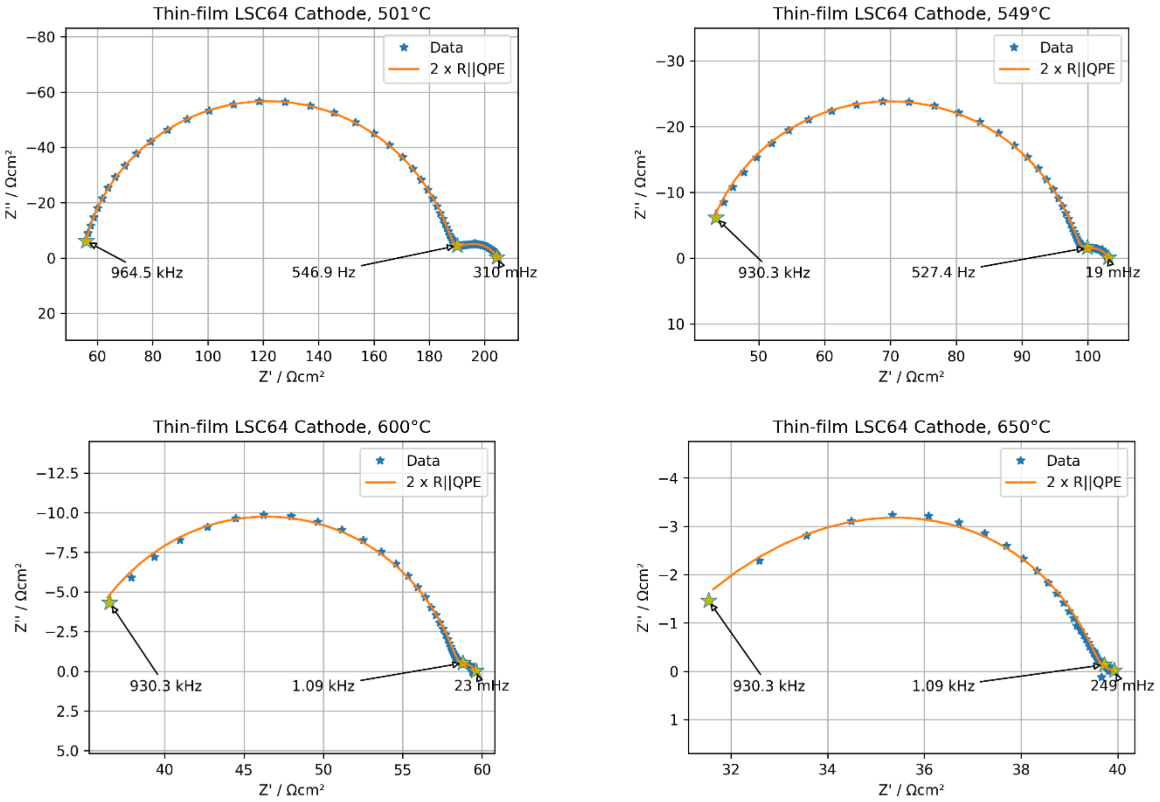

*Figure 105: Selected impedance spectra of the LSC64 thin-film cathode measured between 500°C and 700°C*

From the parameters of the CNLS-fits, the resistances and capacitances of the high-frequency and middle-frequency arcs were calculated, which are plotted in Arrhenius-diagrams in Figure 106.

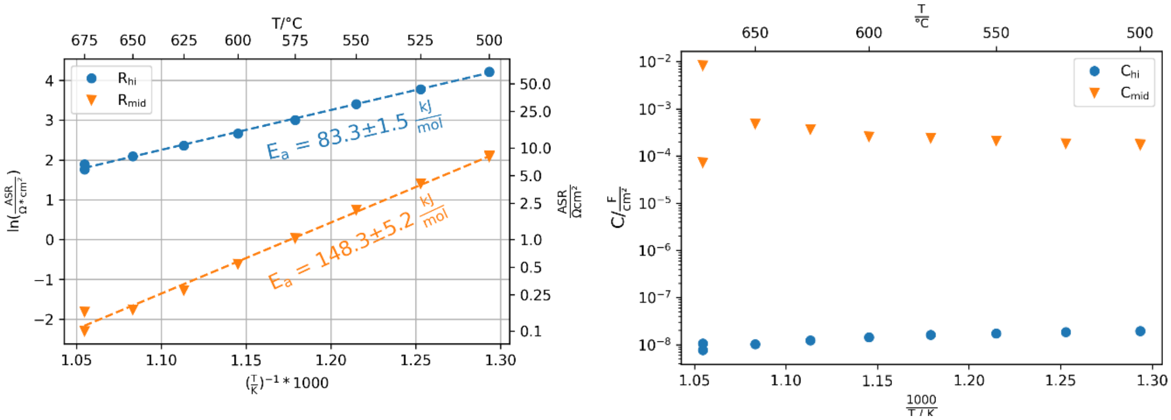

*Figure 106: Resistances (left) and capacitances (right) acquired from impedance spectroscopy as function of temperature*

While the resistivities are thermally activated, the capacitances remain constant over temperature. The capacitance of the middle-frequency arc is about $10^{-3}$ F/cm², which is in the typical range for capacitances caused by the SOFC cathode reaction. Therefore, it is assumed that $R_{mid}$ is the actual polarization resistance of the cathode. The capacitance of the high-frequency process is in the range of $10^{-8}$ F/cm², which might be an indication that the corresponding arc is caused by transport in the electrolyte, probably the grain-boundary resistance. In this case however, it is more likely that the high-frequency arc is an artifact of the electrode, caused by poor electrical contact. This effect has been reported in detail by Hwang et al. [158]. The authors of this study concluded, that these spreading resistances can be easily misinterpreted as grain boundary effects. An indication for this interpretation is the fact that no high-frequency arc was measured at the sample with the current collector layer (see section 4.3.2 on page 137).

The polarization resistance $R_{pol}$ was calculated from $R_{mid}$, which is shown in the Arrhenius-plot in Figure 107. The estimated activation energy for the polarization resistance was around 150 kJ/mol.

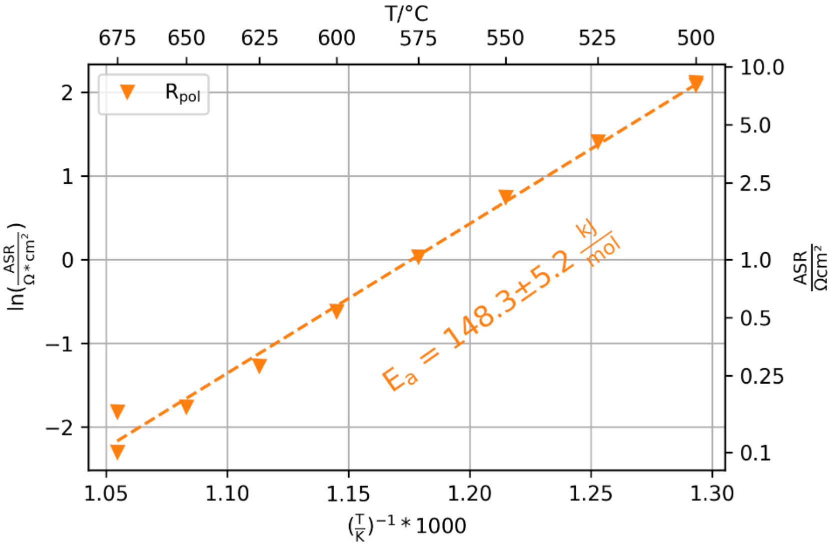

*Figure 107: Arrhenius plot of the area-specific polarization resistance of the LSC64 thin-film cathode*

### 4.3.1.2 Long-term characterization

The long-term experiment was performed at 700°C for a duration of 570 hours. Figure 108 shows selected impedance spectra of the time run.

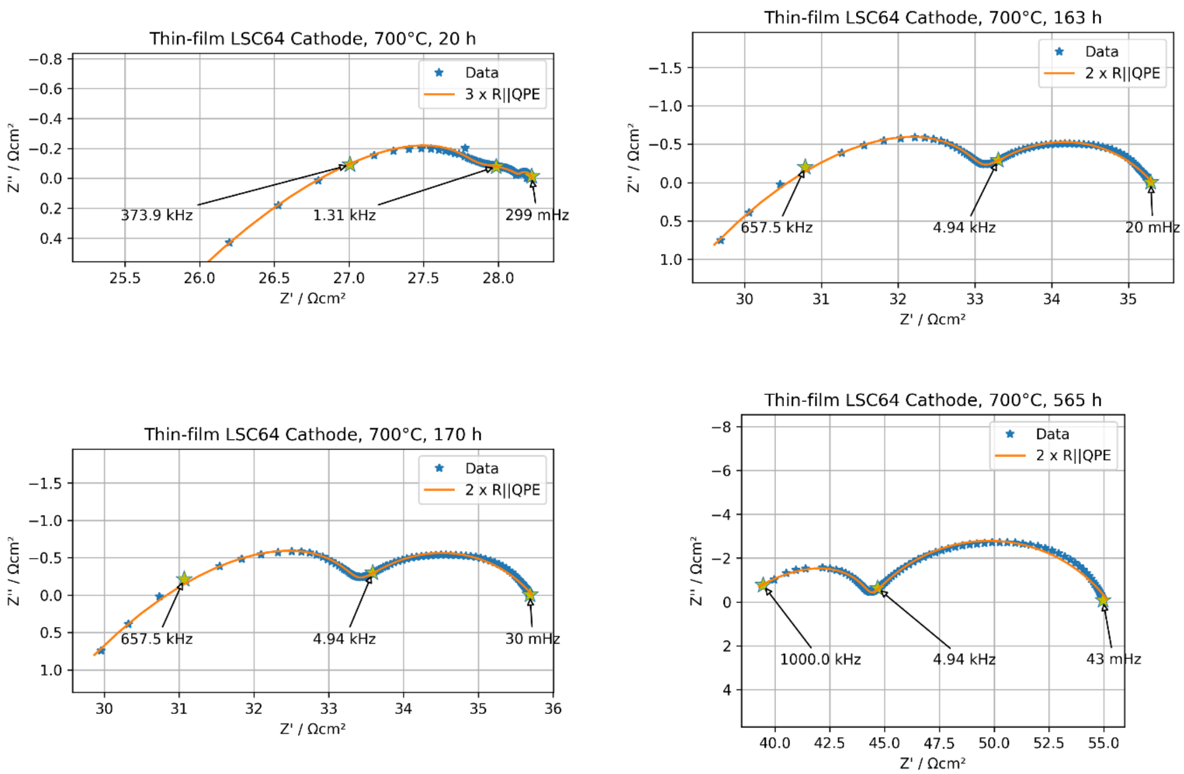

*Figure 108: Selected impedance spectra and CNLS-fits from the long-term experiment*

At the beginning of the long-term experiment, the polarization resistance of the sample was very low. It increased relatively fast, so that after 20 hours it was possible to quantify it in the CNLS-fit. An additional small semicircle appeared in the low-frequency range. Due to its high capacitance, it is likely that this signal was caused by gas transport limitation. It was taken account of in the fitting model by adding an additional R-CPE element to the equivalent circuit. Due to the fast increase of the middle-frequency resistance, the low-frequency arc became unobservable in the impedance spectra after 100 hours.

Figure 109 shows the resistive and capacitive parameters as a function of time. The low-frequency arc was observable only in the first 80-100 hours of the experiment. While the observed resistances showed a fast increase, the calculated capacitances remained almost constant in the same ranges found in the temperature-dependent measurements.

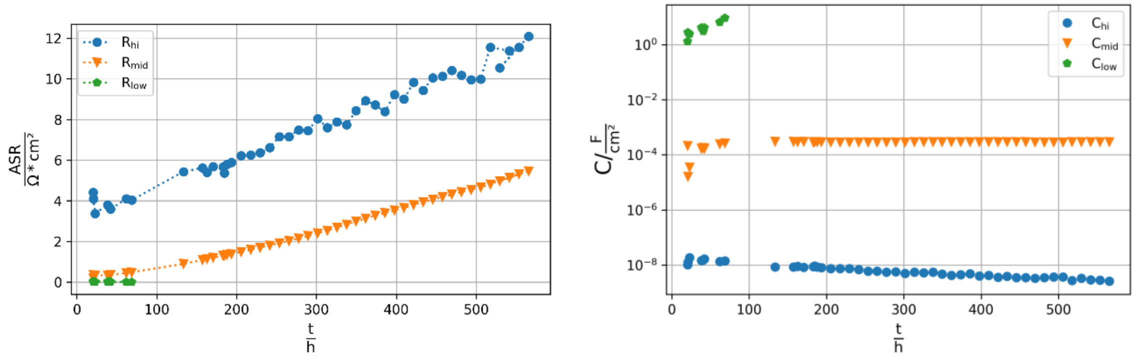

*Figure 109: a) Resistances and b) capacitances calculated from the impedance spectra as function of time*

In Figure 110, the polarization resistance, which was calculated by summing up $R_{mid}$ and $R_{low}$, is plotted over time. The degradation rate was above 10 Ωcm²/1000 h. Thus, the degradation of the cathode was severe and very fast, and the tested cell configuration of thin-film without current collector has to be considered as unstable in the presence of a Cr-source in ambient air.

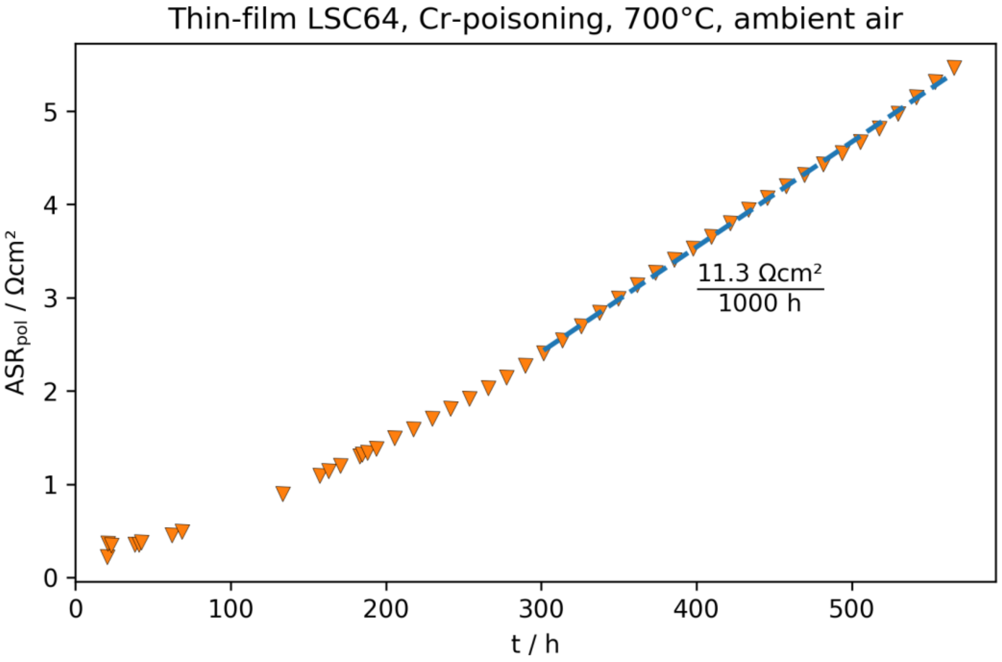

*Figure 110: Area-specific polarization resistance of the thin-film cathode as function of time with calculated degradation rate (increase of $ASR_{pol}$ per 1000 h)*

As explained in section 4.3.1.1 on page 122, the high-frequency resistance $R_{hi}$ is assumed to be an artifact of the electrical contacting rather than the grain boundary resistance of the electrolyte. The results from the long-term experiment support this assumption: $R_{hi}$ increased as well during the long-term experiment, even stronger than $R_{pol}$ (see Figure 111). It is very unlikely that such a strong degradation is caused by a grain boundary-related effect of the electrolyte.

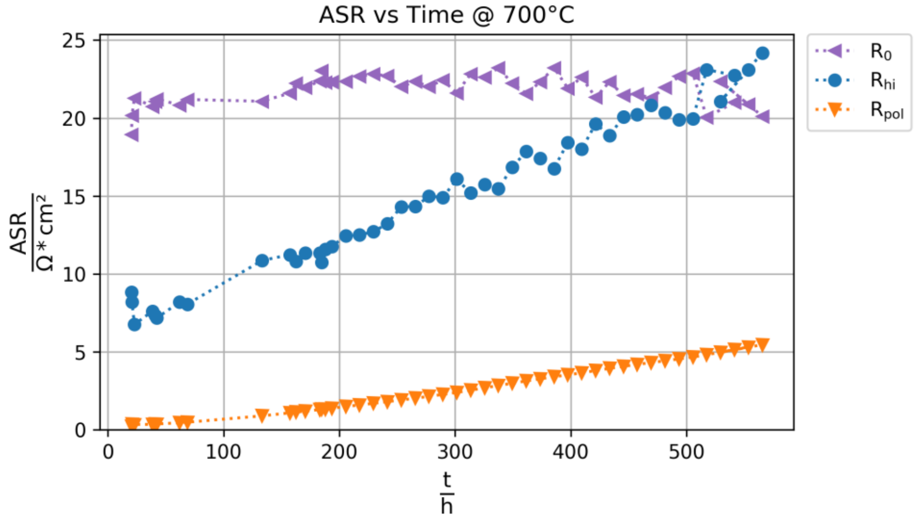

*Figure 111: Comparison of the time-dependences of the polarization resistance $R_{pol}$, the high-frequency resistance $R_{hi}$ and the ohmic resistance $R_0$*

### 4.3.1.3 Post-test analyses

For post-test analyses, a sample was prepared with LSC64 thin-films on one side of a GDC disk and cut into two pieces. One piece was kept in the state as prepared, while the second piece was present in the reactor a few centimeters besides the symmetrical cell during the degradation experiment. It is assumed that the second sample shows the same degradation effects as the cell.

#### SEM of the surfaces

The surfaces of the fresh and the degraded sample were analyzed by SEM. The fresh specimen, shown in Figure 112, had a relatively homogenous surface with nanoscale grains and nanopores in between. A few microcracks with a length of a few µm were found, which might result from tensile stress in the layer during cooling after the annealing process, which is a consequence of the mismatch in the thermal expansion coefficients of GDC and LSC64.

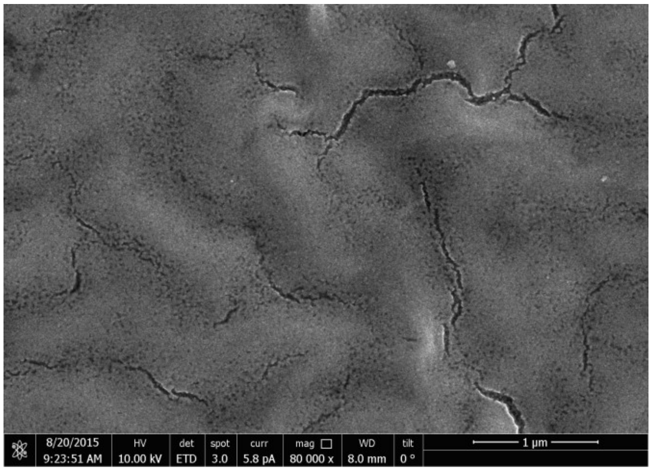

*Figure 112: SEM surface image of a freshly prepared LSC64 thin-film*

The surface images of the degraded sample indicate that the degradation was causing severe changes in the morphology of the thin-films. The degraded sample showed much bigger grains, some of them with shapes of facetted crystals.

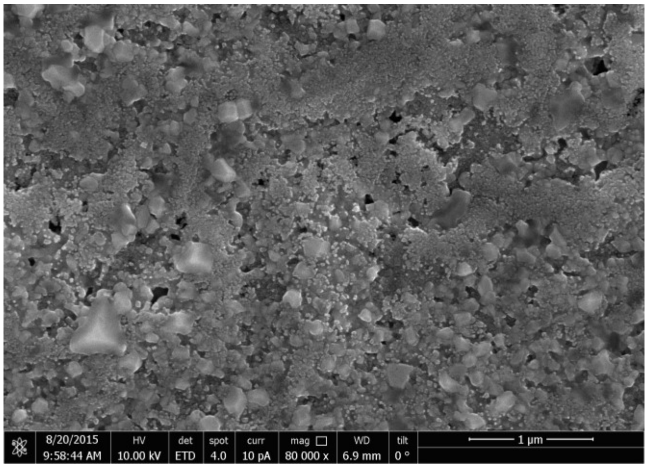

*Figure 113: SEM surface image of a degraded LSC64 thin-film cathode after long-term testing*

The following image gives a direct comparison between the fresh and the degraded sample.

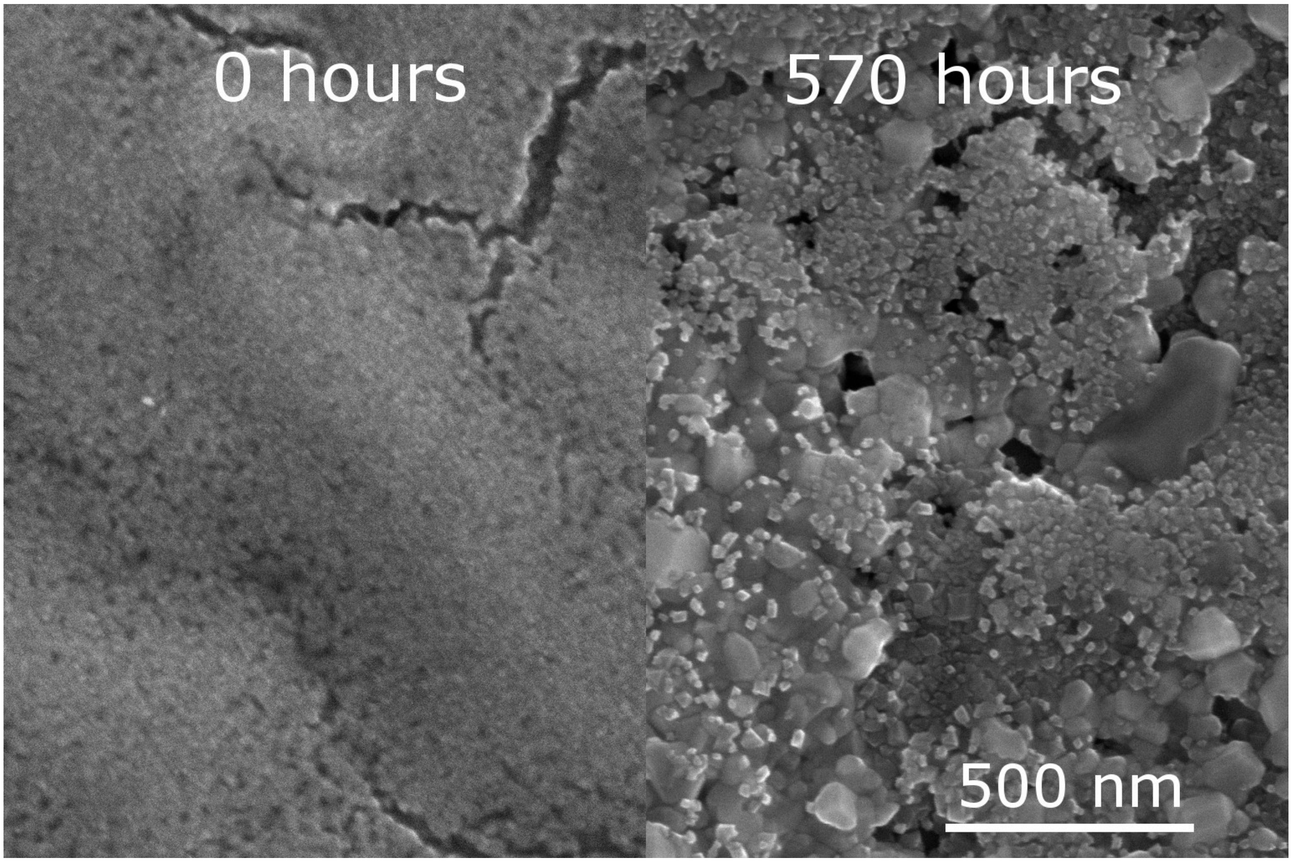

*Figure 114: Direct comparison of the fresh and the degraded LSC64 thin-film*

### *STEM of the cross-sections*

Cross-sectional analyses of the LSC64 thin-films in the fresh and degraded state were performed by STEM. Figure 115 and Figure 116 show STEM-HAADF images of the cross-section of the fresh sample.

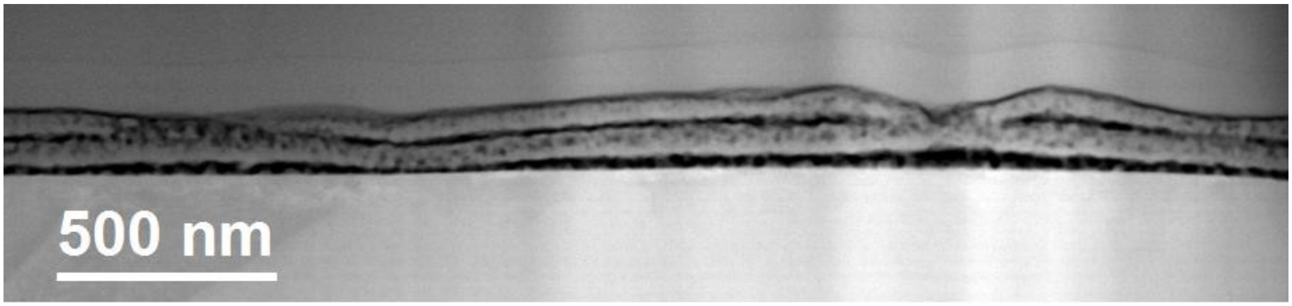

*Figure 115: STEM-HAADF cross-sectional image of the freshly prepared LSC64 thin-film*

The images show a film of about 150 nm thickness on the GDC substrate with nanoscale grains (mean grain size approximately 10-20 nm) and a characteristic double-layered morphology. There are two relatively dense layers with darker regions in between and at the interface to the GDC substrate. The darker layers in the images are zones of high porosity, as a line-scan analysis over the cross-section with EDX confirmed (Figure 117).

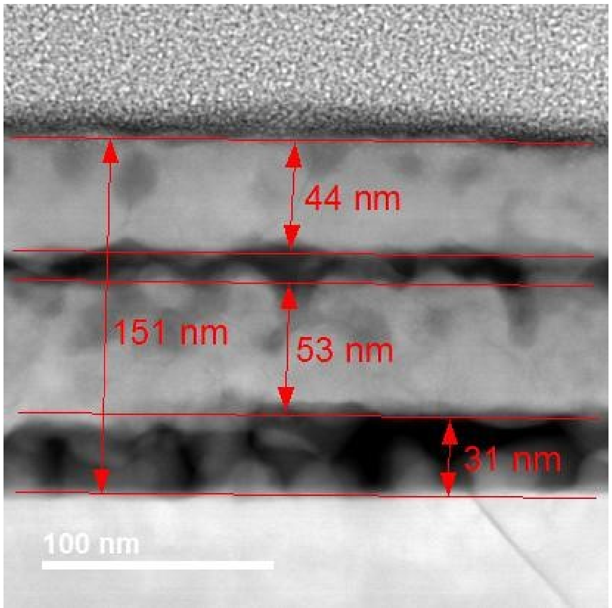

*Figure 116: STEM-HAADF image of the fresh LSC64 thin-film in high magnification; the thickness was estimated to about 150 nm*

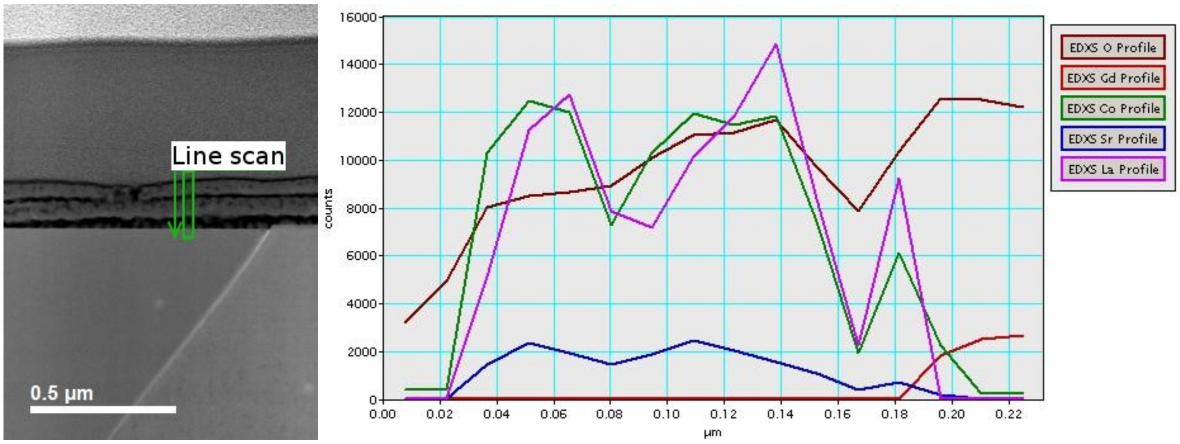

*Figure 117: EDX line-scan analyses of the elements La, Sr, Co and Gd and O over the thin-film*

The layered structure is a result of the thin-film synthesis process, which was carried out in two cycles of spin-coating, drying and annealing, as explained in section 3.2.1.3 on page 32.

Analyses of the cross-section of the degraded sample in STEM confirmed the changes in morphology of the LSC64 film during the experiment. As observed in the STEM-HAADF image (Figure 118), the mean grain size of the degraded thin-film was significantly larger than that of the fresh sample. It increased by about a factor of 10. The different grey-scales of the grains (Z-contrast) in the HAADF-images indicate that different grains have a different chemical composition. Especially, on the top half of each layer slightly darker grains are found.

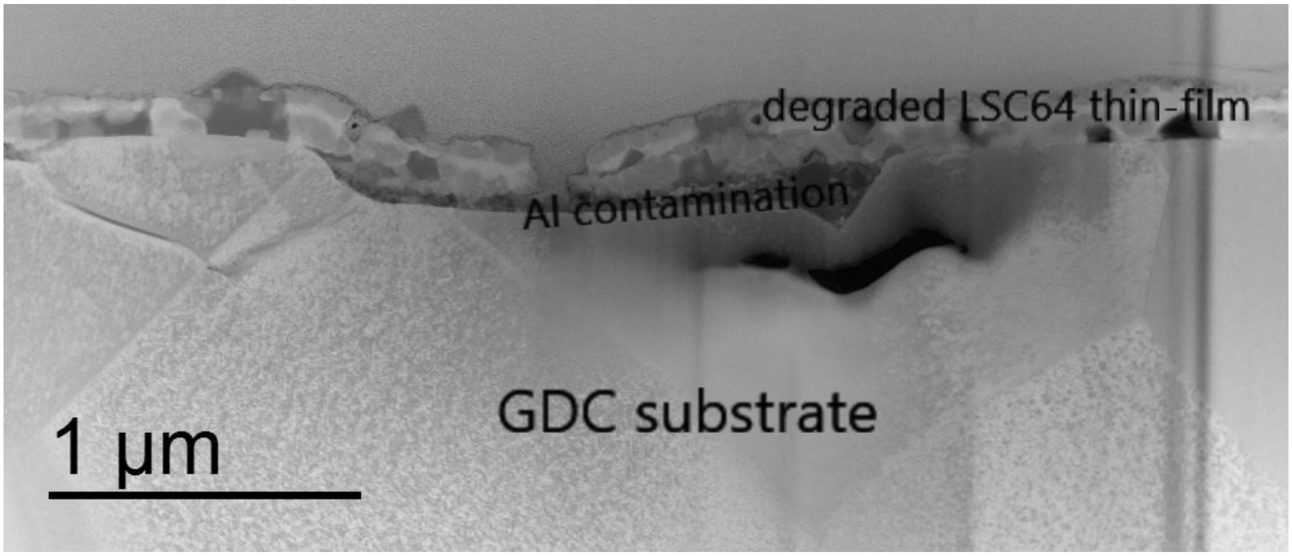

*Figure 118: STEM-HAADF cross-sectional image of the degraded LSC64 thin-film*

Figure 118 also shows a surface damage in the electrolyte in the form of a pit. It is filled with a secondary phase, which was identified as a mixture of alumina and small particles of GDC in EDX and EELS analyses (presented in the next paragraph). This feature has nothing to do with the degradation but is an artifact of the sample preparation: Prior to the thin-film deposition, the GDC substrate was polished with alumina particles in aqueous suspension, which resulted in polishing scratches like the one shown in Figure 118. Cleaning the substrates in ultrasonic baths obviously didn’t fully remove leftover alumina particles. However, it has to be noted that Figure 118 shows only a few microns of a sample with a diameter of 16 mm. Damages like this are likely to occur several times on the sample, but most of the surface is still unaffected. Since alumina is chemically inert, these damages should have had no significant influence on the electrochemical performance of the cathodes,. To avoid such damages and contamination with alumina, the polishing procedure was adapted after this discovery by using diamond suspensions instead of alumina.

Chemical analyzes of selected single grains were performed by EDX and EELS to investigate their chemical composition. An overview of these analyses is shown in Figure 119.

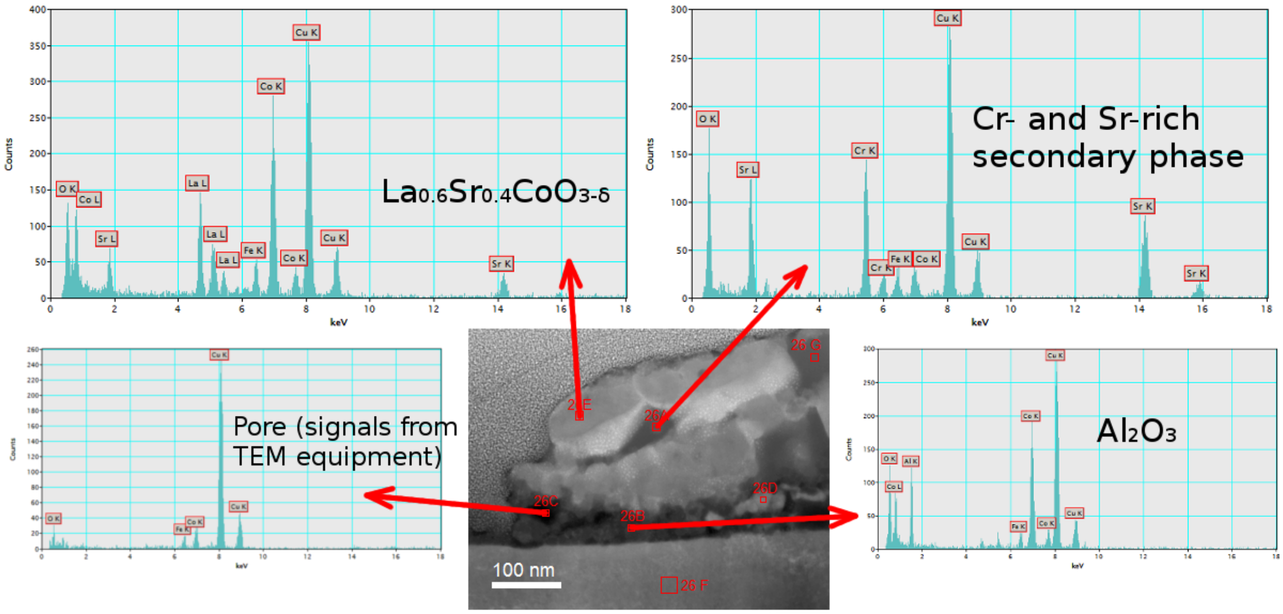

*Figure 119: STEM-HAADF image of the degraded sample and EDX spectra, which were acquired at the marked positions of the sample; the analyses reveal significant changes in the chemical composition of the thin-film*

According to the analyses, the degradation of the cathode was caused by changes in morphology and chemical composition of the thin-film. The most critical mechanism for the degradation is probably the contamination with chromium. It was transported to the sample via the gas phase and formed a secondary phase in the layer structure. This phase is probably $SrCrO_4$, a well-known spinel. The accumulation of $SrCrO_4$ in the cathode (which is confirmed by XPS depth-profiling, see next section) is a critical factor for the cathode performance since it is a phase with low electrical conductivity and poor oxygen exchange activity [110].

Figure 120 shows a direct comparison of the fresh and the degraded LSC64 thin-film. The double layer structure is still visible in the degraded sample.

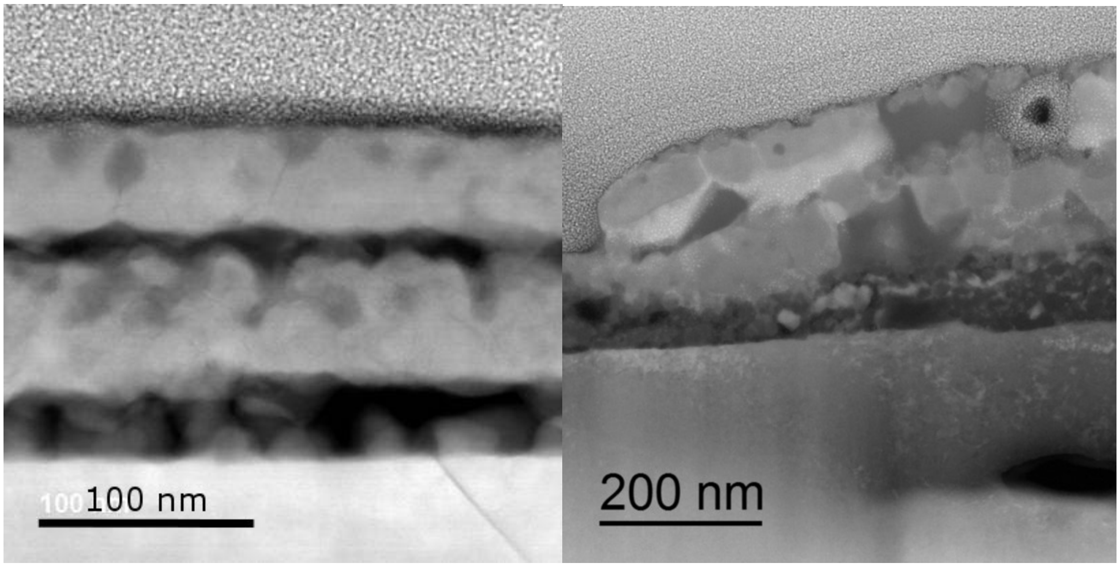

*Figure 120: Direct comparison of the fresh (left) and the degraded (right) LSC64 thin-film*

### *XPS depth profiling analyses*

By elemental depth-profiling analyses with XPS, the chemical composition of the fresh and degraded thin-films could be averaged over a larger sample area with high depth-resolution. This provided important information which was lacking from the STEM analyses (which give images/chemical analyses with high lateral resolution but of a very limited sample region). Figure 121 shows the concentrations of the cations La, Sr and Co of the LSC64 thin-film and Ce of the GDC substrate of the fresh sample as function of the sputter time. The sputter time correlates with the sputtered thickness. This correlation can be estimated approximately from the profile of the Ce concentration, which is practically zero at the beginning and increases when the thin film is removed completely, and the bare substrate is exposed. The transition from layer cations to substrate cations in the profiles is relatively smooth due to surface roughness of the electrolyte.

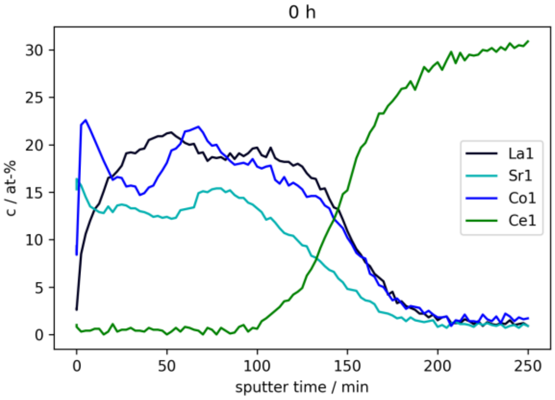

*Figure 121: XPS depth-profiles of La, Sr, Co and Ce of the sample with the fresh LSC64 thin-film*

The elemental depth-profiles of the fresh sample indicate a slightly inhomogeneous distribution of the cations in the thin-film. There is an inverse relation of the La- and Sr-concentration, as the Sr profile has local maxima at local minima of the La-profile. The Co-concentration correlates well with the Sr-profile, but there seems to be an enrichment of Co at the immediate surface and the interlayer.

The inhomogeneities in the depth-profiles correlate quite well with the cross-sectional morphology found in the STEM-HAADF images shown in the section above. Figure 122 gives a direct comparison of the XPS concentration profiles and the STEM-HAADF image of the cross-section. The local peaks in the concentration profiles can be correlated to the layer morphology.

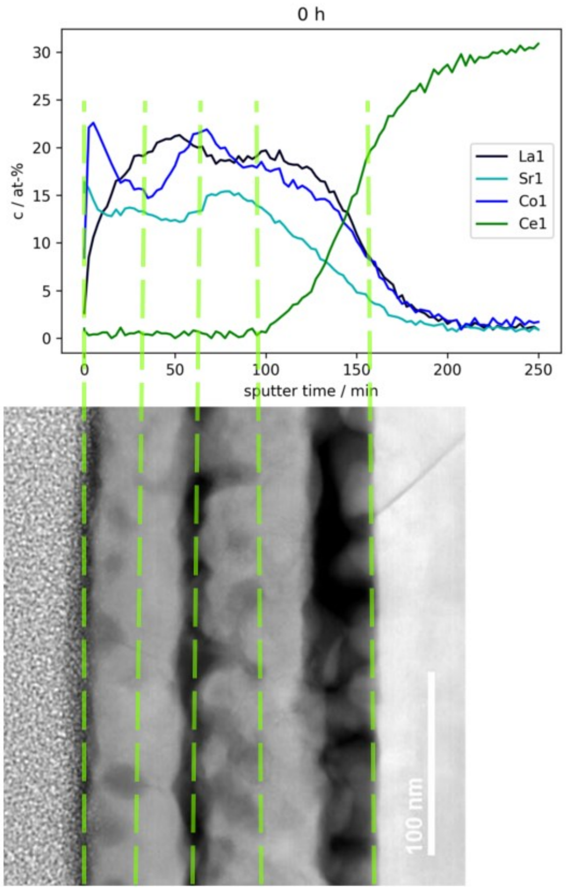

*Figure 122: Estimated correlation between the XPS depth-profiles and the STEM-HAADF cross-sectional image of the fresh LSC64 thin-film*

The same analysis was also performed on the degraded sample. Figure 123 shows the concentration profiles of La, Sr, Co, Ce and now also Cr, which was found in significant amounts over the whole thin-film.

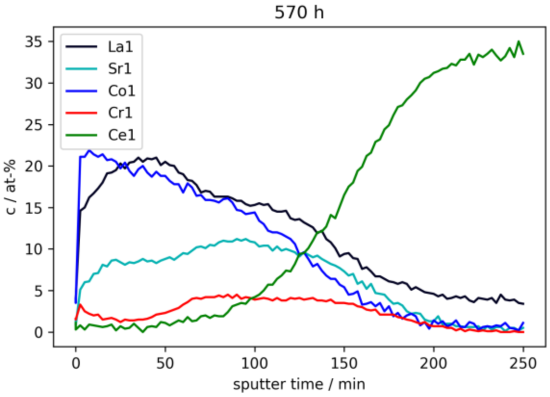

*Figure 123: XPS depth-profiles of the degraded LSC64 sample; significant amounts of Cr were found in the LSC64 thin-film*

Figure 124 sketches the correlation between the elemental depth-profiles and a cross-sectional STEM image of the degraded sample. Cr seems to be enriched at the surface and in the middle of the thin-film, which was porous in the fresh state. This can be explained well by the fact that volatile Cr-species like $CrO_2(OH)_2$ were transported to the cathode via the gas phase, as explained in section 2.2.4.2 on page 15.

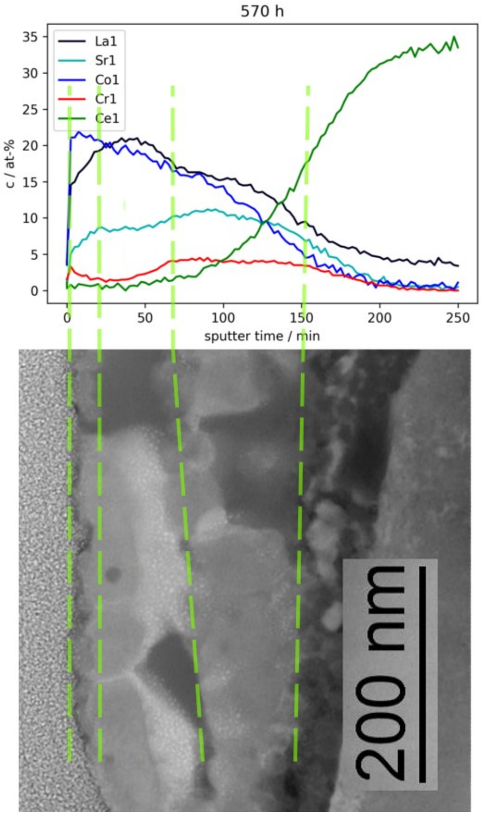

*Figure 124: Estimated correlation between the XPS depth-profiles and the STEM-HAADF image of the degraded LSC64 thin-film*

The XPS depth-profiling analyses also showed that Al, which was found in the STEM images at the interface between film and substrate (see Figure 118 on page 131), is only present in traces over the sample. It was not detected by XPS, which means that the total alumina concentration is negligible.

The correlation of the results from STEM analyses and XPS depth-profiles confirms that the STEM analyses, which are inherently covering only small parts of the whole sample, were in the present case quite representative for the average sample (with the exception of overestimating the amount of alumina contaminations).

## 4.3.2 Thin-film cathodes of LSC64 with current collector

In order to improve the electrical contacting, the long-term experiment was repeated with another LSC64 thin-film sample, which additionally was covered by a thick porous current collector (screen-printed layer of LSCF).

### *4.3.2.1 Short-term characterization and temperature dependence*

In comparison to the experiment without current collector (see previous section), the impedance spectra of the thin-film sample with current collector were significantly different. Figure 125 shows examples for impedance spectra measured on this kind of cathode between 500°C and 700°C:

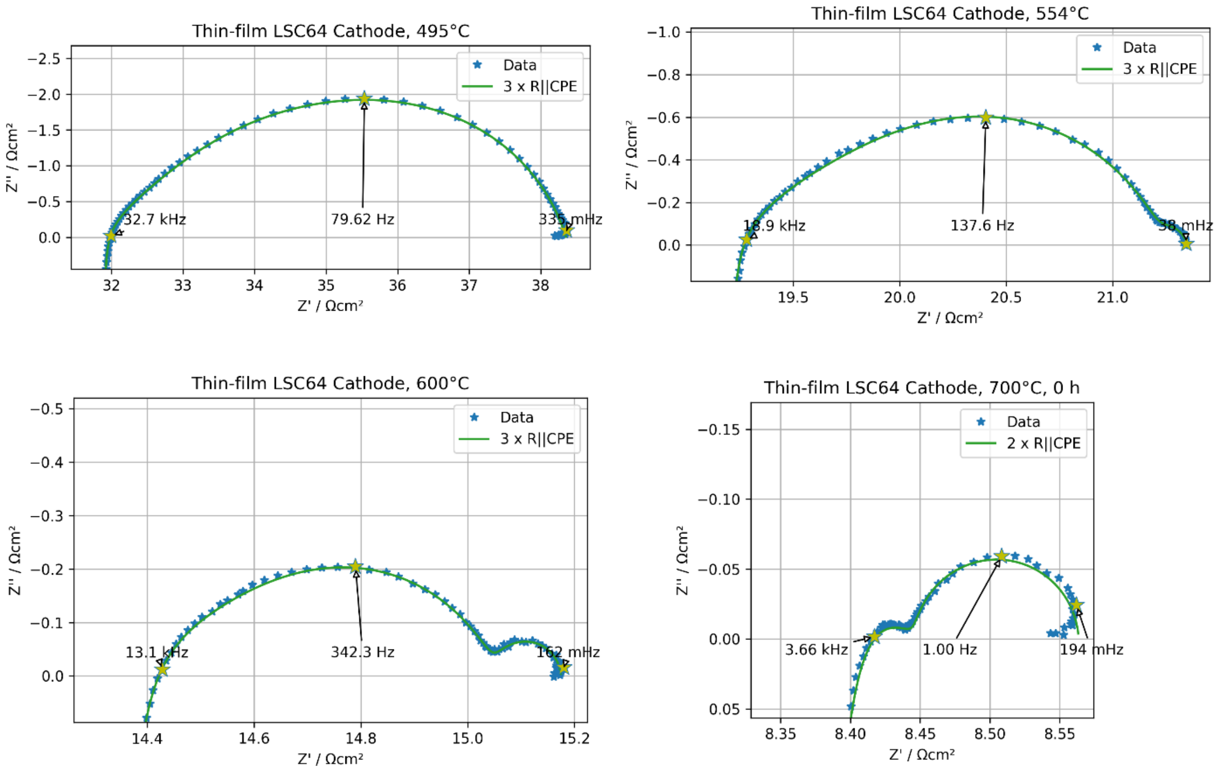

*Figure 125: Selected impedance spectra of the LSC64 thin-film cathode with current collector, measured between 500°C and 700°C*

At 500°C, the spectra show an asymmetric semicircle at higher frequencies, which looks similar to a Gerischer impedance. However, since the shape at lower frequencies is depressed, the spectra could not be fitted well with a Gerischer model. Instead, a model with three R-CPE elements was used to fit the spectra at temperatures below 625°C. In these fits the asymmetric high-frequency arc was described by two overlapping R-CPE elements and the low-frequency semicircle by the third one. At higher temperatures, the high-frequency arc intersected with the inductivity. These impedance spectra were fitted sufficiently with only two R-CPE elements.

Figure 126 shows resistances and capacitances calculated from the parameters of the CNLS-fit. The parameters are named following the nomenclature of the previous sections, using the indices “hi”, “mid” and “low” for the corresponding frequency ranges. However, it should be noted that in the present case the high-frequency parameters are covering a different frequency range than those determined for the thin-film sample without current collector (see section 4.3.1). In the current case both the “hi”- and “mid”-parameters rather come from the two overlapping R-CPE elements which are covering the same arc in the intermediate frequency range.

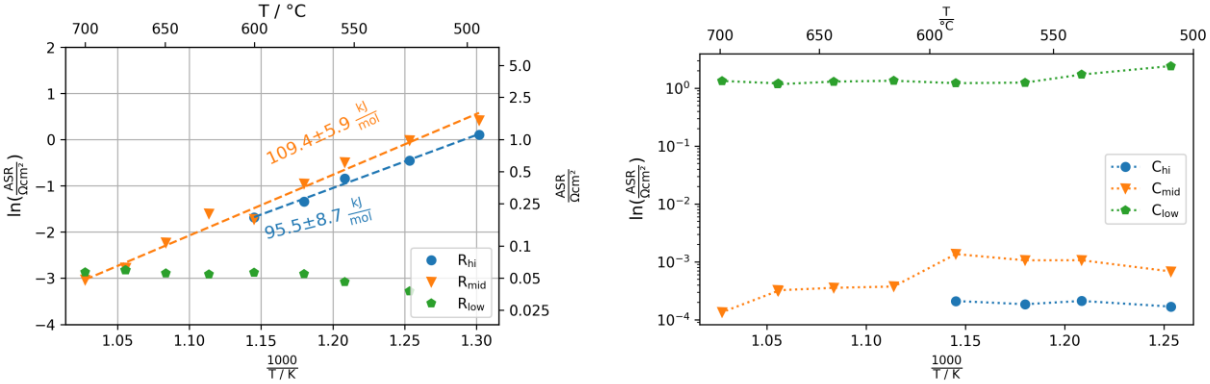

*Figure 126: Resistances and capacitances acquired from impedance spectroscopy as function of temperature*

The calculated mean capacitances $C_{hi}$ and $C_{mid}$ are within one order of magnitude, in the range between $10^{-4}$ and $10^{-3}$ F/cm². From these values it can be assumed that the high-frequency arc is linked to cathode processes. While diffusion might play a role at lower temperatures below 625°C (indicated by a Gerischer-type shape of the impedance arc), the cathode performance seems to be limited by surface exchange and oxygen adsorption at higher temperatures. The low-frequency parameters show a characteristic behavior for gas transport limitation. The capacitance $C_{low}$ is above 1 F/cm² and the resistance $R_{low}$ remains constant over temperature.

Following these assumptions, $R_{hi}$ und $R_{mid}$ can summed up into one parameter, which is defined as the cathode polarization resistance and will be called $R_{pol}$ in the following paragraphs. As Figure 127 shows $R_{pol}$ follows a linear trend in the Arrhenius plot with an activation energy of around 135 kJ/mol. The low-frequency arc will be called $R_{gas\text{-}diff}$.

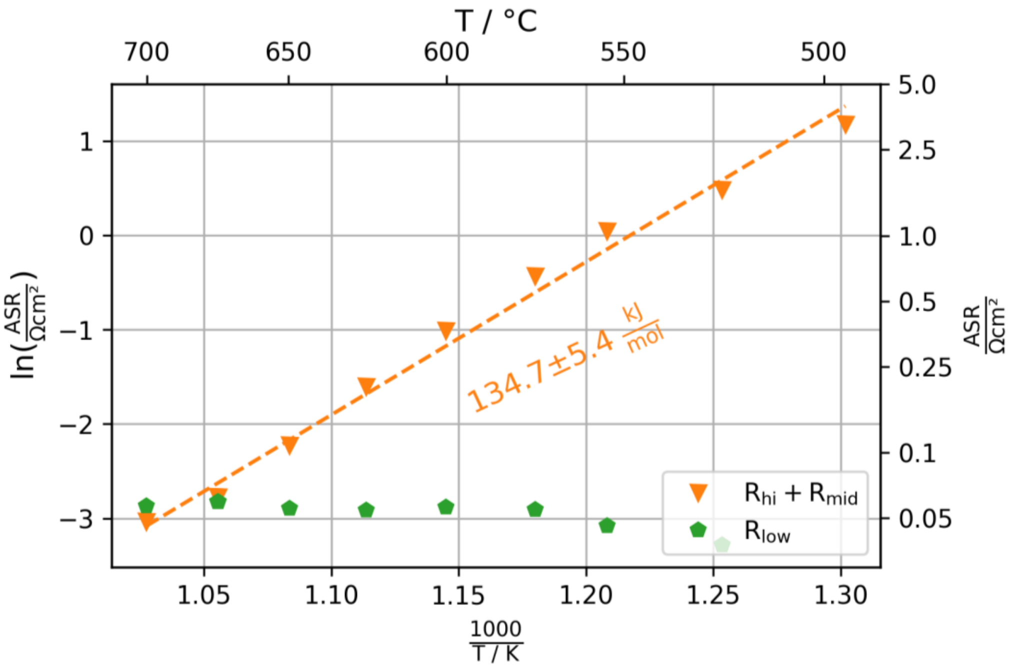

*Figure 127: Area-specific polarization resistance and gas-diffusion resistance of the thin-film LSC64 cathode with current collector*

### *4.3.2.2 Long-term characterization*

The long-term degradation experiment was carried out for 1180 hours at 700°C in ambient air. Selected impedance spectra with applied fitting models are shown in Figure 128.

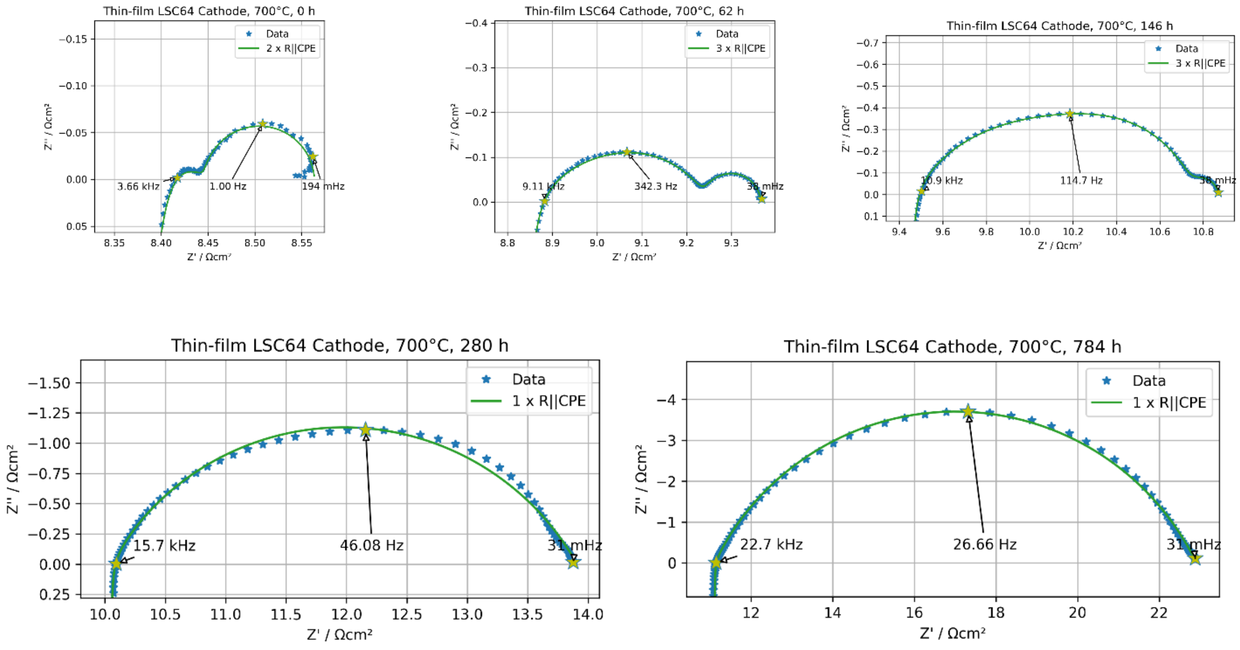

*Figure 128: Selected impedance spectra of the thin-film LSC64 cathode with current collector, measured during the long-term experiment*

Figure 129 gives an alternative view on the evolution of the impedance over time, which shows selected impedance spectra in a Bode plot (imaginary part of the impedance vs. frequency).

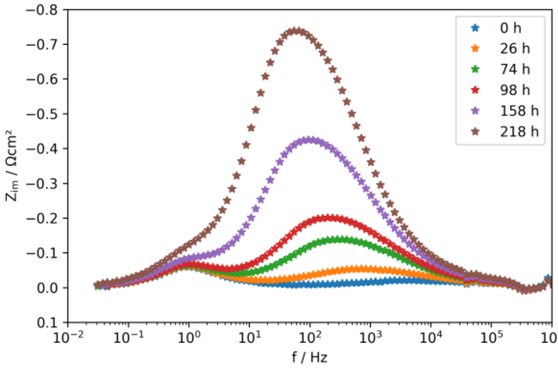

*Figure 129: Bode plots (Z'' over frequency) of selected impedance spectra from the long-term experiment*

The Cole-Cole and Bode plots of the impedance spectra show the strong change of the electrochemical response due to degradation. A fast-growing impedance arc with a peak frequency of a few 100 Hz causes a strong increase of the polarization resistance. Due to the changes in the shape of the spectra, the fitting model had to be adapted. In the first 250 hours, the impedance spectra could be fitted well with models using two or three R-CPE elements. Afterwards, the fits became sufficient by using only one R-CPE element.

From the fitting parameters, the resistances and capacitances were calculated, which are plotted in Figure 130. As already seen in the temperature-dependent measurements, the capacitances $C_{hi}$ and $C_{mid}$ were within the range of $10^{-4}$ and $10^{-3}$ at the very beginning of the experiment. However, there seemed to be a shift in $C_{hi}$ and $C_{mid}$ in the first few hours, where both capacitances increased by one order of magnitude.

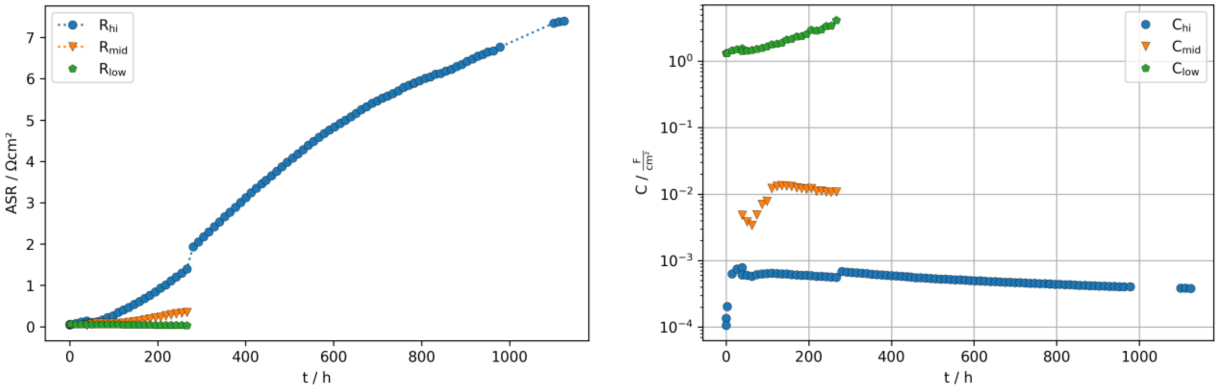

*Figure 130: Resistances and capacitances from the impedance spectra of the long-term experiment, plotted against testing time*

The resistivities increased significantly during the long-term experiment. All the resistive parameters $R_{hi}$, $R_{mid}$ and $R_{low}$ were summarized to define the polarization resistance $R_{pol}$ (plotted in Figure 131). The degradation rate was about 4.5 Ωcm²/1000 h. This is still a degradation rate far too high for any technical application. However, it is noteworthy that the thin-film sample with the current collector degraded significantly slower than the one without current collector, where the increase of $R_{pol}$ was more than twice as fast.

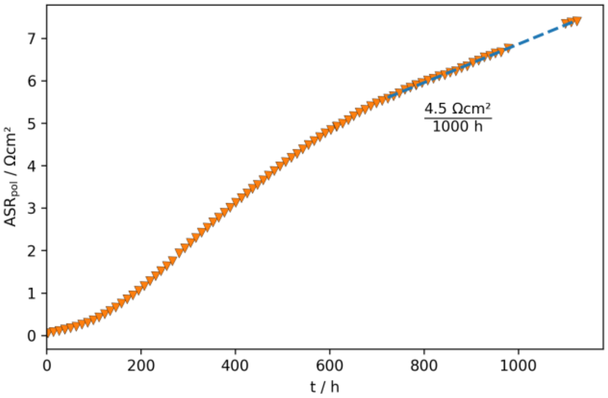

*Figure 131: Area-specific polarization resistance of the LSC64 thin-film cathode with current collector as function of time and calculated degradation rate (increase of ASR$_{pol}$ per 1000 h)*

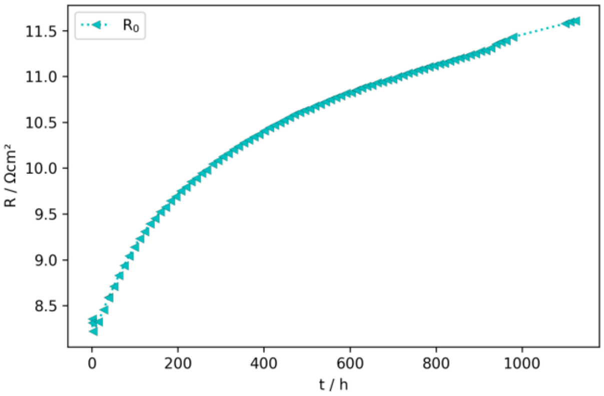

*Figure 132: Ohmic resistance of the sample as function of time.*

It has to be noted that also the ohmic resistance $R_0$ showed a significant degradation. The increase of $R_0$ can be explained by a decrease of the in-plane electrical conductivity of the thin-film due to the degradation.

### 4.3.2.3 Post-test analyses

Since both experiments were performed under the same conditions the degradation mechanism should be in principle similar to those observed for the thin-film cathode without current-collector. It can be assumed that the poisoning of the thin-film cathode with chromium was the main degradation mechanism. Therefore, reference is made to section 4.3.1.3 on page 127, where the post-test analyses of that sample are presented in detail.

With the current sample with thin-film cathodes and current collectors, only one additional post-test analysis of the degraded cell was performed with SEM. For this analysis it was necessary to uncover the LSC64 thin-film, which was of interest for the analysis, from the thick screen-printed LSCF current collector. However, since this screen-printed layer was not sintered on the sample, its mechanical bonding was quite low. Therefore, it was relatively easy to remove the current collector.

### *SEM of the surfaces*

Figure 133 shows surface images of a fresh thin-film on the left side and the degraded thin-film cathode (current collector was removed before analysis) on the right. According to these images significant morphological changes occurred during the long-term experiment. The nanoscale grains of the thin-film cathode are much larger in the degraded state. There might also be a decrease in porosity.

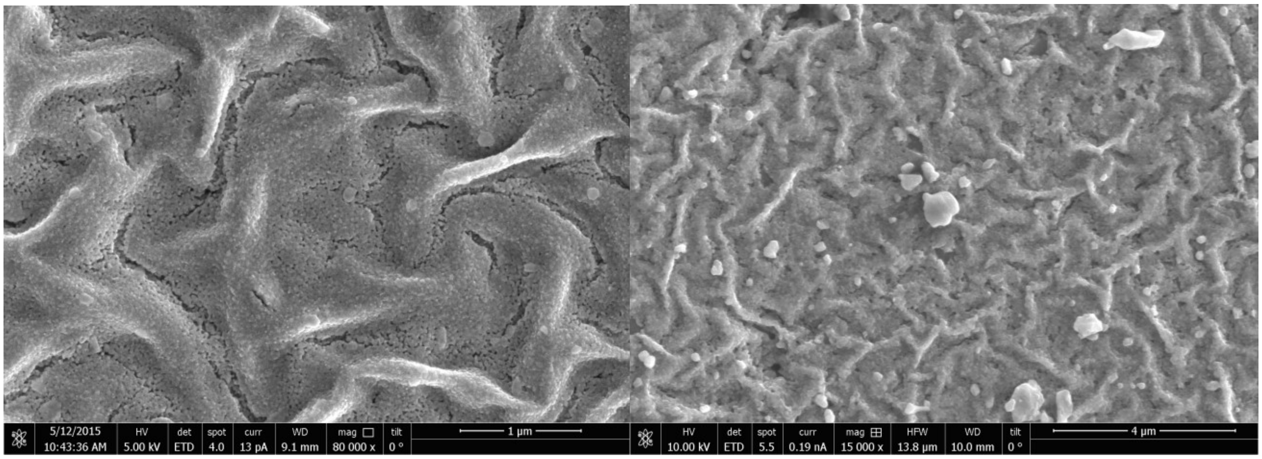

*Figure 133: SEM surface images of the fresh LSC64 thin-film (left) and the degraded LSC64 thin-film cathode (current collector was removed before analysis)*

However, compared to the results found for the sample without current collector, the morphological changes are not so severe. In combination with the results of electrochemical testing, this might be an indication that the current collector has a protective function for the thin-film (for instance as a getter for Cr and other impurities which are transported via the gas phase towards the cathode).

## 4.3.3 Screen-printed LSCF cathodes

The third long-term experiment under Cr-poisoning conditions was performed with a symmetric cell with screen-printed LSCF-cathodes with a thickness of about 30 µm [157].

### 4.3.3.1 Short-term characterization and temperature dependence

EIS measurements were performed at selected temperatures between 500°C and 700°C. After reaching 700°C the sample was cooled down to 500°C and the temperature-dependent EIS measurement series was repeated. The purpose of the two heating cycles was to determine whether the measured impedance behavior was reversible. It turned out that a small degradation already occurred during the heating cycles, since the measured resistances were higher in the second heating cycle compared to the first one. Figure 134 shows impedance spectra at 500°C, 600°C and 700°C, in the first and the second cycle, respectively.

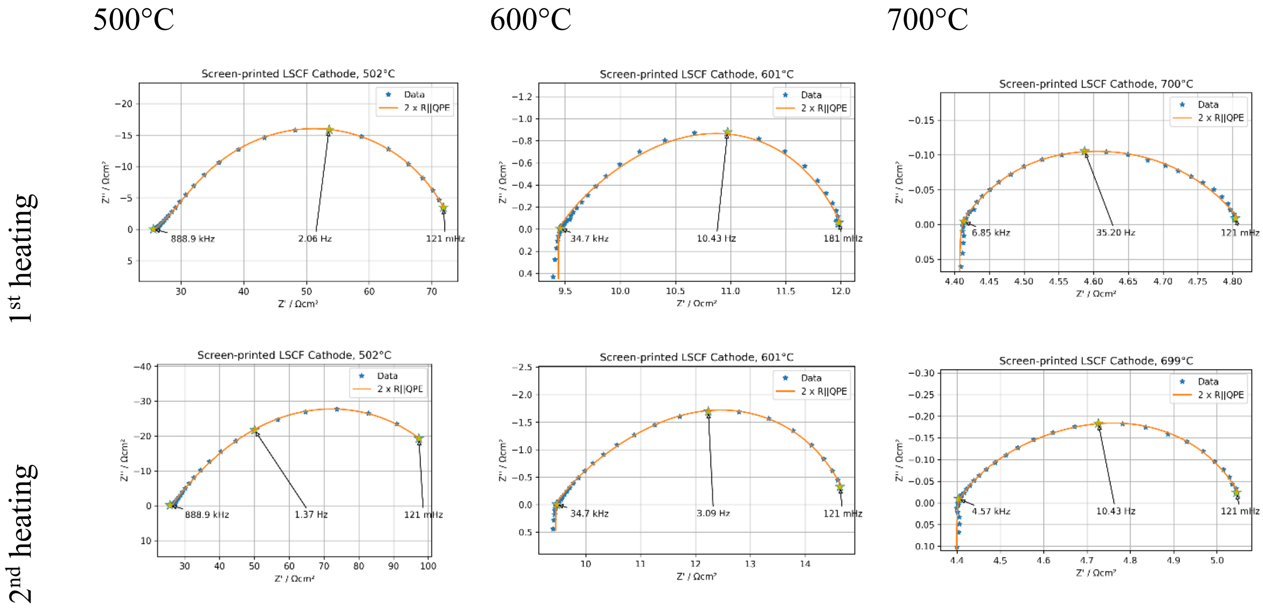

*Figure 134: Selected impedance spectra of the LSCF cathode, measured between 500°C and 700°C*

The impedance spectra bore a resemblance to a Gerischer impedance. However, the data was fitted more accurately by an equivalent circuit model with two R-CPE elements, which overlapped to fit the asymmetric shape of the impedance arc. Therefore, the calculated mean capacitances $C_{hi}$ and $C_{mid}$ (named according to the nomenclature from the last sections), were actually in the same order of magnitude, in the range between $10^{-3}$ and $10^{-1}$ F/cm², as Figure 135b) shows.

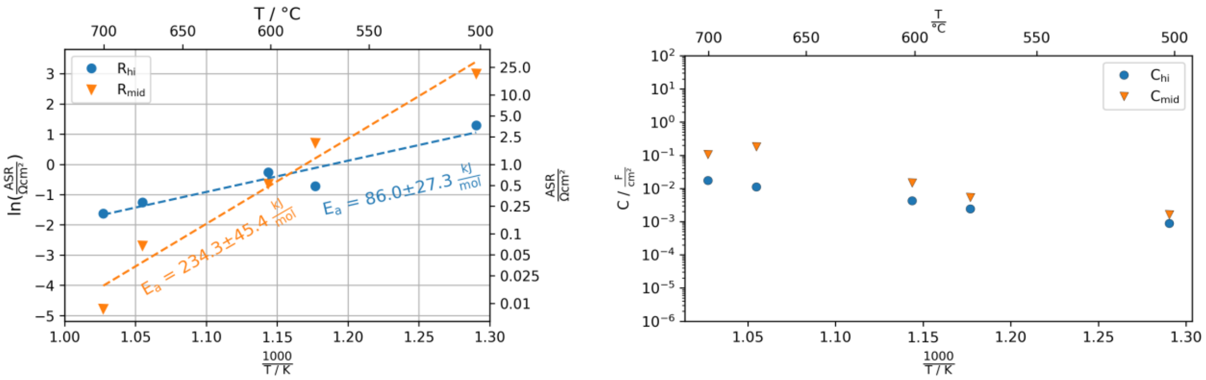

*Figure 135: a) Resistances and b) capacitances acquired from impedance spectroscopy as function of temperature*

The corresponding resistances $R_{hi}$ and $R_{mid}$ are plotted against the inverse temperature in Figure 135a). However, since they are covering the same impedance arc, it is more useful to sum both resistances. The sum can be defined as the polarization resistance $R_{pol}$ of the cathode. As Figure 136 shows, the temperature dependency of $R_{pol}$ is linear in the Arrhenius plot. The activation energy is around 150 kJ/mol. Figure 136 also shows that degradation occurred already in the temperature runs during short-term characterization. In the second heating cycle, the polarization resistance was already 1.5 to 2 times higher than in the first cycle.

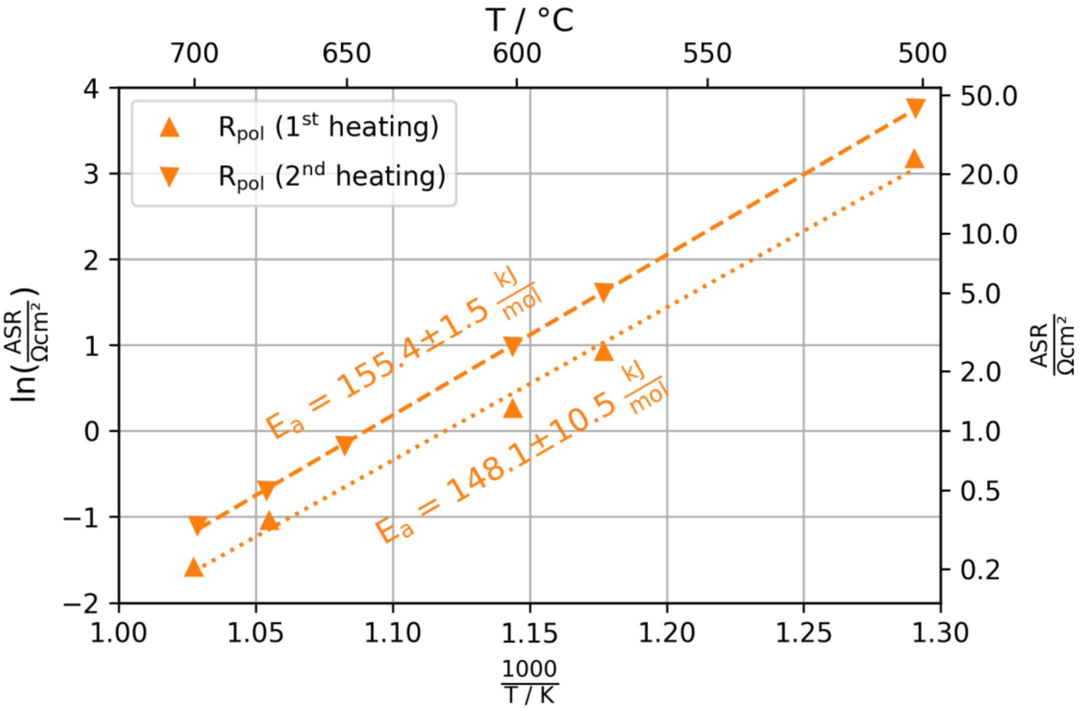

*Figure 136: Area-specific polarization resistance of the screen-printed LSCF cathode as function of temperature, measured in two heating cycles*

### 4.3.3.2 Long-term characterization

As described above, the long-term experiment was separated into two periods. In the first period, Cr contamination was the predominant degradation mechanism. The degradation caused a relatively strong increase of the polarization resistance. However, the impedance spectra could still be fitted by the equivalent circuit model with two R-CPE elements. Figure 137 shows selected impedance spectra of the first period.

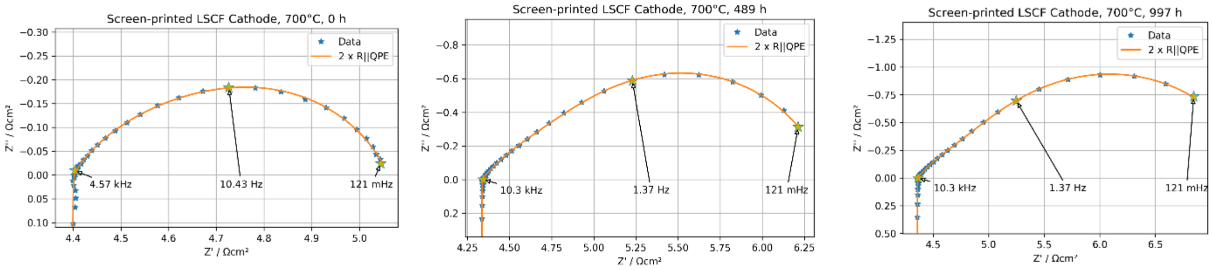

*Figure 137: Selected impedance spectra, measured in the first period of the long-term experiment (Cr-poisoning)*

After sputtering Si onto the cathode (second period), the impedance spectra changed their shape, so that adding a third R-CPE element to the fitting model became necessary in order to describe all features of the spectra by CNLS-fits. As Figure 138 shows, an additional semicircle gradually appeared at low frequencies.

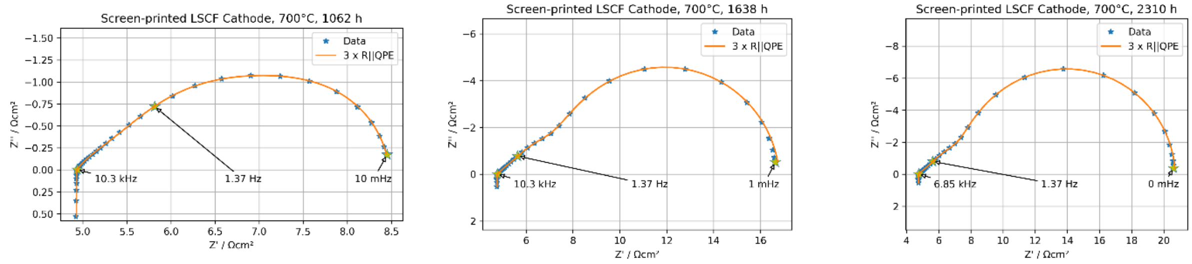

*Figure 138: Selected impedance spectra, measured in the second period of the long-term experiment (Cr- and Si-poisoning)*

Figure 139 shows the resistances $R_{hi}$, $R_{mid}$ and $R_{low}$ and the calculated corresponding capacitances. Again it should be noted that the three parameters were obtained from overlapping R-CPE elements which fit one arc in the impedance spectra.

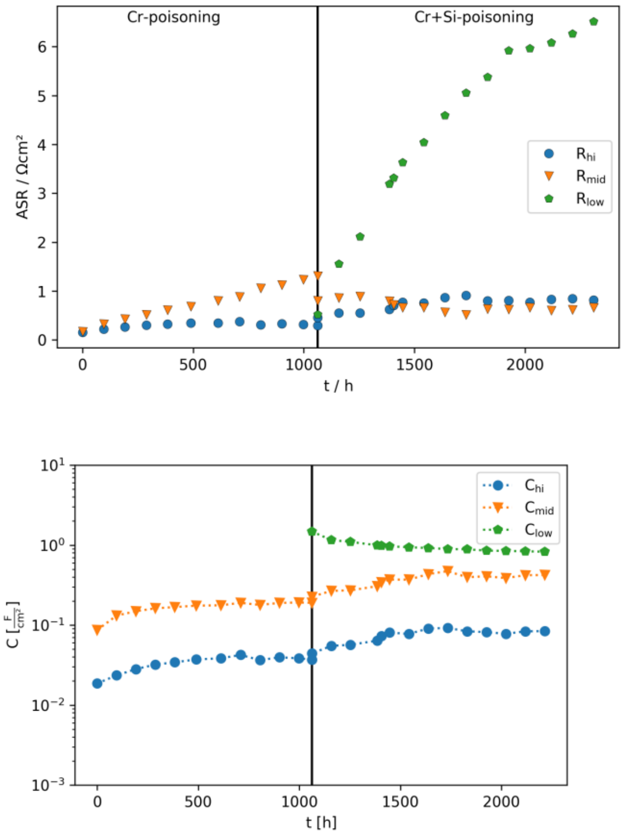

*Figure 139: a) Resistances and b) capacitances calculated from impedance spectra, as function of the elapsed time of the long-term experiment*

There are notable details in the time-dependent behavior of the three resistive parameters. While the high-frequency parameter $R_{hi}$ seems to be rather constant over time, degradation was especially pronounced at lower frequencies, as indicated by the increase in $R_{mid}$ and $R_{low}$. $R_{pol}$ was defined as the sum of all three parameters. In Figure 140, besides $R_{pol}$, also the high-frequency parameter is plotted again. From the time-dependent behavior of both resistances, it might be argued that $R_{hi}$ would represent the polarization resistance of the cathode if no contamination with Cr and Si would have taken place.

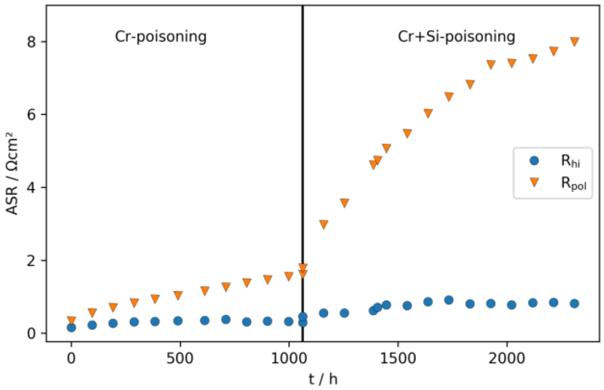

*Figure 140: Area-specific polarization resistance of the screen-printed LSCF cathode and the resistivity parameter at high frequencies as function of time*

In Figure 141, the polarization resistance is plotted with estimated degradation rates. The high degradation rates between 1 and 5 Ωcm² per 1000 hours underline the negative impact of Cr and Si on the cathode performance.

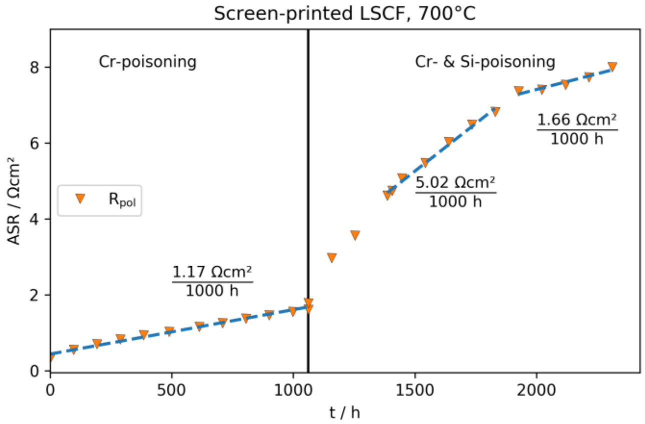

*Figure 141: Area-specific polarization resistance of the LSCF-cathode as function of time, estimated degradation rates (increase in ASR per 1000 h)*

#### 4.3.3.3 Post-test analyses

Analyses were performed with SEM and STEM on the cell after the long-term experiment. Additional SEM analyses were performed on a sample with LSCF layer, which represents the as-prepared state of the cell.

##### SEM of the surfaces and cross-sections

A fresh LSCF layer and the degraded cathode from the long-term experiment are shown in Figure 142. The images depict a homogeneous, porous microstructure. On the grain surfaces of the degraded sample nanoscale degradation phases are observed. These particles are formed by the reaction of LSCF with the sputtered silicon on the surface during the experiment.

Figure 143 shows a cross-sectional view of the degraded cell. The cathode layer is quite homogeneous in the cross-section. It was not possible to detect Si and Cr in the sample by EDX, probably because the total concentrations were below the detection limit.

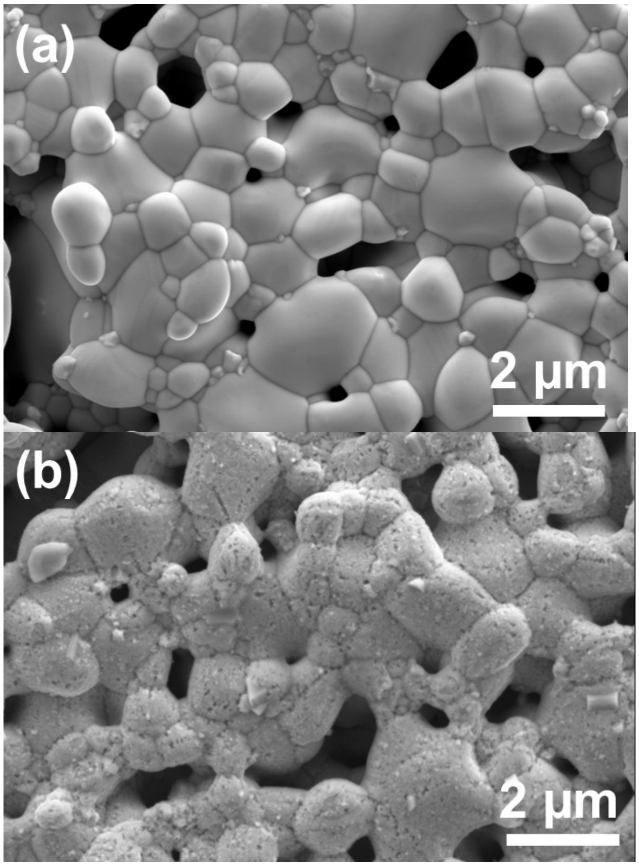

*Figure 142: SEM surface images of a) the fresh LSCF layer and b) the degraded LSCF cathode (from [157])*

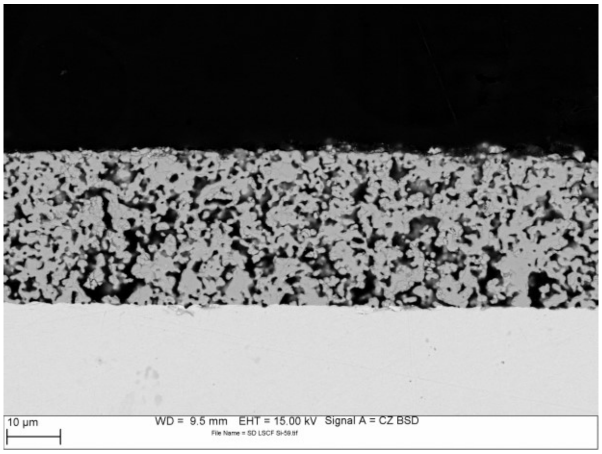

*Figure 143: SEM cross-sectional image of the degraded cathode*

### *STEM of the cross-sections*

A STEM sample was prepared from the near-surface region of the degraded cathode by FIB. Figure 144 shows the STEM-HAADF images of the sample. A silicate-layer was found on the top surface of the LSCF grains, as shown in Figure 144b).

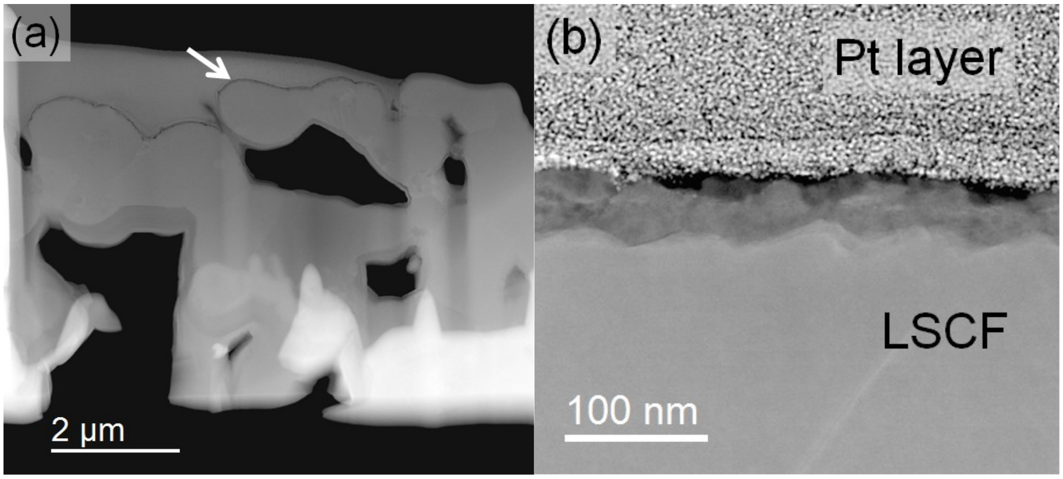

*Figure 144: a) STEM-HAADF survey image and b) zoom image of the cross-section of the degraded LSCF cathode at the surface (from [157])*

An elemental mapping analysis with EDX and EELS of the surface region provided further details on the chemical composition of the silicate-layer on the surface.

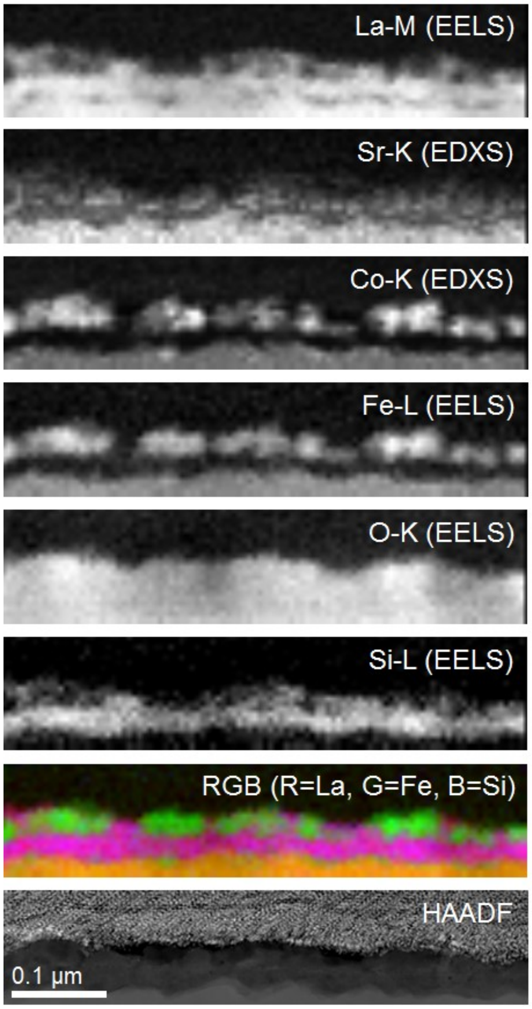

*Figure 145: STEM-HAADF image of the silicate-layer at the surface of the degraded LSCF cathode and EDX/EELS mapping analyses (from [157])*

As Figure 145 shows, Si occurs on the same areas with La, Sr and O, which indicates, that the surface layer consists of a lanthanum strontium silicate, $(La,Sr)_xSi_yO_z$. The silicate phase is electrically isolating and therefore blocks the oxygen surface exchange. On top of this silicate layer, Co, Fe and O are found in nanoscale grains. These elements precipitated from the bulk LSCF phase when it reacted with Si and probably formed a Co-Fe spinel phase.

## 4.4 Electrochemical properties and long-term stability of cathodes with different microstructures on YSZ electrolytes

In order to study degradation effects of the cathode-electrolyte interface, LSC64 cathodes with different microstructures were deposited directly on YSZ-substrates (without protective diffusion barrier layer). The electrochemical properties and the long-term stability of the cells were investigated by EIS. Figure 146 shows the cathode architectures, which were used for these experiments.

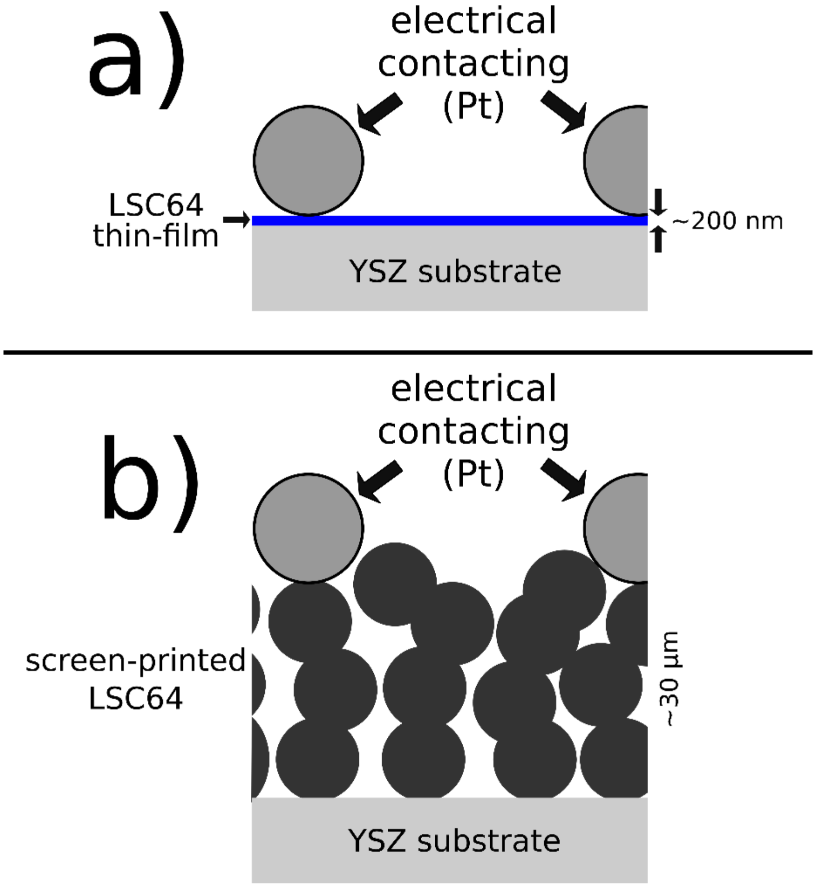

*Figure 146: Sketches of the cathode architectures characterized in the interface-degradation experiments: a) LSC64 thin-film, b) screen-printed LSC64*

### 4.4.1 Thin-film cathodes of LSC64 on YSZ

LSC64 thin-film cathodes on YSZ were characterized by EIS in the temperature range between 500°C and 700°C. Afterwards, long-term tests at 700°C and 800°C were performed, where impedance spectra were measured every 4 hours.

#### *4.4.1.1 Short-term characterization and temperature dependence*

Figure 147 shows impedance spectra of the cell measured at different temperatures. The spectra consist of asymmetric arcs which could be fitted well with an equivalent circuit model containing two or three R-CPE elements, which are slightly overlapping. At temperatures below 600°C, a dedicated high-frequency arc is found, which shifts to lower frequencies at higher temperatures.

At the low-frequency side there are some noisy data points, which were caused by temperature fluctuations during the impedance measurement. These points were neglected for fitting.

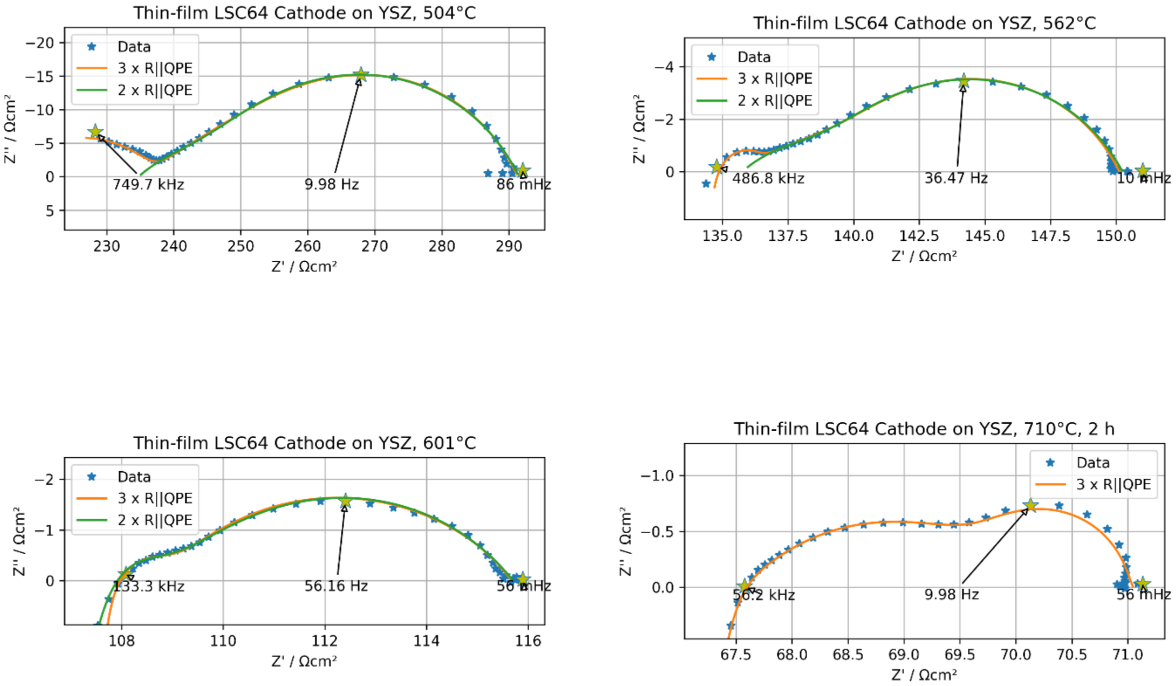

*Figure 147: Impedance spectra of the LSC64 thin-film cathode on YSZ measured at different temperatures*

Figure 148 shows the resistances and capacitances calculated from the fitting parameters of the R-CPE elements as a function of temperature in an Arrhenius plot. The capacitances are almost temperature independent. $C_{hi}$ is in the range of a double-layer capacitance, therefore $R_{hi}$ and $C_{hi}$ might be linked to the charge transport at the cathode-electrolyte-interface. $C_{mid}$ and $C_{low}$ are capacitances covering the oxygen reduction mechanism.

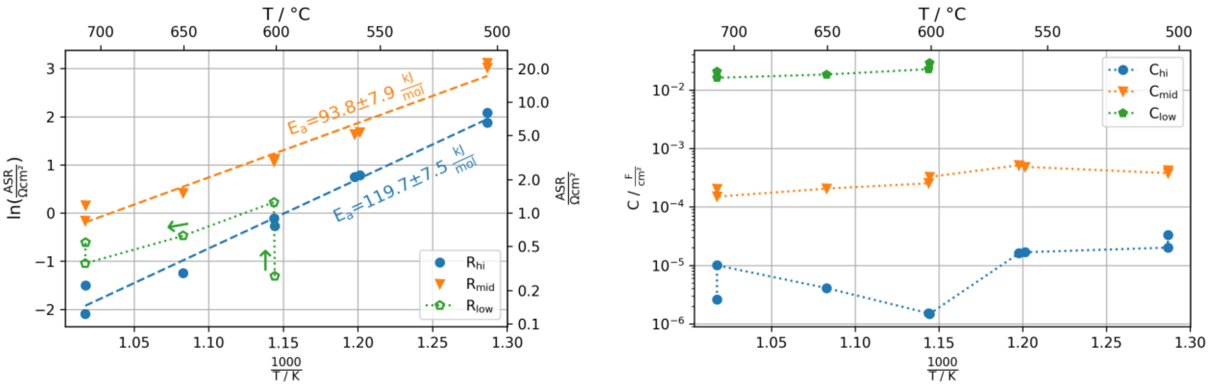

*Figure 148: Arrhenius-plots of resistances (left) and capacitances (right) calculated from the parameters of the CNLS-fits*

While the resistive parameters $R_{hi}$ and $R_{mid}$ follow an almost linear trend in the Arrhenius plot, $R_{low}$ shows a significant superimposed time-dependent evolution. The dotted line and the arrows in Figure 148 indicate the chronological order in which the measurements were performed. The steps found at 600°C and 700°C indicate that the sample already shows a relatively quick degradation at these temperatures.

Since the three parameters $R_{hi}$, $R_{mid}$ and $R_{low}$ originate from overlapping impedance arcs, the total polarization resistance $R_{pol}$ of the cathode was calculated by summarizing all three values. As Figure 149 shows, $R_{pol}$ follows a linear trend with an activation energy around 88 kJ/mol.

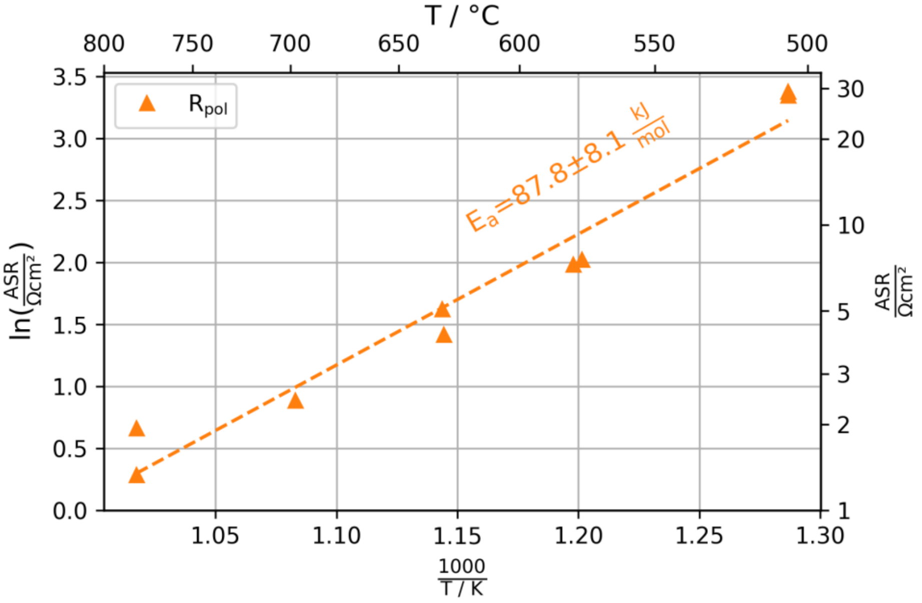

*Figure 149: Arrhenius plot of $R_{pol}$ as function of temperature*

### 4.4.1.2 Long-term characterization

After reaching 700°C, the sample was held at this temperature and impedance spectra were measured in intervals of 4 hours. Figure 150 and Figure 151 show selected impedance spectra from this series. The spectra could be fitted with the previously used model containing three R-CPE elements. However, fitting the data was challenging and the parameters obtained from the fits should be considered as estimations.

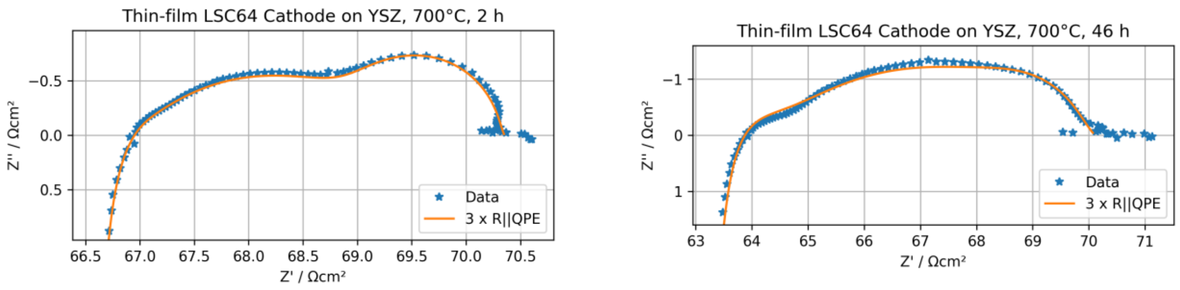

*Figure 150: Selected impedance spectra of the time run at 700°C*

It can be stated that the polarization resistance increased significantly within 46 hours. As the frequency-dependent plot in Figure 151b indicates, the degradation lead to an increase in the impedance especially at intermediate frequencies. The intermediate-frequency peak increased while the position of the peak maximum shifted from 1 kHz towards 100 Hz, and thus intersected with the low-frequency arc.

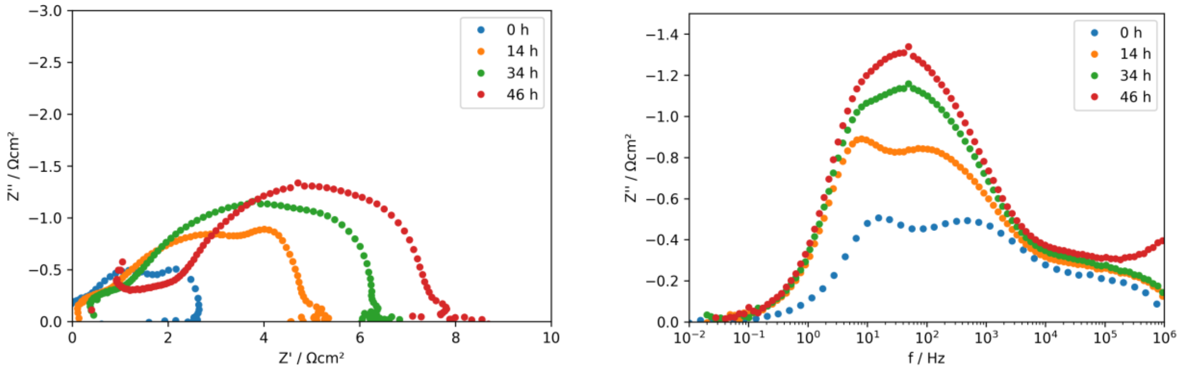

*Figure 151: Complex plane plot (left) and Bode-plot (right) of selected impedance spectra of the time run at 700°C; the ohmic resistance and inductivity were subtracted from the spectra*

Evaluation of the fitting parameters (Figure 152) showed that the capacitances were found in the same orders of magnitude as in the temperature-dependent measurements (see Figure 148). The capacitances remained almost constant. However, the high-frequency capacitance $C_{hi}$ was fluctuating, which is an indication that the fitting results were uncertain (especially at higher frequencies, where the inductivity has a gaining influence). The calculated resistances (Figure 152a) were fluctuating as well. Nevertheless, it is recognizable that $R_{hi}$ and $R_{low}$ remained almost constant, while the value of $R_{mid}$ approximately doubled. Therefore, the increase of $R_{mid}$ was the main driver for the degradation of the cathode polarization resistance $R_{pol}$, which was defined as the sum of the three resistance parameters and is plotted in Figure 153.

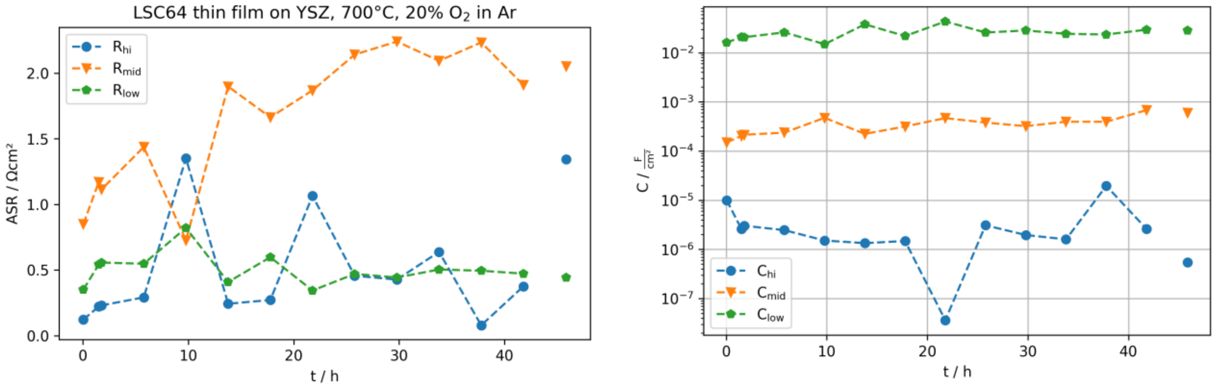

*Figure 152: Resistances (left) and capacitances (right) acquired at the time-run at 700°C as function of time*

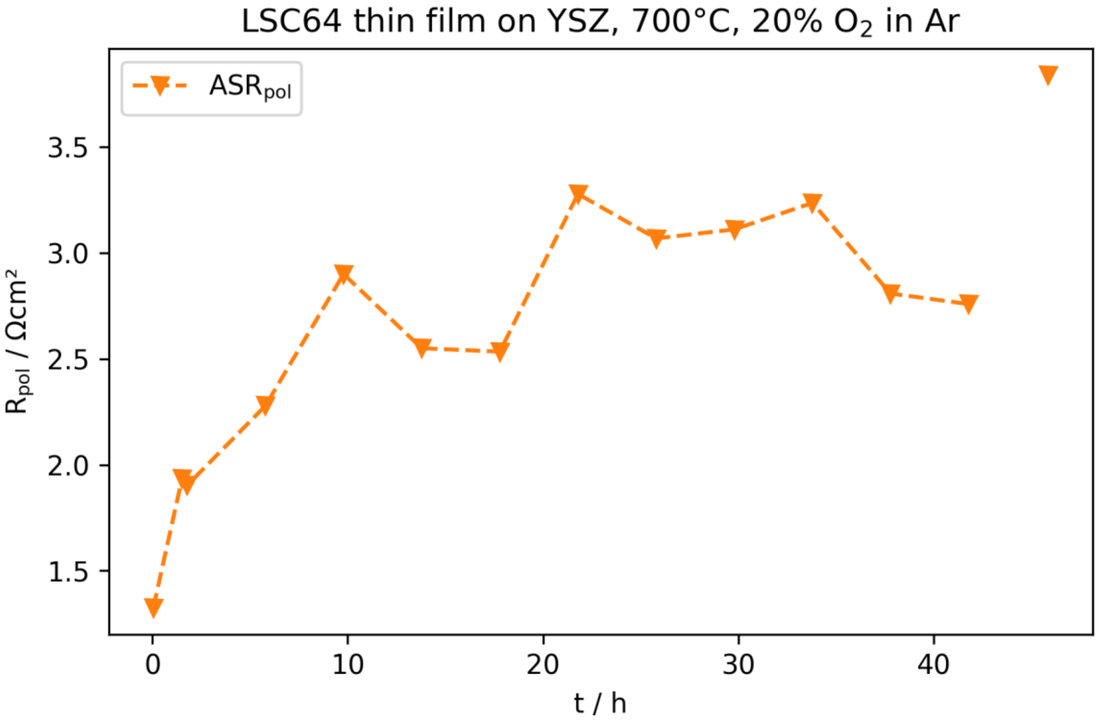

*Figure 153: $R_{pol}$ as function of time during the degradation experiment at 700°C*

Since the impedance spectra of this time-dependent experiment were difficult to interpret, the time run was stopped after 46 hours. To further investigate the degradation mechanisms at the cathode-electrolyte-interface, the experiment was adapted by changing the temperature to 800°C. It turned out that more precise data could be obtained at this temperature. Therefore, this second time-run experiment was performed for 1072 hours.

Figure 154 shows impedance spectra at selected times of the long-term experiment at 800°C. The spectra could be fitted well with three R-CPE elements. It is notable that the shape of the spectra changed significantly during the experiment due to degradation effects visible at different characteristic frequencies.

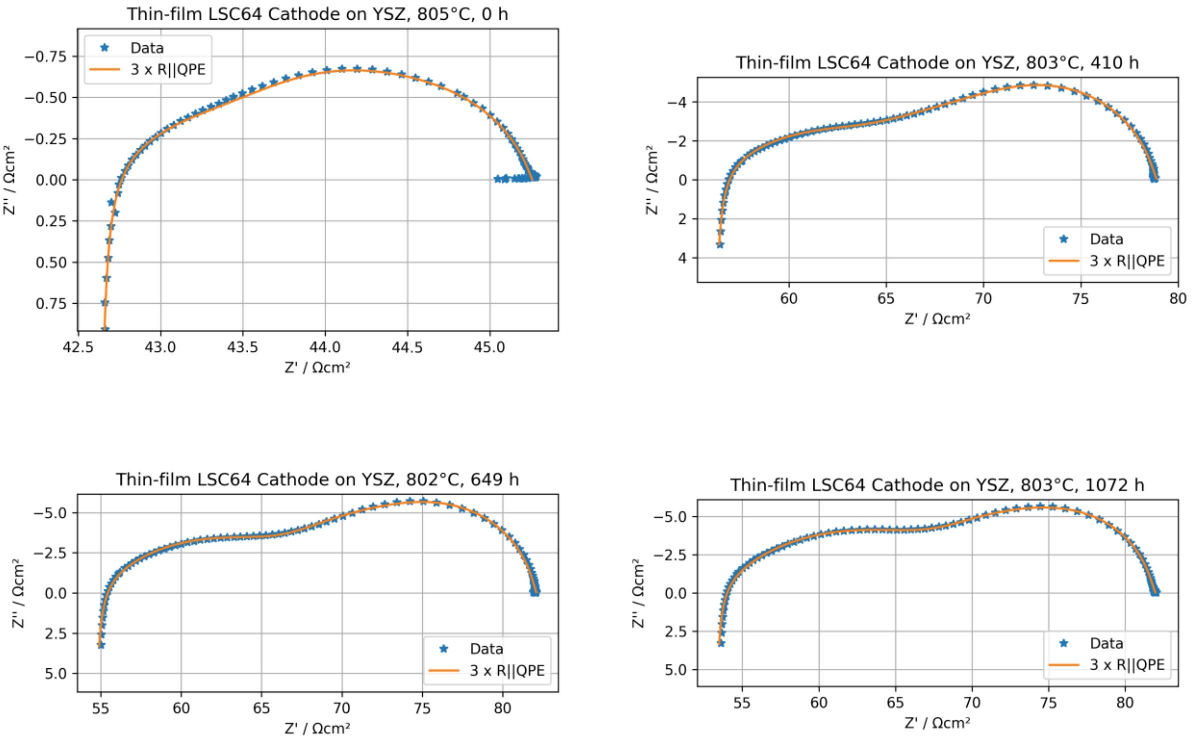

*Figure 154: Selected impedance spectra of the time run at 800°C with curves from the CNLS-fits*

The plots in Figure 155 give a more detailed view on the time-dependent evolution of the impedance spectra. Here, the spectra are depicted in a complex plane or Cole-Cole plot, where the ohmic resistance and the inductivity were subtracted from the raw data. In Figure 155b the same data is shown in a Bode plot with the imaginary part of the impedance over frequency. These figures indicate that the degradation is quite fast.

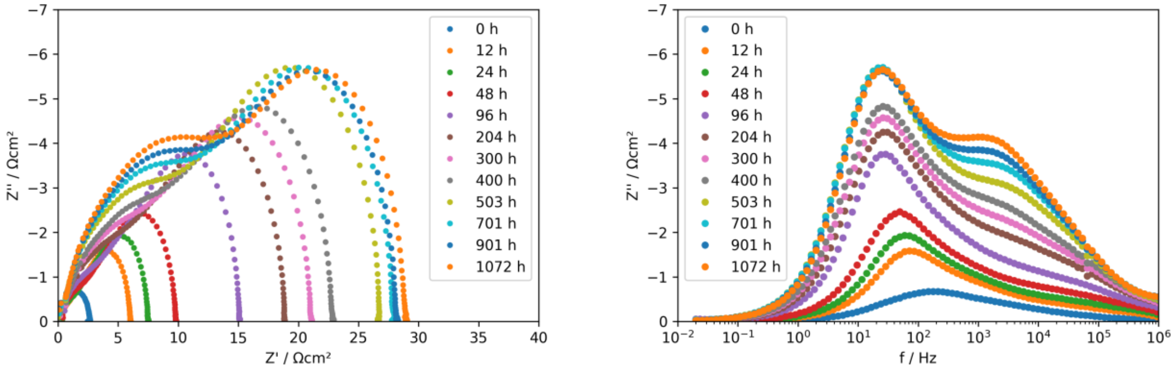

*Figure 155: Cole-Cole plot (left) and Bode plot (right) of selected impedance spectra of the long-term experiment at 800°C; the ohmic resistance and the inductivity were subtracted from the data.*

Figure 155 also shows in detail, at which frequencies the degradation took place. During the first 100 hours, the peak in the range between 100 Hz and 1 kHz grew and the peak shifted towards lower frequencies. Afterwards, a second peak grew at frequencies of a few kHz, causing a further increase of the impedance.

This time-dependent behavior can be clearly seen in the fitted parameters and the calculated capacitances and resistances. As Figure 156 shows, the capacitance at high frequencies $C_{hi}$ is in the range between $10^{-6}$ and $10^{-5}$ F/cm², which is typical for double-layer capacitances. Therefore, $R_{hi}$ is assumed to represent the resistance of the cathode-electrolyte-interface. $C_{mid}$ and $C_{low}$ are found between $10^{-4}$ and $10^{-3}$ F/cm² and cover rate-limiting steps of the oxygen reduction reaction of the cathode. All the capacitances remained relatively constant over time, which indicates that the corresponding mechanisms were the same over the whole experiment.

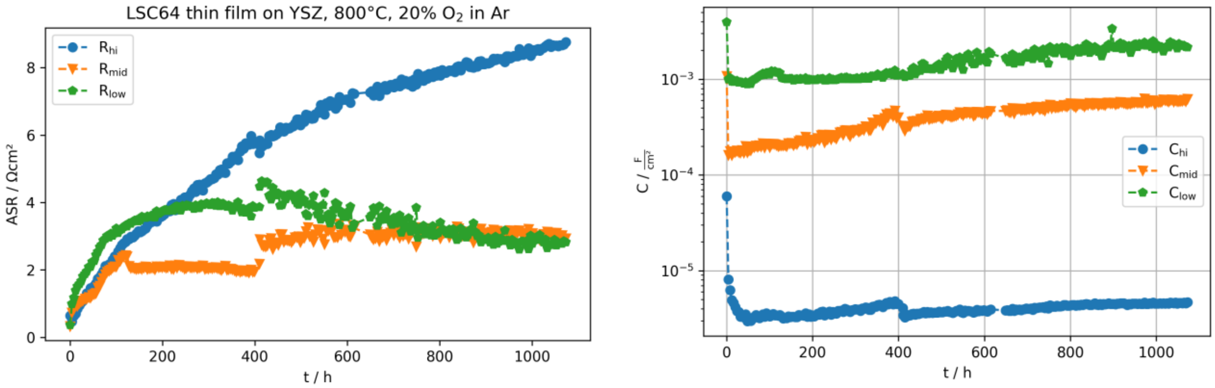

*Figure 156: Resistances (left) and capacitances (right) from the fitting parameters as function of time*

The resistances in Figure 156 (left) show different trends over time: $R_{mid}$ and $R_{low}$ increased fast in the first 100 hours, afterwards they remained almost constant over time. $R_{low}$ even seemed to decrease slightly, however this might be an artifact of the CNLS-fit. In contrast, $R_{hi}$ showed a degressive increase during the whole experiment. This behavior is quite plausible if we assume that $R_{mid}$ and $R_{low}$ are resistances of the cathode oxygen reduction reaction and $R_{hi}$ is the interfacial resistance. As discussed in section 2.2.4.4 on page 18, the direct contact of LSC64 with YSZ leads to a reaction and formation of secondary phases at the interface which involves interdiffusion of the respective cations. Over time, an electrically insulating layer of zirconate phases (e.g. $La_2Zr_2O_7$ or $SrZrO_3$) is formed, causing an increasing interfacial resistance. By post-test analyses of the degraded cell and a reference sample which represents the state after preparation, these assumptions could be confirmed and examined in more detail. These results will be presented in section 4.4.1.3.

The polarization resistance of the thin-film cathode was defined by summing up $R_{hi}$, $R_{mid}$ and $R_{low}$. Its time-dependent behavior is plotted in Figure 157. The polarization resistance grew degressively and reached a plateau after about 600 hours. This plateau is an indication that the degradation effects of the thin-film cathode, which had a thickness of only 100-200 nm, had reached a state close to equilibrium at the end of the experiment.

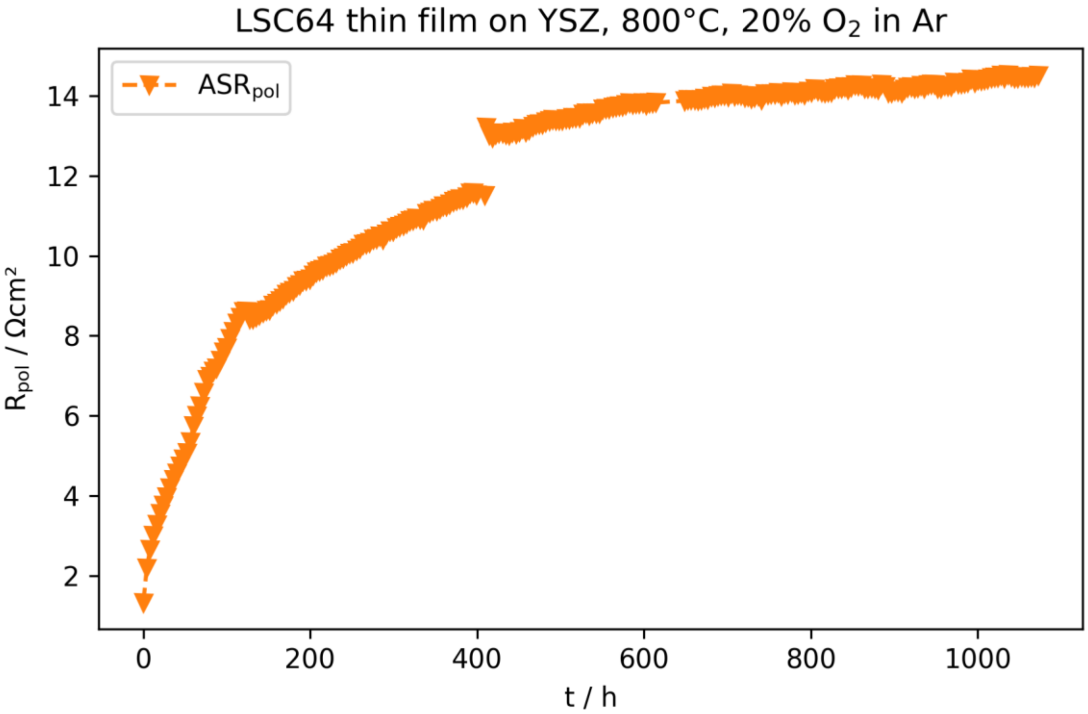

*Figure 157: $R_{pol}$ of the LSC64 thin-film cathode on YSZ as function of time*

### 4.4.1.3 Post-test analyses

The degraded symmetric cell was investigated in post-test analyses after finishing the long-term experiments. To compare the degraded cathode layer with the original state after preparation, a sample with an LSC64 thin-film on one side was prepared with the same parameters as that on the symmetric cell. These samples were characterized by SEM on the surface and at the cross-section as well as by STEM.

*Table 11: Overview over the analyzed samples*

| | Fresh LSC64 on YSZ | Degraded LSC64 on YSZ |
|---|---|---|
| SEM surface | ✓ | ✓ |
| SEM cross-section | ✓ | ✓ |
| STEM cross-section | | ✓ |

### *SEM of the surfaces*

Figure 158 shows the surfaces of the fresh and degraded sample in overview images. The thin-films on both samples show the typical wave-like surface structure but generally seem to be quite homogenous.

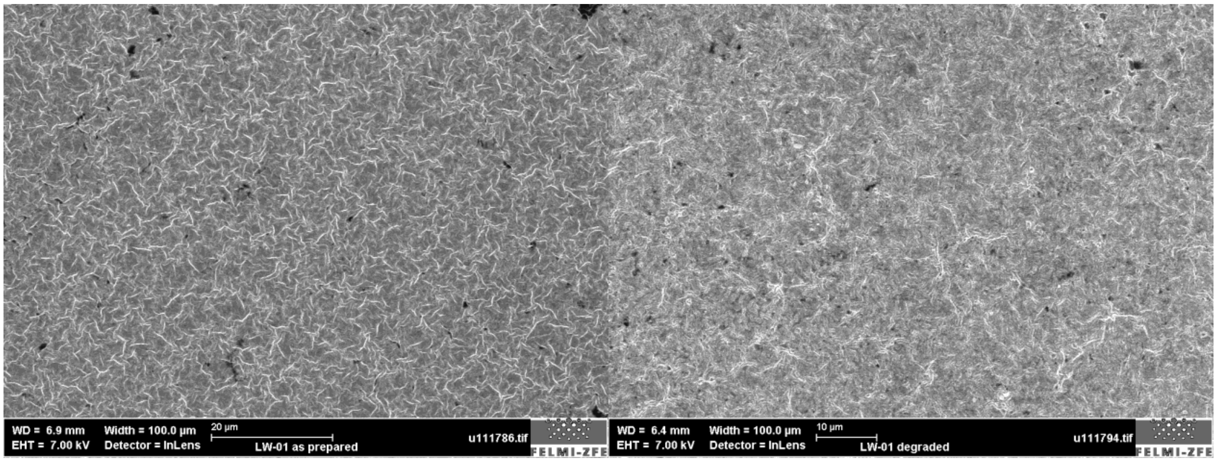

*Figure 158: SEM-SE overview images of the fresh thin-film sample (left) and the degraded thin-film cathode (right)*

In higher magnification, morphological differences between the fresh and the degraded samples become apparent. As Figure 159 shows, the degraded cathode exhibits significantly bigger grains and the grain size distribution is more inhomogeneous.

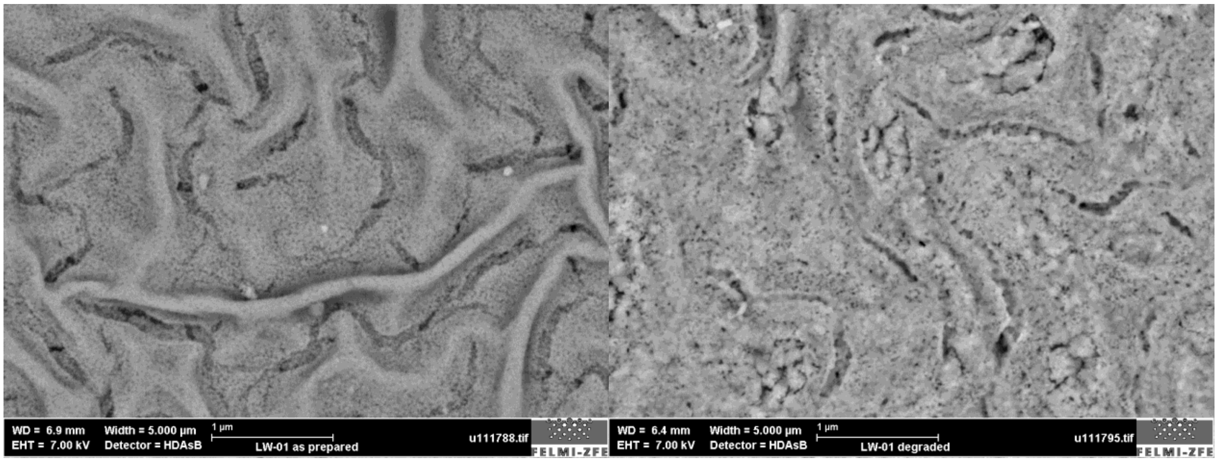

*Figure 159: SEM-BSE images of the fresh thin-film sample (left) and the degraded thin-film cathode (right)*

Figure 160 shows further differences on the sub-µm scale. The grains of the degraded sample are sharp-edged and facetted, while those of the fresh sample are more globular.

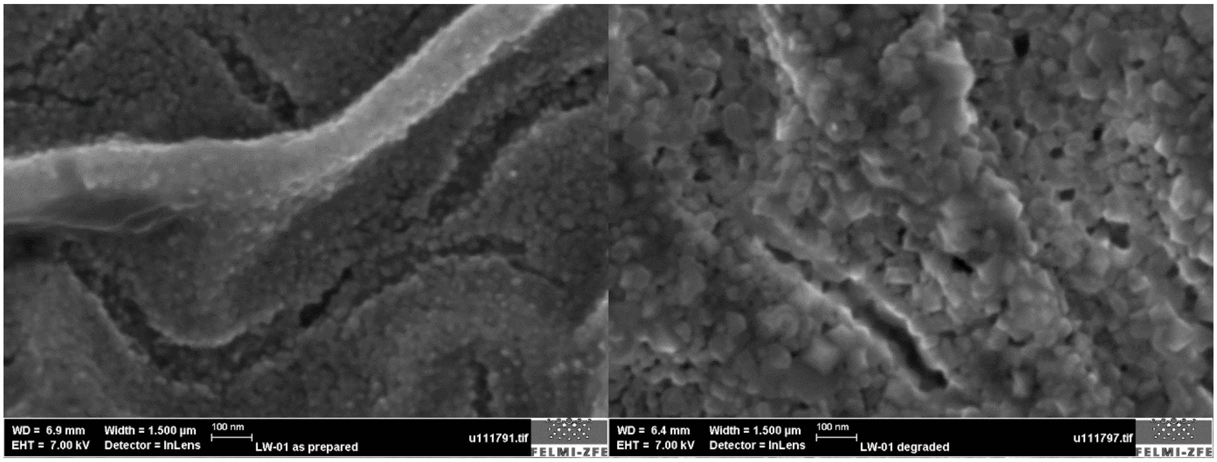

*Figure 160: SEM-SE images of the fresh thin-film sample (left) and the degraded thin-film cathode (right)*

### *SEM of the cross-sections*

Additional SEM images were acquired on cross-sectional samples which were prepared by ion sputtering. Figure 161 depicts the cross-sectional images of the fresh cathode and the layer on the degraded cell. These images show again the already known double-layer structure of the spin-coated thin-films, as well as the uneven wave-like structure of the upper layer, which is also evident in the surface images.

The comparison of the two samples also reveals differences in the morphology and the grain size distribution. Holding and characterizing the cell at 800°C for over 1000 hours caused grain coarsening and also a growth of the pores. This seemed to be the case especially for the porous region in between the two spin-coated layers, since are large gaps were found between the top and bottom layer of the degraded thin-film, which are not present in the fresh state. These gaps, which seemed to manifest at positions of wave hills of the top layer, probably also had an influence on the degradation of the impedance, since it can be assumed that they reduce electrical contact. In contrast to the double-layer interface, no relevant morphological changes could be found at the interface between the bottom layer and the substrate.

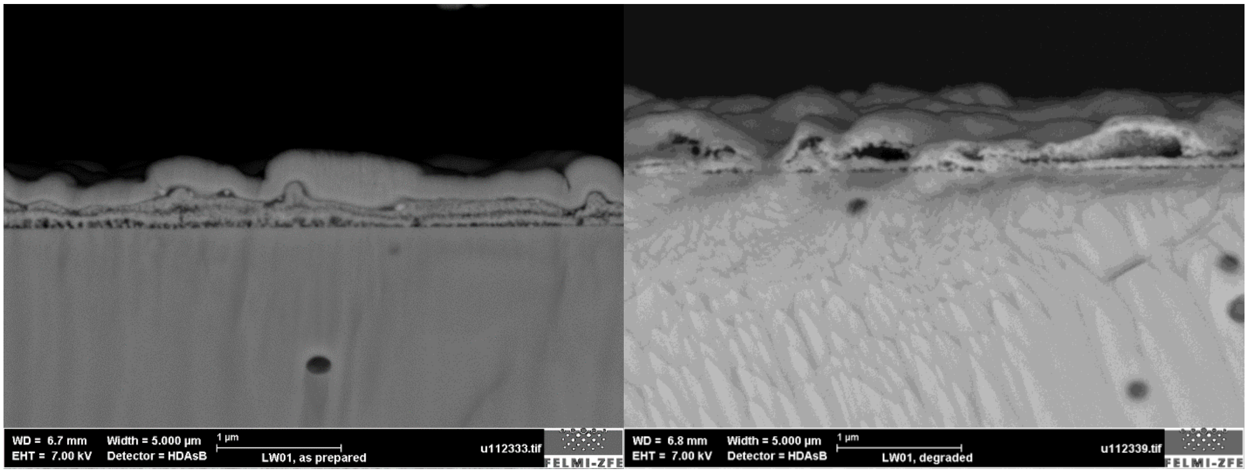

*Figure 161: Cross-sectional SEM images of the fresh thin-film (left) and the degraded thin-film cathode (right)*

EDX analyses were performed on selected positions of the fresh and degraded samples. Figure 162 and Figure 163 show the results of these analyses for the fresh and the degraded state, respectively.

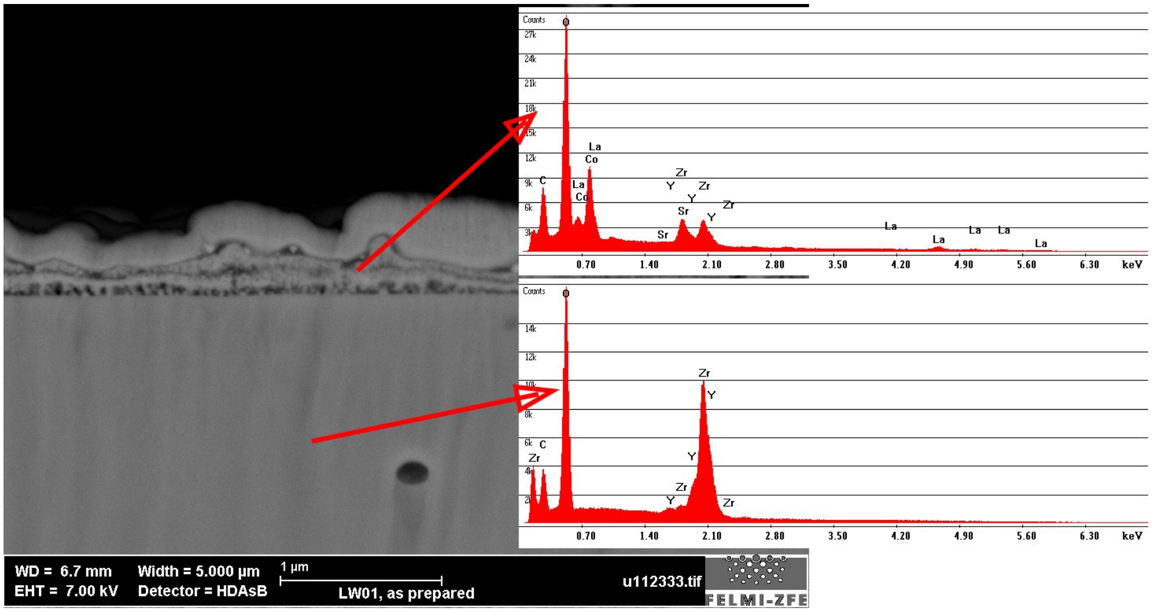

*Figure 162: SEM-BSE cross-sectional image and EDX analyses on selected positions of the fresh LSC64 thin-film and the YSZ electrolyte*

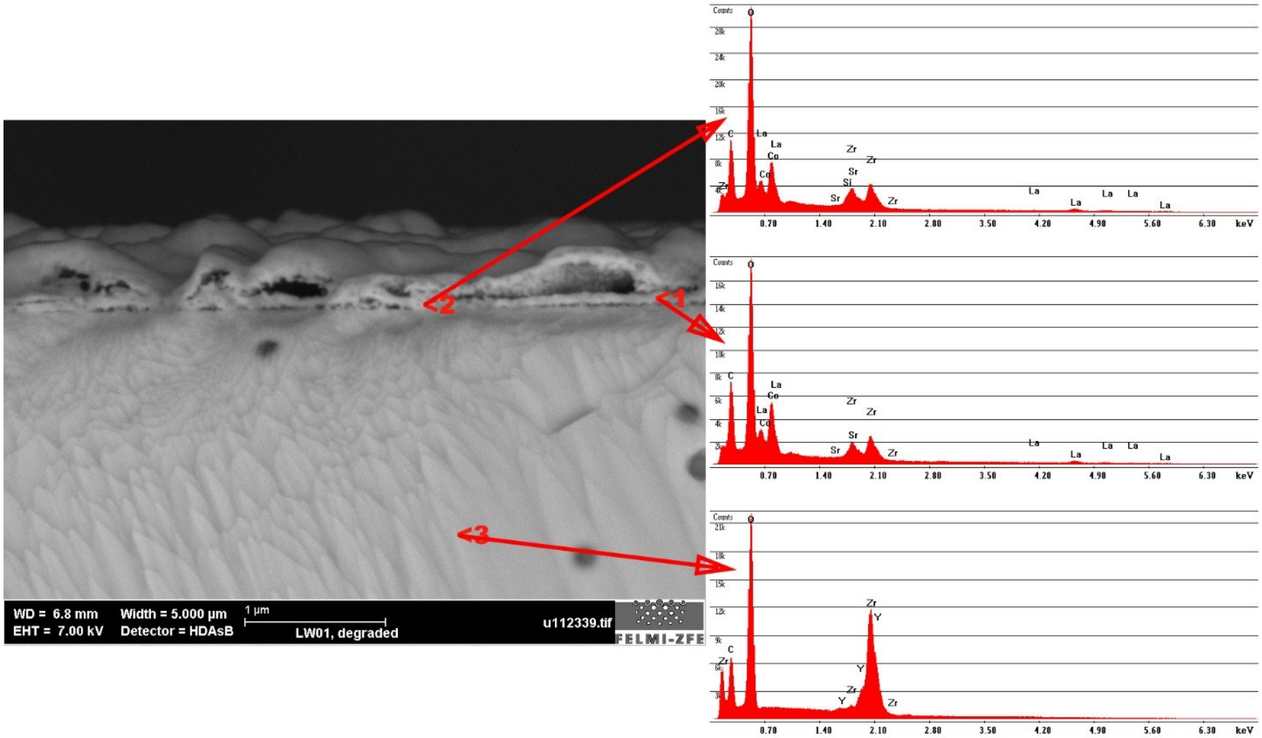

*Figure 163: SEM-BSE cross-sectional image and EDX analyses on selected positions of the degraded LSC64 thin-film and the YSZ electrolyte*

As expected, local EDX analyses showed the elements Zr, Y and O in the YSZ electrolyte substrates, and La, Sr, Co and O in whereas in the cathodes. Due to the relatively large excitation volume of the electron beam, signals of Zr and Y were detected as well in the LSC64 thin-films.

One notable finding was a possible detection of Si at a position near the cathode-electrolyte-interface of the degraded sample, marked in Figure 163 as position 2, which might be a local impurity of the YSZ substrate. According to the specification from the manufacturer, the YSZ powder from which the substrates were produced, contained small amounts of Si, which could be detected especially in precipitates of the YSZ electrolyte (examples for this finding will be shown in section 4.4.2.3, Figure 183 on page 182). However, Si was found only on a few local positions and therefore might not have a significant influence on the degradation. Apart from this, no clear evidence for interdiffusion of cations from the electrolyte and the cathode at the interface could be found, which is probably due to the limited lateral resolution of SEM-EDX analysis.

As a general conclusion of the SEM analyses of the surfaces and the cross-sections it can be said that the thin-film LSC64 cathodes have undergone significant morphological changes during the long-term experiment at 800°C, namely grain growth together with the formation of larger voids out of initially porous zones. However, STEM analyses of the degraded sample provided additional information on chemical degradation effects, which will be presented in the following subsection.

#### *STEM of the cross-sections*

From the degraded sample, a TEM lamella was prepared, which included the LSC64 thin-film as well as the YSZ substrate, to further investigate structural and chemical causes of the degradation.

Figure 164 shows a STEM-HAADF overview image of the sample. It depicts once more the double-layer structure of the thin-film on the YSZ substrate. The bottom layer covers the YSZ substrate well, but the interface is quite porous. The upper layer is more uneven and shows again the wave structures which have also been found in the surface- and cross-sectional images. At positions of wave hills, there are larger gaps between the two layers. In some cases, these gaps had been filled by Pt during the preparation of the TEM lamella, in other cases they remained empty.

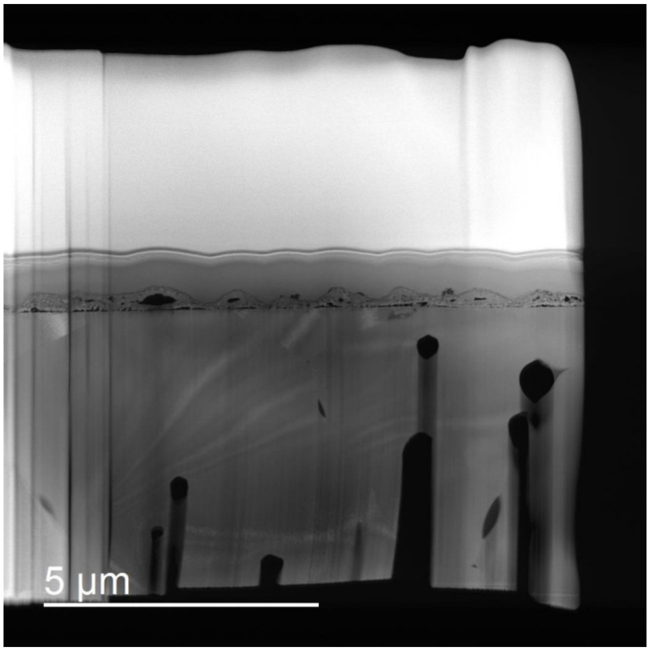

*Figure 164: STEM-HAADF overview image of the degraded sample with the LSC64 thin-film cathode and the YSZ electrolyte substrate*

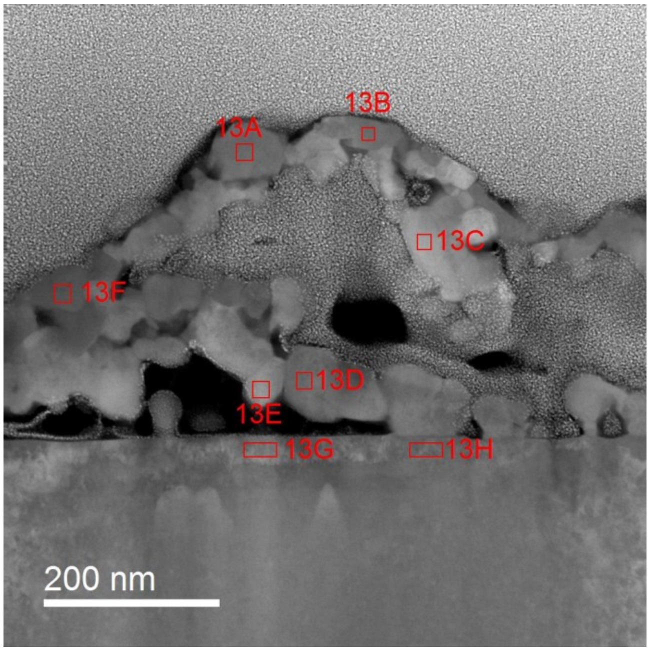

*Figure 165: STEM-HAADF cross-sectional image of the degraded LSC64 thin-film cathode on YSZ; EDX- and EELS-analyses performed at the marked positions are shown in Figure 166 and Figure 167*

Figure 165 shows a detailed view of the sample in higher magnification. The layers are formed by grains with a diameter of 50-100 nm. The different greyscales of the grains indicate variations in the chemical composition (Z-contrast).

To check whether concentration inhomogeneities occur, individual grains of the thin-film, which are marked in Figure 165 (positions 13A-13E), were analyzed by EDX and EELS. The results are shown in Figure 166. The analyses revealed that the chemical composition is quite heterogeneous. There are individual grains with a high amount of Co, while others exhibit a higher amount of La and Sr. One notable finding was the occurrence of significant amounts of manganese on the cathode layer. This could be confirmed by EDX as well as by EELS. This is a contamination which was most likely brought into the cathode during the long-term experiment. For electrochemical characterization, the samples were contacted by Pt-meshes, which were pressed on the cathode layers by spring force. Prior to the current experiment, a cell with a cathode of $La_xSr_{1-x}MnO_{3-\delta}$ (LSM) was characterized in the same experimental reactor. Since the Pt-meshes were neither replaced nor thoroughly cleaned between the two experiments, traces of LSM probably remained on the meshes causing this contamination. Due to the low thickness of the LSC64 cathode in the current experiment, the amount of these impurities was enough to deposit detectable amounts of Mn.

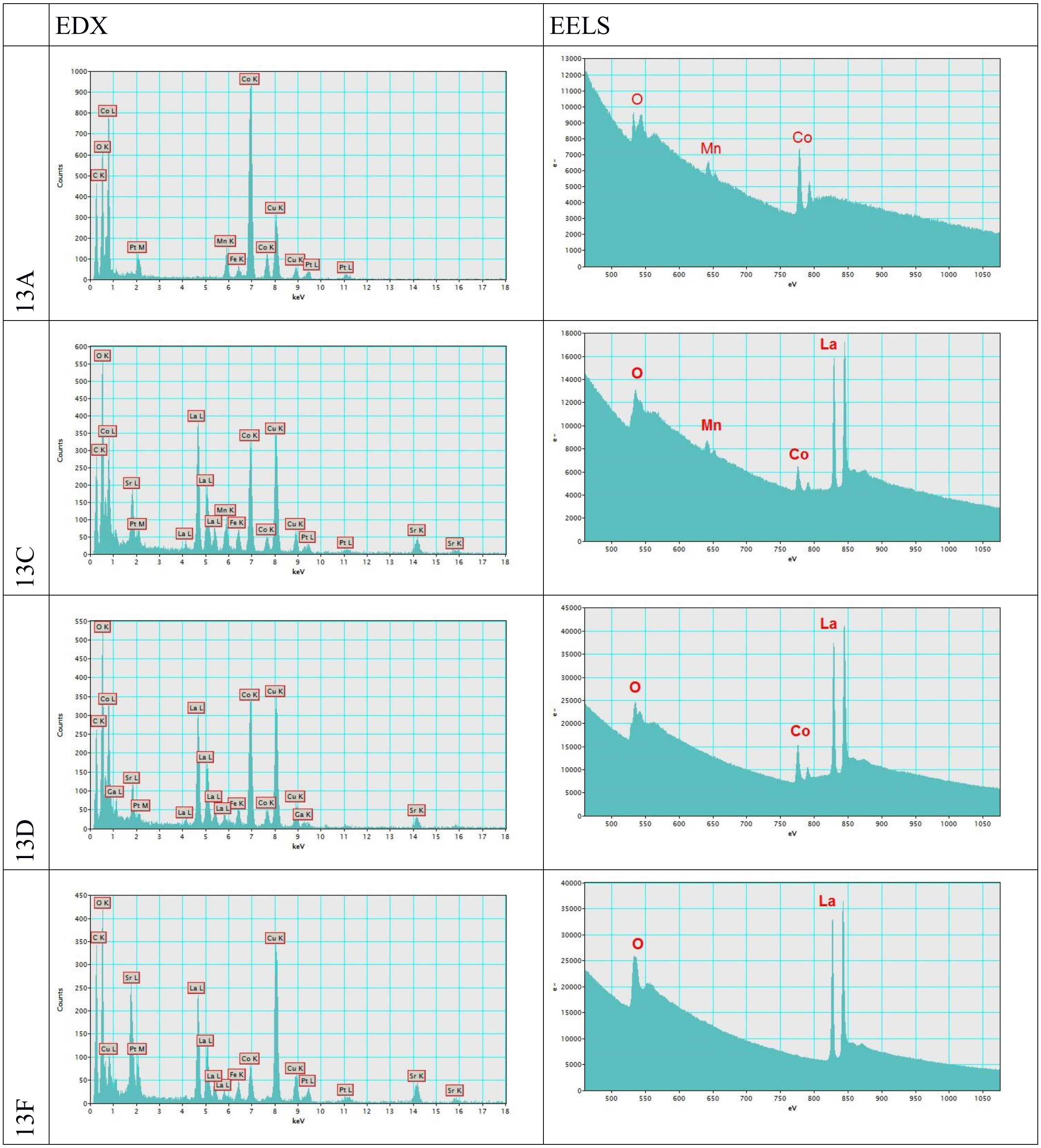

*Figure 166: EDX and EELS spectra acquired from selected positions of the LSC64 thin-film (see Figure 165 for position markers)*

Further localized analyses were performed in the YSZ substrate in a region close to the cathode-electrolyte-interface. A thin zone underneath the interface shows a different shade of grey indicating the formation of a secondary phase. EDX and EELS analyses were performed at two positions in this region, marked as 13F and 13G in Figure 165. The spectra show that these zones are composed mostly of Zr and Y, but also contain small amounts of La and Co.

| | EDX | EELS |
|---|---|---|
| 13G | 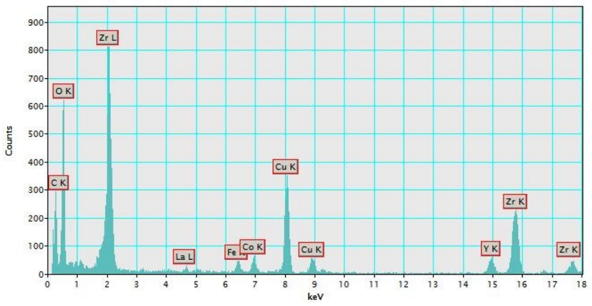 | 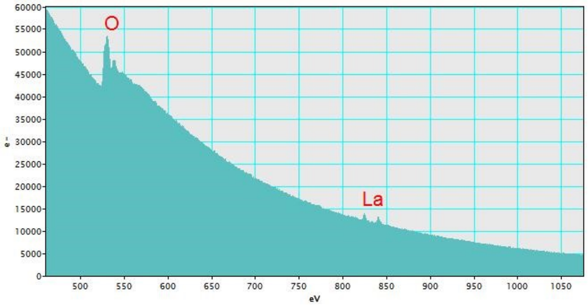 |
| 13H | | 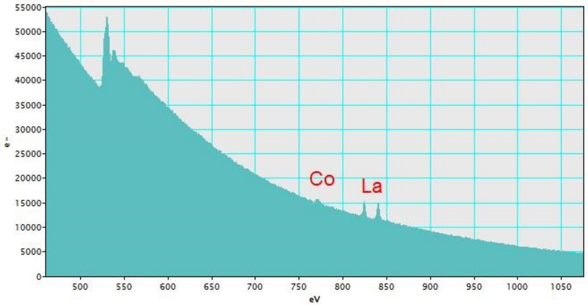 |

*Figure 167: EDX and EELS analyses at selected positions of the YSZ substrate near the interface to the cathode (see position markers in Figure 165)*

The sample was analyzed at another position, which is shown in Figure 168. In this image, the gap between the two LSC64 layers is filled with Pt, which stems from the TEM sample preparation. The reaction layer at the cathode-electrolyte-interface is well visible and could be estimated to a thickness between 50 and 55 nm. EDX and EELS analyses were performed in the YSZ-electrolyte (positions 15A and 15B) as well as in the LSC64 cathode layers (positions 15C and 15D).

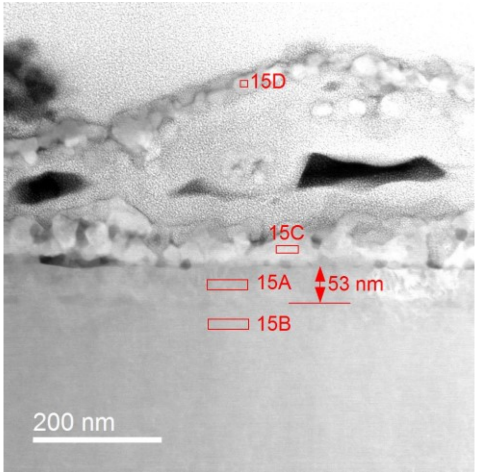

*Figure 168: STEM-HAADF cross-sectional image of the degraded LSC64 thin-film cathode on the YSZ elelctrolyte; EDX- and EELS-analyses performed at the marked positions are shown in Figure 169 and Figure 170*

EDX and EELS spectra of the LSC64 thin-film are given in Figure 169. In the top layer (Position 15D), Mn is found once more, but not at the bottom layer (position 15 C). This is in agreement with the explanation that Mn was brought onto the surface of the sample by direct contact with impurities in the electrode contact.

| | EDX | EELS |
|---|---|---|
| 15C | 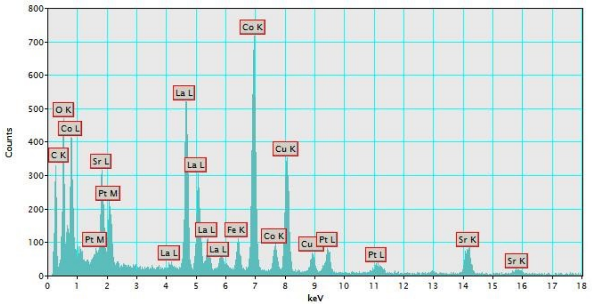 | 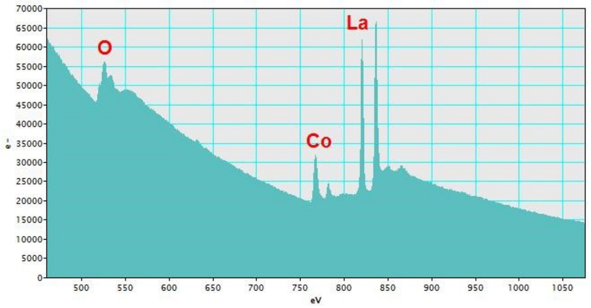 |
| 15D | 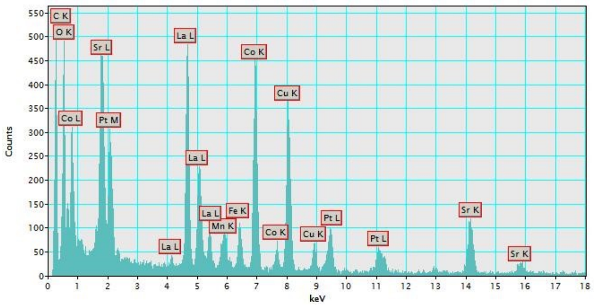 | 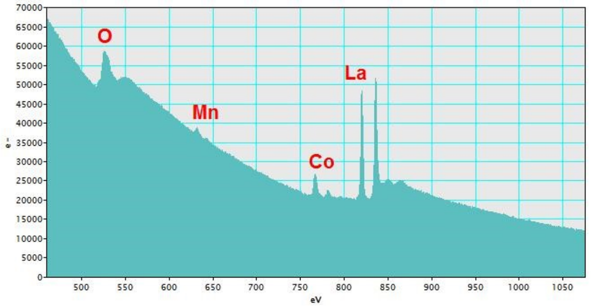 |

*Figure 169: EDX and EELS analyses at selected positions of the LSC64 thin-film of the degraded sample (see position markers in Figure 168)*

Figure 170 compares the acquired spectra from the interfacial layer and from a deeper position in the electrolyte. According to these results, La and Co are found in the YSZ substrate close to the interface, probably forming a secondary phase (zirconate).

| | EDX | EELS |
|---|---|---|
| 15A | 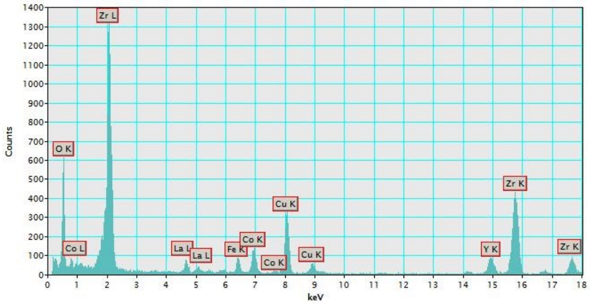 | 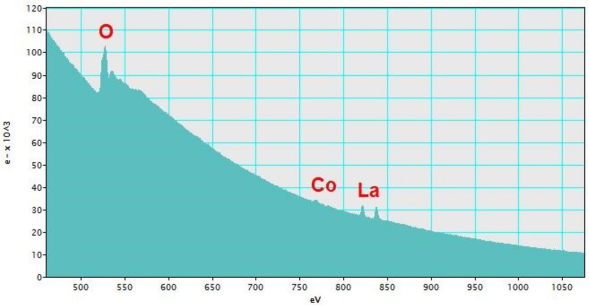 |
| 15B | 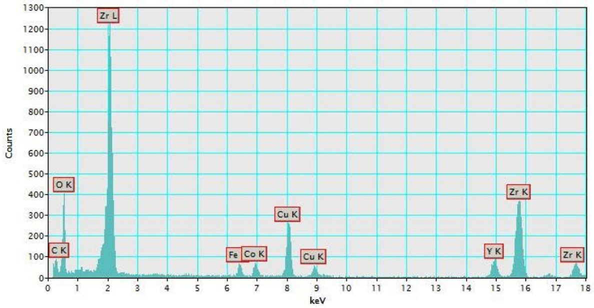 | 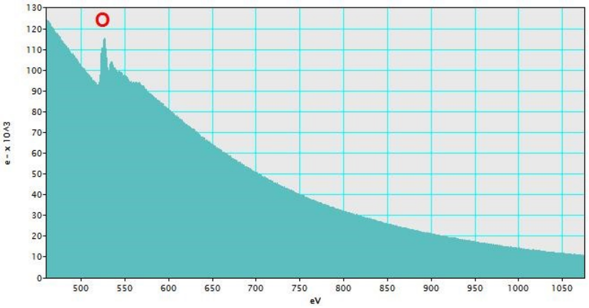 |

*Figure 170: EDX and EELS analyses at selected positions of the YSZ substrate of the degraded sample (see position markers in Figure 168)*

To investigate the concentration of La as a function of the vertical position in the substrate in more detail, a line scan analysis with EELS was performed at the interface between cathode and electrolyte. In this analysis, the intensity of the La peaks in the EELS spectrum was measured as function of distance along the interface. According to the results shown in Figure 171, La is found in the YSZ electrolyte within a 50 nm thick layer at the interface, where its concentration remains constant. At the bottom border of this layer, the La concentration immediately drops to zero. This behavior can be explained by a secondary phase, which was formed in this interfacial region during the degradation experiment. This secondary phase may be a pyrochlore-type zirconate, for instance $La_2Zr_2O_7$ (see section 2.2.4.4 on page 18).

It is assumed that this reaction layer at the cathode-electrolyte-interface is the main reason for the cell degradation which was observed in the EIS measurements. However, it is unclear whether the phase is actually $La_2Zr_2O_7$. According to several studies found in literature, only $SrZrO_3$ is formed in direct contact of LSC/LSCF and YSZ at temperatures below 1000°C, while $La_2Zr_2O_7$

is only formed at higher temperatures [44, 45, 122, 126]. Worth mentioning here, is a study by Dieterle et al., who investigated the stability of thin-films of $La_{0.5}Sr_{0.5}CoO_{3-\delta}$ on YSZ substrates at 700°C and 1000°C [122]. They found only $SrZrO_3$ as secondary phase at the interface, but no $La_2Zr_2O_7$. According to thermodynamic calculations in this work, the pyrochloric phase $La_2Zr_2O_7$ is not formed at 800°C in ambient air. Another questionable finding are the traces of Co, which were found in the interlayer, according to the analyses in Figure 167 and Figure 170. This could be an indication for a solid solution of Co in the pyrochloric phase. However, such a solid solution has not been reported in literature to the knowledge of the author.

Due to its low thickness at the cathode-electrolyte-interface, a more detailed analysis of the reaction layer is a quite challenging task. Another analysis of the fresh and degraded sample has been performed by XRD, however no indication for a secondary phase was found there due to its low volume percentage. Further information about this layer could be gained by XPS depth-profiling analyses, which however have not been performed in the scope of the present work.

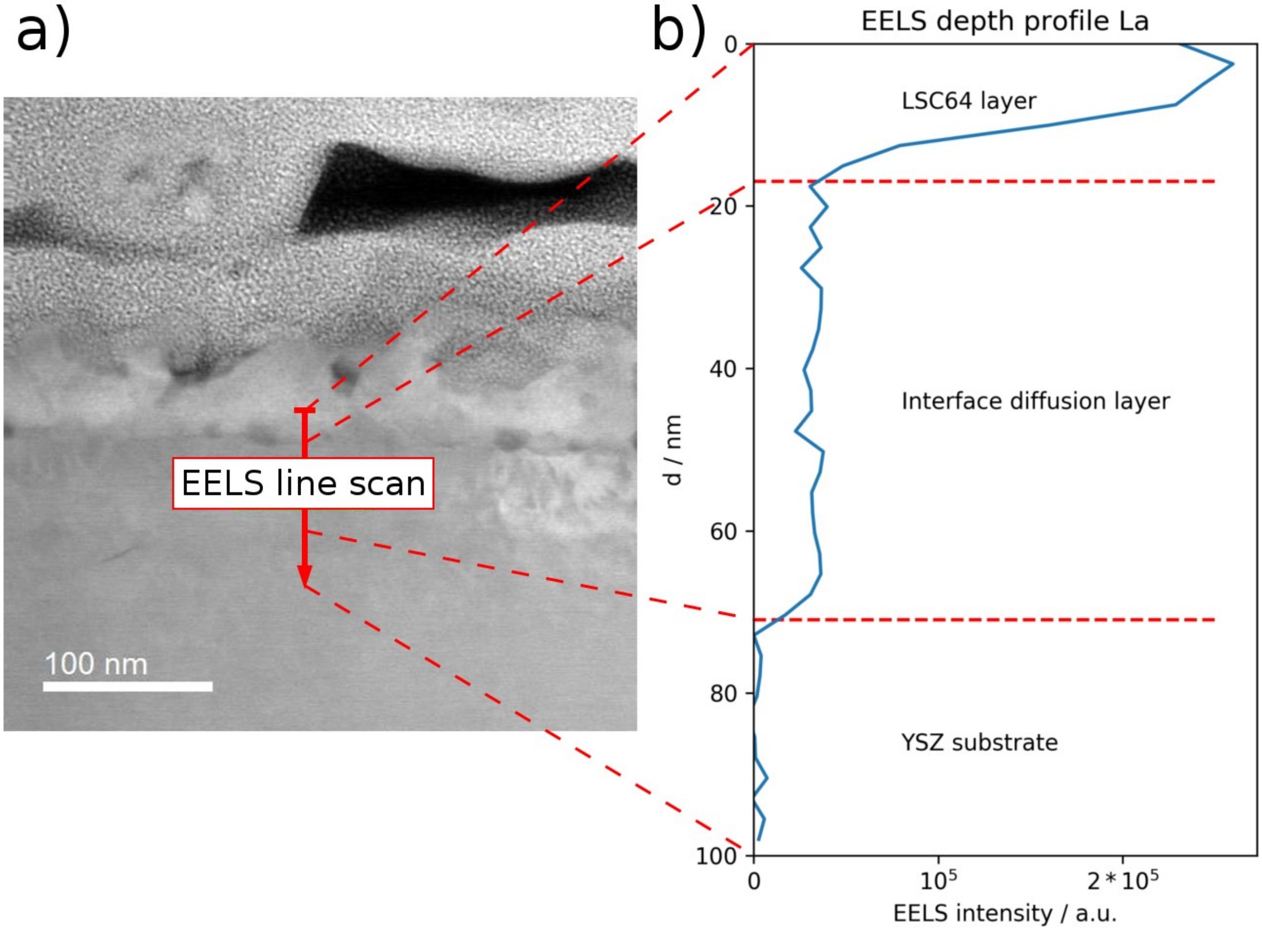

*Figure 171: a) STEM-HAADF cross-sectional image of the degraded cathode-electrolyte-interface, the red arrow marks the position of the line scan analysis; b) depth profile of the intensity of the La EELS-signal*

## 4.4.2 Screen-printed cathodes of LSC64 on YSZ

### *4.4.2.1 Short-term characterization and temperature dependence*

During heating of the sample, impedance spectra were measured at selected temperatures between 500°C and 700°C in steps of about 50 K. As Figure 172 shows, the impedance spectra exhibit two overlapping arcs. There are some points at low-frequencies (plotted at the right side of the Cole-Cole plots) which are noisy. This is probably an artifact caused by small temperature fluctuations during the impedance measurement. These points were neglected for the CNLS-fits.

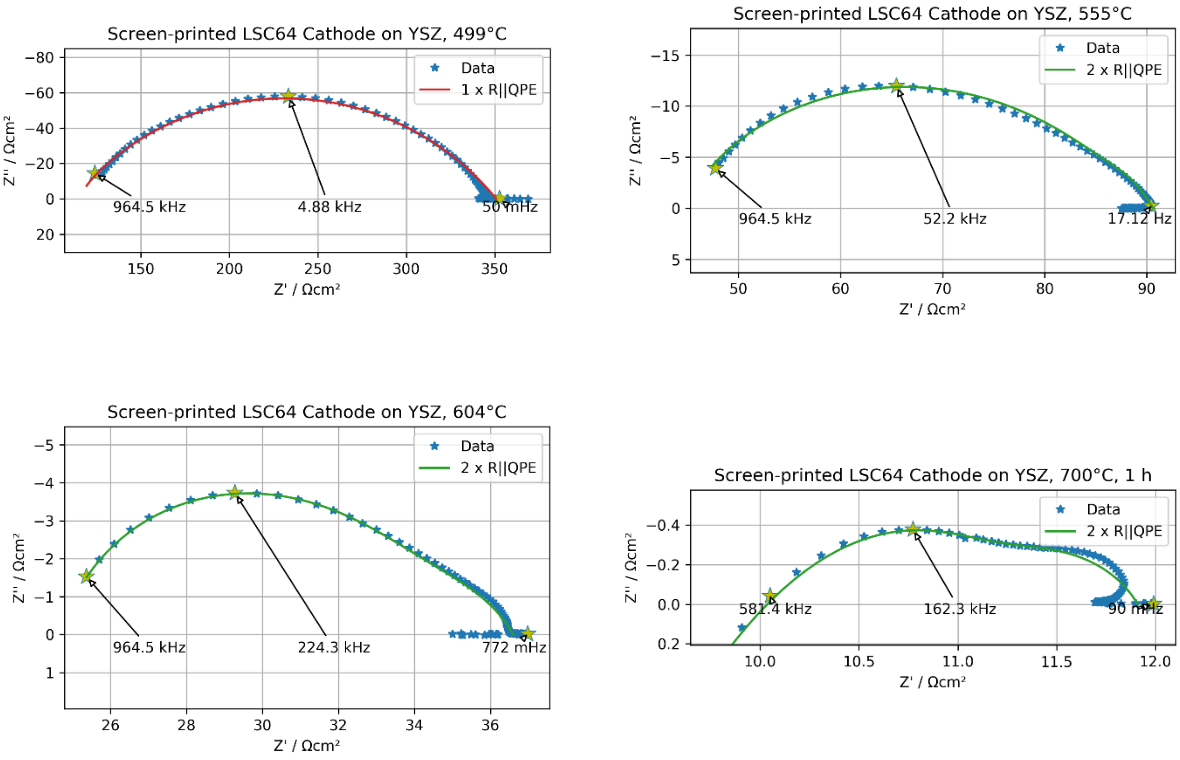

*Figure 172: Impedance spectra of the cell with screen-printed LSC64 cathodes on YSZ measured at different temperatures*

For fitting of the data, an equivalent circuit model with two R-QPE elements was used. According to the nomenclature used in the last sections, the capacitive and resistive parameters were called $C_{hi}$ and $R_{hi}$ for the high-frequency arc, $C_{mid}$ and $R_{mid}$ for the intermediate- and low-frequency range.

As Figure 173 b) shows that the capacitances $C_{hi}$ and $C_{mid}$ can be clearly distinguished. $C_{hi}$ is in the range between $10^{-8}$ and $10^{-7}$ F/cm². Capacitances in this order of magnitude can be in principle linked to transport processes in the electrolyte, for example grain boundary resistances. However, in this case a spreading resistance caused by poor electrical contacting (as described in [158] and also found in section 4.3.1), is a possible explanation for the high-frequency arc. Since the LSC64 cathode layers of the symmetric cell were just dried, but not sintered, prior to the testing, it is likely that the electrical contacting was poor at the beginning of the experiment. A further indication for the validity of this hypothesis is the fact that $R_{hi}$ and $R_{mid}$ show similar activation energies in the Arrhenius plot (Figure 173 left).

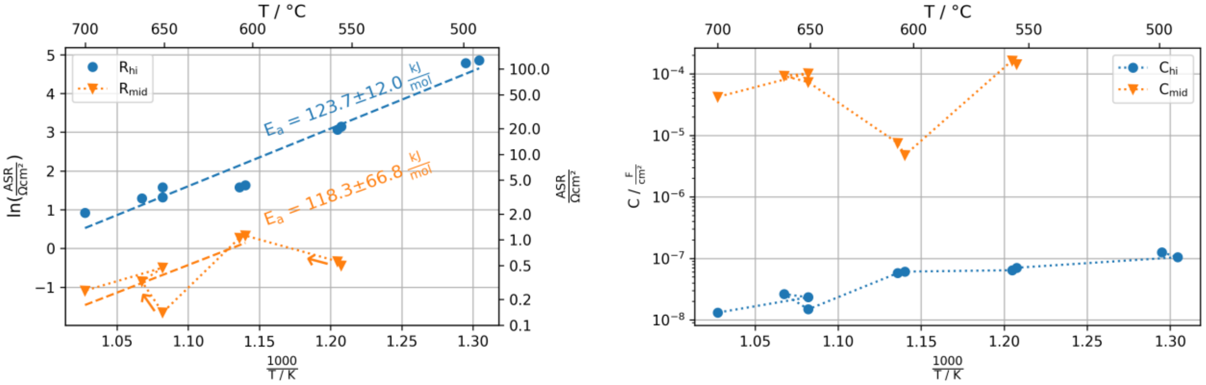

*Figure 173: Resistances and activation energies (left) and capacitances (right) calculated from the parameters of the CNLS-fits*

Figure 173 a) also shows that the values for $R_{mid}$ scatter significantly. This is because this parameter was not only dependent on temperature but also on time. The dotted lines between the data points and the arrows indicate the chronological order in which the measurements were performed. This effect can be found especially with the measurements performed between 650°C and 670°C. 17 hours passed between the first and the second measurement at this temperature, in which a significant degradation occurred.

In the short-term temperature run, $R_{mid}$ is considered as the polarization resistance of the cathode of this sample. It is plotted again in Figure 174. However, as already mentioned above, the values could not be accurately determined due to degradation.

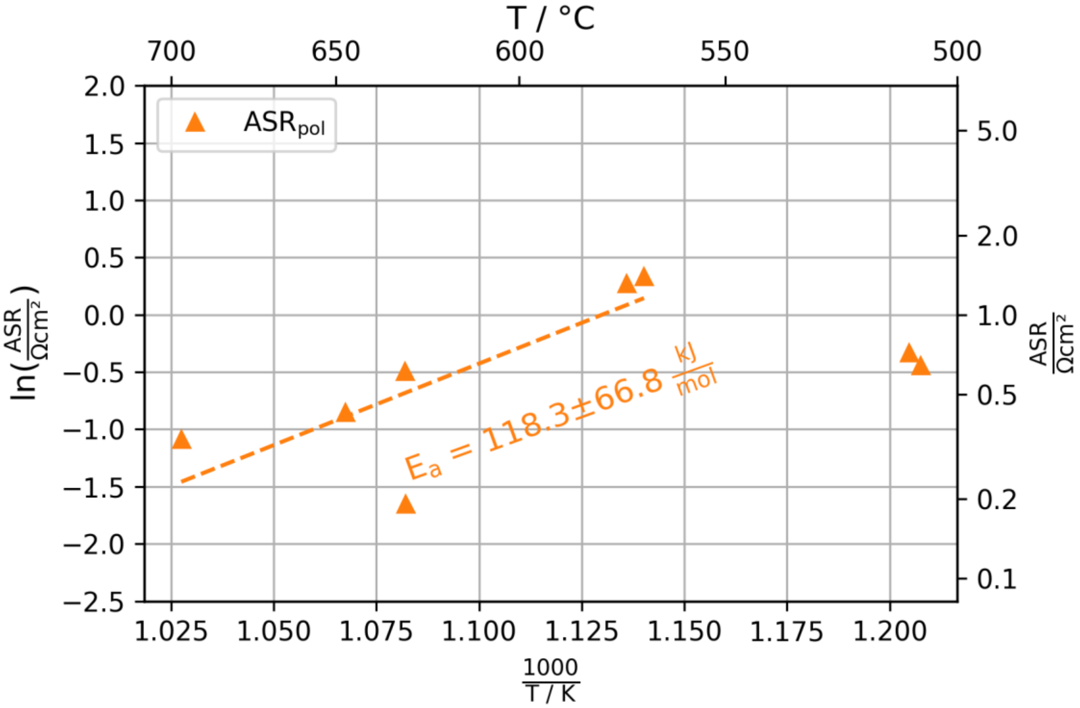

*Figure 174: Arrhenius plot of ASR$_{pol}$ of screen-printed LSC64 electrodes on YSZ*

### 4.4.2.2 Long-term characterization

After reaching 700°C, the sample was characterized in a long-term experiment for 666 hours. The impedance spectra were fitted once more with the two-R-CPE model previously used for the temperature-dependent measurements. Significant changes occurred in the impedance spectra over time. As the Cole-Cole plots in Figure 175 show, the spectra changed their shape. The most notable change was a shift of the peak frequency of the high-frequency arc. At the beginning, two separate arcs were visible in the impedance spectrum. During the experiment, the high-frequency arc moved to lower frequencies, leading to an overlap with the low-frequency arc.

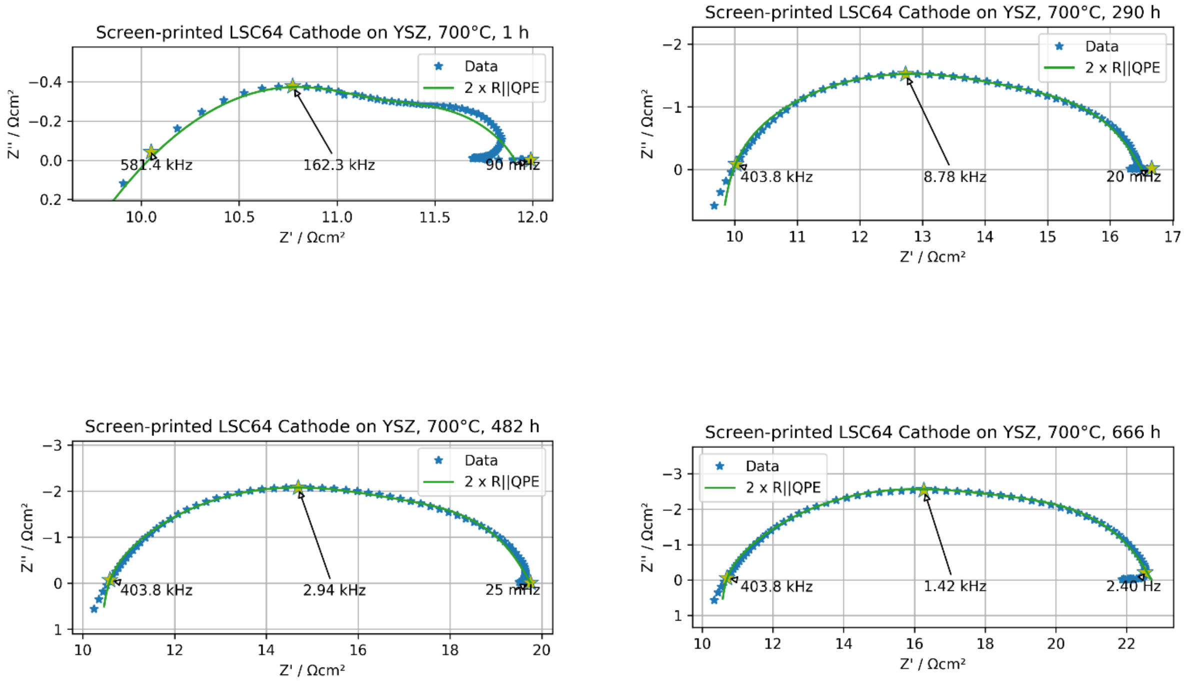

*Figure 175: Impedance spectra of the sample with screen-printed LSC64 on YSZ, measured during the long-term experiment at 700°C*

This time-dependent effect can be comprehended on the basis of the Bode-plot in Figure 176 right). In the first 5 hours, the peak frequency of the high-frequency arc was even above 3 MHz (the maximum frequency of the measurements), but it moved to moderate frequencies within a very short time-span. This effect might be actually another indication for the assumption that the high-frequency arc is caused by spreading resistance. While the electrical contact of the sample was quite poor at the beginning of the experiment, it improved during the first 10 hours because the LSC64 grains started sintering. After 200 hours, the peak frequency stabilized at about 30 kHz. At this point, the strong degradation of the polarization resistance started to dominate the impedance characteristics of the sample.

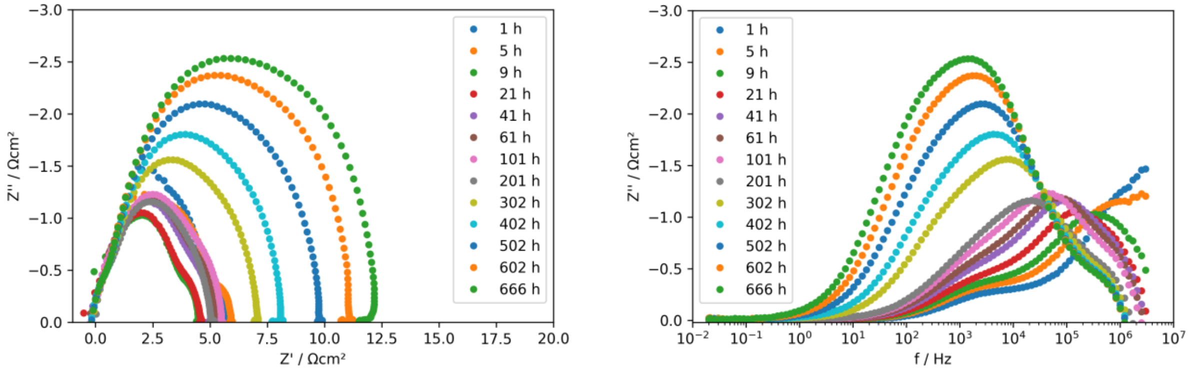

*Figure 176: Complex plane plot (left) and Bode-plot (right) of selected impedance spectra from the time run at 700°C; the ohmic resistance and inductivity were subtracted from the spectra*

The resistances and capacitances calculated from the parameters of the R-CPE elements of the fitting model are plotted against experimental time in Figure 177. The shift of the peak frequency led to an increase of $C_{hi}$ by one order of magnitude, from $10^{-8}$ to $10^{-7}$ F/cm² in the first few hours. It increased further, up to $8 \times 10^{-6}$ F/cm² during the experiment. This is in the typical range for a double-layer capacitance. Therefore, it is assumed that the rate-limiting mechanism causing the high-frequency arc changed during the experiment, from spreading resistivity due to poor electrical contacting, to transport limitations at the cathode-electrolyte-interface. $C_{mid}$ remained relatively constant between $10^{-4}$ and $10^{-3}$ F/cm² and is probably linked to the oxygen reduction reaction.

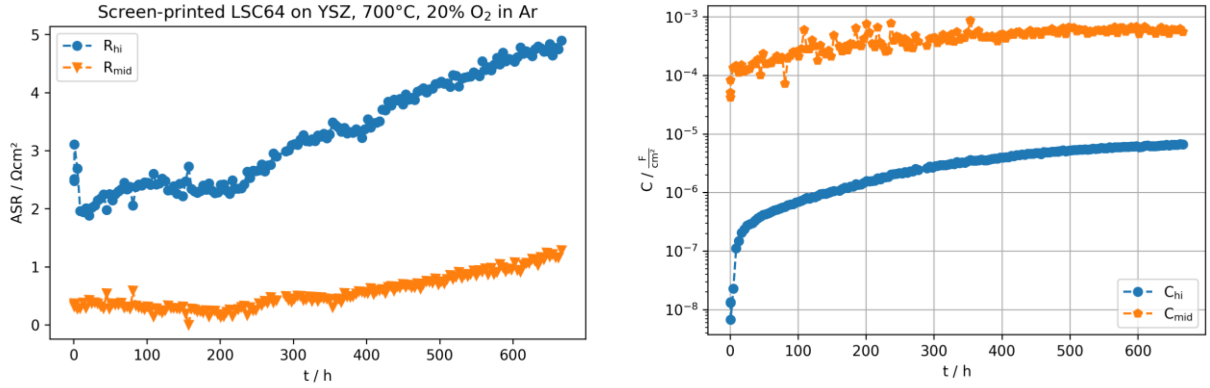

*Figure 177: Resistances (left) and capacitances (right) acquired at the time-run at 700°C as function of time*

A possible reason for these developments in the impedance spectra over time is in-situ sintering of the dried cathode layers at 700°C. While the grains of the screen-printed cathode layer were in poor contact at the beginning of the experiment, it sintered together during the experiment, which improved the electrical contact.

The resistances $R_{hi}$ and $R_{mid}$ remained relatively constant during the first 200 hours and increased quite fast afterwards. The increase of $R_{hi}$ was significantly higher, which means that the degradation of the cathode was primarily due to effects at the cathode-electrolyte-interface. However, also $R_{mid}$ was affected by the degradation.

The polarization resistance $ASR_{pol}$, which is plotted in Figure 178, was calculated by summarizing $R_{hi}$ and $R_{mid}$. It is notable that the polarization resistance remained constant or even slightly decreased during the first 200 hours of the experiment. This behavior might be explained by in-situ sintering as well, which had a positive influence on the cathode performance in this timeframe. However, after 200 hours degradation effects became predominant, leading to a significant increase of $ASR_{pol}$.

$ASR_{pol}$ showed an almost linear increase in the observed experimental period. This is a different behavior than that of the thin-film LSC64 cathode on YSZ presented in the section above, where $R_{pol}$ reached a plateau after about 600 hours. These differences in the time-dependent performance might be explained by the different dimensions of the cathode layer. The estimated degradation rate of the screen-printed cathode was about 7 Ωcm² per 1000 hours.

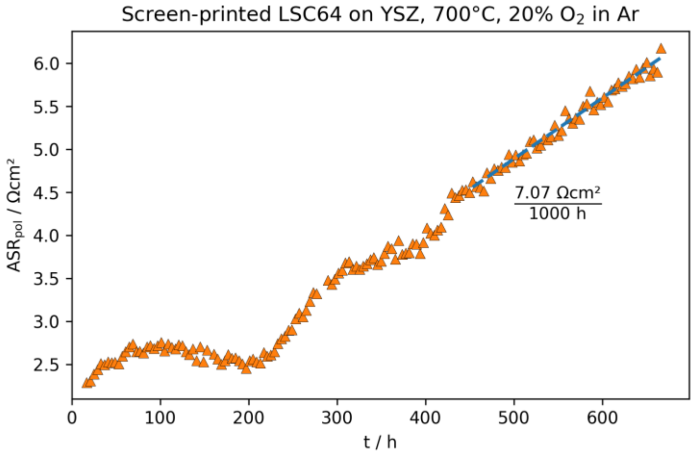

*Figure 178: Area-specific polarization resistance of the screen-printed LSC64 cathode on YSZ as function of time and calculated degradation rate (increase in $ASR_{pol}$ per 1000 h)*

### 4.4.2.3 Post-test analyses

For post-test analyses, a sample of YSZ with a screen-printed LSC64 layer similar to the cathodes of the symmetric cell was prepared. One part of the sample remained in the state as prepared, while another part was present in the impedance reactor besides the cell to cover the degraded state. Both parts were characterized by SEM on the surface and at the cross-section. A cross-section of the degraded sample was additionally analyzed by STEM.

*Table 12: Overview over the analyzed samples*

| | Fresh LSC64 layer on YSZ | Degraded LSC64 layer on YSZ |
|---|---|---|
| SEM surface | ✓ | ✓ |
| SEM cross-section | ✓ | ✓ |
| STEM cross-section at the interface | | ✓ |

### *SEM of the surfaces*

Figure 179 shows surface images of the fresh and degraded sample. Due to the unsintered state of the cathode on the fresh sample, the electrical conductivity was low. Therefore, it was necessary to coat the sample with carbon for SEM imaging. The degraded sample had a sufficient electrical conductivity. This is also the reason that the images of the fresh sample are slightly blurred.

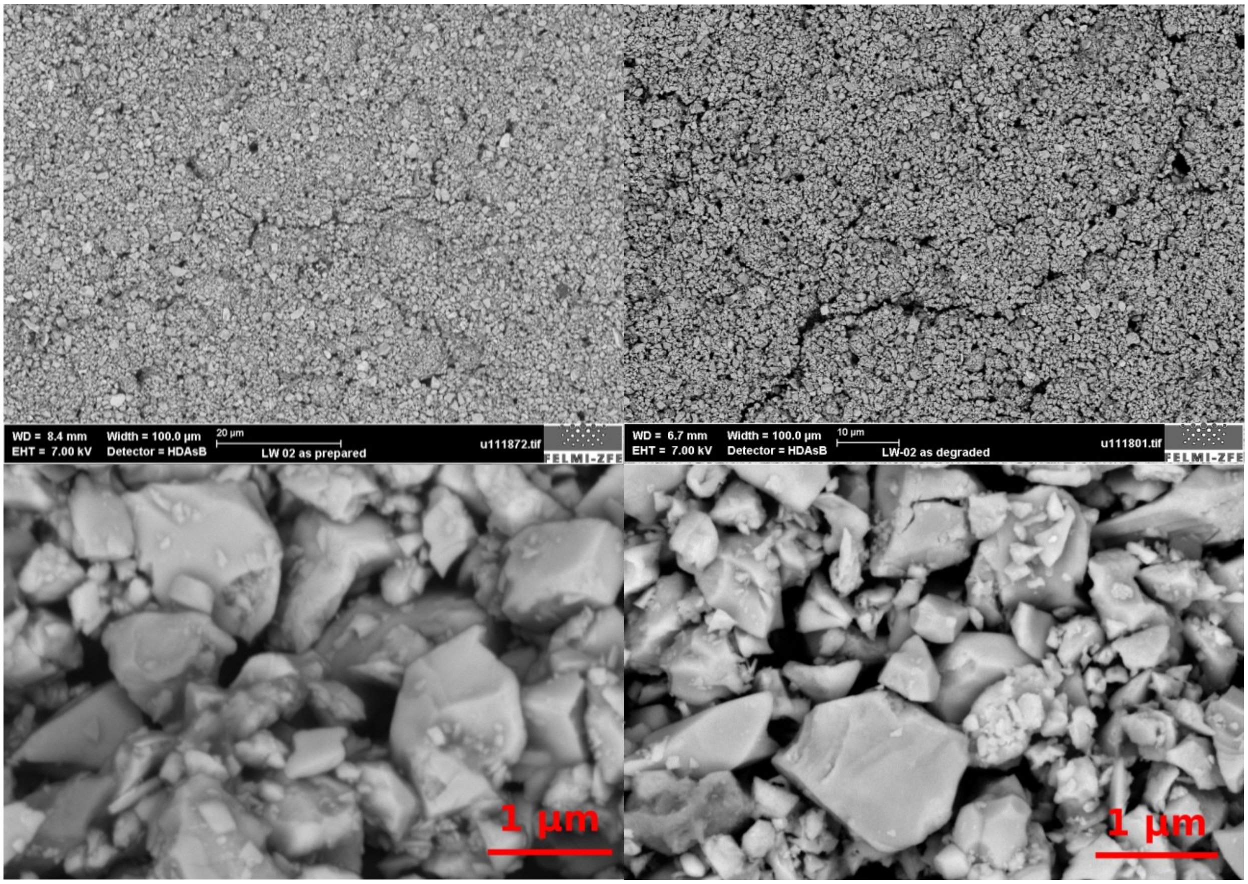

*Figure 179: SEM surface images of the fresh (left) and degraded (right) screen-printed LSC64 cathodes*

There was no indication for degradation to be found on the surface images. The only irregularity was a grain consisting of a cobalt-rich phase, probably $Co_3O_4$ (Figure 180). However, this phase was only found on one position of the sample, so it could be a secondary phase originating from the LSC64 powder.

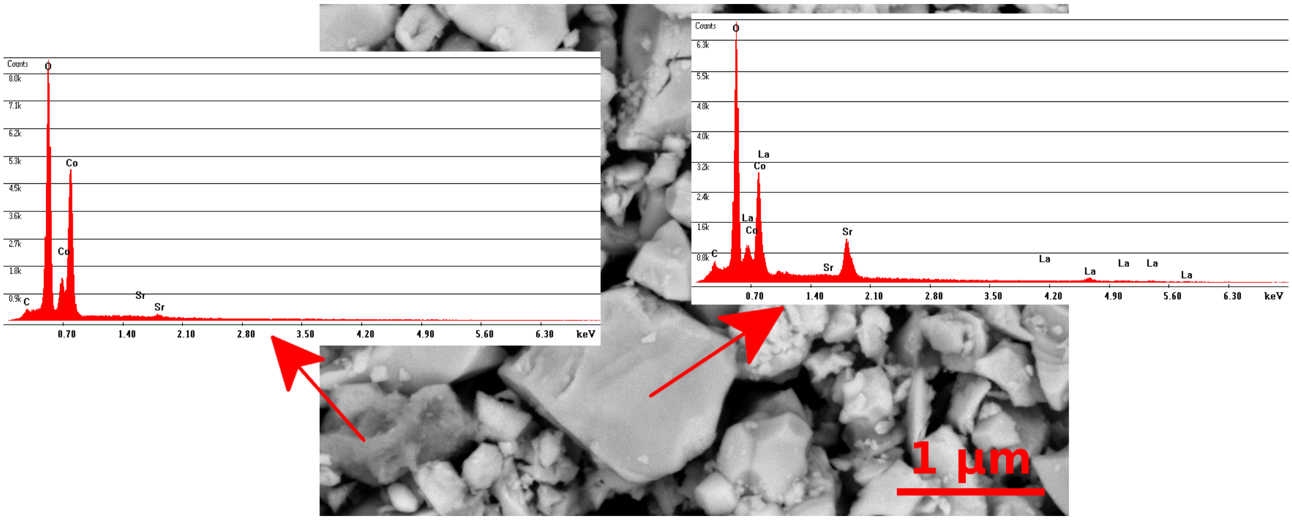

*Figure 180: SEM image and EDX analyses at selected positions of the sample. The darker grain at the bottom left is a Co-rich phase, while the other grains are pure LSC64.*

### SEM of the cross-sections

Cross-sections from the fresh and degraded sample were prepared by an ion sputtering technique and characterized by SEM-EDX.

The cross-sectional images of the fresh (Figure 181) and the degraded sample (Figure 182) show details of the morphology of the screen-printed cathodes. Both screen-printed films showed the intended porous microstructure but were inhomogeneous. Globular agglomerates were found, which are well visible in the secondary electron images. These agglomerates are a result of the powder synthesis and created larger pores in the screen-printed layers. In comparison of the fresh and the degraded cathode layers, it can be seen that the agglomerates compacted during the long-term experiment. This densification of the agglomerates caused a growth of the pores in between and probably also cracks along the cathode layer. The YSZ substrates are quite dense and homogeneous. However, the backscattered electron images showed indications for secondary phases at grain boundaries of the electrolyte.

During the preparation of the samples for SEM, redeposition effects had occurred, caused by transport and deposition of evaporated material from the electrolyte into the porous structure of the screen-printed layers. This effect was particularly evident in the degraded sample, where a large amount of YSZ was deposited in the pores between the agglomerates. The round, drop-like shapes of the big grains in Figure 182 are typical outcomes of such redeposition effects.

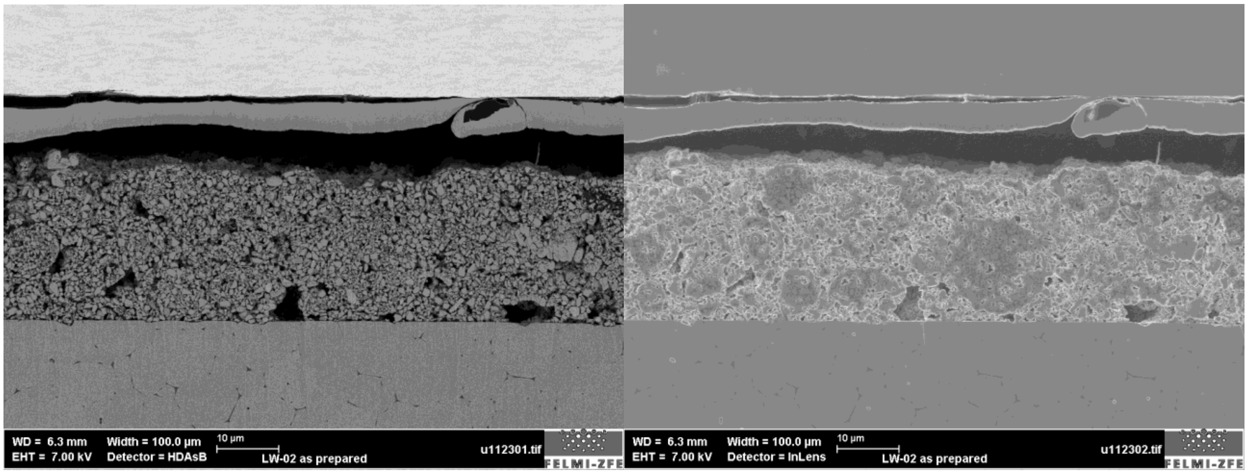

*Figure 181: SEM-BSE (left) and –SE (right) cross-sectional images of the screen-printed LSC64 cathode on the YSZ electrolyte in the state after preparation*

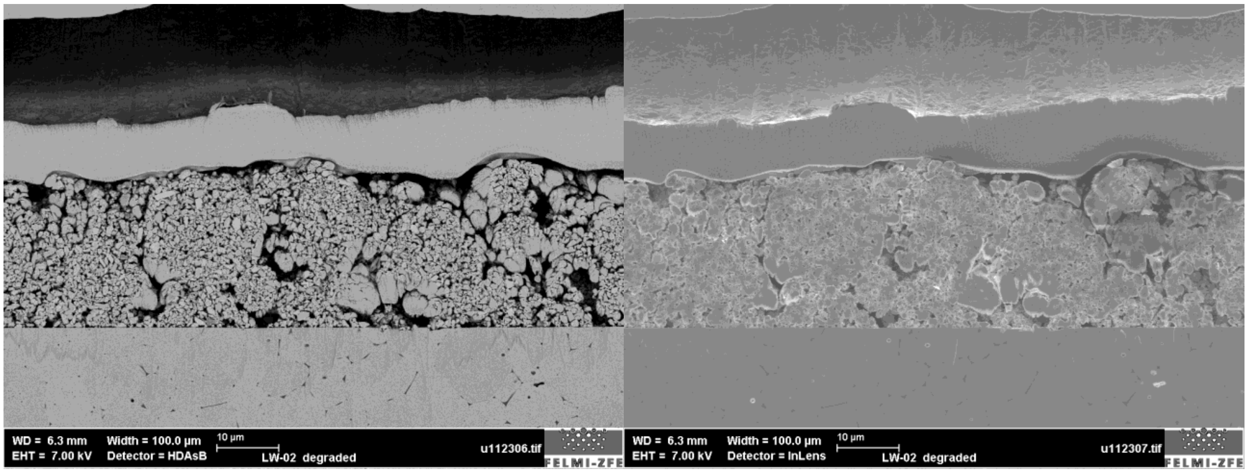

*Figure 182: SEM-BSE (left) and –SE (right) cross-sectional images of the screen-printed LSC64 cathode on the YSZ electrolyte after the long-term experiment at 700°C*

On the samples, localized chemical analyses were performed with EDX. Figure 183 and Figure 184 show the results obtained for the fresh sample. As expected, La, Sr, Co and O were found in the cathode layer, and Zr, Y and O in the substrate. An analysis was also performed on a grain boundary precipitate (Figure 183, position 3). According to EDX, impurities, which stem from the YSZ powder from which the substrates were manufactured, are accumulated in the grain boundary region, especially Si. As already mentioned on page 83, the accumulation of Si on the grain boundaries of solid electrolytes is a well-known finding in electrolyte materials, in doped zirconia as well as in doped ceria [17, 151, 152, 159, 160].

In the analyses of the degraded sample (Figure 185 and Figure 186), significant amounts of Zr and Y were detected in an area scan of the LSC64 layer (Figure 185, position 2). However, it is evident that this finding is a result of the significant redeposition of YSZ in the pores of the LSC64 layer. Imaging and analyses at higher magnification (Figure 186) show that the single

LSC64 grains of the cathode layer have the expected composition but are surrounded by redeposited YSZ material.

From the SEM-EDX analyses, no clear conclusions on the cause of the observed degradation could be drawn. This is due do the high influence of redeposition, but also because of the local resolution of SEM-EDX which is limited due to the large excitation volume of the electron beam, which might be larger than the volumes of secondary phases or diffusion profiles caused by degradation mechanisms.

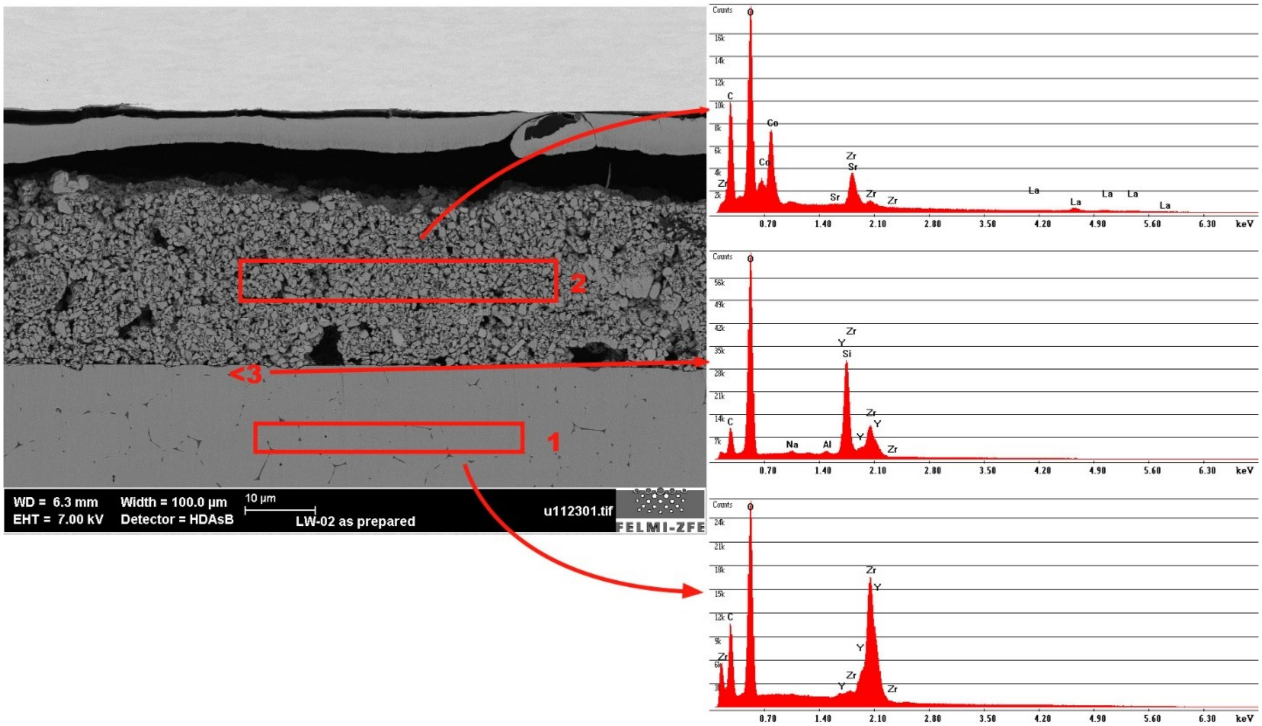

*Figure 183: SEM-BSE cross-sectional image of the fresh screen-printed LSC64 film on YSZ and EDX analyses of the electrolyte, the cathode and a region close to the cathode-electrolyte-interface*

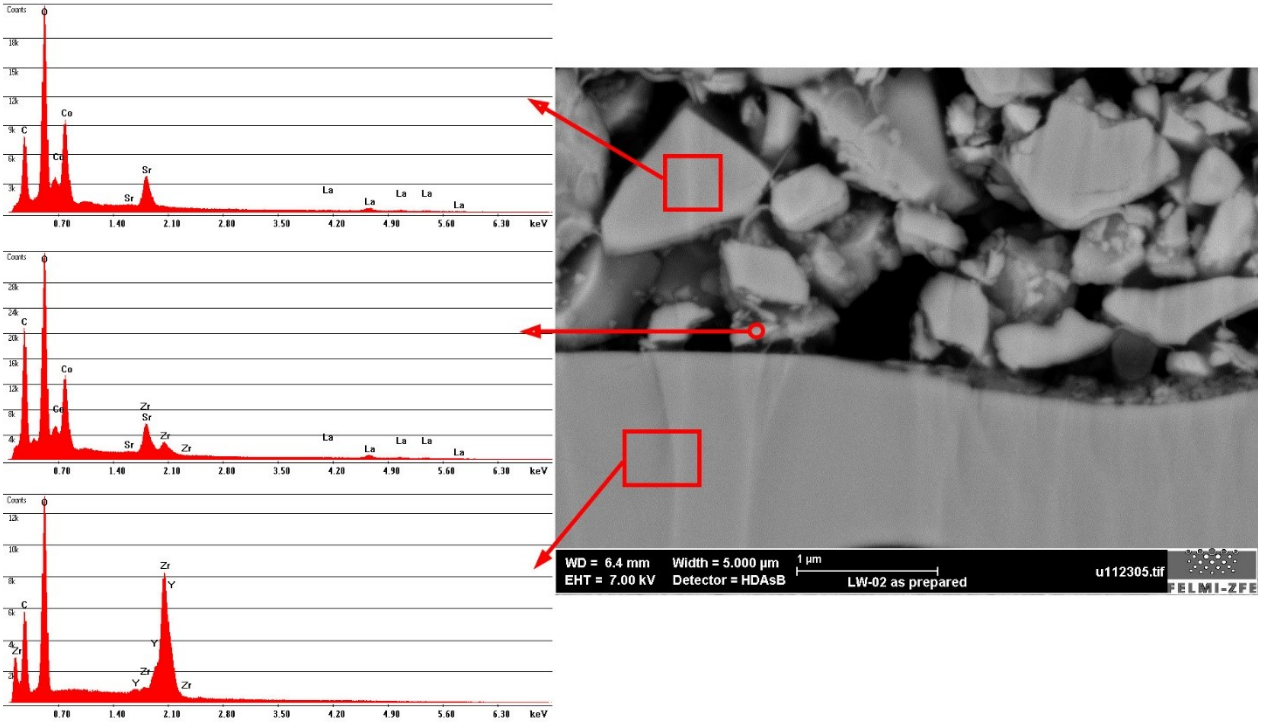

*Figure 184: SEM-BSE cross-sectional image of the fresh screen-printed LSC64 film on YSZ and EDX analyses of the marked regions obtained at higher magnification*

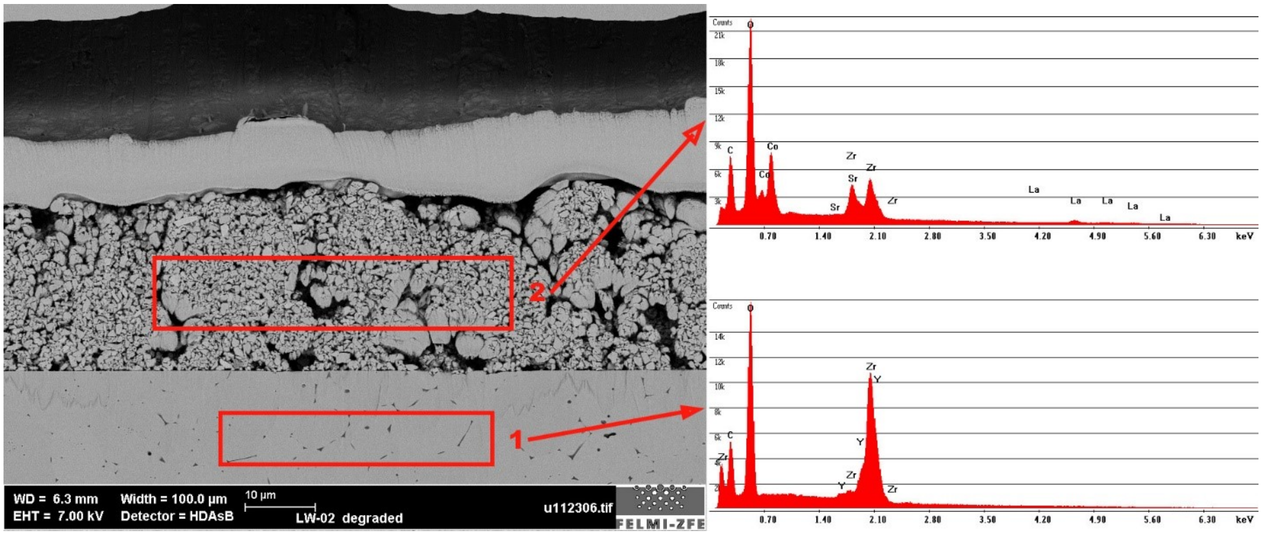

*Figure 185: SEM-BSE cross-sectional image of the degraded screen-printed LSC64 film on YSZ and EDX analyses of the electrolyte (1) and the cathode (2)*

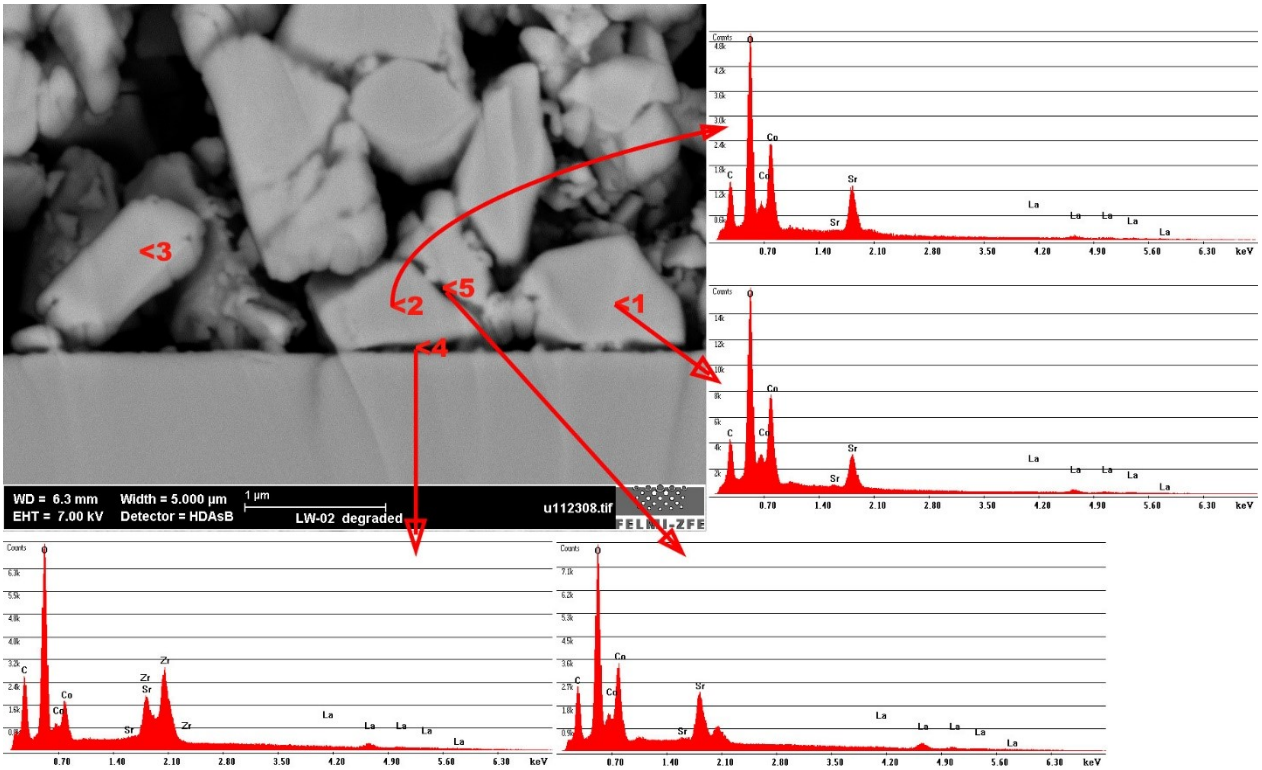

*Figure 186: SEM-BSE cross-sectional image of the degraded screen-printed LSC64 film on YSZ and EDX analyses of the marked regions obtained at higher magnification*

### *STEM of the cross-sections at the cathode-electrolyte-interface*

From the degraded sample, a TEM lamella was prepared, which covered the interface region between the screen-printed cathode and the electrolyte substrate. The lamella was imaged by STEM-HAADF and chemically analyzed at selected positions by EDX and EELS.

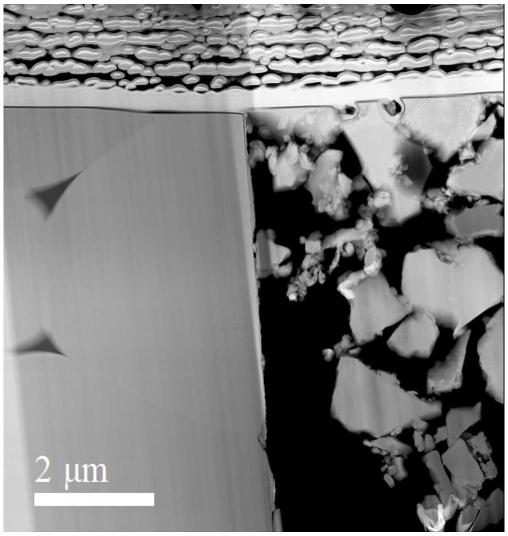

*Figure 187: STEM-HAADF image of the degraded sample; the dense YSZ electrolyte is shown on the left and the porous screen-printed LSC64 cathode on the right side of the image*

It was quite difficult to prepare a representative lamella out of the sample, since the screen-printed layer was quite porous and the contact areas between cathode and electrolyte were inhomogeneous. As Figure 187 shows, the lamella contained only few grains of LSC64 which were in direct contact with YSZ. Analyses of the electrolyte and the cathode by EDX and EELS are shown in Figure 188 and Figure 189.

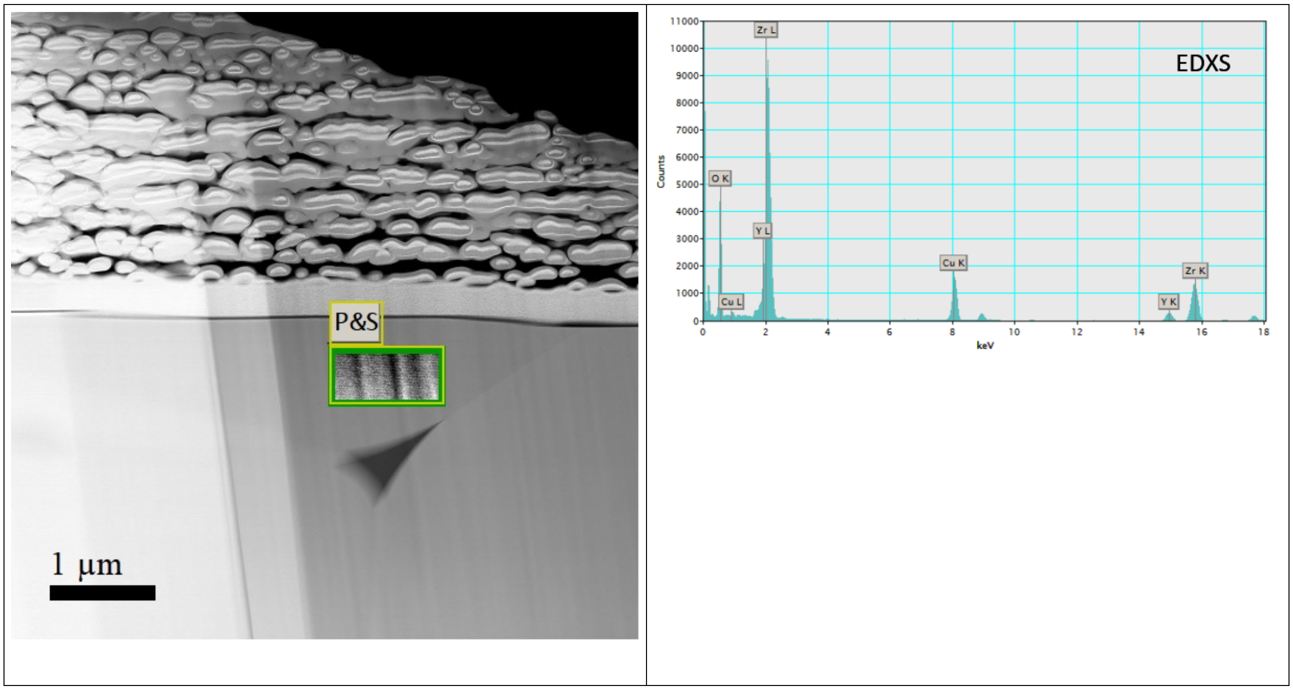

*Figure 188: STEM-HAADF image (left) and EDX analysis from the marked region of the YSZ electrolyte (right) of the degraded sample*

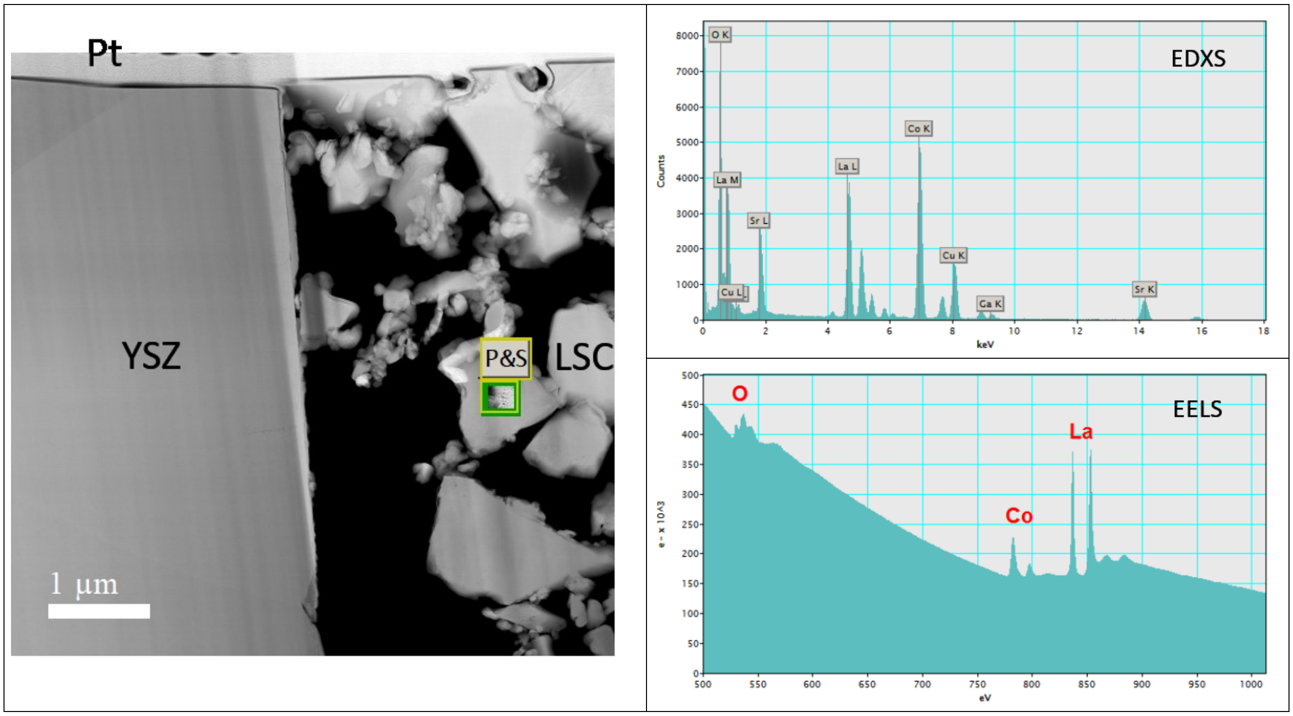

*Figure 189: STEM-HAADF image (left) and EDX and EELS analyses (right) from the marked region of the screen-printed LSC64 layer of the degraded sample*

At the cathode-electrolyte-interface, a line scan analysis with EELS was performed to gain information on possible cation interdiffusion at the interface between LSC64 and YSZ. As Figure 190 shows, there was still a small gap between the LSC64 grain and the electrolyte. However, since significant amounts of Sr and La were found in the YSZ electrolyte close to the interface, delamination of the cathode must have taken place during TEM preparation (*after* the EIS experiment). Similar to the results obtained for the LSC64 thin-film on YSZ (see above), the formation of $La_2Zr_2O_7$ and/or $SrZrO_3$ at the cathode-electrolyte-interface of the screen-printed LSC64 cathode on YSZ is assumed as the predominant cause of degradation.

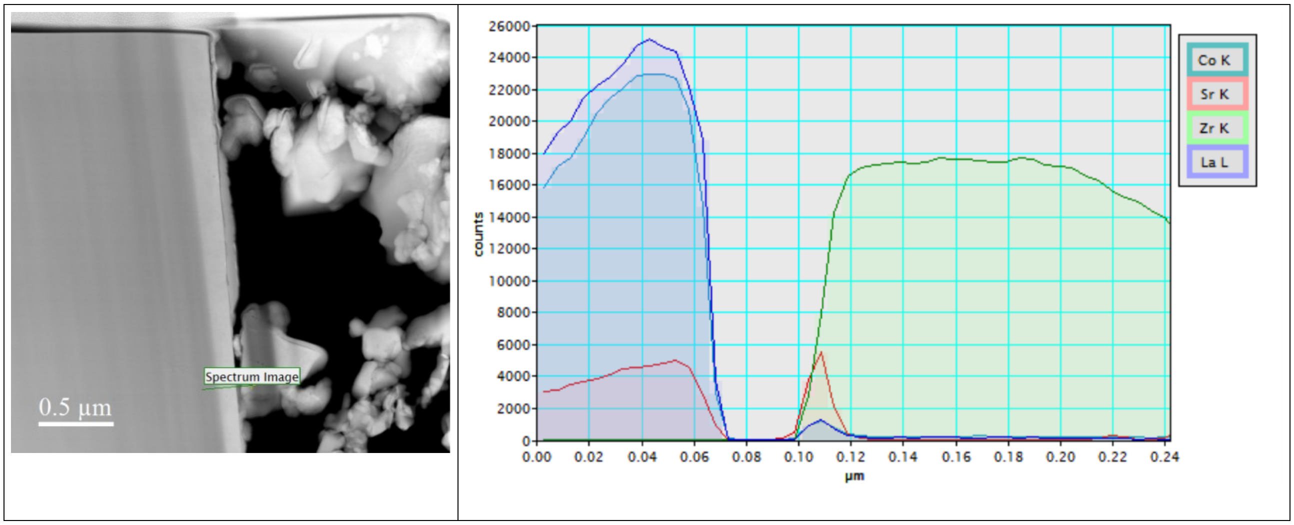

*Figure 190: STEM-HAADF image (left) and EELS line scan at marked region of the cathode-electrolyte-interface of the degraded screen-printed LSC64 cathode on YSZ*

## 4.5 Structure-property-relationships of the investigated samples and degradation phenomena

In the previous sections, electrochemical properties, long-term stability, and degradation mechanisms of cathodes with different microstructures were presented. In the following section, the most important findings from the experiments will be discussed and interrelated.

### 4.5.1 Short-term characteristics of cathodes with different microstructures

SOFC cathodes made of LSC64 with different microstructures were characterized by EIS under comparable conditions. As the Arrhenius plot in Figure 191 shows, the magnitude and temperature dependence of the polarization resistance $ASR_{pol}$, was strongly influenced by the microstructure. The µm-scale screen-printed cathodes and the nanoscale thin-film cathodes had similar activation energies between 120 and 130 kJ/mol, but the latter had significantly smaller polarization resistances. An exception of this trend was the infiltrated cathode: Here not only the $ASR_{pol}$ but also the activation energy was clearly smaller. This caused a polarization resistance below 1 $\Omega cm^2$ even at 500°C.

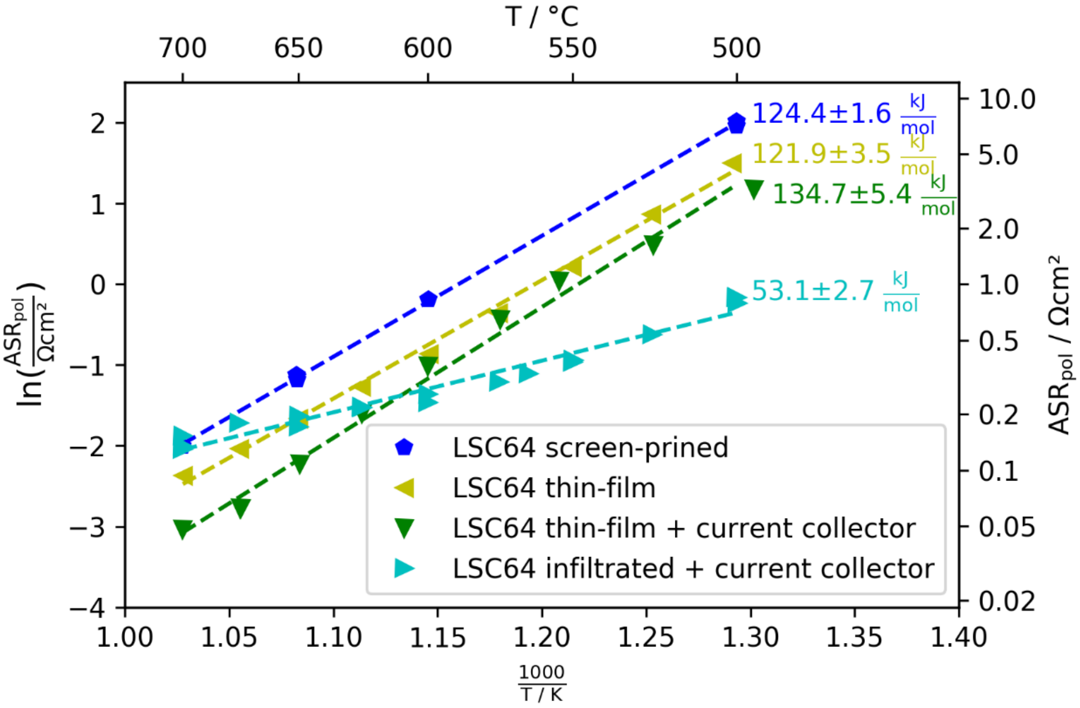

*Figure 191: Polarization resistances of LSC64 cathodes with different microstructures as function of temperature*

The difference in the activation energies between the infiltrated cathode and the other cathode types is noteworthy and indicates the influence of architecture and morphology on the temperature-dependent performance of a cathode. From Figure 191 it can be concluded, that the screen-printed and the thin-film cathodes show the same cathode mechanisms, while the mechanisms for the infiltrated cathode are significantly different. It is worth mentioning that the activation energy of $ASR_{pol}$ of the infiltrated cathode is with about 55 kJ/mol in the range of the activation energy of the ionic conductivity of GDC [17, 18]. This is an indication that the cathode polarization resistance is influenced by bulk diffusion of oxygen vacancies inside the GDC backbone, rather than inside the infiltrated MIEC. The infiltrated material purely acts as catalyst for the surface exchange reaction of oxygen. These assumptions have been made by Nicholas et al. for their proposed SIMPLE model, which describes the performance of infiltrated cathodes by an approach with simplified geometry [147, 161].

The assumptions of this model are also supported by the occurrence of Gerischer-type arcs in all impedance spectra. As already mentioned in section 2.3.2 on page 22, the Gerischer impedance is a characteristic feature of impedance spectra of mixed ionic-electronic conducting cathodes like LSC64 and LSCF, which occurs, when bulk diffusion is the limiting mechanism at high frequencies and surface oxygen exchange is the relevant mechanism at low frequencies. The occurrence of a Gerischer impedance could be confirmed for all characterized cathode types. Screen-printed cathodes of LSC64 and LSCF showed this shape at all measured temperatures, from 500°C to 700°C. For the thin-film cathodes, the shape was clearly visible on impedance spectra measured up to 600°C. Starting with 625°C, the 45° slope on the high-frequency side began to vanish due to overlap with the stray inductance. With the infiltrated cathode on the other hand, Gerischer impedances were only found in spectra below 500°C (Figure 192). At 500°C, the intermediate frequency arc was already so small, that a distinct shape wasn't recognizable any more. Above 600°C this arc even was below detection limit. This trend indicates, that bulk diffusion inside the infiltrated LSC64 grains was a rate limiting factor only at temperatures below 500°C and the oxygen reduction kinetics of these cathodes were quite fast.

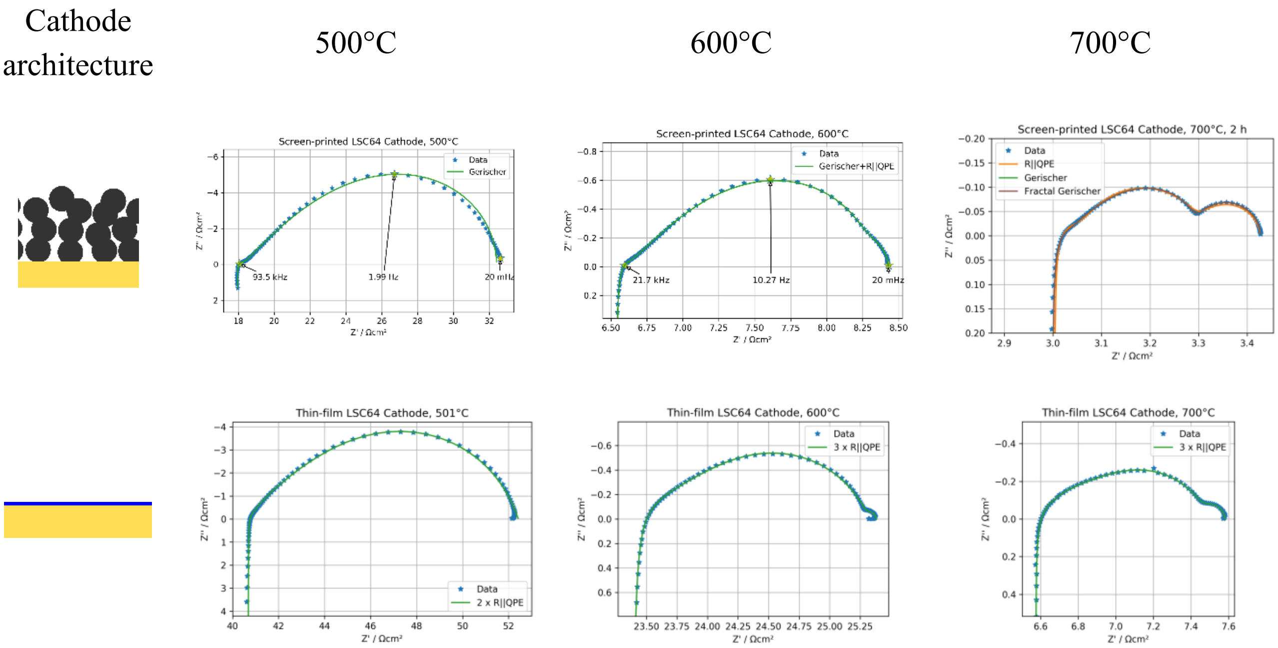

*Figure 192: Impedance spectra of the screen-printed and the thin-film LSC64 cathodes, measured at 500-700°C; the characteristic shape of the Gerischer impedance is apparent to a greater or lesser extent in all spectra*

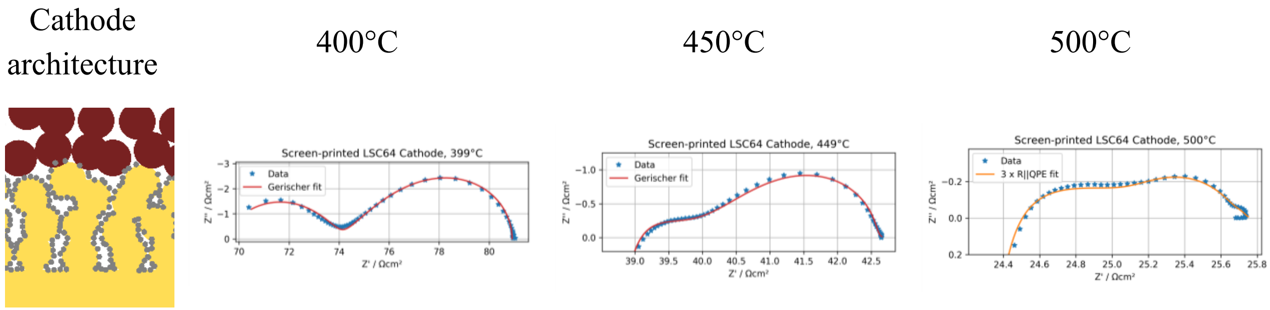

*Figure 193: Impedance spectra of the infiltrated LSC64 cathode, measured at 400-500°C; the characteristic shape of the Gerischer impedance is found only at low temperatures*

Another comparison is given in Figure 194, where selected impedance spectra of different cathode morphologies, all measured at 700°C, are shown in a Bode plot ($Z_{im}$ vs. f). All impedances show a peak at low frequencies of about 1 Hz. This characteristic low-frequency signal was found with every sample at temperatures above 550-600°C. Due to the temperature-independent nature of the effect it is assumed to be caused by limitations of gas-phase transport of $O_2$. The fact that this feature was found in all samples, regardless of the cathode microstructure, is an indication that this effect was caused by the testing equipment rather than the cathode morphology. Significant differences between the specific cathode types were found at frequencies above 5 Hz. While the impedance of the screen-printed cathode (state-of-the-art fabrication method and typical microstructure in the technical application) exhibited a peak frequency of about 50 Hz, the ones of the thin-film cathodes were about 5 kHz, and the infiltrated cathode showed a peak frequency at 20 kHz.

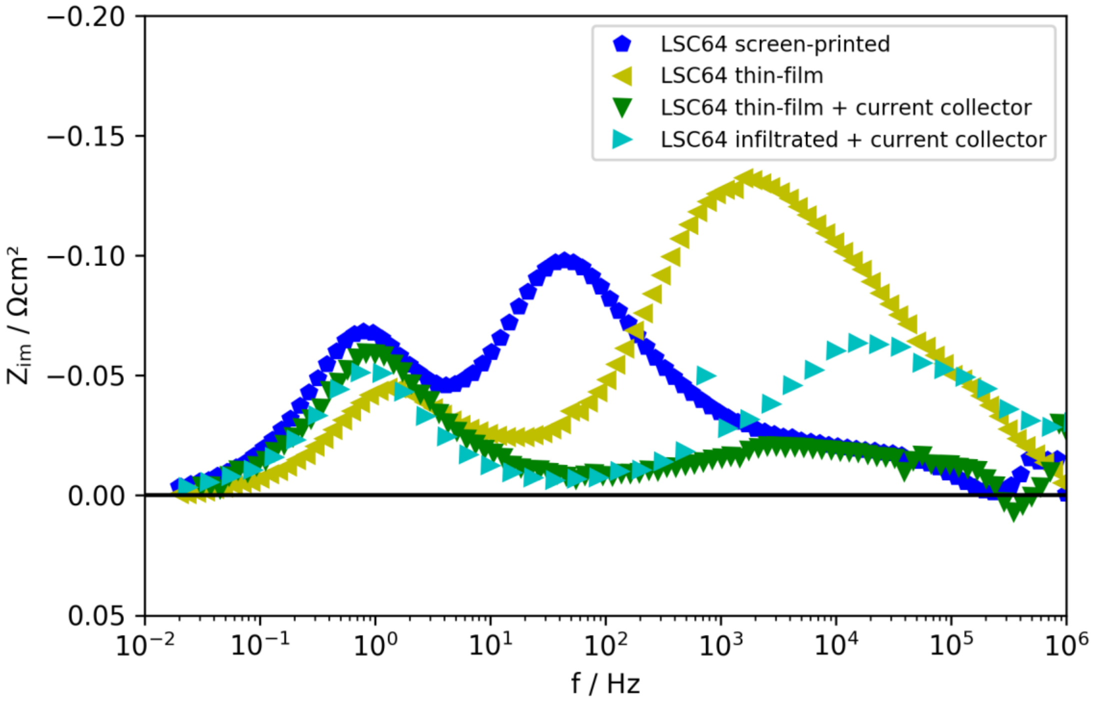

*Figure 194: Bode plots of selected impedance spectra of LSC64 cathodes with different microstructures measured at 700°C*

### 4.5.2 Influence of humidity and Si-poisoning on the long-term performance of different cathode materials and cathodes with different microstructures

Several long-term experiments, where the humidity of the testing atmospheres was controlled and modified, were performed. Based on the results it can be stated that dry testing gas atmospheres lead to reasonably stable operating conditions, but degradation effects occur when as humidity comes into play. Post-test analyses suggest that Si-poisoning was the dominant mechanism causing the observed degradation phenomena when the critical factors “humidity” and “presence of Si-source” coincided.

With the conductivity relaxation experiment of LCF91 the influence of humidity was evident, leading to a strong decrease of the apparent (chemical) oxygen surface exchange coefficient $k_{chem}$ by three orders of magnitude. This behavior is well known and has been reported for different mixed-conducting materials in similar experiments [118-120]. Figure 195 shows a comparison the current experiment with LCF91 at 700°C with a long-term investigation of LSCF at 600°C [119], performed also in the presence of a Si-source and gas phase humidity.

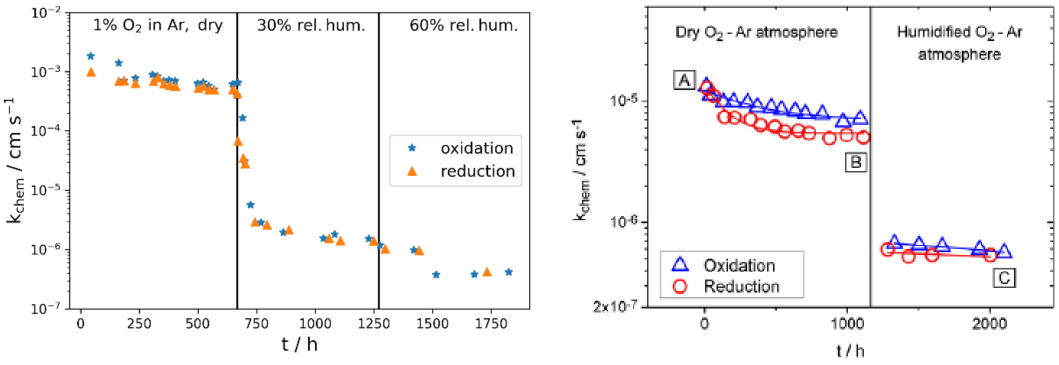

*Figure 195: Comparison of the time-dependence of $k_{chem}$ of LCF91 at 700°C (left) and LSCF at 600°C (right, from [119]); predominant degradation mechanism in both cases was Si-poisoning*

For all these experiments, Si-poisoning in humid atmospheres has been found as the main cause of the degradation [119]. It is obvious that this degradation mechanism works the same way for different mixed-conducting materials: Si which occurs in the form of the volatile species $Si(OH)_4$ is deposited on the surface of the sample, where it forms a thin $SiO_x$ or silicate layer.

Similar degradation mechanisms could be found in the long-term electrochemical impedance experiments with model cathodes of LSC64 as well. However, it could be shown that the cathode morphology had a strong impact on the extent of the observed degradation, and certain cathode architectures were beneficial for the long-term stability. Figure 196 shows a comparison of the results of these long-term experiments with different cathode microstructures.

The fastest and most severe degradation was found for thin-film cathodes of LSC64 without current collector, as described in detail in section 4.2.1. The degradation rate of $ASR_{pol}$ was between 0.2 and 0.4 Ωcm²/1000 h. The presence of Si could be confirmed in porous regions of the degraded cathodes, which is consistent with the known behavior of Si to deposit on the surface of perovskite-structured materials [121].

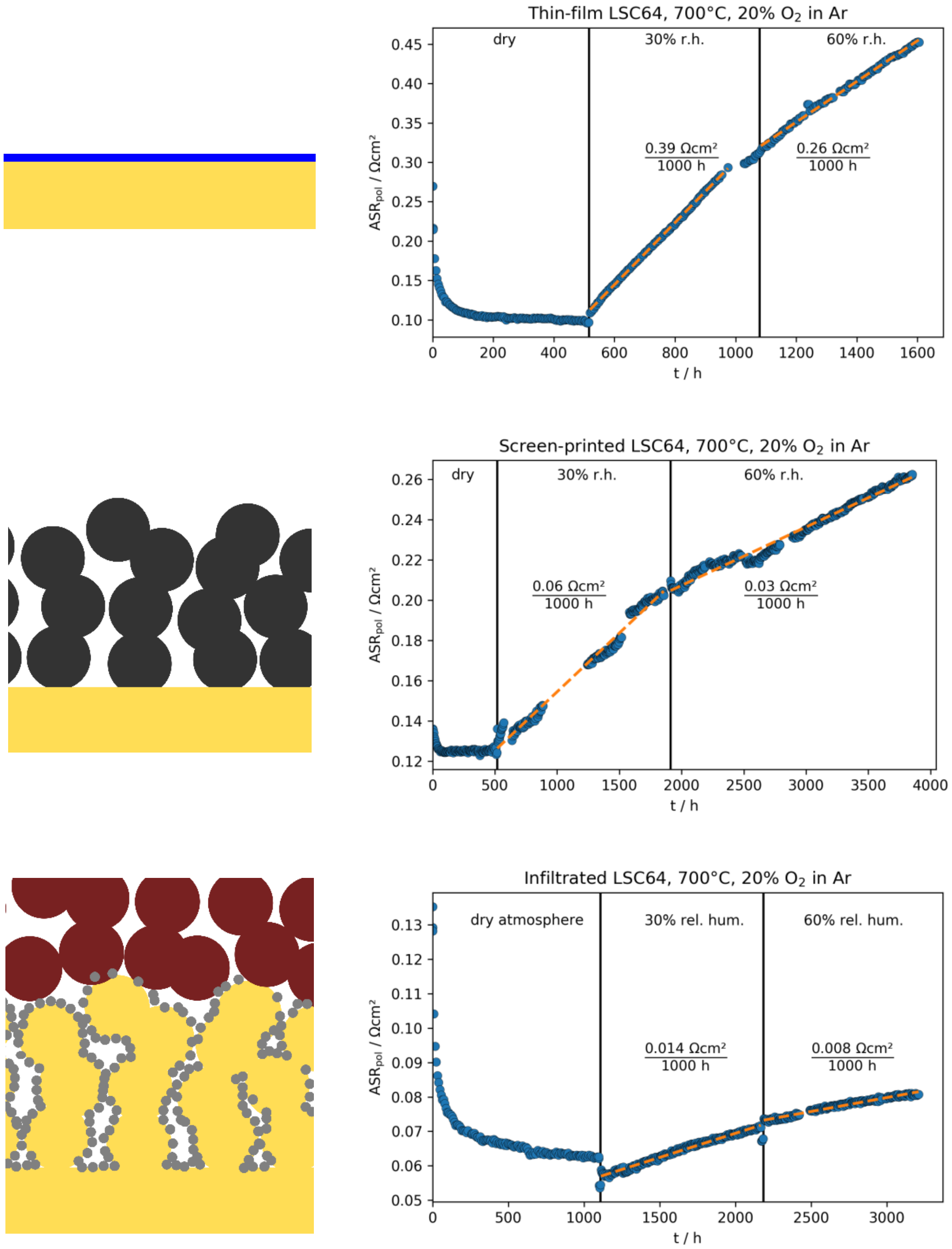

*Figure 196: Comparison of the long-term behavior of thin-film-, screen printed and infiltrated cathodes of LSC64 during EIS measurements at 700°C in dry and humid atmospheres; the assumed predominant degradation mechanism in all cases was Si-poisoning*

The screen-printed cathode (see section 4.2.3) and the infiltrated cathode of LSC64 (section 4.2.2) degraded much slower and to significantly lesser extents than the thin-film cathode. As marked in the plots of Figure 196, the polarization resistance of the screen-printed cathode increased by 0.03-0.06 $\Omega cm^2$/1000 h, the infiltrated cathode at even smaller rates of 0.008-0.014 $\Omega cm^2$/1000h. The high stability might be explained by the large surface areas of these cathode structures due to high porosities and increased cathode thickness (screen-printed cathodes) or coating of a porous scaffold with nanoscale particles (infiltrated cathodes). The high surface area is thus not only beneficial for the prime purpose of the cathode (surface oxygen exchange between gas phase and ceramic electrode) but fulfills a getter-function for impurities. The infiltrated cathode, which showed the highest stability in the long-term tests, also had the largest surface area. Besides the infiltrated backbone with the coat of nanoscale particles it also contained the porous current collector layer on top. This current collector might have acted as an additional protective layer by adsorbing a large amount of Si and other contaminants and protecting the active layer underneath. Following these assumptions, a general strategy to reduce the impact of Si-poisoning on the long-term stability of mixed-conducting perovskite-type cathodes could be the combination of active infiltrated cathode layers and thick porous getter layers with high affinity towards Si and other impurities.

The fact that no Si could be detected at all in post-test analyses of the screen-printed and the infiltrated samples seems to be in agreement with the corresponding slow degradation rates. That doesn't necessarily mean that absolutely no Si was present. Since the experimental conditions were the same, it can be assumed that Si gas-phase transport and -deposition occurred in all three experiments and was the main source of degradation. However, the actual concentrations of Si in the screen-printed and infiltrated cathode were probably below the detection limits of the applied EDX analyses. It has to be mentioned that Si and Sr have similar characteristic energies in EDX spectra, so that small concentrations of Si are hard to detect in presence of high amounts of Sr. The traceability of Si in the thin-film cathode is also facilitated due to its low dimensionality and the well-defined geometry, which makes the preparation of TEM samples much easier, compared to porous microstructures. Therefore, such thin-films are good model systems to study degradation phenomena on SOFC cathodes, at least qualitatively.

Apart from Si-poisoning, indications for other transport phenomena caused by humidity were found in post-test analyses. The thin-film cathode showed a significant grain growth in presence of humidity. SEM images of the conventional screen-printed cathode revealed the formation of surface precipitates in presence of humidity. These surface structures were formed out of the bulk LSC64 phase. Both phenomena might have been caused by the gas-phase transport of Sr, due to the formation of volatile $Sr(OH)_2$ out of the cathode itself in humid atmospheres. On the infiltrated cathode, clear signs for this specific transport phenomenon could be demonstrated by SEM-EDX. Besides that, traces of contamination with Cr and S were found. STEM analyses revealed that these contaminants formed the secondary phase $Sr(Cr,S)O_4$ in a few regions of the sample. These phases might have had an influence on the degradation as well.

### 4.5.3 Influence of Cr-poisoning on the long-term performance of cathodes with different microstructures

In the Cr-poisoning experiments with LSC64 and LSCF cathodes of various architectures, the observed degradation effects were significantly stronger than in the experiments without Cr-sources. Degradation rates above 1 Ωcm²/1000 h were observed, which are far too high for any technical application. Again, the cathode microstructure had a significant influence on the degradation rate, as the comparison in Figure 197 shows.

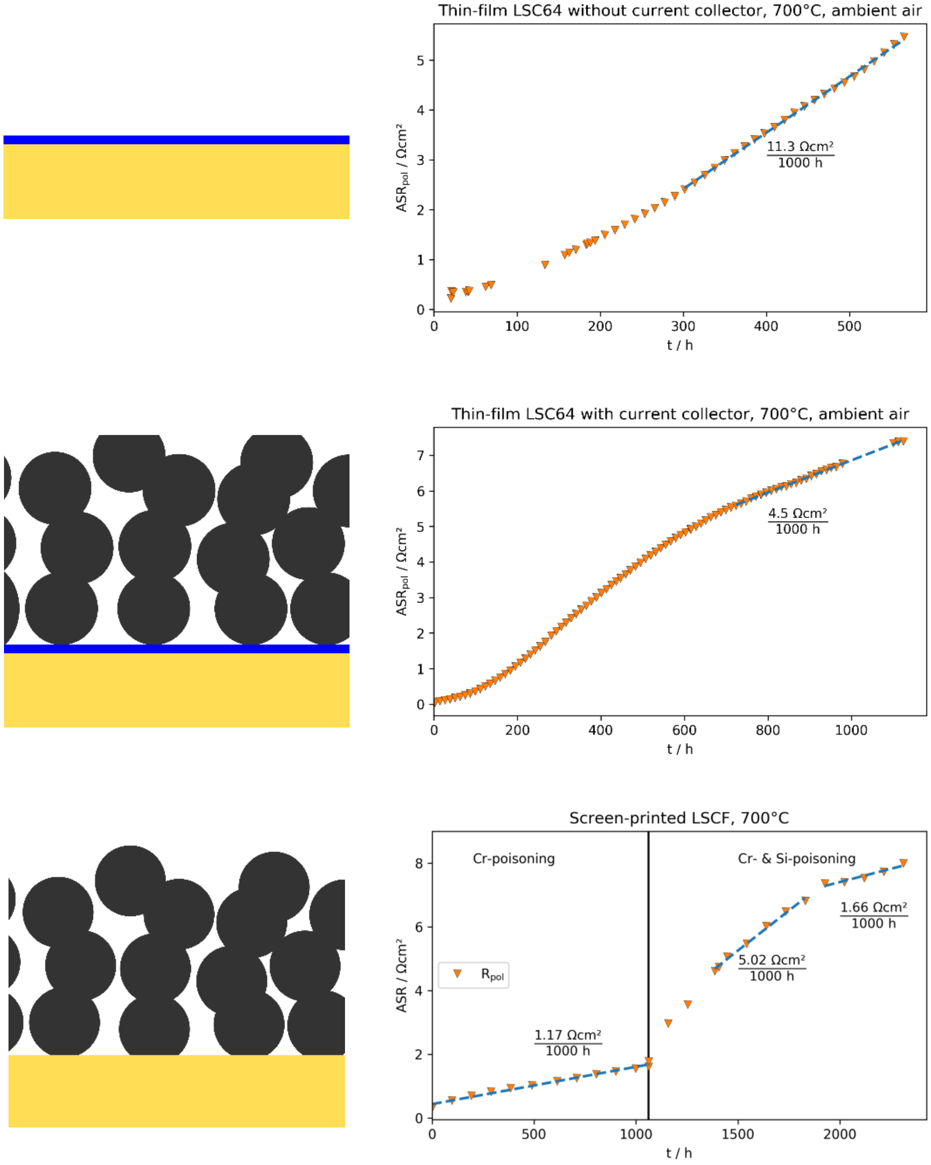

*Figure 197: Comparison of the long-term behavior of thin-film LSC64 cathodes without and with current collector, as well as screen printed LSCF-cathodes during EIS measurements at 700°C in humid atmospheres; predominant degradation mechanism in all cases was Cr-poisoning*

The thin-film cathode without current collector degraded with the fastest rate. According to post-test analyses, Cr was found in a significant volume fraction (about 20%) of the thin-film. Due to the low thickness of these cathodes, small amounts of Cr had a strong influence on the cathode performance. The thin-film cathode with an additional microstructured porous current-collector degraded with a slightly lower rate. This could be an indication that the current collector acted as a protective layer (getter for impurities). If that was the case, the protective effect was still too low to be a useful countermeasure against Cr-poisoning.

The screen-printed porous microscale LSCF cathode degraded significantly slower under Cr-poisoning conditions than the relatively dense nanoscale thin-film cathodes of LSC64. These differences can be explained well by the larger volume of the screen-printed cathode compared to the thin-films, in a way that a smaller fraction of the cathode volume was affected by Cr. In the second period of the long-term experiment, the Si-layer sputtered on top of the LSCF cathode further increased the cathode degradation. However, the way in which Si was brought into the cathode system did probably not represent the usual mechanism of Si-poisoning through gas transport, since Si was deposited in a large amount on the outer surface but was probably not distributed into deeper regions of the cathode.

All in all, Cr poisoning has to be considered as a critical issue for SOFC development, which might not be easily overcome by changes in the chemistry or morphology of the cathode. Instead, preventing Cr-sources in the stack by protective coatings on Cr-based alloy interconnectors is currently state-of-the-art. Further, avoiding the gas phase transport of volatile Cr-species by reducing humidity in the cathode atmosphere (drying of the supplied ambient air) might be a reasonable strategy to prohibit Cr-poisoning of the cathode.

### 4.5.4 Long-term stability of LSC64 cathodes with different microstructures in direct contact with YSZ electrolytes

By long-term investigations of LSC64 cathodes on YSZ electrolytes it was shown that the combination of these two materials is not suitable for the operation of SOFCs. Polarization resistances were significantly higher already at the beginning of the long-term experiments and degraded very fast.

The time-dependent trend of $ASR_{pol}$ showed different behavior for the screen-printed cathode and the thin-film cathode (Figure 198). While the resistance of thin-film cathode reached a plateau after approximately 600 hours, those of the screen-printed one still increased linearly. These differences can be explained by the different dimensions of the cathode layer. While the thin-film has a thickness of about 100 nm, the screen-printed layer was about 30 µm thick.

Another noticeable difference was the in-situ sintering of the screen-printed LSC64 cathode, which was not sintered at the beginning of the long-term experiment. The unsintered cathode exhibited a large high-frequency arc, which vanished in the first hours of the long-term experiment (see section 4.4.2.2 on page 175). The slight decrease of $ASR_{pol}$ during the first 200 hours (see Figure 198 bottom) might be caused by this sintering effect as well.

In post-test analyses of the thin-film sample a, well-defined layer with a constant concentration of La was found at the interface between cathode and electrolyte. Therefore it is assumed that $La_2Zr_2O_7$ was formed as interfacial secondary phase, which acted as blocking layer for the oxygen diffusion. This is an effect found by various studies, however most of them $SrZrO_3$ was found as interfacial layer rather than $La_2Zr_2O_7$ [45, 122]. On the degraded screen-printed cathode no conclusions on the degradation mechanism could be drawn.

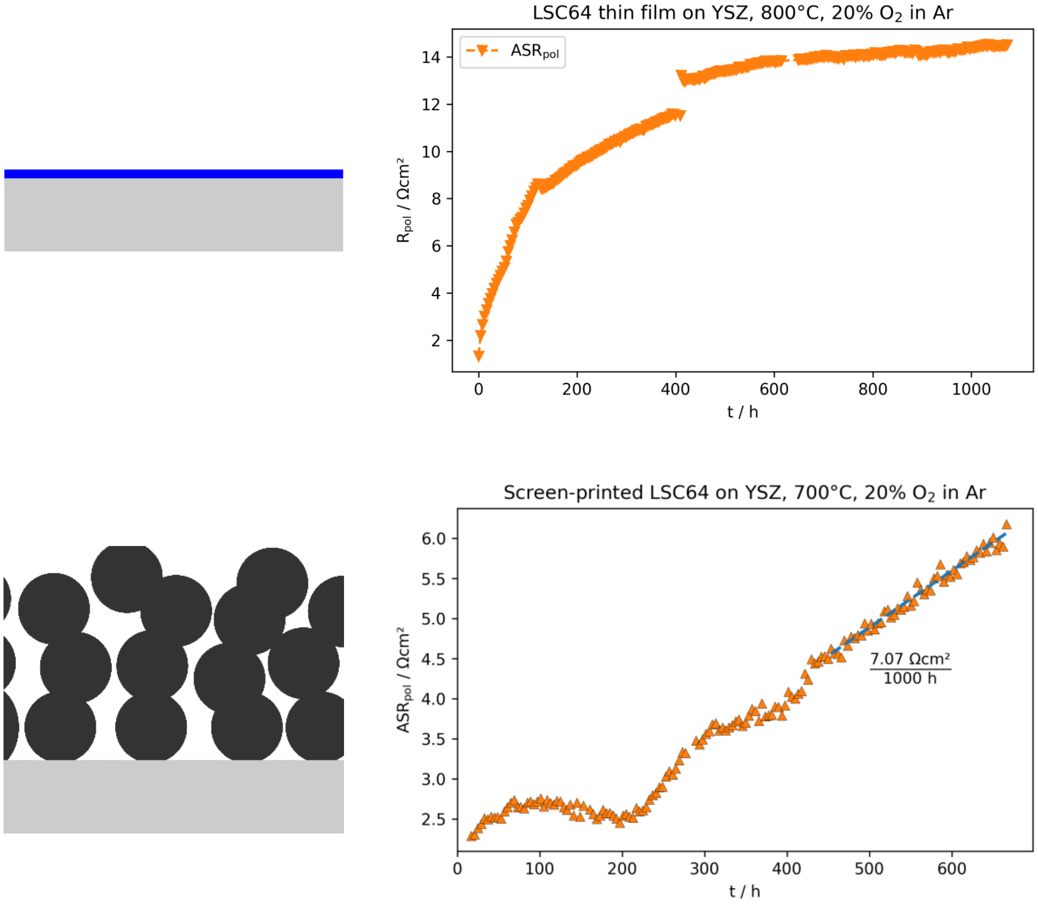

*Figure 198: Comparison of the long-term degradation of thin-film and screen-printed LSC64 cathodes on YSZ electrolytes*

# 5 Conclusions

In the present thesis, two potential solid oxide fuel cell (SOFC) cathode materials, $La_{0.9}Ca_{0.1}FeO_{3-\delta}$ (LCF91) and $LaNi_{0.6}Fe_{0.4}O_{3-\delta}$ (LNF64), and model cathodes of the state-of-the-art materials $La_{0.6}Sr_{0.4}CoO_{3-\delta}$ (LSC64) and $La_{0.6}Sr_{0.4}Co_{0.2}Fe_{0.8}O_{3-\delta}$ (LSCF) with different microstructures were prepared and characterized by dc-conductivity relaxation (CR) and electrochemical impedance spectroscopy (EIS). Relevant parameters for the cathode performance, like the chemical oxygen surface exchange coefficient $k_{chem}$ and the area-specific polarization resistance $ASR_{pol}$, were determined as a function of temperature. In long-term degradation experiments with durations between 1500 and 3800 hours, bulk samples and model cathodes with different microstructures were exposed to typical SOFC cathode operating conditions. Tests were performed in dry or humidified test gas atmospheres, in absence or presence of silicon and chromium sources. Thus, the degradation of the samples could be monitored in-situ under conditions of Si- and Cr-poisoning. These experiments, together with extensive post-text analyses by complementary techniques (SEM, XPS, STEM), provided further insights into the mechanisms of SOFC cathode degradation.

CR experiments with bulk samples of LNF64 and LCF91 showed that LCF91 is a more promising candidate for application as SOFC cathode, due to its superior oxygen exchange kinetics. Nevertheless, LNF64 may still be a useful component of composite cathodes or current collectors due to its relatively high electrical conductivity. LCF91 showed fast oxygen exchange kinetics with $k_{chem}$ around $10^{-3}$ cm/s. However, during the long-term experiment at 700°C, a significant decrease of $k_{chem}$ by three orders of magnitude was found under critical operating conditions (gas phase humidity and presence of a Si-source), which was correlated to Si-poisoning within the first 20 nm of the surface. This particular degradation mechanism has also been found in literature for other mixed-conducting cathode materials.

Systematic EIS experiments with model cathodes of LSC64 and LSCF in different architectures revealed that the long-term performance is determined by the morphology and microstructure of the cathode. Conventional screen-printed and microstructured cathodes of LSC64, which are widely used in commercial fuel cells, showed only a moderate increase of the polarization resistance (about 0.03 $\Omega cm^2$ in 1000 hours) at 700°C under Si-poisoning conditions. However, a screen-printed cathode of LSCF, which was exposed to Cr-poisoning conditions at the same temperature, showed degradation rates of $ASR_{pol}$ above 1 $\Omega cm^2$ in 1000 hours. The different results of these two experiments with Si-poisoning and Cr-poisoning lead to the conclusion that the latter is the more critical degradation mechanism for SOFC cathodes.

Also, nanostructured cathode designs, which have gained tremendous interest in the scientific community in recent years, were characterized with respect to their electrochemical properties and long-term stability. To the knowledge of the author, these were the first systematical studies on the stability of cathodes with nanoscale morphology in humid atmospheres on timescales of 1000 hours. LSC64 cathodes with two different architectures were synthesized by sol-gel methods. On the one hand, thin-film electrodes with thicknesses around 200 nm were obtained by spin-coating, on the other hand a composite structure consisting of a microstructured porous $Ce_{0.9}Gd_{0.1}O_{2-\delta}$ (GDC) backbone coated with nanoparticles of LSC64 was synthesized by wet infiltration. Although both cathode designs were based on nanocrystalline LSC64, they differed significantly in their electrochemical behavior, especially with regard to temperature dependence and long-term stability. Under Si-poisoning conditions, the thin-film cathode showed a relatively fast increase of $ASR_{pol}$ of about 0.3 $\Omega cm^2$ in 1000 hours, while the infiltrated cathode hardly degraded at all. This is a strong indication that the influence of Si-poisoning on the cathode performance decreases with the actual size of the cathode surface area. This correlation might be explained by the fact that Si-poisoning is a contamination which is affecting primarily the surface of cathodes. In contrast to that, Cr contamination of the cathode is affecting the bulk as well, since Cr was shown to diffuse deeper into the LSC64 or LSCF bulk. This was confirmed in the present experiments, where LSC64 thin-film cathodes degraded at least four times faster due to Cr-poisoning than the porous microstructured LSCF cathode.

Experiments with LSC64 cathodes on YSZ showed that this material combination is not stable due to interdiffusion of cations at the interface and formation of electrically insulating secondary phases. In the technical application, a diffusion barrier between YSZ electrolytes and most cathode materials will be inevitable. However, from the scientific point of view, the present EIS experiments indicated that the cathode thickness and microstructure had a significant influence on the time-dependent evolution of the polarization resistance. While the increase of $ASR_{pol}$ of the thin-film cathode reached a plateau after some time, it showed a nearly linear increase with the screen-printed cathode. Post-test analyses of the thin-film cathode revealed that the degradation was predominantly caused by the formation of $La_2Zr_2O_7$, rather than other secondary phases, which have been reported in literature.

Generally, the present experiments with systematic variation of cathode microstructure show that thin-film cathodes are highly sensitive to critical operating conditions, much more so than cathodes with other morphologies. Therefore, thin film cathodes might not be suitable for use in technical SOFC applications, but are excellent model electrodes for basic scientific investigations due to their well-defined geometry. Microscale porous thick film cathodes are relatively robust electrodes which currently represent the state-of-the-art in SOFC applications. However, certain critical operating conditions lead to significant degradation. In the present study, excellent results were obtained with infiltrated nanoscale LSC64 on a porous thick film GDC backbone. These electrodes show exceptionally low values of $ASR_{pol}$ and good long-term stability and may become an interesting alternative to current state-of-the-art cathodes in the next generation of SOFCs.

# 6 References

1. Weber, A. and E. Ivers-Tiffée, *Materials and concepts for solid oxide fuel cells (SOFCs) in stationary and mobile applications.* Journal of Power Sources, 2004. **127**(1–2): p. 273-283.
2. *Bloom Energy*. [cited 2018 2018-03-26]; Available from: https://bloomenergy.com/.
3. *Hexis*. [cited 2018 2018-03-26]; Available from: http://www.hexis.com/.
4. *Fuel Cell Engineering for Heavy-Duty On and Off-Road Vehicles*. [cited 2018 2018-03-26]; Available from: https://www.avl.com/en/fuel-cell-engineering1/-/asset_publisher/gYjUpY19vEA8/content/fuel-cell-engineering-for-heavy-duty-on-and-off-road-vehicles.
5. *Nissan announces development of the world's first SOFC-powered vehicle system that runs on bio-ethanol electric power*. 2016-06-14 [cited 2018 2018-03-26]; Available from: https://newsroom.nissan-global.com/releases/160614-01-e.
6. Yamamoto, O., *Solid oxide fuel cells: fundamental aspects and prospects.* Electrochimica Acta, 2000. **45**(15): p. 2423-2435.
7. Choudhury, A., H. Chandra, and A. Arora, *Application of solid oxide fuel cell technology for power generation—A review.* Renewable and Sustainable Energy Reviews, 2013. **20**: p. 430-442.
8. Shao, Z. and M.O. Tade, *Intermediate-Temperature Solid Oxide Fuel Cells: Materials and Applications*. 1 ed. 2016, Berlin Heidelberg: Springer-Verlag. 266.
9. Bocarsly, A. and D.M.P. Mingos, eds. *Fuel Cells and Hydrogen Storage*. Structure and Bonding. 2011, Springer: Berlin Heidelberg.
10. Zhou, X.-D. and S.C. Singhal, *FUEL CELLS | SOLID OXIDE FUEL CELLS | Overview*, in *Encyclopedia of Electrochemical Power Sources*, J. Garche, Editor. 2009, Elsevier: Amsterdam. p. 1-16.
11. Connelly, N.G., et al., *Point defect (Kröger-Vink) notation*, in *Nomenclature of Inorganic Chemistry - IUPAC recommendations 2005*. 2005, The Royal Society of Chemistry. p. 238-241.
12. Tilley, R.J., *Appendix B Summary of the Kröger–Vink Defect Notation*, in *Perovskites*. 2016.
13. K. Momma and F. Izumi, *VESTA 3 for three-dimensional visualization of crystal, volumetric and morphology data.* J. Appl. Crystallogr., 2011. **44**: p. 1272-1276.
14. Fergus, J.W., *Electrolytes for solid oxide fuel cells.* Journal of Power Sources, 2006. **162**(1): p. 30-40.
15. Tietz, F., *Thermal expansion of SOFC materials.* Ionics, 1999. **5**(1): p. 129-139.
16. Mahato, N., et al., *Progress in material selection for solid oxide fuel cell technology: A review.* Progress in Materials Science, 2015. **72**: p. 141-337.
17. Steele, B.C.H., *Appraisal of* $Ce_{1-y}Gd_yO_{2-y/2}$ *electrolytes for IT-SOFC operation at 500°C.* Solid State Ionics, 2000. **129**(1): p. 95-110.
18. Mogensen, M., N.M. Sammes, and G.A. Tompsett, *Physical, chemical and electrochemical properties of pure and doped ceria.* Solid State Ionics, 2000. **129**(1): p. 63-94.
19. Ishihara, T., H. Eto, and J. Yan, *Intermediate temperature solid oxide fuel cells using LaGaO3 based oxide film deposited by PLD method.* International Journal of Hydrogen Energy, 2011. **36**(2): p. 1862-1867.
20. Shri Prakash, B., et al., *Electrolyte bi-layering strategy to improve the performance of an intermediate temperature solid oxide fuel cell: A review.* Journal of Power Sources, 2018. **381**: p. 136-155.

21. Galloway, K.V. and N.M. Sammes, *FUEL CELLS | SOLID OXIDE FUEL CELLS | Anodes*, in *Encyclopedia of Electrochemical Power Sources*, J. Garche, Editor. 2009, Elsevier: Amsterdam. p. 17-24.
22. da Silva, F.S. and T.M. de Souza, *Novel materials for solid oxide fuel cell technologies: A literature review.* International Journal of Hydrogen Energy, 2017. **42**(41): p. 26020-26036.
23. Hui, S., et al., *Metal-supported solid oxide fuel cell operated at 400–600°C.* Journal of Power Sources, 2007. **167**(2): p. 336-339.
24. Tucker, M.C., *Progress in metal-supported solid oxide fuel cells: A review.* Journal of Power Sources, 2010. **195**(15): p. 4570-4582.
25. Franco, T., et al., *Development of Metal-Supported Solid Oxide Fuel Cells.* ECS Transactions, 2011. **35**(1): p. 343-349.
26. Sammes, N.M. and B.R. Roy, *FUEL CELLS | SOLID OXIDE FUEL CELLS | Cathodes*, in *Encyclopedia of Electrochemical Power Sources*, J. Garche, Editor. 2009, Elsevier: Amsterdam. p. 25-33.
27. Sun, C., R. Hui, and J. Roller, *Cathode materials for solid oxide fuel cells: a review.* J Solid State Electrochem, 2010. **14**(7): p. 1125-1144.
28. Banerjee, A. and O. Deutschmann, *Elementary kinetics of the oxygen reduction reaction on LSM-YSZ composite cathodes.* Journal of Catalysis, 2017. **346**: p. 30-49.
29. Jørgensen, M.J. and M. Mogensen, *Impedance of Solid Oxide Fuel Cell LSM/YSZ Composite Cathodes.* Journal of The Electrochemical Society, 2001. **148**(5): p. A433-A442.
30. Barbucci, A., et al., *Characterisation of composite SOFC cathodes using electrochemical impedance spectroscopy. Analysis of Pt/YSZ and LSM/YSZ electrodes.* Electrochimica Acta, 2002. **47**(13): p. 2183-2188.
31. Holtappels, P. and C. Bagger, *Fabrication and performance of advanced multi-layer SOFC cathodes.* Journal of the European Ceramic Society, 2002. **22**(1): p. 41-48.
32. Nielsen, J. and J. Hjelm, *Impedance of SOFC electrodes: A review and a comprehensive case study on the impedance of LSM:YSZ cathodes.* Electrochimica Acta, 2014. **115**: p. 31-45.
33. Zhao, Y., et al., *Recent progress on solid oxide fuel cell: Lowering temperature and utilizing non-hydrogen fuels.* International Journal of Hydrogen Energy, 2013. **38**(36): p. 16498-16517.
34. Brett, D.J.L., et al., *Intermediate temperature solid oxide fuel cells.* Chemical Society Reviews, 2008. **37**(8): p. 1568-1578.
35. Marinha, D., L. Dessemond, and E. Djurado, *Comprehensive review of current developments in IT-SOFCs.* Current Inorganic Chemistry, 2013. **3**(1): p. 2-22.
36. Mizusaki, J., et al., *Electrical conductivity and Seebeck coefficient of nonstoichiometric* $La_{1-x}Sr_xCoO_{3-d}$. Journal of the Electrochemical Society, 1989. **136**(7): p. 2082-2088.
37. Petrov, A.N., et al., *Crystal structure, electrical and magnetic properties of* $La_{1-x}Sr_xCoO_{3-y}$. Solid State Ionics, 1995. **80**: p. 189-199.
38. Sitte, W., E. Bucher, and W. Preis, *Nonstoichiometry and transport properties of strontium-substituted lanthanum cobaltites.* Solid State Ionics, 2002. **154-155**: p. 517-522.
39. Egger, A., et al., *Comparison of oxygen exchange kinetics of the IT-SOFC cathode materials* $La_{0.5}Sr_{0.5}CoO_{3-\delta}$ *and* $La_{0.6}Sr_{0.4}CoO_{3-\delta}$. Solid State Ionics, 2012. **225**(0): p. 55-60.
40. Dutta, A., J. Mukhopadhyay, and R.N. Basu, *Combustion synthesis and characterization of LSCF-based materials as cathode of intermediate temperature solid oxide fuel cells.* Journal of the European Ceramic Society, 2009. **29**(10): p. 2003-2011.
41. Preis, W., E. Bucher, and W. Sitte, *Oxygen exchange kinetics of* $La_{0.4}Sr_{0.6}FeO_{3-\delta}$ *by simultaneous application of conductivity relaxation and carrier gas coulometry.* Solid State Ionics, 2004. **175**(1): p. 393-397.
42. Mai, A., et al., *Ferrite-based perovskites as cathode materials for anode-supported solid oxide fuel cells: Part I. Variation of composition.* Solid State Ionics, 2005. **176**(15): p. 1341-1350.

43. Ried, P., et al., *Synthesis and Characterization of* $La_{0.6}Sr_{0.4}Co_{0.2}Fe_{0.8}O_{3-\delta}$ *and* $Ba_{0.5}Sr_{0.5}Co_{0.8}Fe_{0.2}O_{3-\delta}$*.* Journal of The Electrochemical Society, 2008. **155**(10): p. B1029-B1035.
44. Backhaus-Ricoult, M., *SOFC – A playground for solid state chemistry.* Solid State Sciences, 2008. **10**(6): p. 670-688.
45. Mai, A., et al., *Time-dependent performance of mixed-conducting SOFC cathodes.* Solid State Ionics, 2006. **177**(19): p. 1965-1968.
46. Kubicek, M., et al., *Cation diffusion in* $La_{0.6}Sr_{0.4}CoO_{3-\delta}$ *below 800 °C and its relevance for Sr segregation.* Physical Chemistry Chemical Physics, 2014. **16**(6): p. 2715-2726.
47. Berger, C., E. Bucher, and W. Sitte, *Mass and charge transport properties of* $La_{0.9}Ca_{0.1}FeO_{3-\delta}$*.* Solid State Ionics, 2017. **299**: p. 46-54.
48. Geary, T.C. and S.B. Adler, *Oxygen nonstoichiometry and defect chemistry of the mixed conductor* $La_{0.9}Ca_{0.1}FeO_{3-\delta}$ *at low oxygen partial pressure.* Solid State Ionics, 2013. **253**: p. 88-93.
49. Dimitrakopoulos, G. and A.F. Ghoniem, *A two-step surface exchange mechanism and detailed defect transport to model oxygen permeation through the* $La_{0.9}Ca_{0.1}FeO_{3-\delta}$ *mixed-conductor.* Journal of Membrane Science, 2016. **510**: p. 209-219.
50. Hunt, A., G. Dimitrakopoulos, and A.F. Ghoniem, *Surface oxygen vacancy and oxygen permeation flux limits of perovskite ion transport membranes.* Journal of Membrane Science, 2015. **489**: p. 248-257.
51. Hunt, A., et al., *Measuring the oxygen profile and permeation flux across an ion transport membrane and the development and validation of a multistep surface exchange model.* Journal of Membrane Science, 2014. **468**: p. 62-72.
52. Wu, X.-Y., et al., *Toward enhanced hydrogen generation from water using oxygen permeating LCF membranes.* Physical Chemistry Chemical Physics, 2015. **17**(15): p. 10093-10107.
53. Chiba, R., F. Yoshimura, and Y. Sakurai, *An investigation of* $LaNi_{1-x}Fe_xO_3$ *as a cathode material for solid oxide fuel cells.* Solid State Ionics, 1999. **124**(3-4): p. 281-288.
54. Bevilacqua, M., et al., *Influence of synthesis route on morphology and electrical properties of* $LaNi_{0.6}Fe_{0.4}O_3$*.* Solid State Ionics, 2006. **177**(33–34): p. 2957-2965.
55. Lee, S., et al., *Solid oxide fuel cell cathodes prepared by infiltration of* $LaNi_{0.6}Fe_{0.4}O3$ *and* $La_{0.91}Sr_{0.09}Ni_{0.6}Fe_{0.4}O_3$ *in porous yttria-stabilized zirconia.* Journal of Power Sources, 2009. **193**(2): p. 747-753.
56. Chen, J., et al., *Optimization of* $LaNi_{0.6}Fe_{0.4}O_{3-\delta}$ *cathode for intermediate temperature solid oxide fuel cells.* Journal of Alloys and Compounds, 2009. **487**(1–2): p. 377-381.
57. Chen, J.Y., et al., *Thermal stability, oxygen non-stoichiometry and transport properties of* $LaNi_{0.6}Fe_{0.4}O_3$*.* Solid State Ionics, 2011. **192**(1): p. 424-430.
58. Sereda, V.V., et al., *Oxygen nonstoichiometry, defect structure and related properties of* $LaNi_{0.6}Fe_{0.4}O_{3-\delta}$*.* Journal of Materials Chemistry A, 2015. **3**(11): p. 6028-6037.
59. Niwa, E., et al., *Oxygen nonstoichiometry and electrical conductivity of* $LaNi_{0.6}Fe_{0.4}O_{3-\delta}$ *at high temperatures under various oxygen partial pressures.* Solid State Ionics, 2015. **274**: p. 119-122.
60. Komatsu, T., et al., *Cr poisoning suppression in solid oxide fuel cells using* $LaNi(Fe)O_3$ *electrodes.* Electrochemical and Solid-State Letters, 2006. **9**(1): p. A9-A12.
61. Zhen, Y.D., et al., $La(Ni,Fe)O_3$ *as a cathode material with high tolerance to chromium poisoning for solid oxide fuel cells.* Journal of Power Sources, 2007. **170**(1): p. 61-66.
62. Stodolny, M.K., et al., *Impact of Cr-poisoning on the conductivity of* $LaNi_{0.6}Fe_{0.4}O_3$*.* Journal of Power Sources, 2011. **196**(22): p. 9290-9298.
63. Stodolny, M.K., et al., *Cr-poisoning of a* $LaNi_{0.6}Fe_{0.4}O_3$ *cathode under current load.* Journal of Power Sources, 2012. **209**(0): p. 120-129.
64. Beckel, D., et al., *Thin films for micro solid oxide fuel cells.* Journal of Power Sources, 2007. **173**(1): p. 325-345.

65. Kreutz, E.W., *Pulsed laser deposition of ceramics – fundamentals and applications.* Applied Surface Science, 1998. **127–129**(0): p. 606-613.
66. Schöning, M.J., et al., *Can pulsed laser deposition serve as an advanced technique in fabricating chemical sensors?* Sensors and Actuators B: Chemical, 2001. **78**(1–3): p. 273-278.
67. Greer, J.A. and M.D. Tabat, *Large-area pulsed laser deposition: Techniques and applications.* Journal of Vacuum Science & Technology A: Vacuum, Surfaces, and Films, 1995. **13**(3): p. 1175-1181.
68. Yoon, J., et al., *Nanostructured cathode thin films with vertically-aligned nanopores for thin film SOFC and their characteristics.* Applied Surface Science, 2007. **254**(1): p. 266-269.
69. Boukamp, B.A., et al., *The impedance of thin dense oxide cathodes.* Solid State Ionics, 2011. **192**(1): p. 404-408.
70. Chang, K.-C., et al., *Synchrotron X-ray studies of model SOFC cathodes, part I: Thin film cathodes.* Solid State Ionics, 2017. **311**: p. 118-126.
71. Stämmler, S., et al., *Phase constitution, Sr distribution and morphology of self-assembled La-Sr-Co-O composite films prepared by PLD.* Solid State Ionics, 2017. **303**: p. 172-180.
72. Li, Y., et al., *Pulsed laser deposition of* $Ba_{0.5}Sr_{0.5}Co_{0.8}Fe_{0.2}O_{3-\delta}$ *thin film cathodes for low temperature solid oxide fuel cells.* Surface and Coatings Technology, 2017. **320**: p. 344-348.
73. Su, Q., et al., *Enhanced electrochemical properties of Bi-layer* $La_{0.5}Sr_{0.5}CoO_{3-\delta}$ *cathode prepared by a hybrid method.* Electrochimica Acta, 2011. **56**(11): p. 3969-3974.
74. Hildenbrand, N., et al., *Improved cathode/electrolyte interface of SOFC.* Solid State Ionics, 2011. **192**(1): p. 12-15.
75. Peters, C., A. Weber, and E. Ivers-Tiffée, *Nanoscaled* $(La_{0.5}Sr_{0.5})CoO_{3-\delta}$ *Thin Film Cathodes for SOFC Application at 500 °C <* $T$ *< 700 °C.* Journal of The Electrochemical Society, 2008. **155**(7): p. B730-B737.
76. Januschewsky, J., et al., *Optimized* $La_{0.6}Sr_{0.4}CoO_{3-\delta}$ *Thin-Film Electrodes with Extremely Fast Oxygen-Reduction Kinetics.* Advanced Functional Materials, 2009. **19**(19): p. 3151-3156.
77. Januschewsky, J., et al., $La_{0.6}Sr_{0.4}CoO_{3-\delta}$ *(LSC) thin film electrodes with very fast oxygen reduction kinetics prepared by a sol-gel route.* Zeitschrift für Physikalische Chemie, 2012. **226**(9-10): p. 889-899.
78. Hayd, J., et al., *Nanoscaled* $La_{0.6}Sr_{0.4}CoO_{3-\delta}$ *as intermediate temperature solid oxide fuel cell cathode: Microstructure and electrochemical performance.* Journal of Power Sources, 2011. **196**(17): p. 7263-7270.
79. Hayd, J., U. Guntow, and E. Ivers-Tiffée, *Electrochemical Performance of Nanoscaled* $La_{0.6}Sr_{0.4}CoO_{3-\delta}$ *as Intermediate Temperature SOFC Cathode.* ECS Transactions, 2010. **28**(11): p. 3-15.
80. Klotz, D., et al., *Nano-Scaled Mixed Conductors for High Performance SOFCs at ≤ 600°C.* ECS Transactions, 2014. **61**(1): p. 23-29.
81. Hayd, J. and E. Ivers-Tiffée, *Detailed Electrochemical Study on Nanoscaled* $La_{0.6}Sr_{0.4}CoO_{3-\delta}$ *SOFC Thin-Film Cathodes in Dry, Humid and* $CO_2$*-Containing Atmospheres.* Journal of The Electrochemical Society, 2013. **160**(11): p. F1197-F1206.
82. Jiang, S.P., *A review of wet impregnation—An alternative method for the fabrication of high performance and nano-structured electrodes of solid oxide fuel cells.* Materials Science and Engineering: A, 2006. **418**(1–2): p. 199-210.
83. Jiang, Z., C. Xia, and F. Chen, *Nano-structured composite cathodes for intermediate-temperature solid oxide fuel cells via an infiltration/impregnation technique.* Electrochimica Acta, 2010. **55**(11): p. 3595-3605.
84. Jiang, S.P., *Nanoscale and nano-structured electrodes of solid oxide fuel cells by infiltration: Advances and challenges.* International Journal of Hydrogen Energy, 2012. **37**(1): p. 449-470.

85. Chiba, R., et al., *A study of cathode materials for intermediate temperature SOFCs prepared by the sol-gel method.* Solid State Ionics, 2004. **175**(1–4): p. 23-27.
86. Liu, M., et al., *Enhanced performance of LSCF cathode through surface modification.* International Journal of Hydrogen Energy, 2012. **37**(10): p. 8613-8620.
87. Zeng, R. and Y. Huang, *Enhancing surface activity of* $La_{0.6}Sr_{0.4}CoO_{3-\delta}$ *cathode by a simple infiltration process.* International Journal of Hydrogen Energy, 2017. **42**(10): p. 7220-7225.
88. Zhao, F., R. Peng, and C. Xia, *A* $La_{0.6}Sr_{0.4}CoO_{3-\delta}$*-based electrode with high durability for intermediate temperature solid oxide fuel cells.* Materials Research Bulletin, 2008. **43**(2): p. 370-376.
89. Shah, M. and S. Barnett, *Solid oxide fuel cell cathodes by infiltration of* $La_{0.6}Sr_{0.4}Co_{0.2}Fe_{0.8}O_{3-\delta}$ *into Gd-Doped Ceria.* Solid State Ionics, 2008. **179**(35-36): p. 2059-2064.
90. Shah, M., P.W. Voorhees, and S.A. Barnett, *Time-dependent performance changes in LSCF-infiltrated SOFC cathodes: The role of nano-particle coarsening.* Solid State Ionics, 2011. **187**(1): p. 64-67.
91. Zhan, W., et al., *Long-term stability of infiltrated* $La_{0.8}Sr_{0.2}CoO_{3-\delta}$*,* $La_{0.58}Sr_{0.4}Co_{0.2}Fe_{0.8}O_{3-\delta}$ *and* $SmBa_{0.5}Sr_{0.5}Co_{2.0}O_{5+\delta}$ *cathodes for low temperature solid oxide fuel cells.* International Journal of Hydrogen Energy, 2015. **40**(46): p. 16532-16539.
92. Samson, A.J., et al., *Highly durable anode supported solid oxide fuel cell with an infiltrated cathode.* Journal of Power Sources, 2012. **216**(Supplement C): p. 124-130.
93. Yang, Z., et al., *A short review of cathode poisoning and corrosion in solid oxide fuel cell.* International Journal of Hydrogen Energy, 2017. **42**(39): p. 24948-24959.
94. Mebane, D.S., *A variational approach to surface cation segregation in mixed conducting perovskites.* Computational Materials Science, 2015. **103**: p. 231-236.
95. Finsterbusch, M., et al., *Electrochemically driven cation segregation in the mixed conductor* $La_{0.6}Sr_{0.4}Co_{0.2}Fe_{0.8}O_{3-\delta}$*.* Solid State Ionics, 2012. **212**: p. 77-80.
96. Araki, W., M. Miyashita, and Y. Arai, *Strontium surface segregation in* $La_{0.6}Sr_{0.4}Co_{0.2}Fe_{0.8}O_{3-\delta}$ *subjected to mechanical stress.* Solid State Ionics, 2016. **290**: p. 18-23.
97. Hjalmarsson, P., M. Søgaard, and M. Mogensen, *Electrochemical performance and degradation of* $(La_{0.6}Sr_{0.4})_{0.99}CoO_{3-\delta}$ *as porous SOFC-cathode.* Solid State Ionics, 2008. **179**(27–32): p. 1422-1426.
98. Tietz, F., A. Mai, and D. Stöver, *From powder properties to fuel cell performance - A holistic approach for SOFC cathode development.* Solid State Ionics, 2008. **179**(27-32): p. 1509-1515.
99. Liu, R.R., et al., *Influence of water vapor on long-term performance and accelerated degradation of solid oxide fuel cell cathodes.* Journal of Power Sources, 2011. **196**(17): p. 7090-7096.
100. Jiang, S.P. and X. Chen, *Chromium deposition and poisoning of cathodes of solid oxide fuel cells – A review.* International Journal of Hydrogen Energy, 2014. **39**(1): p. 505-531.
101. Quadakkers, W.J., et al., *Metallic interconnectors for solid oxide fuel cells – a review.* Materials at High Temperatures, 2003. **20**(2): p. 115-127.
102. Sachitanand, R., et al., *Evaluation of the oxidation and Cr evaporation properties of selected FeCr alloys used as SOFC interconnects.* International Journal of Hydrogen Energy, 2013. **38**(35): p. 15328-15334.
103. Gindorf, C., L. Singheiser, and K. Hilpert, *Vaporisation of chromia in humid air.* Journal of Physics and Chemistry of Solids, 2005. **66**(2): p. 384-387.
104. Hilpert, K., et al., *Chromium vapor species over solid oxide fuel cell interconnect materials and their potential for degradation processes.* Journal of the Electrochemical Society, 1996. **143**(11): p. 3642-3647
105. Chen, X., et al., *Chromium deposition and poisoning in dry and humidified air at* $(La_{0.8}Sr_{0.2})_{0.9}MnO_{3+\delta}$ *cathodes of solid oxide fuel cells.* International Journal of Hydrogen Energy, 2010. **35**(6): p. 2477-2485.

106. Yokokawa, H., et al., *Thermodynamic considerations on Cr poisoning in SOFC cathodes.* Solid State Ionics, 2006. **177**(35–36): p. 3193-3198.

107. Schuler, J.A., et al., *Cr-poisoning in (La,Sr)(Co,Fe)*$O_3$ *cathodes after 10,000h SOFC stack testing.* Journal of Power Sources, 2012. **211**: p. 177-183.

108. Schuler, J.A., et al., *Combined Cr and S poisoning in solid oxide fuel cell cathodes.* Journal of Power Sources, 2012. **201**: p. 112-120.

109. Bucher, E., et al., *Oxygen exchange kinetics of* $La_{0.6}Sr_{0.4}CoO_{3-\delta}$ *affected by changes of the surface composition due to chromium and silicon poisoning.* Solid State Ionics, 2017. **299**: p. 26-31.

110. Schrödl, N., et al., *Long-term stability of the IT-SOFC cathode materials* $La_{0.6}Sr_{0.4}CoO_{3-\delta}$ *and* $La_2NiO_{4+\delta}$ *against combined chromium and silicon poisoning.* Solid State Ionics, 2015. **276**: p. 62-71.

111. Stanislowski, M., et al., *Reduction of chromium vaporization from SOFC interconnectors by highly effective coatings.* Journal of Power Sources, 2007. **164**(2): p. 578-589.

112. Lacey, R., et al., *Evaluation of Co and perovskite Cr-blocking thin films on SOFC interconnects.* Solid State Ionics, 2010. **181**(27-28): p. 1294-1302.

113. Opila, E.J., et al., *Predicting oxide stability in high-temperature water vapor.* JOM, 2006. **58**(1): p. 22-28.

114. Opila, E.J., D.S. Fox, and N.S. Jacobson, *Mass spectrometric identification of Si-O-H(g) species from the reaction of silica with water vapor at atmospheric pressure.* Journal of the American Ceramic Society, 1997. **80**(4): p. 1009-1012.

115. Kaur, G., *Solid Oxide Fuel Cell Components - Interfacial Compatibility of SOFC Glass Seals*. 1 ed. 2016: Springer International Publishing. 408.

116. Schlehuber, D., et al., *Long-term operation of a* $La_{0.58}Sr_{0.4}Co_{0.2}Fe_{0.8}O_{3-\delta}$*-membrane for oxygen separation.* Journal of Membrane Science, 2010. **351**(1-2): p. 16-20.

117. Viitanen, M.M., et al., *Silica poisoning of oxygen membranes.* Solid State Ionics, 2002. **150**(3-4): p. 223-228.

118. Bucher, E. and W. Sitte, *Long-term stability of the oxygen exchange properties of* $(La,Sr)_{1-z}(Co,Fe)O_{3-\delta}$ *in dry and wet atmospheres.* Solid State Ionics, 2011. **192**: p. 480-482.

119. Bucher, E., et al., *Oxygen exchange kinetics of* $La_{0.58}Sr_{0.4}Co_{0.2}Fe_{0.8}O_3$ *at 600°C in dry and humid atmospheres.* Solid State Ionics, 2011. **191**: p. 61-67.

120. Bucher, E., et al., *Impact of humid atmospheres on oxygen exchange properties, surface-near elemental composition, and surface morphology of* $La_{0.6}Sr_{0.4}CoO_{3-\delta}$*.* Solid State Ionics, 2012. **208**: p. 43-51.

121. Bucher, E., et al., *Post-test analysis of silicon poisoning and phase decomposition in the SOFC cathode material* $La_{0.58}Sr_{0.4}Co_{0.2}Fe_{0.8}O_{3-\delta}$ *by transmission electron microscopy.* Solid State Ionics, 2013. **230**: p. 7-11.

122. Dieterle, L., et al., *Structural and chemical properties of nanocrystalline* $La_{0.5}Sr_{0.5}CoO_{3-\delta}$ *layers on yttria-stabilized zirconia analyzed by transmission electron microscopy.* Journal of Materials Science, 2008. **43**: p. 3135-3143.

123. Mai, A., et al., *Ferrite-based perovskites as cathode materials for anode-supported solid oxide fuel cells: Part II. Influence of the CGO interlayer.* Solid State Ionics, 2006. **177**(19): p. 2103-2107.

124. Horita, T., et al., *Visualization of oxide ionic diffusion at SOFC cathode/electrolyte interfaces by isotope labeling techniques.* Solid State Ionics, 2014. **262**: p. 398-402.

125. Kiebach, R., et al., *Stability of* $La_{0.6}Sr_{0.4}Co_{0.2}Fe_{0.8}O_3/Ce_{0.9}Gd_{0.1}O_2$ *cathodes during sintering and solid oxide fuel cell operation.* Journal of Power Sources, 2015. **283**: p. 151-161.

126. Tu, H.Y., et al., $Ln_{0.4}Sr_{0.6}Co_{0.8}Fe_{0.2}O_{3-\delta}$ *(Ln=La, Pr, Nd, Sm, Gd) for the electrode in solid oxide fuel cells.* Solid State Ionics, 1999. **117**(3): p. 277-281.

127. Egger, A., *Rare earth nickelates as cathodes for solid oxide fuel cells*, in *Department of General, Analytical and Physical Chemistry*. 2013, Montanuniversitaet Leoben, Austria. p. 231.
128. Preis, W., M. Holzinger, and W. Sitte, *Application of the van der Pauw method to conductivity relaxation experiments on* $YBa_2Cu_3O_{6+\delta}$. Monatshefte für Chemie, 2001. **132**: p. 499-508.
129. den Otter, M.W., et al., *Reactor flush time correction in relaxation experiments.* Journal of the Electrochemical Society, 2001. **148**(2): p. J1-J6.
130. Yasuda, I. and M. Hishinuma, *Electrical conductivity and chemical diffusion coefficient of Sr-doped lanthanum chromites.* Solid State Ionics, 1995. **80**(1): p. 141-150.
131. Yasuda, I. and M. Hishinuma, *Electrical Conductivity and Chemical Diffusion Coefficient of Strontium-Doped Lanthanum Manganites.* Journal of Solid State Chemistry, 1996. **123**(2): p. 382-390.
132. den Otter, M.W., L.M. van der Haar, and H.J.M. Bouwmeester, *Numerical evaluation of eigenvalues of the sheet diffusion problem in the surface/diffusion mixed regime.* Solid State Ionics, 2000. **134**(3-4): p. 259-264.
133. Jorcin, J.-B., et al., *CPE analysis by local electrochemical impedance spectroscopy.* Electrochimica Acta, 2006. **51**(8–9): p. 1473-1479.
134. Boukamp, B.A. and H.J.M. Bouwmeester, *Interpretation of the Gerischer impedance in solid state ionics.* Solid State Ionics, 2003. **157**(1–4): p. 29-33.
135. Adler, S.B., J.A. Lane, and B.C.H. Steele, *Electrode Kinetics of Porous Mixed-Conducting Oxygen Electrodes.* Journal of the Electrochemical Society, 1996. **143**(11): p. 3554-3564.
136. Adler, S.B., *Mechanism and kinetics of oxygen reduction on porous* $La_{1-x}Sr_xCoO_{3-\delta}$ *electrodes.* Solid State Ionics, 1998. **111**(1–2): p. 125-134.
137. Nechache, A., et al., *Diagnosis of a cathode-supported solid oxide electrolysis cell by electrochemical impedance spectroscopy.* Electrochimica Acta, 2016. **210**: p. 596-605.
138. Dittrich, H. and A. Bieniok, *MEASUREMENT METHODS | Structural Properties: X-Ray and Neutron Diffraction*, in *Encyclopedia of Electrochemical Power Sources*, J. Garche, Editor. 2009, Elsevier: Amsterdam. p. 718-737.
139. Tonti, D. and R. Zanoni, *MEASUREMENT METHODS | Electronic and Chemical Properties: X-Ray Photoelectron Spectroscopy*, in *Encyclopedia of Electrochemical Power Sources*, J. Garche, Editor. 2009, Elsevier: Amsterdam. p. 673-695.
140. Hofmann, S., *Characterization of nanolayers by sputter depth profiling.* Applied Surface Science, 2005. **241**(1): p. 113-121.
141. Wang, J.Y., U. Starke, and E.J. Mittemeijer, *Evaluation of the depth resolutions of Auger electron spectroscopic, X-ray photoelectron spectroscopic and time-of-flight secondary-ion mass spectrometric sputter depth profiling techniques.* Thin Solid Films, 2009. **517**(11): p. 3402-3407.
142. Marassi, R. and F. Nobili, *MEASUREMENT METHODS | Structural and Chemical Properties: Scanning Electron Microscopy*, in *Encyclopedia of Electrochemical Power Sources*, J. Garche, Editor. 2009, Elsevier: Amsterdam. p. 758-768.
143. Marassi, R. and F. Nobili, *Measurement methods - Structural and chemical properties: Transmission electron microscopy*, in *Encyclopedia of electrochemical power sources*, J. Garche, Editor. 2009, Elsevier: Amsterdam. p. 769-789.
144. van der Walt, S., S.C. Colbert, and G. Varoquaux, *The NumPy Array: A Structure for Efficient Numerical Computation.* Computing in Science & Engineering, 2011. **13**(2): p. 22-30.
145. Newville, M., et al., *LMFIT: Non-Linear Least-Square Minimization and Curve-Fitting for Python*. 2014.
146. Hunter, J.D., *Matplotlib: A 2D graphics environment.* Computing In Science & Engineering, 2007. **9**(3): p. 90-95.

147. Nicholas, J.D., et al., *Use of the Simple Infiltrated Microstructure Polarization Loss Estimation (SIMPLE) model to describe the performance of nano-composite solid oxide fuel cell cathodes.* Physical Chemistry Chemical Physics, 2012. **14**(44): p. 15379-15392.
148. Lide, D.R., *CRC Handbook of Chemistry and Physics*. 76th ed. ed. 1995-1996, Boca Raton, Florida: CRC Press Inc.
149. Nielsen, J., et al., *Effect of low temperature in-situ sintering on the impedance and the performance of intermediate temperature solid oxide fuel cell cathodes.* Journal of Power Sources, 2014. **245**: p. 418-428.
150. Budiman, R.A., et al., *Electronic conduction mechanism and defect chemical model of* $LaNi_{0.4}Fe_{0.6}O_{3-\delta}$*.* Solid State Ionics, 2017. **310**: p. 148-153.
151. Pérez-Coll, D., P. Núñez, and J.R. Frade, *The role of* $SiO_2$ *and sintering temperature on the grain boundary properties of* $Ce_{0.8}Sm_{0.2}O_{2-\delta}$*.* Journal of Power Sources, 2011. **196**(20): p. 8383-8390.
152. Zhang, T.S., et al., *Different conduction behaviors of grain boundaries in* $SiO_2$*-containing 8YSZ and CGO20 electrolytes.* Solid State Ionics, 2006. **177**(13): p. 1227-1235.
153. Burye, T.E. and J.D. Nicholas, *Improving* $La_{0.6}Sr_{0.4}Co_{0.8}Fe_{0.2}O_{3-\delta}$ *infiltrated solid oxide fuel cell cathode performance through precursor solution desiccation.* Journal of Power Sources, 2015. **276**(0): p. 54-61.
154. Zhao, F., et al., *A high performance intermediate-temperature solid oxide fuel cell using impregnated* $La_{0.6}Sr_{0.4}CoO_{3-\delta}$ *cathode.* Journal of Alloys and Compounds, 2009. **487**(1–2): p. 781-785.
155. Schuler, A.J., et al., *Sulfur as Pollutant Species on the Cathode Side of a SOFC System.* ECS Transactions, 2009. **25**(2): p. 2845-2852.
156. Yu, Y., et al., *Chemical characterization of surface precipitates in* $La_{0.7}Sr_{0.3}Co_{0.2}Fe_{0.8}O_{3-\delta}$ *as cathode material for solid oxide fuel cells.* Journal of Power Sources, 2016. **333**: p. 247-253.
157. Perz, M., et al., *Long-term degradation of* $La_{0.6}Sr_{0.4}Co_{0.2}Fe_{0.8}O_{3-\delta}$ *IT-SOFC cathodes due to silicon poisoning.* Solid State Ionics, 2016. **288**: p. 22-27.
158. Hwang, J.-H., et al., *Experimental limitations in impedance spectroscopy:: Part IV. Electrode contact effects.* Solid State Ionics, 1997. **98**(1): p. 93-104.
159. Badwal, S.P.S., *Grain boundary resistivity in zirconia-based materials: effect of sintering temperatures and impurities.* Solid State Ionics, 1995. **76**(1-2): p. 67-80.
160. Lane, J.A., J.L. Neff, and G.M. Christie, *Mitigation of the deleterious effect of silicon species on the conductivity of ceria electrolytes.* Solid State Ionics, 2006. **177**(19): p. 1911-1915.
161. Shah, M., J.D. Nicholas, and S.A. Barnett, *Prediction of infiltrated solid oxide fuel cell cathode polarization resistance.* Electrochemistry Communications, 2009. **11**(1): p. 2-5.